# The role of p53 cofactor JMY in the regulation of gene expression in human tumours during DNA damage

Ignacio Rodriguez Pastrana

A thesis submitted in partial fulfilment of the requirements of Nottingham Trent University for the degree of Doctor of Philosophy.

**July 2023**

# Acknowledgements

I want to thank my supervisor Dr Amanda S Coutts, for your endless support, encouragement and patience and your invaluable guidance, mentorship and advice during these last four years. I am extremely grateful for the opportunity to complete my PhD as part of your research group. I hope to live up to the scientist you have mentored me to become.

To my supervisory team, Dr Cristina Montiel-Duarte, Prof Sergio Rutella and Prof Graham Ball, for your feedback, critique and assistance during the project. Especially, I want to thank Dr Cristina Montiel-Duarte for your empathy and comradeship outside academia; you helped me see this career path from a different perspective. I also want to thank Dr Graham Hickman and Dr Dominic Craske for sharing their expertise in microscopy and for all their assistance during this project.

To the rest of the members of the Coutts' lab (past and present). Dr Eleni Birli and Hanne Hansen, thank you for all your help and support and for making and enjoyable and friendly working environment within the lab.

To all my colleagues, I am incredibly grateful for your friendship. All of you have made this PhD project an enjoyable and memorable moment of my life. It has been an absolute pleasure. A special thanks to Laura Lestón-Pinilla, your invaluable friendship and support made a massive impact on my persona.

A mi familia. A mis padres y mi hermana, muchas gracias por vuestro apoyo incondicional, por siempre estar a mi lado en los momentos más difíciles y por siempre guiarme cuando más lo necesito. Sin vosotros no habría conseguido acabar esta etapa y ser quien soy ahora.

Ao meu marido Vitor, você sabe o quão importante é para mim. Sem você hoje não estaria aqui, não haveria conseguido acabar o meu doutorado. Obrigado por todo seu amor e apoio, você conseguiu encontrar luz de mim neste momento difícil. Jamais vou poder devolver tanto amor como o que você me dá.

To every one of you, thank you!

# Abstract

The tumour suppressor p53 is a nuclear transcription factor that orchestrates a myriad of cellular pathways, including cell cycle arrest, DNA repair, and apoptosis in response to stress. JMY is a DNA damage responsive actin nucleator which exhibits dynamic cellular localisation depending on different stressors. Upon specific genotoxic stress conditions, JMY undergoes nuclear accumulation, where it enhances p53 transcriptional activity. To expand our understanding of the transcriptional regulatory role of nuclear JMY, we performed a transcriptomic analysis to identify JMY-mediated changes in gene expression during etoposide-induced DNA damage. Our findings reveal novel functions of nuclear JMY in DNA repair, paraspeckle biogenesis, and alternative splicing. Notably, the absence of JMY compromises the expression of p53-dependent targets involved in DNA repair, leading to impaired activation of the DNA damage response and the accumulation of DNA lesions. Moreover, we demonstrate that JMY's Arp2/3-dependent actin nucleation role promotes the p53-dependent expression of DNA repair factors and enhances DNA repair. Remarkably, the loss of JMY sensitises tumour cells to chemotherapeutic agents, reducing cell survival and proliferation. These results are reflected in human tumours where lower *JMY* levels are correlated with increased overall patient survival.

Additionally, our findings demonstrate that JMY impacts on the p53-dependent transcriptional regulation of lncRNA *NEAT1_2* and thus paraspeckle biogenesis. Although the mechanisms are incompletely understood, we observe that the disruption of paraspeckles increases tumour cell sensitivity to DNA damaging agents. Furthermore, our study establishes that JMY is required for the expression of U2 snRNP-related splicing factors and shows that JMY modulates alternative splicing during DNA damage. Collectively, these results provide further insights into the transcriptional regulatory role of nuclear JMY within human tumour cells during DNA damage and can lead to potential clinical opportunities to target key cellular pathways such as the p53 signalling response and alternative splicing.

# Table of contents

# Publications and oral presentations

Publications.

Rodriguez-Pastrana, I., Birli, E., & Coutts, A. S. (2023). p53-dependent DNA repair during the DNA damage response requires actin nucleation by JMY. Cell Death & Differentiation, 1–12. https://doi.org/10.1038/s41418-023-01170-9.
Rodriguez-Pastrana, I., Hansen, H., Birli, E., & Coutts, A. S. (2023). p53 cofactor JMY impacts alternative splicing during DNA damage through modulating paraspeckle biogenesis (in preparation).

Oral presentations.

| | |
|---|---|
| June 2020 – NTU STAR conference. | *p53 cofactor JMY regulates gene expression in human cancers.* |
| Feb 2021 - John van Geest meeting. | *p53 cofactor JMY regulates gene expression in human cancers.* |
| Sep 2021 – CellLaVie! Conference (flask talk). | *The role of p53 cofactor JMY in DNA repair.* |
| Nov 2021 - John van Geest meeting. | *The role of the p53 co-factor JMY in the regulation of gene expression in human cancer.* |
| May 2022 – SST department seminar. | *p53-dependent DNA repair during the DNA damage response requires actin nucleation by JMY.* |
| Jun 2022 – BACR 60th meeting (poster). | *p53-dependent DNA repair during the DNA damage response requires actin nucleation by JMY.* |
| Nov 2022 - John van Geest meeting. | *The role of p53 cofactor JMY in paraspeckle formation during DNA damage.* |
| Jun 2023 – EACR2023 congress (poster). | *p53 cofactor JMY is required for the formation of paraspeckles during DNA damage.* |

# List of figures

# List of tables

# List of abbreviations

General list of abbreviations.

The complete list of general abbreviations is detailed in SI Table 1.1.

List of gene and protein abbreviations.

The complete list of gene and protein abbreviations is detailed in SI Table 1.2.

# Chapter 1: Introduction.

## 1.1. The DNA damage response.

The induction of DNA damage – Role of genotoxic stressors.

Our DNA is constantly threatened by a wide range of conditions that are able to induce DNA damage. DNA lesions can arise from both endogenous and exogenous factors [1]. Endogenous sources of DNA damage are commonly byproducts from cellular metabolic processes, resulting in hydrolysis, oxidation, alkylation, and mismatch of DNA bases. In comparison, exogenous factors are external physical and chemical agents, including ionising radiation, ultraviolet (UV) radiation and a wide variety of chemical compounds [2]. As a result of the persistent exposure to genotoxic stressors, cells have developed sophisticated signalling mechanisms, referred to as the DNA damage response (DDR), to counter these threats [3].

The DDR is commonly initiated by the arrest of the cell cycle, which is thought to grant sufficient time to repair the DNA lesion before cell division [2]. Cells can activate highly specialised DNA repair pathways to resolve DNA lesions [1]. When cells are exposed to prolonged DNA damaging conditions or if the DNA lesion remains unrepaired, cells can initiate apoptosis (referred to as programmed cell death) as a preventive mechanism to reduce the propagation of genomic errors [1]. The importance of the DDR is highlighted by the fact that tumour cells present defects or aberrant expression of key components within these pathways, leading to the reliance of tumour cells on compensatory and often less efficient mechanisms [4]. Unrepaired DNA lesions result in increased mutational burden and genomic instability, two key hallmarks of tumour cells [5]. Due to the high proliferative rate of cancer cells and their dependency on error-prone DDR pathways, the majority of DNA damaging agents, such as in conventional chemotherapy, exert their effects by generating DNA lesions. In contrast, targeted agents inhibit particular targets that promote tumour cell proliferation and survival, like essential proteins involved within the DDR [6]. Throughout this project, etoposide and 4-nitroquinoline-1-oxide (4NQO), have been employed to induce DNA damage and activate the DDR. Etoposide is routinely employed in treating various malignancies such as testicular, prostate, bladder, stomach, and lung cancer, whereas 4NQO has been described to act against specific carcinomas like oral squamous cell carcinoma [7,8].

Etoposide is a potent inhibitor of topoisomerase II, which is a key protein involved in the regulation of DNA topology, such as resolving excessive strain within the double helix [9]. Eukaryotic cells present two isoforms of topoisomerase II (TOP2), where TOP2$\alpha$ is required during DNA replication and chromosome segregation, whilst TOP2$\beta$ is needed during transcription [10]. TOP2 presents three domains referred to as N-, DNA- and C-gate, respectively. TOP2 homodimers bind to duplex DNA via nucleophilic attack to the phosphate group within the DNA backbone [9]. Initially, the TOP2 N-gate binds with a DNA duplex (G-segment) and leads to its retention within the DNA-gate [11]. A second DNA duplex (T-segment) is recruited to the N-gate, in an ATP-dependent manner, which results in conformational changes of TOP2, leading to the cleavage of both strands of the G-segment [12]. This cleavage allows TOP2 to move the T-segment from the N-gate to the C-gate, where the T-segment is released. After the release of the T-segment, further conformational changes in TOP2 cause the ligation and release of the G-segment [11]. This cycle allows TOP2 to remove supercoil twists (excessive torsion) and resolve tangled or knotted duplex DNA [13]. Finally, TOP2 returns to its original conformation presenting an open N-gate for recruiting new G-segments [9]. Under non-perturbed conditions, TOP2 is able to ligate the G-segment as described above. However, when TOP2 activity is compromised, the G-segment intermediate can be left unligated resulting in double-strand DNA breaks (DSBs) [13]. Etoposide binds to one of the subunits of the TOP2 homodimer through a direct interaction within the ATP binding domain [14]. This interaction stalls TOP2 in a conformation that is unable to ligate the transient G-segment intermediate, leading to the formation of DNA strand breaks [13,14].

4NQO is a synthetic chemotherapeutic agent (UV-radiation mimetic) derived from a quinoline that induces base substitutions within the DNA, primarily GC to AT transitions [15]. To acquire its mutagenic activity, 4NQO needs to be metabolised by NAD(P)H-quinone oxidoreductase [16]. This metabolic process is performed in two steps where 4NQO is first converted into 4-hydroxyaminoquinoline-1-oxide (4HAQO) intermediate, which is then metabolised into 4-aminoquinoline-1-oxide (4AQO) [17]. A seryl-tRNA synthetase catalyses the binding between these 4NQO intermediates and DNA and requires the presence of ATP and $Mg^{2+}$ [18]. Both 4HAQO and 4AQO present a potent mutagenic nitro group that, when bound to DNA, induces the transition of two guanines and an adenine [18]. This results in the formation of quinolone mono-adducts which are hypothesised to drive the mutagenic and genotoxic role of 4NQO [17,19]. For example, the oxidation of these

quinolone mono-adducts to 8-hydroxydeoxyguanosines (8OHdG) promotes the transversion of guanines to thymines resulting in DNA adducts. Deficient repair of these DNA lesions can also evolve into single-strand DNA breaks (SSBs) [16].

DNA repair pathways.

In response to the aforementioned DNA damaging agents, cells initiate a myriad of signalling pathways resulting in cell cycle arrest, hence stopping cellular proliferation. This arrest is believed to promote the expression of DNA repair factors that can attempt to repair the damaged DNA before cell division [3]. Different cellular DNA repair pathways can be activated depending on the dose and exposure to specific genotoxic stressors [20]. In response to these DNA lesions, cells activate highly specialised DNA repair pathways [3]. Despite the extensive characterisation of the sequential events comprising these pathways, the precise cellular mechanisms controlling the activation of specific DNA repair processes, as well as the intricate interplay between these pathways, remain poorly understood.

The accumulation of endogenous metabolic byproducts (*e.g.* reactive oxygen species), defective DNA repair, and abortive TOP1 activity leads to modifications in nucleobases that, when unresolved, result in the formation of SSBs [2]. In response to SSBs, cells present two main repair mechanisms, including base excision repair (BER) and nucleotide excision repair (NER) pathways [21]. In response to DSBs, cells activate two main repair mechanisms, including non-homologous end joining (NHEJ) and homologous recombination (HR) [22]. The following paragraphs describe the details of the aforementioned DNA repair pathways.

The BER pathway is initiated by the recognition of the aberrant nucleotide by DNA glycosylases (Fig. 1.1a). In humans, there are two families of DNA glycosylases, including monofunctional and bifunctional enzymes [23]. Monofunctional DNA glycosylases recognise the aberrant nucleotide and remove the sugar-phosphate backbone, followed by the elimination of the nucleotide via apurinic/apyrimidinic (AP) nucleases like APE1, leading to the formation of SSBs [24]. Alternatively, bifunctional DNA glycosylases directly process the abnormal nucleotide, leading to the formation of SSBs in the absence of AP nucleases [23]. The formation of these SSBs generates unconventional 5'- and 3'-ends that require further processing for subsequent ligation. These intermediates include the formation of 5'-

deoxyribosephosphate (dRP), 3'-phosphate and 3'-phosphoglycolate ends compared with the conventional 5'-phosphate (5'-P) and 3'-hydroxyl (3'-OH) ends [1]. DNA polymerase β processes the 5'-dRP end through its AP lyase activity to create a 5'-P end, while PNKP and APE1 process the 3'-phosphate/3'-phosphoglycolate ends, forming a 3'-OH end (Fig. 1.1a). These processing steps are catalysed by XRCC1 cofactor [25]. Following the processing of both SSB ends, the single-nucleotide gap can be repaired by two mechanisms, including short-patch or long-patch. In the short-patch repair, a single nucleotide is introduced by DNA polymerase β and DNA polymerase λ. Within the long-patch repair, 2-10 nucleotides are introduced by DNA polymerase δ and DNA polymerase ε, which requires the presence of PCNA to displace the 5'-end. [26]. The overhanging single-stranded DNA is subsequently removed by FEN1 endonuclease (Fig. 1.1a) [27]. Ultimately, DNA ligase III and DNA ligase I are responsible for the ligation step in the short-patch and long-patch repair processes, respectively (Fig. 1.1a) [26]. Other factors, such as PARP1 and PARP2, are suggested to play a role in the early stages of the BER pathway through the recognition of SSBs and subsequent recruitment of BER factors [25].

The NER pathway resolves SSBs derived from alterations that thermodynamically destabilise the DNA double helix, irrespective of a physical lesion [28]. The NER pathway is initiated by the identification of the DNA lesion by the XPC-RAD23B heterodimer (Fig. 1.1b), where RAD23B acts as a cofactor preventing the proteasomal degradation of XPC [29]. The stabilisation of the XPC-RAD23B heterodimer adjacent to the DNA lesion promotes the recruitment of TFIIH, a multiprotein complex consisting of three subunits, including the core (XPB, XPA), cyclin-activated kinase (CAK) and bridge (XPD) [30]. Upon recruitment, TFIIH disassembles the CAK subunit, enabling the activation of XPA and XPD helicases. XPA and XPD then unwind a small segment upstream of the DNA lesion, forming a dsDNA-ssDNA junction [31]. The subsequent interaction of XPC with the DNA lesion induces further conformational changes in the TFIIH complex, facilitating the intercalation of XPA between the DNA double helix downstream of the damaged site. Subsequently, XPA transfers the DNA region containing the lesion to XPD for scanning [31]. The XPD core is formed by a tight pocket that allows unperturbed dsDNA to pass through. However, thermodynamically destabilised DNA will get stalled. Upon encountering these lesions, blocked XPD leads to conformational changes in XPA, which unwinds the flanking regions to the damaged DNA site [31]. Then, RPA is rapidly recruited to ssDNA overhangs through its interaction with

XPA, which promotes the subsequent recruitment of XPG, and ERCC1-XPF endonucleases to the DNA lesion (Fig. 1.1b) [30]. XPF will then catalyse the first cut forming a 3'-OH end, whilst XPG induces the second cut producing the 5'-P end [31]. DNA polymerase δ and DNA polymerase ε use these nucleotide ends to fill the single-nucleotide gap. Ultimately, the ligation is performed by DNA ligase I and DNA ligase III (Fig. 1.1b) [21].

The NHEJ repair is initiated by the recruitment of the Ku heterodimeric complex to DSBs (Fig. 1.1c) [32]. This Ku heterodimer is composed of XRCC5 (Ku80) and XRCC6 (Ku70) subunits and presents a ring-like structure that serves as a scaffold for the recruitment of NHEJ repair factors [33]. The stabilisation of the Ku heterodimeric complex within the DSB leads to the recruitment and activation of DNA-PK (Fig. 1.1c) [33]. However, this complex is unstable in DSBs, presenting long overhanging ssDNA ends [32]. To increase the stability of the complex, DNA-PK initiates a signalling response that promotes the formation of blunt or sort ssDNA ends. Initially, DNA-PK recruits and activates APTX, which removes covalently linked radicals (*e.g.* adenylate groups) to generate canonical 5'-P ends. These ends are recognised by Artemis, which triggers the subsequent binding of PNKP [34]. Both proteins employ their endonuclease activity to generate blunt or short ssDNA segments with 3'-OH ends [34]. This processing increases the stability of the Ku heterodimer, whereas DNA-PK facilitates the recruitment and activation of other NHEJ factors, such as XRCC4 and XLF [35]. The recruitment of XRCC4 and XFL to the damaged DNA site further reinforces the stability of the complex and promotes the recruitment of DNA polymerase μ and DNA polymerase λ, which will connect the flanking edges of the DSB. Ultimately, the ligation is catalysed by DNA ligase IV [32].

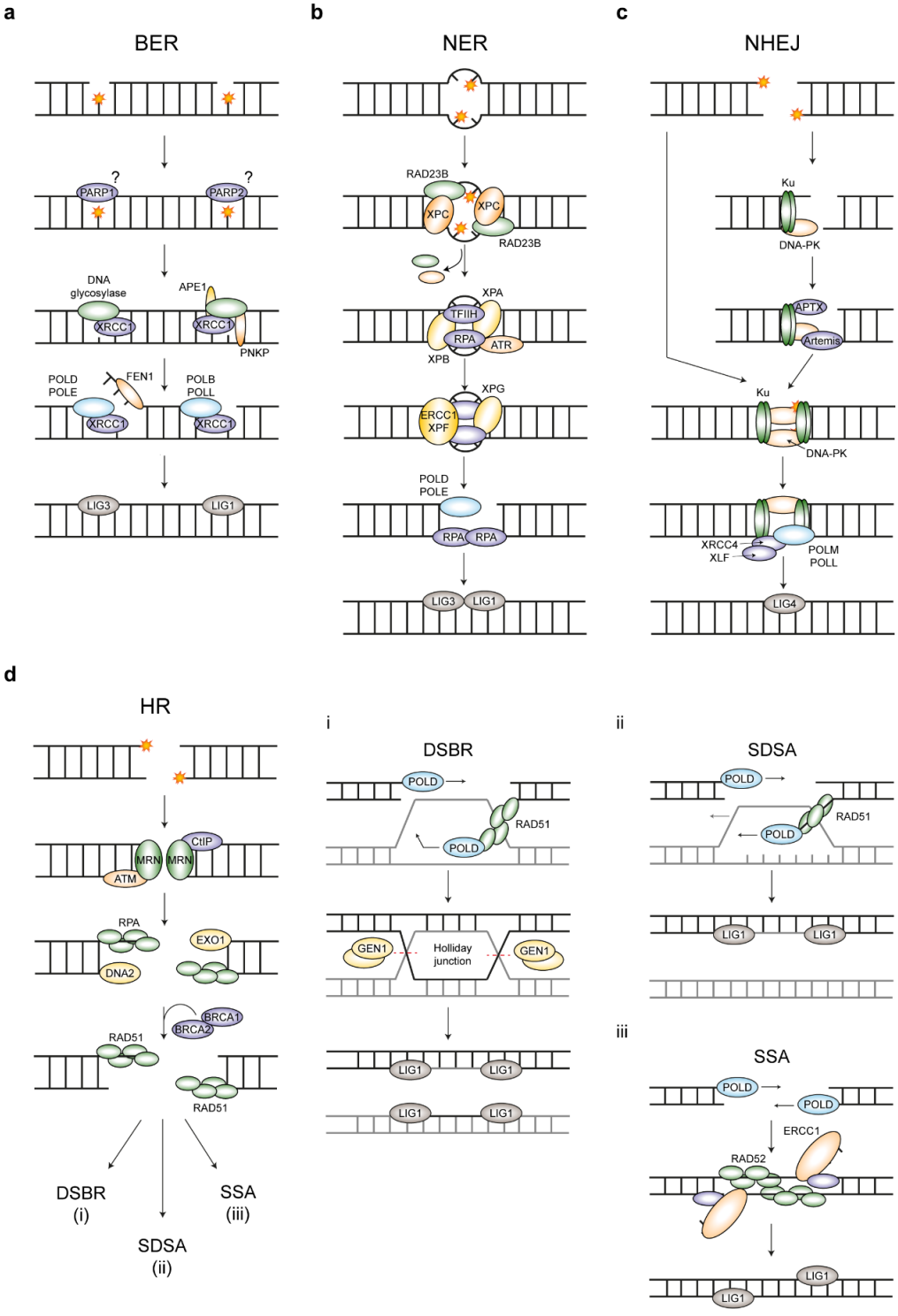


***Figure 1.1. DNA repair pathways. a-d)*** *Schematic representation of the main human DNA repair pathways, including base excision repair pathways (**a**, BER), nucleotide excision repair (**b**, BER), non-homologous end joining (**c**, NHEJ) and homologous recombination (**d**, HR). The proteins involved in these pathways are highlighted in the figure, and their HUGO gene nomenclature is detailed in the list of gene abbreviations. The figure was adapted from* [1].

NHEJ is considered an error-prone repair pathway compared to HR because the latter uses an accessory DNA fragment presenting a homologous sequence (*e.g.* sister chromatid) as a template to repair the damaged DNA [1]. HR is initiated by the recruitment of the MRN complex to DSBs (Fig. 1.1d). This complex is composed of MRE11, RAD50 and NBS1, and it is activated via ATM and CtIP [36]. The activation of the MRN complex leads to the recruitment of EXO1 and DNA2 exonucleases (Fig. 1.1d), which degrade the unprotected flanking edges of the DSB producing overhanging ssDNA segments presenting 3'-OH ends. This process is known as DNA end resection (hereafter referred to as resection) [37].

The overhanging ssDNA segments are rapidly coated with RPA, which is then replaced with RAD51 in a process controlled by BRCA1 and BRCA2 [38]. RAD51 forms a ribonucleoprotein (RNP) complex with the ssDNA and leads to the invasion of the sister chromatid, forming a displacement loop (D-loop, Fig. 1.1d) [39]. Within the D-loop, RAD51 promotes base-pairing interactions with the complementary strand of the sister chromatid, searching for homologous sequences (known as donors). Upon recognition of the donor sequence and stabilisation of the interaction between the strands, DNA polymerase δ uses the 3'-OH end of the invading strand as a primer to start the synthesis of a new DNA fragment using the genomic information from the donor sequence [22]. D-loop structures can be resolved by two main mechanisms, including canonical DSB repair (DSBR) and synthesis-dependent DNA strand annealing (SDSA). In the DSBR, DNA polymerase δ extends the invading strand without displacing the D-loop resulting in the formation of a 4-way DNA strand structure called a Holliday junction (Fig. 1.1d). These structures are resolved by GEN1, which symmetrically cuts in the intersection of the four DNA strands, generating DNA intermediates that are ligated by DNA ligase I [40]. In the SDSA mechanism, DNA polymerase δ extends the invading strand while displacing the D-loop, which avoids the formation of Holliday junctions (Fig. 1.1d). Then, the non-invading strand of the damaged chromatid facilitates the re-annealing with the invading strand [22]. Ultimately, ligation is catalysed by DNA ligase I [1]. Although less frequent, HR can also be resolved by single-strand annealing (SSA, Fig. 1.1d) [41].

NHEJ repair operates throughout the cell cycle, whereas HR is restricted to the S-G2 phase due to the requirement for homologous sequences [22]. Although the detailed mechanisms are incompletely understood, during the G1 phase, DNA-PK can phosphorylate and activate 53BP1, which forms a ribonucleoprotein (RNP)

that inhibits the recruitment of the MRN complex to the DSB [36]. The activation of BRCA1 during the S-G2 phase can induce the detachment of 53BP1 and, thus, the initiation of HR [39].

ATM, ATR and DNA-PK, key proteins in the DNA damage response.

Cells are constantly exposed to genotoxic stressors that induce DNA lesions [2]. Due to the broad spectrum of DNA damaging agents, cells have developed highly specialised regulatory mechanisms to respond to such genotoxic stress. These mechanisms are collectively known as the DDR [6]. As described, the activation of the DDR results in cell cycle arrest and expression of DNA repair factors to resolve the DNA lesions before cellular proliferation. If there is prolonged exposure to genotoxic stressors or the DNA lesion is left unrepaired, cells can initiate apoptosis as a preventive mechanism to reduce the propagation of genomic errors [3]. Tumour cells frequently present mutations in DNA repair factors and often rely on error-prone DDR pathways [4], which, combined with their high proliferative rate increases the genomic instability of tumour cells [6,42]. This process, wherein the loss of one cellular pathway results in high reliance on another pathway, which is not essential under normal conditions, is known as synthetic lethality [6]. However, these characteristics provide a therapeutic opportunity to target DDR pathways and thereby strategically killing tumour cells [6].

An extensive body of research supports the clinical use of inhibitors targeting key DNA repair factors [42,43]. These inhibitors have shown notable improvements in patient survival compared to conventional DNA damaging chemotherapeutic agents [44]. The mechanism of action of the vast majority of these inhibitors relies on the overaccumulation of unrepaired DNA lesions, due to the high proliferation rate of tumour cells and their dependency on error-prone DNA repair pathways [42,45]. Frequently, these DDR inhibitors are administered in combination with conventional chemotherapy or other DDR inhibitors, augmenting their toxicity [46]. Some examples include inhibitors targeting PARP1, ATM, ATR, DNA-PK, CHK1, CHK2 and WEE1 (reviewed in [47]). Notably, ATM, ATR and DNA-PK are three kinases belonging to the phosphatidylinositol 3-kinase-related kinases (PIKKs), which mainly control the DDR [48]. Given their central role in orchestrating DNA repair, the following sections describe their characteristics and functions of PIKKs during the DDR.

ATM, ATR and DNA-PK are colossal polypeptides that present similar structures, where the kinase domain is located at the C-terminus. Flanking this kinase region, PIKKs present an upstream FRAP-ATM-TRRAP (FAT) domain and a downstream PIKK regulatory domain (PRD) and FAT C-terminal (FATC) motif [48]. The FAT and kinase domains form the catalytic subunit of the PIKKs, where the FAT region promotes the correct folding of the kinase domain [49]. Additionally, the FATC region is proposed to interact with activating factors such as TIP60 to enhance the activation of PIKKs [50]. Deletions of either the FAT or FATC domains, but not both simultaneously, have been shown to impair the kinase function of PIKKs [51]. However, the precise folding structure that results in the interaction between the FAT and FATC domains and how it regulates PIKK activity is incompletely understood. The N-terminus of PIKKs consists of tandem HEAT repeats, each composed of two $\alpha$-helices linked via a short loop. The HEAT domain facilitates PIKKs protein-protein and protein-DNA interactions [48].

These PIKKs regulate a wide variety of signalling responses through their control of phosphorylation events. Within the target proteins, the S/T-Q motifs are the preferred sites for phosphorylation [48]. ATM, ATR and DNA-PK share certain targets and present common functions during the DDR [48]. For example, these three PIKKs require the presence of cofactors for their recruitment to DNA damage sites, where they undergo conformational changes that trigger autophosphorylation events resulting in the activation of these PIKKs [52]. ATM and DNA-PK are recruited to DSBs through their interaction with NBS1 (MRN complex) [53] and the Ku heterodimer [33], whilst ATR is recruited to a wide range of DNA lesions (both SSBs and DSBs) via ATRIP [54]. Interestingly, a recent study demonstrated that ATM promotes the phosphorylation of NHEJ repair factors, including DNA-PK, at the DNA damage sites [55]. These results suggest crosstalk for the role of these PIKKs during DNA repair.

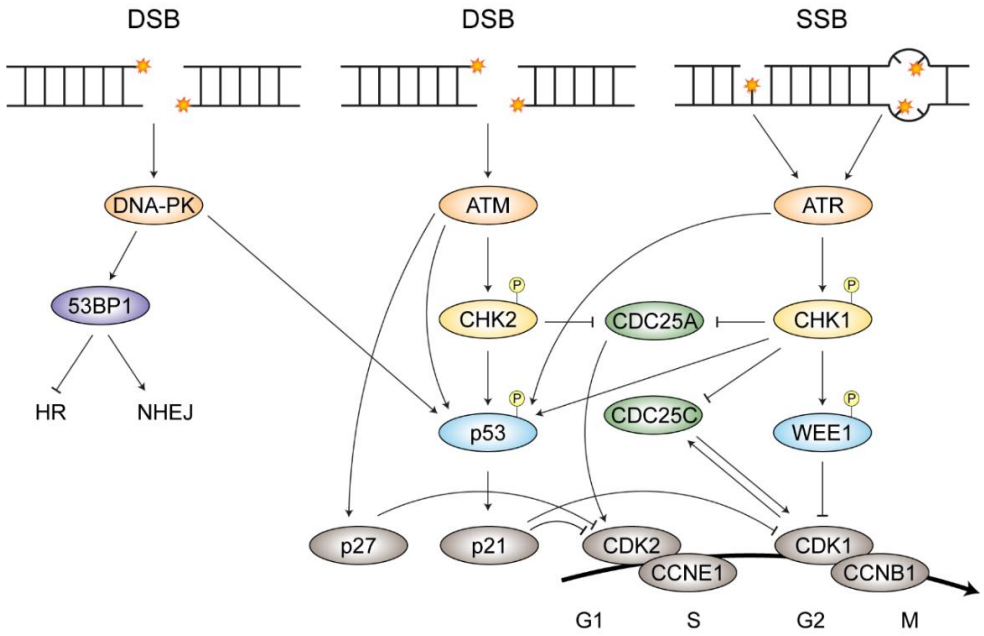


***Figure 1.2. Role of PIKKs in the DNA damage response.*** *Diagram of the phosphorylation events controlled by PIKKs (ATM, ATR and DNA-PK) during the DNA damage response. The principal PIKK substrates are highlighted in the figure and their full names are detailed in the list of gene abbreviations. The figure was adapted from* [6]*.*

Additionally, ATM, ATR and DNA-PK share important targets involved in the DDR. For instance, all three PIKKs promote the phosphorylation of H2AX at $S^{139}$, referred to as γH2AX [56]. This histone modification promotes chromatin relaxation, enhancing the recruitment of DNA repair factors [57]. Moreover, in response to DNA damage, these three PIKKs can impact cell cycle progression as well as promote the activation of tumour suppressor p53 [48]. In particular, ATM promotes the phosphorylation and activation of CHK2, which results in the subsequent activation of p53 [58]. ATM has also been described to directly phosphorylate p53 [59,60]. By orchestrating the p53-dependent expression of *CDKN1A* (p21), ATM controls the G1-S phase checkpoint, leading to cell cycle arrest in response to DNA damage (Fig. 1.2) [61]. ATR regulates the cell cycle through the phosphorylation and activation of CHK1, which results in the subsequent inactivation of the CDC25 family of phosphatases which are required for the activation of cyclin-dependent kinases, resulting in G2-M phase arrest (Fig. 1.2) [62]. Similar to ATM, ATR can also phosphorylate p53 resulting in its stabilisation and activation, further enhancing cell cycle arrest (Fig. 1.2) [63]. Lastly, although the detailed role of DNA-PK during the cell cycle remains incompletely understood, it is known that during the G1 phase,

DNA-PK promotes the phosphorylation of 53BP1 (Fig. 1.2) [36]. 53BP1 is recruited to DSBs to both enhance NHEJ and inhibit HR repair pathways. Contrarily, during the S-G2 phase, the activity of DNA-PK is inhibited, which reduces the activation and recruitment of 53BP1 to DSBs, and as a result, the HR pathway is activated [36]. Additionally, DNA-PK can directly phosphorylate p53 in response to genotoxic stress to further regulate the DDR (Fig. 1.2) [64].

Collectively, these studies suggest that during the DDR, all three PIKKs lead to the phosphorylation and activation of p53 [59,60,63,64]. p53 presents a crucial role within the DDR as it controls the transcriptional expression of target genes involved in cell cycle arrest, DNA repair and apoptosis [65].

## 1.2. The human tumour suppressor p53.

p53 structure and functionality in human tumours.

The tumour suppressor p53 is a fundamental transcription factor that is activated in response to a wide variety of stressors [66]. Depending on the dose and time of exposure, p53 can induce a myriad of cellular processes, including cell cycle arrest, DNA repair and induction of programmed cell death [65]. p53 was first discovered as an interacting protein bound to the T-antigen simian virus 40 (SV40), a viral particle that has the ability to induce neoplastic transformation of various mammalian cells [67,68]. p53 was initially thought to function as an oncogene due to its high expression in tumour cells and ability to confer tumorigenic potential to non-malignant cells [69]. However, an extensive body of research strongly supports a tumour suppressor role for p53. It has been demonstrated that the conflicting results regarding the role of p53 were due to the use of mutated p53 clones (obtained from tumour cells) in early studies [66].

The tumour suppressor *TP53* is transcribed from the short arm of chromosome 17 (17p13.1) and results in the expression of a 44kDa protein that presents five domains (Fig. 1.3a) [70]. At the N-terminus, p53 has a transactivation domain (TAD) that can be divided into two subregions named TAD1 and TAD2 (Fig. 1.3a). Both TAD1 and TAD2 are required to control p53-mediated transcriptional expression as they can interact with transcriptional regulators and chromatin remodelling factors promoting p53 activity [66]. The TADs are followed by a proline-rich region (PRD, Fig. 1.3a) which is composed of five tandem PXXP motifs (where P denotes proline and X is any amino acid), and, although incompletely understood, the

polyproline track has been proposed to modulate the interaction with several p53-binding proteins impacting on tumour cell growth [71].

The proline-rich region bridges the TADs with the core DNA binding domain (DBD, Fig. 1.3a), which is responsible for the DNA recognition [72]. p53 recognises a sequence-specific motif (hereafter referred to as p53 response elements) formed by two 10bp copies of a palindromic 5'-RRRCWWGYYY-3' sequence separated by a spacer of 0-20 nucleotides (Fig. 1.3b) [73]. These motifs are highly conserved, supported by the fact that single nucleotide mutations, particularly at the central WW nucleotides, compromise the p53 recruitment to target genes and thus their expression [74]. These p53 response elements are located within the promoter region or near the transcription start site, generally within the first exon-intron, of p53 target genes [75].

In its active conformation, p53 forms a nuclear tetrameric complex (Fig 1.3c), which is required for the ability of p53 to bind with DNA [72]. p53 oligomerisation occurs in response to stress and is conducted via its tetramerisation domain (TD), which is located downstream of the core DNA binding region (Fig. 1.3a). In response to DNA damage, a two-step oligomerisation process occurs where two p53 monomers first dimerise through antiparallel $\beta$-sheet interaction followed by tetramerization of two pre-assembled dimers via interaction through their $\alpha$-helices within the TD (Fig. 1.3c, d) [76]. This tetrameric conformation promotes p53 binding to the p53 response elements within the target genes [72]. The last domain within the p53 protein corresponds to the C-terminus (CTD) that functions as a hotspot domain for posttranslational modifications (PTMs), which modulate p53 activity (Fig. 1.3a) [77]. In this domain, p53 also presents both nuclear localisation and export signals necessary for p53 to exert its function as a nuclear transcription factor [66]. Importantly, the TADs, CTD and the sequence between the DNA binding and tetramerization domains do not present an ordered three-dimensional structure and are categorised as intrinsically disordered (ID), which favours p53 interaction with a wide variety of cofactors which also impact p53 activity (Fig. 1.3d) [78].

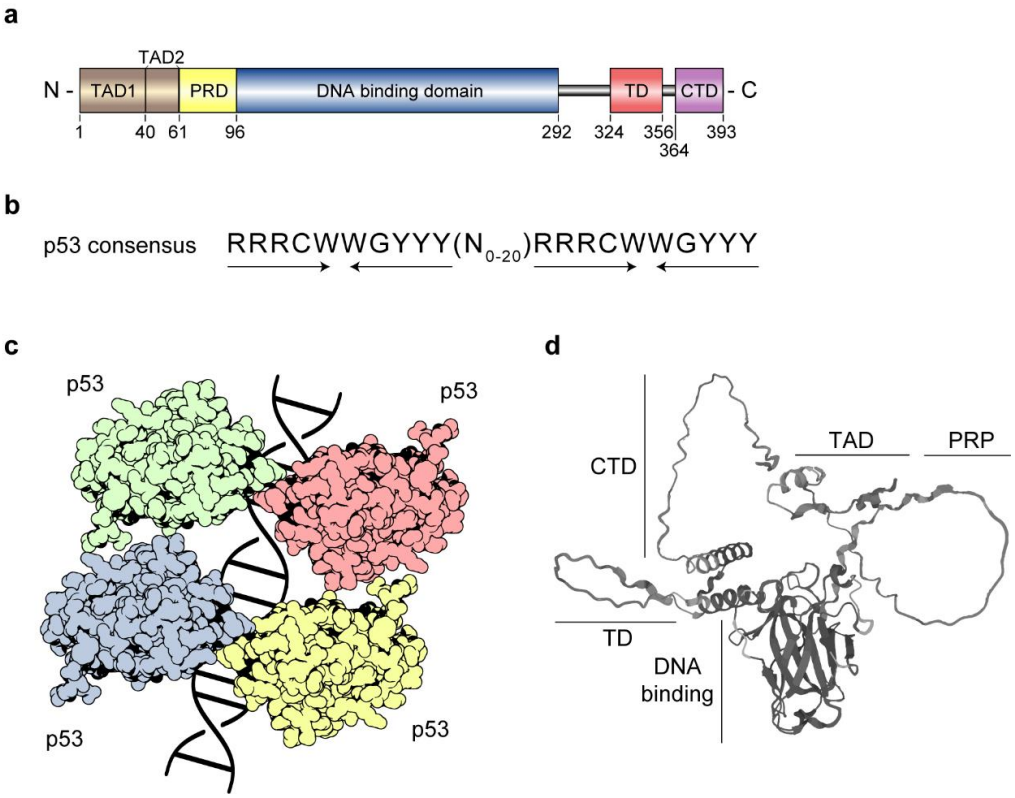


***Figure 1.3. p53 protein structure. a)*** *Schematic representation of the p53 protein structure. TAD: transactivation domain, PRD: proline-rich domain, TD: tetramerization domain and CTD: carboxyl-terminal domain. The numbers below p53 protein structure represent amino acid positions.* ***b)*** *Consensus sequence of p53 response elements (R denotes any purine, W represents adenine or thymine, and Y denotes any pyrimidine). The start and end points of each 10bp palindromic sequence are highlighted with the arrows, whilst the spacers between them are represented with N (denoted as any nucleobase), with the subscript indicating the number of nucleotides. Panels (a-b) were adapted from* [77]. ***c)*** *Representation of the active p53 tetrameric complex bound to DNA (original panel).* ***d)*** *3D modelling of the p53 protein structure adapted from Alpha Fold* [79] *shows the structured DNA binding domain compared with the intrinsically disordered TAD, PRP and CTD regions.*

The fundamental role of p53 in preventing tumour formation and progression is highlighted by the fact that over 50% of human cancers exhibit mutations in the p53 protein, while the remaining tumours display deficiencies in the pathways responsible for controlling p53 activity [80]. Although p53 can present a wide variety of mutations throughout its protein structure, the vast majority are missense mutations within the DNA binding domain [81]. p53 mutations can either induce

conformational changes in the p53 protein structure (structural mutants) or compromise its ability to bind with DNA (contact mutants). Both types of mutations result in the inactivation of p53 transcriptional activity [82].

These mutations affect p53 activity via three different mechanisms, including loss-of-function (LOF), gain-of-function (GOF) and dominant-negative (DN). Briefly, LOF refers to the inability of p53 to perform its tumour suppressor role because mutations within p53's DBD impede its recruitment to DNA and thus compromise the transcriptional expression of its target genes [81]. GOF refers to a set of mutations that shifts the behaviour of p53 from its tumour suppressor role to function as an oncogene. In this case, p53 can boost malignancies by enhancing tumour metastasis or through metabolic reprogramming to adapt to low-nutrient environments [83]. Lastly, DN phenotypes occur when a mutant version of a p53 protein forms tetramers with wilt-type p53 counterparts, inhibiting the activity of the latter isoform [84].

Regulation of p53 activity – Crosstalk between cofactors and PTMs.

Since p53 controls a myriad of cellular processes in response to stress, p53 activity must be tightly regulated [65]. The function of p53 is controlled both via a plethora of PTMs (Fig 1.4) and through its interaction with cofactors. It is important to mention the crosstalk between these two mechanisms, as changes in p53 PTMs can significantly impact its interaction with cofactors, while several p53 cofactors can induce PTMs within p53 protein [85].

During non-perturbed conditions, p53 is maintained at low levels via its interaction with E3 ubiquitin ligase MDM2 (HDM2 in humans, hereafter referred to as MDM2) [86]. Ubiquitination is an enzymatic stepwise post-translational modification consisting of the transfer of ubiquitin subunits to the target protein. This process is catalysed by three enzymes, including E1 ubiquitin-activating, E2 ubiquitin-conjugating and E3 ubiquitin-ligating enzymes [87]. Different types of ubiquitination events can occur on the p53 protein, which dictates its cellular localisation, activity and interaction with cofactors [88]. Monoubiquitination induces the nuclear export of p53, while polyubiquitination leads to its proteasomal degradation [85,89]. MDM2 inhibits p53 activity either via its direct interaction, which blocks p53 transcriptional role, or by promoting the proteasomal degradation of p53 [90].

Specifically, MDM2 controls the transfer of ubiquitin groups to six p53 lysine residues located within the CTD of p53 ($K^{370}$, $K^{372}$, $K^{373}$, $K^{381}$, $K^{382}$, and $K^{386}$; Fig. 1.4a) [87]. The expression levels of MDM2 also impact the activity of p53, as when MDM2 is expressed at low levels, it conducts a monoubiquitination reaction leading to p53 nuclear export [91,92]. In contrast, high levels of MDM2 promote the polyubiquitination of p53 and its proteasomal-mediated degradation [90]. Besides MDM2, other E3 ubiquitin-ligating enzymes can also control p53 activity, although the molecular mechanisms are incompletely understood. MDMX/MDM4, a member of the MDM2 protein family, form heterodimers with MDM2 that have been shown to strengthen the ubiquitination activity of MDM2 [93]. Additionally, PIRH2 promotes the ubiquitination of p53 tetramers leading to their degradation (Fig 1.4) [94]. Ubiquitin groups can also be removed from p53 by deubiquitinases (DUBs), including several members of the ubiquitin-specific proteases (USPs) protein family. DUBs generally promote p53 stabilisation and activation [85].

However, in response to a wide range of stressors, p53 is stabilised and activated through a series of phosphorylation events [87]. p53 presents a cluster of serine and threonine residues at its N-terminus that are commonly phosphorylated (Fig 1.4) [66]. Although some residues are constitutively phosphorylated and have been proposed to enhance the MDM2-mediated degradation of p53, most of the serine and threonine sites are phosphorylated in response to stress, enhancing p53 activity [65]. DNA damage leads to the rapid phosphorylation of $S^{15}$ and $S^{20}$ by ATM, ATR and DNA-PK (Fig 1.4) [95]. These PTMs reduce the interaction between p53 and MDM2 and thus increase its stability and activation, which leads to the subsequent binding of p53 to its target genes [74]. Additionally, the phosphorylation of $T^{18}$ promotes the interaction between p53 and the acetyltransferase p300, which competes with MDM2 [96]. Interestingly, depending on the dose and time of exposure to different genotoxic stressors, the phosphorylation of p53 residues varies [74]. For example, low levels of $\gamma$-irradiation primarily induce the rapid phosphorylation of the TADs within p53 ($S^6$, $S^{15}$, $T^{18}$, and $S^{20}$), whereas ultraviolet radiation induces the phosphorylation of the these residues as well as the CTD of p53 [97,98]. However, how these different phosphorylation events in response to specific DNA damaging agents impact the activity of p53 remains to be elucidated. When the stress stimulus is released and the DDR is inactivated, the activity of p53 has to be terminated, returning p53 expression to basal levels [65]. Although several dephosphorylation events have been described to reduce the transcriptional

activity of p53, MDM2-mediated degradation remains the primary negative regulator of p53's expression and activity [87].

In addition to the phosphorylation and ubiquitination events, p53 can also be acetylated (Fig 1.4), which is mainly controlled by two acetyltransferases named CBP and p300 [99]. These acetyltransferases are often referred to as CBP/p300 because they are highly homologous and often considered interchangeable due to their similar activity and shared targets [99]. CBP/p300 enhances the activity of p53 via two mechanisms. First, given the role of CBP/p300 as histone acetyltransferases, they control the acetylation of H3K27 at p53 target genes leading to chromatin relaxation and enhancing the transcriptional expression of the target [100]. Additionally, both CBP and p300 physically interact with p53 promoting the acetylation of six p53 lysine residues located within the CTD of p53 ($K^{370}$, $K^{372}$, $K^{373}$, $K^{381}$, $K^{382}$, and $K^{386}$; Fig 1.4) [101]. Acetylation of these residues enhances p53 oligomerisation and recruitment to target genes leading to their expression [85], although the detailed mechanisms are incompletely understood.

Acetylation and ubiquitination are mutually exclusive PTMs as they occur in the same residues (Fig 1.4), which implies that when p53 interacts with CBP/p300, there is a reduction in the MDM2-mediated proteasomal degradation of p53 [87]. During DNA damage, acetylation and phosphorylation events concomitantly occur, leading to the activation of p53 [85]. Additionally, p53 can be acetylated at $K^{120}$, within the DBD, by TIP60, MOF and MOZ acetyltransferases (Fig 1.4) [99,102]. Although the impact of this PTM in the activity of p53 remains to be elucidated, it has been proposed that acetylation at $K^{120}$ residue increases the affinity of p53 for pro-apoptotic targets, which may result in their transcriptional expression [102]. p53 acetylation events are reversible in a process controlled by HDAC1 and SIRT1 deacetylases. It has been proposed that both HDAC1 and SIRT1 repress p53 function through deacetylation, leading to the MDM2-dependent p53 polyubiquitination and thus its degradation [103].

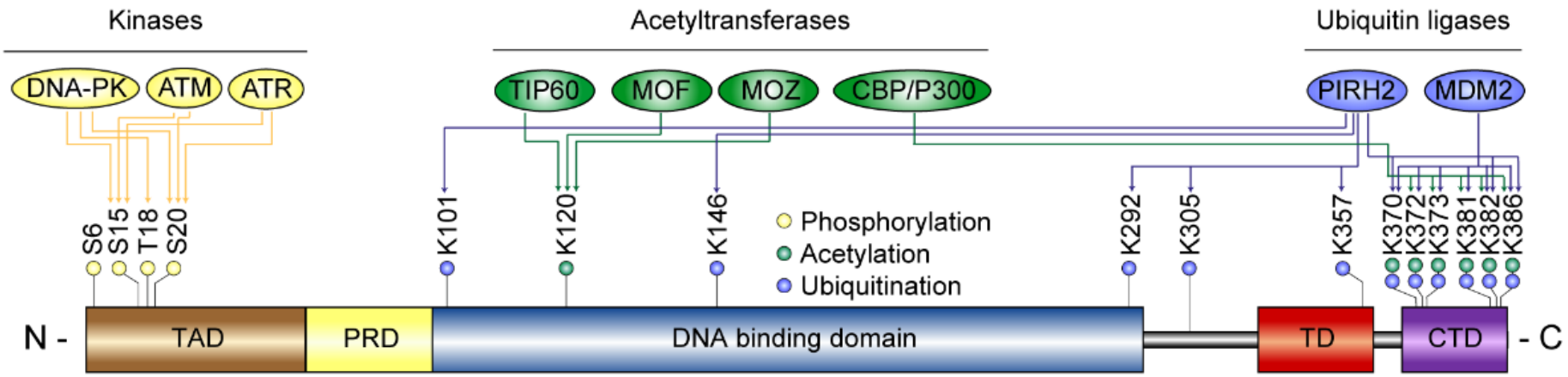


***Figure 1.4. p53 post-translational modifications. a)*** *Schematic representation of the p53 protein structure highlighting the amino acids (S: serine, T: threonine and K: lysine) with the most frequent p53 post-translational modifications (yellow: phosphorylation, blue: ubiquitination and green: acetylation). The main enzymes controlling this processing are represented above the p53 protein structure. The figure was adapted from* [85].

As described, the activity of p53 is tightly regulated by PTMs, which involved the interaction of p53 with various cofactors [87]. In addition to these PTMs, the activity of p53 can be influenced by certain cofactors that, although not directly reported to induce PTMs on the p53 protein, are known to affect its activity. The section below briefly describes the significance of several of these cofactors in regulating the transcriptional activity of p53.

An early study conducted by Shikama and colleagues discovered a p300 interacting protein that was able to enhance the activity of p53 [104]. This new cofactor was named junction-mediating and regulatory protein (JMY). Due to the central role of JMY in this project, a detailed description of its structure and cellular activities is described later in this introduction (section 1.3).

Additionally, p53 cofactor STRAP, was identified as a JMY interactor [105]. STRAP presents a unique protein structure formed by six tandem tetratricopeptide (TPR) repeats, facilitating and strengthening the interaction between JMY and p300 [105]. STRAP physically interacts with both JMY and p300 through its N-terminal and C-terminal domains, respectively [105]. During DNA damage, ATM and CHK2 phosphorylate STRAP, which increases its stability and results in nuclear accumulation. Nuclear STRAP promotes the interaction between JMY, p300 and p53, increasing the p53 transcriptional activation of *BAX* and *GADD45* [106,107]. Interestingly, p53 levels and stability are also regulated by STRAP, as the overexpression of the latter prevents the MDM2-mediated degradation of p53 [106]. However, further studies are required to improve the mechanistic understanding of how STRAP influences the stability of p53.

In addition, other cofactors such as the apoptosis-stimulating protein of p53 (ASPP) protein family, PML and 53BP1 can also regulate p53 transcriptional activity [108]. Briefly, the ASPP protein family includes ASPP1, ASPP2 and iASPP [109]. ASPP1 and ASPP2 interact with the DBD of p53, promoting its recruitment to pro-apoptotic genes resulting in the expression of *BAX* and *PUMA*. Contrarily, iASPP interacts with and negatively regulates p53, reducing its activity which correlates with increased cell survival [110]. In addition, p53 can be recruited to PML nuclear bodies in response to DNA damage, which contributes to the stabilisation of p53 through its interaction with other factors such as CHK1 and CBP. PML bodies have also been described to increase p53 levels through sequestering MDM2 within the nucleoli [111]. Lastly, despite the central role of 53BP1 in DNA

repair, the transcriptional activity of p53 is also enhanced by 53BP1, where the interaction between p53 and 53BP1 results in increased expression of p53 target genes such as *p21* and *MDM2*. Interestingly, this regulatory mechanism is independent of the role of 53BP1 in DNA repair [112].

p53 is a master regulator of DNA repair.

DNA damage triggers the activation of p53 which controls a myriad of cellular processes, including an initial arrest of the cell cycle, which is thought to grant sufficient time to promote the expression of DNA repair factors. When cells are exposed to prolonged DNA damaging conditions or if the DNA lesions remain unrepaired, p53 promotes the expression of pro-apoptotic targets leading to the activation of the programmed cell death pathway [65]. Although p53 has been proposed to participate in several DNA repair mechanisms, its role within these repair pathways remains poorly understood. p53 can modulate DNA repair via two mechanisms, either by controlling the expression of DNA repair genes or through its interaction with components of the DNA repair machinery (reviewed in [113]).

In the NER pathway, p53 plays an important role in the resolution of destabilised DNA base pairs (Fig. 1.5). At a transcriptional level, p53 promotes the expression of components such as *DDB2* [114], *PCNA* [115] and *XPC* [116] which are involved in the early recognition of bulky DNA adducts [21]. Defects in the p53-mediated expression of these NER factors have been associated with increased chromosomal instability and sensitivity to UV radiation [117]. Additionally, p53 can directly interact with XPC, XBP and PCNA [113]. While the function of this interaction in the NER pathway remains to be elucidated, it is proposed that p53 is required for the recruitment of XPC to the UV-induced DNA adducts, which enhances the subsequent interaction between XPC and the TFIIH complex resulting in the initiation of the NER response [118].

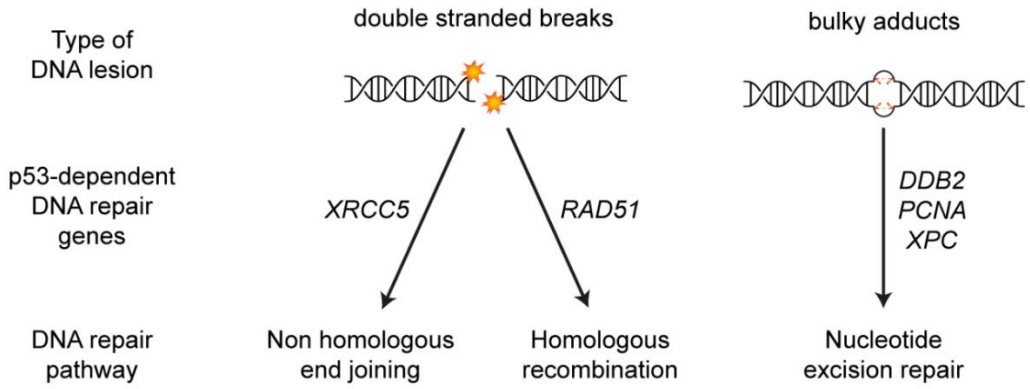


***Figure 1.5. The role of p53 in DNA repair.*** *p53 regulates the expression of DNA repair proteins and thus impact on several repair pathways. The figure was adapted from* [65]*.*

p53 also participates in the repair of DSBs via NHEJ and HR (Fig. 1.5) [119]. Although the role of p53 in the NHEJ pathway remains unclear, it has been described that p53 controls the transcriptional expression of *XRCC5* [120]. Reduced expression of this component compromises the NHEJ pathway by reducing the formation of the Ku heterodimeric complex and subsequent recruitment of DNA-PK, which can hinder the recognition of DSBs [121]. Additionally, p53 plays an important role in HR. Although at a transcriptional level, p53 modulates HR by promoting the expression of *RAD51* [122], most of the described mechanisms by which p53 impacts HR are independent of its transcriptional activity [113]. p53 interacts with the MRN complex and RAD51 resulting in the recognition of DSBs, which has been correlated with increased chromosomal stability, reduced mutational count and gene amplification rates, and suppression of excessive HR [123]. Moreover, in response to replication stress, ATM and ATR phosphorylate and activate p53, which is then recruited to ssDNA stretches through the interaction with RPA, which further supports a regulatory role for p53 in controlling HR rates [124].

Together, these studies indicate that p53 plays a crucial role in DNA repair, where p53 can both regulate the expression of repair proteins as well as interact with DNA repair factors. However, the regulatory mechanisms that control the p53-driven expression of DNA repair proteins during genotoxic remain incompletely understood.

## 1.3. Junction-mediating and regulatory protein (JMY).

The discovery of JMY and its protein structure.

JMY was discovered as a p300-interacting protein by two-hybrid screening using a truncated version of p300 ($p300^{611-2283}$) [104]. This early study was investigating the impact of the CBP/p300 coactivator proteins in the activity of p53. Interestingly, JMY and p300 were found to form a ternary complex with p53 upon actinomycin D-induced stress [104]. *JMY* is transcribed from the long arm of chromosome 5 (5q13.2), and its expression is detected in a wide range of tissues (*e.g.* heart, brain and kidney). *JMY* presents two isoforms, a longer transcript (9.5kb) and a shorter and less abundant isoform (6kb), which are hypothesised to be obtained through alternative splicing [104]. While the role of the shorter isoform remains incompletely understood, the longer transcript is known to be translated into a functional protein of approximately 110kDa. Hereafter, JMY is referred to as the protein obtained from the longer isoform.

The structure of JMY can be divided into three segments (Fig. 1.6). At the N-terminus, JMY contains a highly conserved LC3-interacting region (LIR motif, Fig. 1.6), which is necessary for its recruitment to cytoplasmic autophagosomes [125]. This domain is followed by a cluster of potential phosphorylation sites [104], although their functionality remains incompletely understood. Within this N-terminal region, JMY also presents a p300 binding motif [104]. The central segment of JMY contains three consecutive coiled-coil domains suggested to promote JMY's protein-protein interactions (Fig. 1.6), although their functionality requires further characterisation. Within this central region, JMY also presents a putative nuclear localisation signal (NLS) and a second p300 binding motif [104]. Interestingly, these p300 binding domains within JMY are able to interact with two segments of p300 ($p300^{611-1257}$ and $p300^{1572-2283}$) [104]. At the C-terminus, JMY presents a WCA (WASP-homology-2, central and acidic) domain shared with other members of the WASp (Wiskott–Aldrich syndrome protein) protein family [126,127]. The WASp protein family comprises members of the class I actin nucleating promoting factors [128]. Specifically, JMY has a proline-rich region followed by three tandem repeats of the actin monomer-binding WH2 (WASP-homology-2, $W_aW_bW_c$) domain and a central and acidic (CA) motifs (Fig. 1.6) [126]. The WH2 domains bind actin monomers, the central domain (C) interacts with both actin and the Arp2/3 complex, whereas the acidic motif (A) functions as an Arp2/3-binding domain [126,127]. JMY also presents a second NLS between the first two WH2 repeats ($WH2_aWH2_b$, Fig. 1.6) [126].

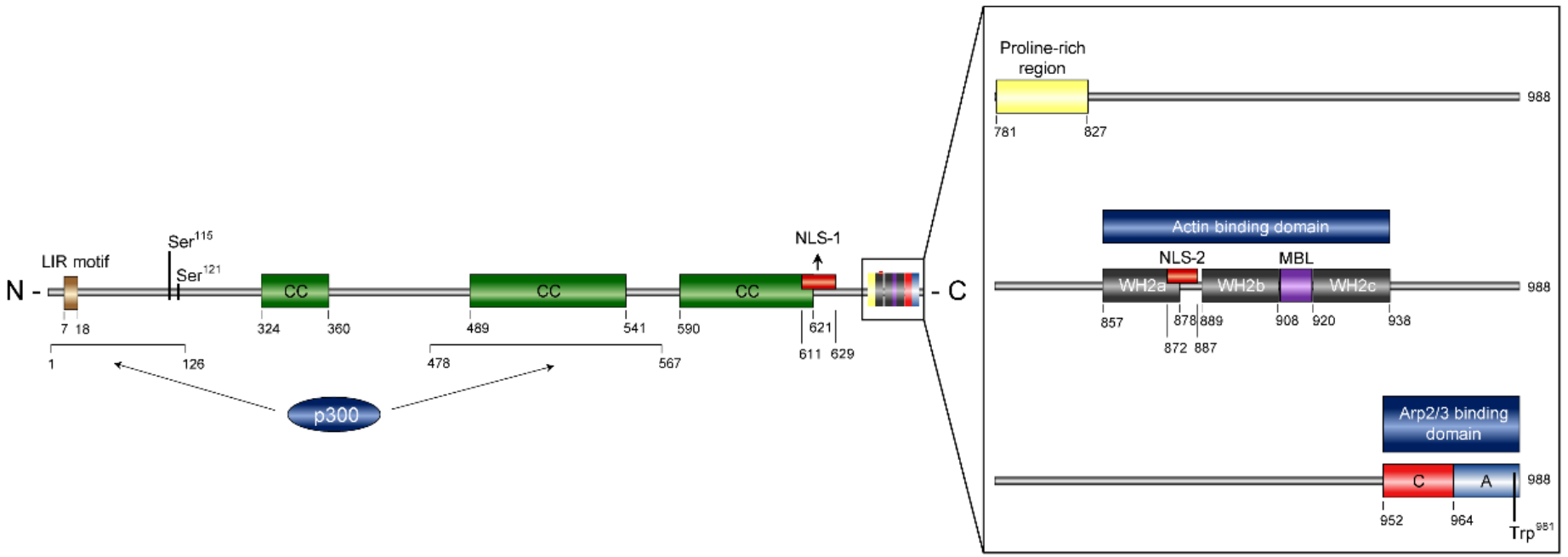


***Figure 1.6. JMY protein structure.*** *Schematic representation of the protein domains of JMY and its p300-binding regions. The number below JMY's structure represents amino acid positions. A: acidic, C: central, CC: coiled-coil, LIR: LC3-interacting region, MBL: monomer binding linker, NLS: nuclear localisation signal, Ser: serine, Trp: Tryptophan and WH2: Wiskott–Aldrich syndrome homology region 2. Original figure.*

The regulatory mechanisms during the expression of *JMY*.

Several studies support that JMY is a DNA damage-responsive protein whose expression increases during specific genotoxic stress conditions [127,129,130]. Despite this, the specific transcriptional mechanisms controlling *JMY* mRNA expression during DNA damage are incompletely understood. Coutts et al.'s work provided the first evidence that *JMY* levels increase during a wide range of hypoxic conditions, including mild hypoxia (0.5-2%) to anoxia (<0.02%) [131]. Hypoxia is a deprivation of oxygen supply to maintain adequate homeostasis. Due to the highly proliferative rate of tumour cells, the oxygen demand surpasses the oxygen supply, generating a hypoxic microenvironment favouring tumour development [132]. Increased hypoxic levels are correlated with poorer patient outcomes [133]. Cellular adaptation to hypoxic conditions is regulated by changes in gene expression, which are controlled by a family of transcription factors called hypoxia-inducible factors (HIFs). HIF comprises an oxygen-sensitive $\alpha$ subunit (HIF-$\alpha$) and a constitutively expressed $\beta$ subunit (HIF-$\beta$) [134]. The former is kept at low levels during normoxia as HIF-$\alpha$ is rapidly polyubiquitinated via PHD, FIH-1 and pVHL and degraded by the proteasome [135]. When the oxygen level drops, HIF-$\alpha$ stabilises and translocates to the nucleus, dimerising with HIF-$\beta$ [136]. This heterodimer binds to hypoxia response elements (HREs), promoting the expression of target genes involved in tumour cell survival, proliferation, metabolic adaptation, angiogenesis and tumour cell migration and invasion [134].

The increased expression of *JMY* mRNA during hypoxic conditions is mediated through the recruitment of HIF1$\alpha$ to the promoter of *JMY*, where six hypoxia response elements (HRE) can be found. Five of these HREs are grouped in a conserved cluster shared across different species (*e.g.* mouse, human and bull), whereas human *JMY* presents an additional distal motif [131]. Mutations within these HREs result in variations in *JMY* expression levels where the mutation of the five-copied cluster abolishes the expression of *JMY*. These results characterise *JMY* as a novel HIF1$\alpha$ target [131]. Moreover, it has been proposed that the overexpression of specific members of the E2F protein family, including E2F1 and E2F2, in U2OS osteosarcoma cells could regulate *JMY* expression levels [137]. However, whether the promoter of *JMY* presents E2F binding motifs and the mechanisms by which E2F factors control *JMY* expression have yet to be determined.

It is known that the protein expression of JMY increases during DNA damage. Coutts and colleagues demonstrated that, under non-perturbed conditions, MDM2 interacts with and negatively regulates JMY via polyubiquitination, which leads to the proteasomal degradation of JMY [129]. Interestingly, the interaction between MDM2 and JMY relies on the presence of MDM2's RING finger domain as a derivative presenting a deletion of the C-terminus ($MDM2^{440-490}$), fails to bind and degrade JMY [129]. MDM2 directly targets JMY for degradation, as evidenced by the fact that the $MDM2^{C464A}$ mutant, which is known to be catalytically inactive [138], can still interact with JMY but fails to induce its degradation [129]. Notably, the treatment with DNA damaging agents, such as UV radiation, etoposide and actinomycin D, increases the protein levels of JMY due to a decreased interaction with MDM2 [129]. Several studies further support the evidence that the expression of JMY is enhanced in response to specific genotoxic stressors [127,130]. It will be relevant for future studies to investigate the detailed mechanisms that regulate JMY levels both under non-perturbed and DNA damage conditions.

The cytoplasmic role of JMY - Actin nucleation drives cell motility and survival.

As described, JMY was discovered as a nuclear p300 interacting protein [104]. Currently, it is known that JMY localises both in the cytoplasm and the nucleus. In the cytoplasm, JMY functions as an actin nucleator due to its C-terminus comprising a WCA region shared with other members of the WASp protein family [126]. The architecture of the WCA domains enables JMY to promote the formation of new actin filaments via two distinct mechanisms. In the presence of the Arp2/3 complex, JMY promotes the formation of branched actin filaments at the side of pre-existing actin fibres [126]. Similar to other members of the WASp protein family, the WH2 domains within JMY promote the interaction with actin monomers and assist the Arp2/3-dependent actin filament formation. The Arp2/3 complex is bound to the CA motifs at the C-terminus of JMY (Fig. 1.6), resulting in the formation of branched actin structures [126].

JMY also promotes the formation of unbranched actin filaments in the absence of the Arp2/3 complex, as well as when replacing a conserved tryptophan residue (Fig. 1.6, $W^{981A}$) known to be essential for the binding of the Arp2/3 complex in all WASp family of proteins [126]. This actin nucleation mechanism is similar to the one reported by Spire, which functions by binding actin monomers together using tandem WH2 domains and a monomer binding linker (MBL) [139,140]. JMY presents

a conserved MBL between its second and third WH2 domains ($WH2_bWH2_c$) necessary for its Arp2/3-independent actin nucleation activity [126]. While the $WH2_bWH2_c$ domains of JMY are sufficient to promote F-actin formation, all three domains are required for JMY's optimal actin nucleation activity [126]. Contrarily to Spire, JMY does not prevent the disassociation of actin monomers from the end of the filaments. This suggests that JMY promotes the nucleation of new filaments that grow from their barbed ends without capping them [126]. These results demonstrate that JMY is unique among the rest of mammalian actin nucleators due to its role in promoting actin nucleation both in an Arp2/3-dependent and independent fashion.

JMY plays a key role in promoting cell motility and invasion through its actin nucleation activity. In highly motile cells, JMY localises to the cellular leading edges and through its Arp2/3-dependent actin nucleation, JMY enhances cell motility by favouring the formation of lamellipodia-like structures [126,127]. Notably, JMY also enhances cell invasion in Matrigel® chamber cell migration assays [127]. Additionally, overexpression of ectopic JMY promotes cell motility, whereas the expression of a JMY derivative lacking the WCA region had no effect, supporting a role for JMY's actin nucleation activity in cell motility [127]. Interestingly, the increased expression of JMY under hypoxic conditions also promotes cell motility suggesting a correlation between cytoplasmic JMY levels and cell migration [131].

Moreover, JMY also impacts cell motility by modulating the expression of cadherins, which are cell-cell adhesion surface molecules [127]. In particular, JMY reduces the expression of E-cadherin in MCF7 breast cancer cells as well as N-cadherin in U2OS and Saos2 osteosarcoma cells. Interestingly, the expression of JMY and cadherins present a negative feedback regulation, as a reduction in the latter leads to an increased expression of JMY and *vice versa* [127]. The absence of JMY reduces cell motility which can be rescued by the concomitant depletion of these cadherins [127]. Collectively, these findings describe that JMY promotes cell motility and invasion both via actin nucleation and through modulating the expression of cadherins.

In addition, cytoplasmic JMY acts as a pro-survival factor by facilitating autophagy through enhancing the formation and maturation of autophagosomes [125]. Autophagy is a catabolic process that allows the recycling of cytoplasmic components and damaged organelles playing an important role in cellular

homeostasis [141]. Autophagy is a stepwise process which is initiated by the formation of phagophores, which are sickle-shaped double-lipid membrane structures. Throughout their maturation the double-lipid membrane elongates forming enclosed organelles referred to as autophagosomes. These autophagosomes engulf the cargo and fuse with the lysosomes in the late steps of autophagy, resulting in the degradation of the cargo [142]. Under non-perturbed conditions, cytoplasmic STRAP has been suggested to sequester and block JMY in an inactive state [143]. However, upon induction of autophagy (*e.g.* nutrient starvation), cytoplasmic JMY colocalises with LC3-containing autophagosomes and interacts directly with LC3B [125]. The interaction between JMY and the autophagosomes occurs via an LC3-interacting region (LIR motif, 'ETLESDWVAVRP') located at JMY's N-terminus (Fig. 1.6). LIR motifs allow the proteins to bind with members of the LC3 family [144]. In particular, the recruitment of JMY to the autophagosomes is abolished by mutations at the conserved tryptophan and valine residues ($W^{13A}$ and $V^{16A}$) [125].

The actin nucleation activity of JMY plays a crucial role in the formation and maturation of autophagosomes. Notably, the ablation of JMY's actin nucleation activity leads to a reduction in both the number and size of these cytoplasmic organelles [125]. JMY acts at the early stages of autophagosome biogenesis, supported by the fact that JMY enhances the formation of LC3-II [125]. However, the impact of JMY on later steps of autophagy requires further investigation as conflicting results on JMY's colocalisation with lysosomal markers have been reported [125,143]. Despite the fact that autophagy can either promote or inhibit tumour progression [141], both the absence of JMY and the inactivation of its actin nucleation role reduce tumour cell survival during metabolic stress (*e.g.* SAHA and nutrient starvation) as well as mTOR inhibition [125].

More recently, cytoplasmic JMY has been suggested to influence cell survival during DNA damage through its impact on the mitochondrial-dependent apoptotic pathway [145]. These studies suggested that JMY's Arp2/3-dependent actin nucleation is required for the formation of perinuclear compartments enriched in actin filaments. These structures were suggested to enhance the assemble of the apoptosome and activation of pro-apoptotic markers (*e.g.* cleavage of caspase-3) [145,146]. Contrarily to the pro-survival role of JMY during starvation [125], these studies suggested that JMY results in increased apoptosis through the release of

cytochrome c and activation of pro-caspases [145,146]. These findings further add to the complexity of JMY's cytoplasmic role in response to stress.

The role of nuclear JMY as a transcriptional regulator.

As described, cytoplasmic JMY plays an important role in cell motility and invasion, as well as impacts on cell survival during metabolic stress. Although the mechanisms are incompletely understood, JMY is known to undergo nuclear accumulation in response to specific genotoxic stressors, including hypoxia, UV radiation and treatment with chemotherapeutic agents like etoposide, actinomycin D and 4NQO [127,129,130].

A mechanism for the nuclear accumulation of JMY has been proposed where DNA damage triggers the formation of cytoplasmic actin filaments. This leads to a decrease in the available pool of cytoplasmic G-actin that interacts with the WH2 domains of cytoplasmic JMY [147]. This reduction is thought to expose the second NLS within JMY located between the $WH2_aWH2_b$ motifs (Fig. 1.6) [126], allowing its recognition by importin β and subsequent nuclear accumulation of JMY [147]. Several studies demonstrate that upon DNA damage, JMY accumulates in the nucleus, where it can interact with nuclear actin [119]. Within the nucleus, JMY's actin nucleation activity impacts its role as a transcriptional cofactor [127,130]. Interestingly, the inhibition of overall cellular actin polymerisation via latrunculin B treatment during DNA damage does not lead to the relocation of JMY to the cytosol [147]. Consequently, further studies are needed to better understand whether the localisation of JMY during genotoxic stress uniquely depends on cytoplasmic actin dynamics, which would provide an improved mechanistic understanding of the regulatory mechanisms controlling cellular localisation of JMY.

Nuclear JMY plays a key role in enhancing the p53-dependent transcriptional regulation and impacts the expression of pro-apoptotic factor *BAX* [104,127]. Initially, it was found that nuclear JMY promotes the p53 transcriptional activity in *BAX*-luciferase reporter assays, which was further enhanced in the presence of p300 [104]. Interestingly, both of JMY's p300 interacting domains were shown to be required for the optimal activation of the p53 activity [104]. Moreover, previous work demonstrated that JMY's Arp2/3-dependent actin nucleation is dispensable to promote p53 activity in *BAX*-luciferase reporter assays [127]. We have recently demonstrated that JMY influences the p53 recruitment to target genes and impacts

on the expression of DNA repair factors. Additionally, we observed that JMY's Arp2/3-mediated actin nucleation is required for its ability to repair DNA lesions and influences p53 transcriptional activation of DNA repair factors [130].

Together, these studies demonstrate that JMY is a DNA damage-responsive actin nucleator with a dual function both via its cytoplasmic role impacting cell motility and survival and via its nuclear function as a transcriptional regulator by promoting p53 activity and DNA repair.

## 1.4. Nuclear actin dynamics.

Actin a new player for nuclear dynamics.

Actin is a highly conserved protein family which comprise three isoforms, including $\alpha$-actin, $\beta$-actin and $\gamma$-actin which differ in the length of their N-terminus. Actin is a highly abundant protein that participates in a myriad of cellular processes, including cell motility, organelle rearrangement and cell-to-cell interactions [148]. Actin can be present both as a monomeric ('globular' or G-actin) subunit or in a polymeric filamentous (F-actin) conformation [149].

Actin polymerisation is a highly dynamic and reversible process initiated by the formation of a small aggregate comprising three actin monomers (referred to as nucleation) [148]. Actin filaments rapidly grow from both ends of the nucleation trimer by incorporating new actin monomers, although F-actin formation is faster at the barbed end. Actin monomers can concomitantly disassemble from the filaments, causing the depolymerisation of these structures [150]. Two types of actin filament structures, including branched filaments and linear fibres, can be found in cells [151]. In conjunction with actin nucleation-promoting factors, the Arp2/3 complex catalyses the polymerisation of the former [152], whereas the latter is controlled by formins [153], Cobl [154], Spire [140] and JMY [126]. To date, the vast majority of studies have focused on the role of cytoplasmic actin. However, in the past decade, a growing body of evidence supports the role of nuclear actin dynamics in the regulation of key nuclear events, including transcription and DNA repair [155].

Like other cytoplasmic proteins, actin needs to be transported into the nucleus. Although the size of actin is very close to the passive diffusion limit of the nucleopores (~40kDa), actin uses an active transport system for both its nuclear

translocation and export [156]. Specifically, actin undergoes nuclear accumulation in complex with cofilin in a process controlled by the importin IPO9 [157]. On the other hand, actin is exported from the nucleus in complex with profilin in a process controlled by the exportin XPO6 [157,158]. The nuclear import and export mechanisms that control the cellular localisation of G-actin seem to be independent of its ability to form filaments since an actin mutant (R62D) resistant to polymerisation retains the ability to shuttle between the cytoplasm and the nucleus [157]. The process of actin's nuclear import and export depend on the concentration of G-actin in both the nucleus and cytoplasm, as well as the availability of IPO9 and XPO6 [157]. Additionally, several actin nucleation-promoting factors like the Arp2/3 complex, WASP and JMY localise both in the cytoplasm and nucleus [127,130,159,160], although the regulatory mechanisms that control this shuttling remain incompletely understood.

The role of nuclear actin during transcription.

A growing body of research supports the role of nuclear actin in regulating gene expression. Nuclear actin can participate in various steps of transcription via its interaction with both the transcription machinery and transcription factors [156]. In eukaryotic cells, transcription is controlled by three enzymes named RNA polymerases I-III. Specifically, RNA polymerase I catalyses the synthesis of rRNAs, RNA polymerase II controls the expression of mRNAs, regulatory non-coding RNAs (ncRNAs) and the vast majority of small nuclear RNAs (snRNAs), whereas RNA polymerase III promotes the synthesis of tRNAs, several snRNAs and the 5S rRNA [161].

Nuclear F-actin enhances the recruitment and transcriptional elongation of RNA polymerase I during the transcription of rRNAs [162]. These findings highlight the importance of nuclear actin polymerisation during the expression of rRNAs as both the inhibition of actin polymerization and the nuclear overexpression of an actin mutant (R62D) resistant to polymerisation significantly impair RNA polymerase I activity [163,164]. Additionally, nuclear actin has been shown to interact with multiple subunits of RNA polymerase III (*e.g.* POLR3C). Although incompletely understood, it is proposed that G-actin is required for the recruitment of RNA polymerase III to the promoter region of target genes like U6 snRNA resulting in its transcriptional expression [165].

The role of nuclear actin in the transcriptional regulation controlled via RNA polymerase II has been investigated in more detail. Nuclear actin is required during several stages of transcription, including initiation and elongation [155]. During transcription initiation, G-actin colocalises within the pre-initiation complex [166,167], and it is required for the correct recruitment of RNA polymerase II at the promoter of actively transcribed genes [167,168]. During transcription elongation, G-actin interacts with CDK9, which is a kinase subunit of the positive transcription elongation factor b (P-TEFb) complex. The interaction between this kinase and G-actin leads to the recruitment of P-TEFb to the transcription elongation complex, which promotes the phosphorylation of RNA polymerase II at $S^2$ to induce its activation and transcription elongation [169]. Inhibition of actin polymerisation enhances this interaction and thus the activation of RNA polymerase II [169]. However, these interactions are still poorly understood at the molecular level, and whether their disruption impacts RNA polymerase II-dependent transcription needs further characterisation.

Several studies described that reducing the nuclear actin pool can result in reduced transcription. The depletion of both IPO9 and cofilin impairs the accumulation of nuclear actin, leading to a reduction in overall transcription, while the accumulation of nuclear actin via an IPO9- and cofilin-independent pathway partially restores overall transcriptional activity in 5-fluorouridine (5-FUrd) incorporation assays [157]. These findings indicate that changes in nuclear actin availability may impact overall transcription. However, the accumulation of nuclear actin via depletion of XPO6 seems to have a marginal effect, suggesting that the mere accumulation of actin in the nucleus is not sufficient to control transcription [157,169,170]. Although G-actin interacts with RNA polymerase II, changes in nuclear actin dynamics (monomeric versus filamentous) within the transcriptional machinery remain incompletely understood. Recent findings demonstrated that basal transcription levels are independent from nuclear actin filament formation [171]. However, in response to different stimuli, actin nucleation mediated by N-WASP and the Arp2/3 complex leads to the clustering and activation of RNA polymerase II. Additionally, the formation of these clusters relies on the dynamic polymerisation and depolymerisation cycle of nuclear actin [171]. Further studies are needed to expand our understanding on the role of actin nucleators and their contribution to nuclear actin dynamics within the RNA polymerase II complex during gene expression.

In addition, nuclear actin interacts with specific transcription factors [150]. One of the most extensively investigated examples is the interaction between nuclear G-actin and MRTF-A, which regulates the expression of genes involved in cytoskeletal dynamics, including actin [172]. MRTF-A presents three tandem RPEL motifs, each functioning as a G-actin binding region [173]. Under non-perturbed conditions, MRTF-A continuously shuttles between the cytoplasm and the nucleus. Increased levels of cytoplasmic actin monomers inhibit the nuclear accumulation of MRTF-A, whilst in the nucleus, exportin CRM1 and nuclear G-actin are required for the nuclear export of MRTF-A [174,175]. Contrarily, treatment with exogenous agents that enhance actin polymerisation (*e.g.* jasplakinolide) or the disruption of the interaction between MRTF-A and both cytoplasmic and nuclear G-actin (*e.g.* cytochalasin D or swinholide A) enhances the nuclear accumulation of MRTF-A as well as hinders its nuclear export [174]. However, how actin dynamics regulate the transcriptional activity of other transcription factors is still poorly understood.

Specific actin nucleation-promoting factors have been described to interact with and influence the activity of a wide range of transcription factors. For example, the inhibition of overall cellular actin polymerisation impairs the ability of JMY to enhance p53 activity in *BAX*-luciferase reporter assays [127]. Additionally, we recently demonstrated that JMY's Arp2/3-driven actin nucleation activity is required for the expression of p53-dependent DNA repair factors [130]. Together, these studies highlight the intricate role of nuclear actin dynamics in the regulation of gene expression.

<u>The role of nuclear actin during DNA repair.</u>

In the past decade, a growing body of evidence supports the role of nuclear actin during DNA repair [176]. Several studies demonstrated that DNA damage (*e.g.* UV radiation) leads to the formation of different nuclear actin structures [177,178]. Nuclear F-actin participates in both homology-directed and NHEJ repair pathways [155]. Recently, two independent studies demonstrated the important role of nuclear actin filament formation, mediated by the Arp2/3 complex, during homology-directed repair of DSBs [178,179]. The pathway is initiated by the MRE11-dependent recruitment of nuclear myosins and the Arp2/3 complex to the DSB. The Arp2/3 complex is activated via its interaction with SCAR and WASH, which results in the formation of nuclear actin filaments towards the nuclear periphery. Concomitantly, myosins recruit UNC45, which travels along the actin fibres to anchor the chromatin

containing the DSB to the nucleopore region, where RAD51-mediated homology-directed repair is initiated [179]. The resolution of these DSBs through homology-directed repair also requires the WASP-mediated activation of the Arp2/3 complex, which enhances the clustering of DSBs, the recruitment of repair factors and DNA end resection [178].

Additionally, nuclear F-actin participates in the NHEJ repair pathway [176], although the role of actin dynamics within this process is incompletely understood. The inhibition of overall actin polymerisation via latrunculin treatment reduces the retention of Ku80 at the DSB [180]. Recent findings demonstrated a direct role of nuclear WASH in the repair of DSBs via NHEJ [181]. Mechanistically, WASH is recruited to DSBs where it interacts with the Ku heterodimeric complex. At these DNA lesions, the WASH-mediated Arp2/3-dependent actin nucleation is required for chromatin relaxation and repair of the DNA lesion through NHEJ. Moreover, nuclear WASH can enhance the activation of DNA-PK [181].

Together, these studies demonstrate a role for nuclear F-actin during DNA repair in response to stress, where the vast majority of these processes are controlled by the Arp2/3 complex and actin nucleation-promoting factors from the WASp protein family [155]. Although it is known that these factors can be localised in the nucleus [178,179], the regulatory mechanisms that control their cellular localisation during DNA damage remain to be elucidated. Actin is constantly shuttling between the cytoplasmic and nuclear compartments. Additionally, genotoxic stressors induce changes in the availability and conformation of nuclear actin [177,178]. It will be relevant for future studies to investigate how these stress-mediated changes in nuclear actin dynamics can affect the activity of actin binding proteins in the nucleus and their impact on DNA repair.

Nuclear actin in nuclear organisation and organelle biogenesis.

As described in the aforementioned sections, nuclear actin plays a fundamental role in transcription and DNA repair. An increasing body of research also supports the role of nuclear actin in nucleoplasm compartmentalisation and the formation of subnuclear organelles. For example, an early study demonstrated that reducing nuclear F-actin formation (*e.g.* latrunculin A treatment or overexpression of *XPO6*) resulted in nucleoli fusion [182] . A more recent study further supports that nuclear F-actin is required for the internal structural organisation of nucleoli, demonstrating

that impaired nuclear actin filament formation led to the fusion of the POLR1E-enriched fibrillar centres within nucleoli [183]. Collectively, these findings highlight that disturbances in nuclear actin filament formation compromise nucleoli organisation, which is known to induce nucleolar stress and reduce rRNA transcription [184].

In addition, nuclear actin has been suggested to contribute to the biogenesis and maintenance of paraspeckles [185–187]. Paraspeckles are non-membranous subnuclear bodies constructed throughout an architectural long non-coding RNA (lncRNA) referred to as *NEAT1_2* [188,189]. Recent studies suggest that cellular confinement obtained by chamber compression [186], culture in stiffer surfaces [185] or microgravity conditions [187], result in changes in nuclear actin filament formation and, thus nuclear morphology. These nuclear remodelling processes are thought to be correlated with changes in paraspeckle formation, size and nuclear localisation independent of the expression of *NEAT1_2*, which suggests that changes in nuclear actin dynamics may be required for the biogenesis of paraspeckles [185–187]. The following section describes the expression of lncRNA *NEAT1_2*, its role in paraspeckle biogenesis and the function of these subnuclear bodies in tumour cell fate during stress.

## 1.5. The role of lncRNA *NEAT1_2* in the formation of paraspeckles

Functional significance of lncRNAs in tumorigenesis, with focus on *NEAT1*.

As mentioned in the previous section, the expression of the vast majority of lncRNAs is controlled by RNA polymerase II [190]. lncRNAs are a collection of RNA molecules that present a length greater than 500nt and do not encode information to produce functional proteins [191,192]. lncRNAs constitute more than 60% of the total RNA expressed in mammalian cells, but the function of most of these lncRNAs remains largely unknown [193]. Similar to mRNAs, lncRNAs can present canonical (mRNA-like) processing, including the presence of a 5' cap and 3' poly(A) tail and alternative splicing of its exonic regions [194]. The expression of lncRNAs is commonly cell-type specific and often lower than the expression of mRNAs [195]. lncRNAs can perform a plethora of functions, including nuclear roles such as modulating DNA replication and DNA repair, regulation of gene expression, control of alternative splicing, and the formation of non-membranous subnuclear condensates [196,197]. For example, lncRNAs can control the transcriptional expression of nearby genes via changes in chromatin architecture through their

interaction with chromatin remodelling complexes [198], as well as promote the formation of transcriptional hubs [199,200] and splicing domains [198,201].

Interestingly, tumour cells commonly present deregulation in the expression of a wide range of lncRNAs (e.g. *NEAT1* and *MALAT1*), which can impact key cancer hallmarks such as sustained proliferation, resistance to cell death, angiogenesis and metastasis [202–206]. For example, in response to several stressors, including DNA damage and hypoxia, p53 promotes the expression of lncRNA *NEAT1* [207]. As described in greater detail in the following sections, the longer isoform of lncRNA *NEAT1,* referred to as *NEAT1_2,* is a fundamental scaffold during the paraspeckle biogenesis [188,189]. Paraspeckles are non-membranous subnuclear domains which are formed in a two-step process [208]. lncRNA *NEAT1_2* orchestrates the recruitment of over 50 RNA-binding proteins that, through liquid-liquid phase separation, result in the formation of organised spherical condensates known as paraspeckles, which can be detected close to nuclear splicing speckles [209]. Although incompletely understood, paraspeckles are thought to be important in the cellular response to stress stimuli, which is suggested to occur through their ability to modulate gene expression [210].

p53 controls the expression of lncRNA *NEAT1* in response to stress.

Although the vast majority of research focuses on the ability of p53 to regulate the expression of protein-coding genes, p53 also modulates the expression of long non-coding RNAs (lncRNA), including *NEAT1* [207,211]. The human *NEAT1* locus encodes two different isoforms (Fig 1.7b), including the shorter *NEAT1_1* transcript (3.7kb) and the longer *NEAT1_2* isoform (22.7kb) [208]. The latter does not present a canonical polyadenylation tail, and it is stabilised, similarly to tRNAs, via RNase P processing resulting in the formation of a triple helix structure at its 3'-end [212,213]. *NEAT1_1* is obtained through alternative 3'-end processing from *NEAT1_2*, and contrarily to this latter isoform, *NEAT1_1* presents a polyadenylation signal (PAS) that enhances its stability [212]. The 3'-end processing leading to *NEAT1_1* isoform expression is controlled by two main complexes (Fig 1.7b), named CFIm (NUDT21 and CPSF6) and Integrator (INTS11). The CFIm complex recognises a series of five UGUA repeats located upstream of the canonical PAS, thus promoting the expression and polyadenylation of *NEAT1_1* [212]. The Integrator complex binds with adjacent sequences flanking the PAS and inhibits the interaction with *NEAT1_2*-promoting factors like HNRNPK, also leading to *NEAT1_1* expression [214]. In

addition, TDP-43 has also been proposed to enhance *NEAT1_1* expression through binding with the same UGUA repeats used by the CFIm complex (Fig 1.7b) [215]. However, the mechanisms by which TDP-43 controls *NEAT1* isoform-specific expression are incompletely understood.

In contrast, HNRNPK and HNRNPM enhance *NEAT1_2* expression. Both HNRNPK and HNRNPM bind with a pyrimidine-rich region adjacent to the PAS (Fig 1.7b). This interaction blocks the recruitment of CFIm and Integrator complexes to *NEAT1* transcripts which promotes the expression of *NEAT1_2* [212]. Mechanistically, HNRNPK can interact with NUDT21, which reduces its interaction with CPSF6 hindering the formation of an active CFIm complex [212]. However, how these factors coordinate to produce specific *NEAT1* isoforms, and which upstream regulatory mechanisms activate these components remains to be elucidated.

Both *NEAT1* transcripts are DNA damage-responsive lncRNAs whose expression is enhanced upon exposure to a wide variety of stressors [216]. For example, during genotoxic stress (*e.g.* etoposide and doxorubicin), p53 is recruited to the *NEAT1* promoter (Fig 1.7c), which results in the expression of both *NEAT1* transcripts [207,217–219]. However, several studies have reported that p53 induces a higher expression of *NEAT1_2* transcript when compared to *NEAT1_1* levels [207]. Even though, the detailed mechanisms that control this p53-driven isoform-specific expression of *NEAT1* transcripts remain to be characterised. Although the increased levels of *NEAT1* transcripts are best known to occur upon DNA damage, other stressors have also been reported to induce *NEAT1* expression. Hypoxia can also lead to the expression of both *NEAT1* transcripts. Mechanistically, HIF2$\alpha$ is recruited to the *NEAT1* promoter (Fig 1.7c), which results in the expression of both *NEAT1* isoforms [220,221]. Interestingly, p53 has also been described to enhance *NEAT1* expression under hypoxic conditions [207]. Furthermore, proteotoxic stress induced by proteasomal inhibition increases the recruitment of RNA polymerase II and p53 to the *NEAT1* promoter, which induces the expression of *NEAT1* transcripts [222]. Additionally, in response to metabolic stress and mitochondrial dysfunction, *NEAT1* levels increase via ATF2-dependent transcriptional regulation [223].

As described, several transcription factors can regulate *NEAT1* expression in response to various stressors. However, little is known about the negative regulation of *NEAT1* expression. It has been proposed that c-MYC and E2F1 can

be recruited to the *NEAT1* promoter (Fig 1.7c). This interaction may inhibit *NEAT1* expression in liquid malignancies, although the regulatory mechanisms are incompletely understood [224,225]. Collectively, these studies support that, in response to different stressors, *NEAT1* transcripts are predominantly activated. However, whether this activation is isoform-specific, the upstream signalling responses that lead to *NEAT1* expression and the negative regulation controlling *NEAT1* levels have not yet been elucidated.

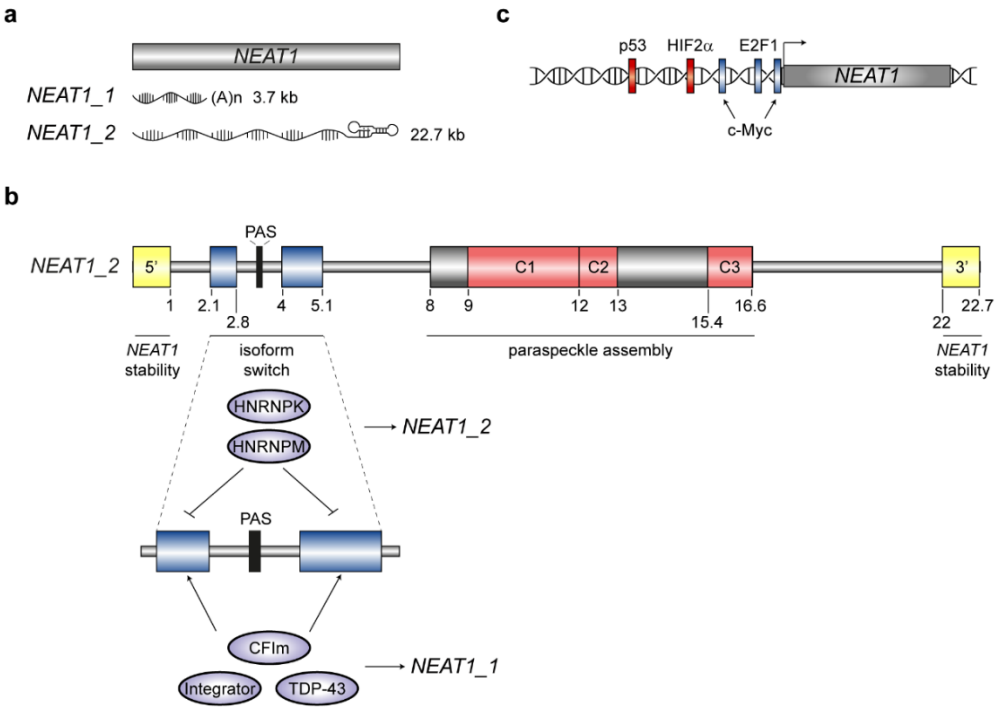


***Figure 1.7. lncRNA NEAT1_2 architecture. a)*** *Representation of the human NEAT1 locus and the two encoded transcripts, including the short NEAT1_1 and the long NEA1_2, whereas each transcript's size (kb) is detailed on the right.* ***b)*** *Schematic representation of the lncRNA NEAT1_2 domains. A zoomed view of the isoform switch domain is represented below with the NEAT1_2 promoting and inhibiting-related factors. C1-C3: Represent the three subdomains within the central NEAT1_2 region. The position of each domain relative to the 5'-end is detailed below (kb).* ***c)*** *Diagram of NEAT1 promoter region and the position of the main transcription factors where red and blue represent promoting and inhibiting factors, respectively. Figure was adapted from* [208].

*NEAT1_2* architecture and its role in the formation of paraspeckles.

As described, *NEAT1* can be transcribed into two different isoforms, the shorter polyadenylated *NEAT1_1* (3.7kb) and the longer *NEAT1_2* (22.7kb) [212]. While the function of *NEAT1_1* remains incompletely understood, *NEAT1_2* is a known architectural scaffold for the formation of paraspeckles [188,189]. Paraspeckles are non-membranous subnuclear bodies that were first identified in close proximity to nuclear splicing speckles [209]. These subnuclear bodies are visible as discrete foci in cultured cells and range in number from 2-30 [226]. Paraspeckles are composed of approximately 50 RNA-binding proteins (Table 1.1) arranged along the lncRNA *NEAT1_2* [210]. Notably, these subnuclear structures are dependent on *NEAT1_2* expression as *NEAT1* knockout cells fail to form these structures, which can only be rescued by overexpressing *NEAT1_2* but not *NEAT1_1* [212].

**Table 1.1. Essential paraspeckle-associated components**

| Target | Paraspeckle zone | Paraspeckle function | Protein category |
|---|---|---|---|
| *NEAT1_2* | 5'- and 3'-end (Shell) Central domain (Core) | Structural scaffold | N/A |
| *DAZAP1* | Shell | Paraspeckle assembly | 1B |
| *HNRNPH3* | NFC* | Paraspeckle assembly | 1B |
| *HNRNPK* | N/A | NEAT1_2 expression | 1A |
| *FUS* | Core | Paraspeckle assembly | 1B |
| *NONO* | Core | NEAT1_2 stability | 1A |
| *PSPC1* | Core | NEAT1_2 stability | 1B |
| *RBM14* | Core and Shell | NEAT1_2 stability | 1A |
| *SFPQ (PSF)* | Core | NEAT1_2 stability | 1A |
| *SMARCA4* | Core and Shell | NFC* | 1B |
| *TDP-43* | Shell | NFC* | 1B |

** N/A: not applicable, NFC: need further characterisation. An updated version of the table from [208,216].*

Paraspeckle biogenesis proceeds in two different steps [208]. Initially, core paraspeckle-associated RNA-binding proteins (*e.g.* NONO and SFPQ) interact with *NEAT1_2* leading to the formation of an intermediate RNP complex (Fig. 1.8a, Table 1.1 class 1A) [212]. Then, although the exact mechanisms have yet to be determined, this pre-formed RNP structure facilitates the aggregation of additional

*NEAT1_2* molecules and RNA-binding proteins via liquid-phase separation (Fig. 1.8a, Table 1.1 class 1B) [227]. These interactions cause *NEAT1_2* to undergo conformational changes adopting a U-shape and result in the formation of organised liquid-liquid structures which exhibit distinct exterior (shell) and interior (core) compartments (Fig. 1.8b) [188].

Recent studies using genome editing via CRISPR-Cas9 have described three main domains in *NEAT1_2* transcript essential for its architectural role during paraspeckle biogenesis [188,189]. Both the 5'- and 3'-ends are required for *NEAT1_2* stability. As described, the 3'-terminal region presents a triple helix structure that increases *NEAT1_2* half-life [212], whilst the deletion of this region leads to *NEAT1_2* degradation and thus reduced detection of paraspeckles [188]. Additionally, the complete deletion of the 5'-end (0-4.5kb) lowers the number of detectable paraspeckles similar to the phenotype observed upon deletion of the 3'-end. Surprisingly, a smaller truncation spanning the first 0-2.8kb region abolishes the expression of both *NEAT1* isoforms and, thus, paraspeckle formation [188]. It is speculated that the interaction of these flanking domains with RNA-binding proteins leads to the formation of specific RNP complexes protecting *NEAT1_2* against degradation [228]. However, these interactors and the protective mechanisms remain to be characterised.

The 5'-end region is followed by the isoform switching domain, which contains a canonical PAS that promotes *NEAT1_1* isoform expression. The deletion of the PAS leads to increased *NEAT1_2* levels which enhance paraspeckle biogenesis [189]. Lastly, *NEAT1_2* central domain comprises eight tandem repeats of the long interspersed nuclear element 1 (LINE1), which belongs to the family of class I transposable elements. These LINE1 repeats are proposed to regulate the interaction between *NEAT1_2* and the vast majority of paraspeckle-associated components [229]. This central domain can be divided into three structurally functional subdomains (C1: 9–12kb, C2: 12–13kb, and C3: 15.4–16.6kb). Simultaneous deletion of both C1 and C2 abolishes paraspeckle biogenesis, whereas the single deletion of these domains has no effect. The removal of the C3 region also results in the loss of paraspeckles, independently from C1 and C2 domains, suggesting a specialised functionality [188]. However, the precise mechanisms by which these regions promote paraspeckle biogenesis require further characterisation.

As described, paraspeckles are ordered liquid-liquid structures that exhibit two distinct regions, including exterior (shell) and interior (core) compartments (Fig. 1.8b). Throughout the formation of paraspeckles, *NEAT1_2* folds into a U-shape with its 5'- and 3'-ends located towards the shell, leaving *NEAT1_2* central segment at the core of the paraspeckle [230]. Recently, it has been described that the deletion of both 5'- and 3'-ends lead to the formation of liquid-liquid structures similar to paraspeckles, hereafter called pseudo-paraspeckles, which lose the conventional shell-core conformation. These pseudo-paraspeckles were reported to be enlarged due to increased retention of *NEAT1_2* molecules [189]. Although previous studies have proposed that conformational changes in paraspeckles can impact their cellular role during stress [222], there is still a lack of mechanistic understanding of how changes in the morphology of paraspeckles can modulate cell fate. Collectively, these structural studies describe three essential domains within *NEAT1_2,* which are crucial for ensuring its stability and functionality during paraspeckle biogenesis.

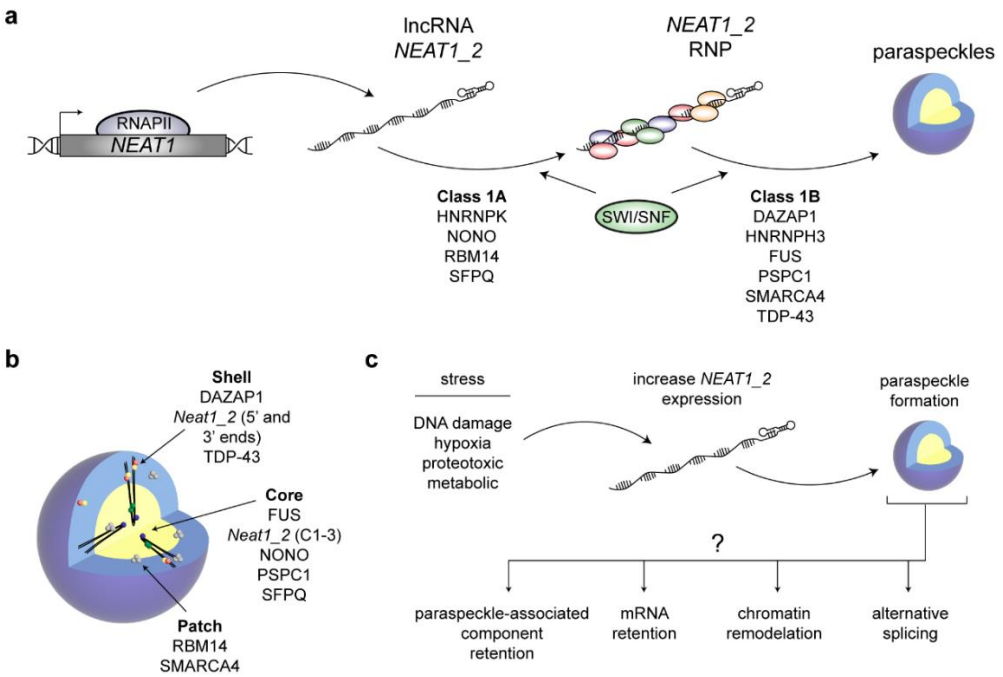


***Figure 1.8. Paraspeckle biogenesis and their cellular role. a)*** *Schematic representation of paraspeckles biogenesis. RNA polymerase II, in combination with several transcription factors, leads to the expression of lncRNA NEAT1_2. Paraspeckle formation is a two-step process where class 1A paraspeckle-associated components interact and stabilise NEAT1_2, which promotes the recruitment of additional RNA binding proteins from class 1B through liquid-liquid*

*phase separation to form paraspeckles.* ***b)*** *Schematic representation of the shell-core paraspeckle organisation and the arrangement of the main paraspeckle-associated components. Panels (a-b) were adapted from* [208]*.* ***c)*** *Diagram represents the role of paraspeckles in the cellular response to stress. Original panel.*

The role of paraspeckles in tumour cell fate during stress.

Although incompletely understood, paraspeckles have been proposed to have an important role in the cellular response to stress stimuli, which is suggested to occur through their ability to regulate gene expression (Fig. 1.8c) [210]. Paraspeckle formation depends on the expression of *NEAT1_2* via RNA polymerase II (Fig. 1.8a). These subnuclear bodies are mainly constructed co-transcriptionally and can interact with active chromatin regions promoting their relaxation and expression [199]. For example, *NEAT1_2* has been shown to interact with acetyltransferase p300, promoting histone acetylation at the transcription start site of endocytosis-related genes [231].

Moreover, several paraspeckle components, such as SFPQ, are sequestered during paraspeckle biogenesis, limiting their availability (Fig. 1.8c). The retention of SFPQ within paraspeckles restricts its transcriptional activity both by inhibiting the expression of pro-apoptotic genes in response to proteotoxic stress [222], or by facilitating the expression of *IL-8* in response to immune activation [232]. Several studies suggest that an enhanced formation of paraspeckles leads to an increased tumour cell resistance to genotoxic stressors, including a wide range of DNA damaging agents as well as hypoxic conditions [207,218,220,221]. It is hypothesised that the retention of paraspeckle-associated components within these subnuclear bodies can be an important mechanism through which tumour cells enhance their resistance to various stressors.

Additionally, paraspeckles can sequester specific mRNAs that present inverted Alu (IRAlus) repeats in their 3'-UTR regions (Fig. 1.8c). This retention occurs via direct interaction between the mRNAs and paraspeckle-associated RNA binding proteins such as NONO and SFPQ [233]. For example, under non-perturbed conditions, *CAT-2* mRNA presents a 3'-UTR IRAlus domain that leads to its retention within paraspeckles. Upon induction of cellular stress, the 3'-UTR region of *CAT-2* mRNA is cleaved through mechanisms that remain uncharacterised, resulting in its release from the paraspeckles, cytoplasmic translocation and protein translation

[234]. Similarly, under hypoxic conditions, *F11R* mRNA accumulates within paraspeckles. Although hypoxia does not alter overall *F11R* protein expression, when oxygen levels return to physiological conditions, there is rapidly released of *F11R* mRNA from paraspeckles, leading to its cytoplasmic protein expression [235]. Together, these studies suggest that the paraspeckle-mediated confinement of IRAlus-containing mRNA reduces their cytoplasmic translocation and subsequent protein translation [236].

The role of paraspeckles in alternative splicing.

A recent study has proposed a novel regulatory mechanism suggesting that paraspeckles may impact tumour cell fate by modulating alternative splicing (Fig. 1.8c) [198]. This study reported a new interaction between paraspeckle-associated and spliceosome components. Several spliceosome factors (*e.g.* U2AF1, HNRNPA and SNRPA) were copurified with NONO, PSPC1 and SFPQ, which are core paraspeckle components. Moreover, the study reported changes in alternative splicing (*e.g. PRPF39*, *METTL17* and *RBM5*), which were proposed to derive from the disruption of paraspeckles via *NEAT1* depletion. The disruption of these subnuclear bodies was suggested to increase the availability of spliceosome factors [198]. This study proposes a new mechanism by which paraspeckles can impact gene expression through sequestering spliceosome components resulting in overall changes in splicing [198]. However, whether the expression of these specific spliced transcripts impacts on cell fate remains incompletely understood.

Together, these studies suggest that paraspeckles can impact gene expression through various mechanisms, including changes in chromatin accessibility, the retention of specific mRNAs and paraspeckle-associated components and by modulating overall splicing.

## 1.6. Alternative splicing – When one gene becomes multiple proteins.

Overview of splicing – Spliceosome assembly and transesterification reactions.

Splicing is a fundamental posttranscriptional processing involving the removal of introns (non-coding sequences) from precursor mRNAs (pre-mRNAs). This process results in the formation of mature mRNAs containing the collection of exons (coding sequences) [237]. Splicing is orchestrated by the spliceosome, which is a multiprotein complex formed by five snRNPs (U1, U2, U4, U5 and U6) and a

broad array of regulatory factors [238]. In eukaryotic cells, there are two spliceosomal complexes, the U2-dependent spliceosome, which is responsible for 99% of intron removals (recognising GT-AG splice sites) and the minor U12-dependent spliceosome (identifying AT-AC splice sites). Similar to the former, the minor spliceosome is also formed by five snRNPs named U11, U12, U4atac, U5 and U6atac [239]. In order for the spliceosome to recognise and remove the non-coding regions from pre-mRNAs, introns are defined by short, conserved motifs at the 5'- and 3'-ends called splice sites (5'SS and 3'SS). In addition, introns present a conserved adenosine branch point (BS) and a polypyrimidine tract (PPT) located upstream of the intronic 3'-end, which are required during intron removal [240].

Splicing is a stepwise process in which the spliceosome assembly is initiated by the interaction between the U1 snRNP and the intronic 5'SS through an ATP-independent base-pairing binding [241]. This junction is required for the subsequent recruitment of SF1 and U2AF subunits to the adenosine BS-PPT and the intronic 3'SS, respectively, forming the E complex (Fig. 1.9a) [242]. After the formation of the E complex, the U2 snRNP is recruited and bound to the adenosine BS in an ATP-dependent manner, an interaction that is stabilised by SF3A and SF3B multiprotein subunits, resulting in the formation of the A complex (Fig. 1.9b) [243]. In particular, SF3B14/SF3B6 (hereafter referred to as SF3B6) and PHF5A, two components of the SF3B complex, assist SF3B1 during the recognition of the adenosine BS [243]. Mechanistically, SF3B1 must form a closed pocket-shape conformation to recognise the adenosine BS, which is promoted by the interaction with PHF5A. The latter binds to the concave surface of SF3B1 and bridges opposed residues from the N- and C-terminal domains of SF3B1, generating the enclosed confirmation [244]. Additionally, SF3B6 interacts with the C-terminus of SF3B1, enhancing the transition from the open-to-close conformation [243]. Following this step, further conformation changes within the A complex lead to the disassembly of SF1 and U2AF subunits [245].

The pre-assembled U4/U6.U5 tri-snRNP is then recruited to the A complex in a reaction catalysed by Prp28, resulting in the formation of the B complex that contains all factors for the transesterification reactions but is still inactive (Fig. 1.9c) [246,247]. The activation of the B complex involves additional conformational changes resulting in the release of U1 and U4 snRNPs and the transfer of the intronic 5'SS to the U5/U6 subunits to form the catalytically active B complex ($B^{act}$/B* complex, Fig. 1.9d) [248]. The intron removal is then conducted via two transesterification

reactions. First, the B* complex promotes the nucleophilic attack of the intronic 5′SS by the adenosine BS resulting in the realise of the upstream exon and the formation of an intron lariat (Fig. 1.9e). This transesterification reaction induces conformational changes in the B* complex, which matures into the C complex, in a process catalysed by Prp2 [243]. The second transesterification reaction consists of the nucleophilic attack of the intronic 3'SS by the released upstream exon. This reaction leads to the removal of the intron lariat [240]. Concomitantly, the junction of the upstream and downstream exons is catalysed by the EJC/TREX complexes [249]. Ultimately, further conformational changes in the C complex lead to the formation of the post-catalytic spliceosome and release of the remaining subunits, including the U2, U5 and U6 snRNPs and auxiliary factors, which can be reused for a new splicing cycle [250].

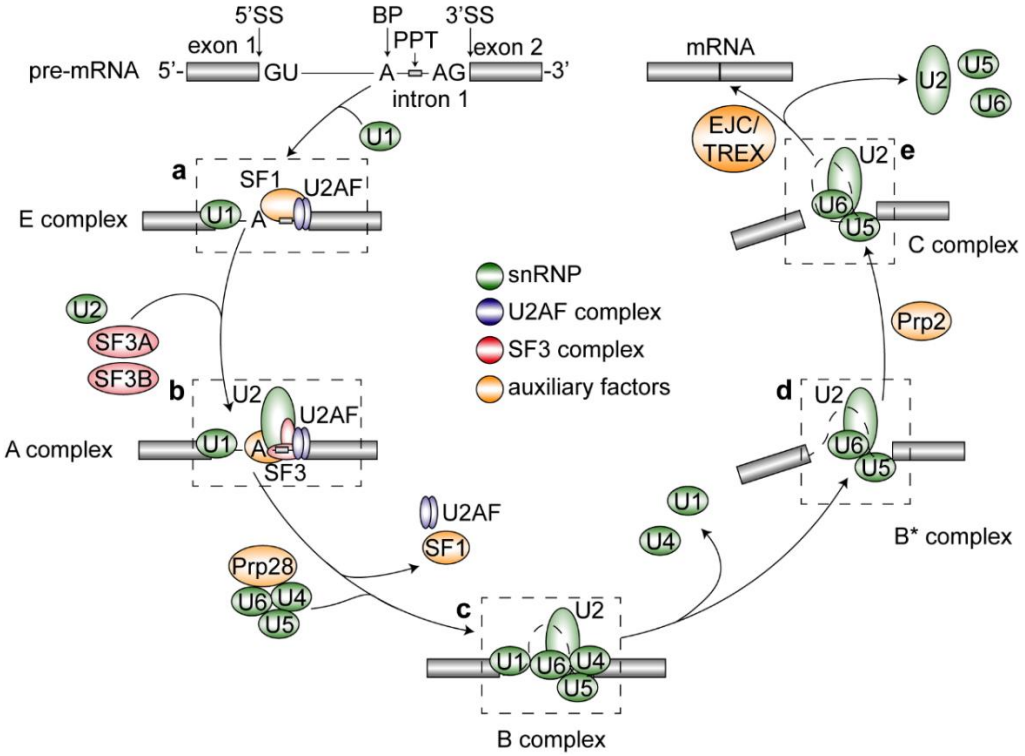


***Figure 1.9. Splicing process.*** *Stepwise spliceosome assembly on a pre-mRNA. The main steps are highlighted with red rectangles and notes as follows:* ***a)*** *U1 snRNP interacts with pre-mRNA to form the E complex,* ***b)*** *U2 snRNP binds with the adenosine BS releasing SF1 and U2AF subunits forming the A complex,* ***c)*** *Pre-assembled U4/U6.U5 tri-snRNP interacts with the previous spliceosomal subunits forming the B complex,* ***d)*** *Dissociation of U1 and U4 snRNPs leading to the formation of the catalytically active spliceosome (B* and C complexes),* ***e)***

*First transesterification reaction and formation of the intron lariat and* ***f)*** *Second transesterification reaction, binding of exons and detachment of the intron lariat with the remaining spliceosomal factors. The figure was adapted from* [251]*.*

The aforementioned splicing process is referred to as canonical splicing, which consists of the processing of all transcribed introns and exons from a particular pre-mRNA [240]. Besides this canonical processing, the spliceosome can also induce various arrangements of exons, retention of introns and the use of non-conventional 5'SS and 3'SS, increasing the diversity of mRNA isoforms. This non-canonical processing is referred to as alternative splicing and has been described to occur in over 95% of human genes [252]. This non-canonical processing can lead to the formation of seven main types of events: i) cassette exon, ii) intron retention, iii) mutually exclusive exons, iv-v) alternative 5'SS and 3'SS and vi-vii) alternative promoter or first exon and alternative poly(A) site or last exon [251].

The process of alternative splicing can produce multiple spliced mRNAs, which can encode proteins with different sequences and functions, despite been originated from a single gene [253]. Although the cellular function of the vast majority of alternatively spliced transcripts remains uncharacterised, specific targets (in a cell type-specific context) have been investigated. For example, *BCL2L1* which encodes for BCL-x, can undergo alternative splicing producing two different isoforms, including BCL-xS and BCL-xL a pro-apoptotic and anti-apoptotic variant, respectively [254]. The aberrant alternative splicing processing of *BCL2L1* reported in glioblastoma cells leads to an enhanced expression of BCL-xL and a reduction in tumour cell death [255].

<u>Deregulation of splicing in tumour cells.</u>

As described, alternative splicing is a tightly controlled process essential for regulating gene expression, which expands the diversity of mRNA transcripts [252]. Therefore, defects and deregulation in the alternative splicing machinery have been associated with human disorders, including tumour formation and progression [256]. Most human cancers exhibit widespread splicing abnormalities, which can lead to the variable use of exonic regions and frequent intron retention events generating aberrant mRNA isoforms [257]. These cancer-specific transcripts have been described to reduce the expression of tumour suppressors or enhanced expression of oncogenes and may influence key cancer hallmarks, including

increased cell proliferation, decreased cell death and resistance to therapy [258]. In human tumour cells, alternative splicing deregulation commonly occurs through both the aberrant expression of spliceosome components (*trans*-acting factors) or mutations in the conserved splice sites within the pre-mRNA molecule (*cis*-acting factors) [251].

Deregulation of *trans*-acting factors can arise from both missense point mutations in core spliceosome components, which are more frequently reported in haematological malignancies or due to changes in the copy number and expression levels of splicing factors which is a common feature of solid tumours [259]. Within the former, an extensive body of research describes *SF3B1* as the most frequently mutated splicing factor in human tumours [256]. *SF3B1* mutations mainly occur between exons 12-15, which encode the HEAT domain responsible for SF3B1 protein-protein and protein-RNA interactions. Mutations in this domain disrupt the ability of SF3B1 to recognise the adenosine BS, a crucial step for forming the spliceosome A complex (Fig. 1.9b) [243]. A recurrent mutation within the $K^{700E}$ residue impacts the ability of SF3B1 to bind with the adenosine BS and leads to the inclusion of 10-30bp of the intronic 3'-end due to the use of a cryptic 3'SS [260]. Mechanistically, this can lead to the expression of aberrant mRNA isoforms promoting cell proliferation and resistance to apoptosis [261]. In addition, *SF3B1* mutations have been described to impact the expression of other spliceosome factors, leading to overall alternative splicing deregulation [262]. Thus, *SF3B1* mutations in tumour cells can result in the aberrant alternative splicing of targets involved in cell survival both by the inaccurate recognition of the adenosine BS or due to changes in the expression of splicing factors. Along with *SF3B1*, other core spliceosome components (*e.g. PHF5A*, *SRSF2* and *U2AF1*) also present mutations which impacts on their role in alternative splicing, although the detailed mechanisms are not fully understood [259]. Mutations within these factors have been proposed to hinder their ability to recognise the adenosine BS and the 5'SS and 3'SS. This may impact the capacity of the spliceosome to accurately include or remove exons and introns during the processing of pre-mRNAs [256].

In addition, the deregulation of alternative splicing can also arise from changes in the expression of splicing factors [259]. For example, core spliceosome components such as PHF5A and SF3B6 have been described to promote tumorigenesis through their impact on alternative splicing. For instance, PHF5A, a subunit of the SF3B complex, is required for the recognition of the adenosine BS within the pre-

mRNA allowing the recruitment of the U2 snRNP to form the A complex (Fig 1.9b) [243]. The increased expression of PHF5A in colorectal cancer cells promotes the retention of the second intron of *TEAD2* as well as the third intron of *KDM3A* pre-mRNAs, which promotes tumour cell proliferation and migration [263,264]. Additionally, reduced expression of PHF5A in breast cancer cells enhances apoptosis by removing the fifth exon of *FASTK* mRNA, which promotes the activation of the intrinsic apoptotic pathway [265]. Thus, these studies suggest that increased expression of PHF5A leads to enhanced tumour cell survival and migration.

SF3B6 which is another subunit of the SF3B complex, is required during the activation of the B complex during the spliceosome formation (Fig. 1.9d). Through its interaction with SF3B1, SF3B6 catalyses conformational changes within the former, leading to the recognition of the adenosine BS [243]. Changes in SF3B6 expression can also modulate tumour cell fate. The reduced expression of SF3B6 in adenocarcinoma cells results in aberrant alternative splicing of *MDM4*, leading to the expression of a smaller protein isoform. Although the detailed mechanisms are incompletely understood, expression of this smaller MDM4 isoform results in increased tumour cell death [266]. Additionally, reduced expression of SF3B6 in HeLa cells results in alternative splicing of *TUBGCP6* pre-mRNA, which is essential for centrosome maturation. The aberrant expression of TUBGCP6 compromises the cellular progression through mitosis, resulting in reduced cell proliferation [267]. Therefore, these studies suggest that decreased expression of SF3B6 leads to a reduction in tumour cell survival.

Other core spliceosome components, such as members of the SR and the HNRNP family of proteins, are also frequently deregulated in tumour cells and have been described to impact tumour progression through modulating alternative splicing [240]. Surprisingly, the regulatory mechanisms that control the expression of the vast majority of spliceosome components are incompletely understood. It has been recently suggested that MYC may promote the expression of specific spliceosome components [268].

Interestingly, nuclear actin has been recently described as an interactor of core and auxiliary splicing factors, whereas changes in nuclear actin availability may modulate alternative splicing [166]. Moreover, the actin nucleator WASP has been shown to modulate alternative splicing via two different mechanisms. At a transcriptional level, WASP hinders the expression of splicing factors (*e.g.* SRSF2)

via a potential interaction with Kruppel-like zinc finger transcription regulators. At a structural level, WASP is required to form nuclear condensates enriched in active RNA polymerase II, nascent RNA and splicing factors. These WASP-dependent nuclear bodies have been proposed to impact alternative splicing by modulating the availability of splicing factors such as SRSF2 [269]. However, it will be relevant for future studies to investigate the precise mechanisms by which actin (or actin polymerisation) modulates the expression of splicing factors and the formation of nuclear splicing speckles and how this may influence overall alternative splicing.

Targeting the spliceosome as a therapeutic cancer approach.

As defects in *trans*-activating splicing factors in human tumours are predominantly heterozygous and mutually exclusive, this implies that cancer cells rely on the presence of at least one functional wild-type allele [270]. This, combined with the fundamental role of alternative splicing during tumorigenesis, has generated significant interest in targeting the spliceosome as a promising therapeutic strategy for treating human malignancies [256]. Multiple approaches are currently being developed and investigated, including the inhibition of core spliceosome subunits and targeting specific alternatively spliced transcripts [251]. The following sections focus on two small molecule spliceosome inhibitors named pladienolide B (hereafter referred to as plad B) and isoginkgetin.

Plad B is a natural macrocyclic lactone that was discovered as a bacterial fermentation product [271]. Plad B intercalates in the tunnel-shape region between the HEAT domain of SF3B1 ($K^{1071}$, $R^{1074}$, $V^{1078}$, $V^{1110}$, $V^{1114}$, $F^{1153}$ and $Y^{1157}$) and two residues from PHF5A ($Y^{36}$ and $R^{38}$) within the U2 snRNP. The interaction of plad B with SF3B1 and PHF5A stalls the SF3B complex into an ‘open’ conformation preventing it from further conformation changes required to enclose SF3B1’s HEAT domain and subsequent recognition of the adenosine BS [272]. This plad B-mediated inhibition of SF3B1 commonly results in the accumulation of pre-mRNA molecules presenting intron retention events [273]. Several studies have described that treatment with plad B can increase tumour cell death and reduce cell proliferation. The inhibition of the spliceosome upon plad B exposure induces widespread intron retention events in chronic lymphocytic leukaemia cells, resulting in the enhanced expression of pro-apoptotic *BCL-xS* and *MCL-1* transcripts and increased activation of apoptosis [274]. More recently, plad B has also been shown to modulate the splicing processing of *CDKN1B* (*p27),* leading to G2-

M phase arrest in glioblastoma cells. Mechanistically, the plad B-mediated inhibition of the spliceosome leads to the use of a cryptic exon 2 in the *p27* pre-mRNA resulting in the expression of a truncated protein that binds to and inhibits cyclins involved in the transition of the G2-M phase [275]. Other studies further support the evidence that treatment with plad B can impair cell proliferation and increase cell death [276–279], although the detailed mechanisms by which the plad B-mediated inhibition of the spliceosome leads to these results remain to be elucidated. Resistance to plad B has already been described in tumours presenting *SF3B1* and *PHF5A* mutations ($SF3B1^{R1074H}$ or $PHF5A^{Y36C}$) [280,281]. In particular, these mutations abolish the interaction of plad B with the residues of the tunnel-shape structure formed between SF3B1 and PHF5A, as described [272].

Novel splicing inhibitors, such as isoginkgetin, have been developed to counteract tumour resistance to plad B. Although incompletely understood, this *Ginkgo biloba* bioflavonoid exhibits a wider spliceosomal inhibition by blocking the recruitment of the U4/U6.U5 tri-snRNP to the spliceosome A complex [282]. Isoginkgetin was discovered during a compound library screening of potential spliceosome inhibitors using a luciferase synthetic construct whose activity was inactivated upon splicing [282]. This study also demonstrated that treatment with isoginkgetin led to intron retention events in several targets, including *TUBB*, *ACTB*, *DNAJB1*, and *GAPDH* and decreased tumour cell proliferation. Surprisingly, the isoginkgetin-mediated effects on cell growth and proliferation were reversible after isoginkgetin washout [282].

Isoginkgetin has been shown to compromise the recruitment of splicing factor BUD31, which is required for the recruitment of the U4/U6.U5 tri-snRNP to form the spliceosome B complex, leading to the removal of the third exon of *BCL2L12* pre-mRNA which results in reduced proliferation of ovarian tumour cells [283]. Further studies support the role of isoginkgetin in impairing tumour cell survival, although the detailed mechanisms are incompletely understood. For example, upon immune activation, treatment with isoginkgetin can induce apoptosis in thyroid tumour cells, in part, through the increased expression of *IL-32*$\alpha$ whilst decreasing *IL-32*$\beta$ and *IL-32*$\gamma$ levels [284]. Moreover, human immortalised epithelial cells present a reduced expression of a longer *TEAD2* isoform upon isoginkgetin treatment, which is suggested to correlate with decreased tumour cell survival [263]. Additionally, prolonged exposure to isoginkgetin has been shown to increase tumour cell sensitivity to starvation and enhance the expression of apoptotic markers (*e.g.*

cleaved PARP1 and pro-caspase-3), in part through modulating the expression of autophagy-related genes [285]. Extensive research has described the role of alternative splicing and the generation of isoform-specific autophagy-related genes in the regulation of autophagy (reviewed in [286]). However, whether the previous results where isoginkgetin increased sensitivity to metabolic stress depends on its ability to modulate alternative splicing, and, thus, the isoform-specific expression of autophagy-related protein remains to be elucidated. Despite these results, isoginkgetin is highly cytotoxic and presents restricted delivery due to its high hydrophobicity, which limits its use in clinical studies [287].

## 1.7. Research aim.

Project rationale

Human tumour suppressor p53 is a fundamental transcription factor that controls a myriad of cellular processes in response to stress, including cell cycle arrest, DNA repair and apoptosis. Therefore, the p53 signalling response must be tightly controlled [65]. p53 activity is regulated by both post-translational modifications within the p53 protein [87] as well as through its interaction with cofactors, such as JMY [127,130].

JMY is a DNA damage-responsive actin nucleator, member of the WASP protein family. JMY mainly localises in the cytoplasm, where it promotes cell motility and invasion through the formation of actin filaments both in an Arp2/3-dependent and independent manner [126,127]. Additionally, cytoplasmic JMY promotes cell survival by enhancing the formation and maturation of autophagosomes during metabolic stress [125]. Notably, under specific genotoxic stress conditions, JMY undergoes nuclear accumulation, where it enhances p53-dependent activity in *BAX*-luciferase reporter assays [41].

This project expands our understanding of the role of nuclear JMY as a transcriptional regulator as well as JMY´s actin nucleation activity during the DNA damage response in human tumours. To investigate how JMY acts as a transcriptional regulator during DNA damage, we employed different DNA damaging agents to induce genotoxic stress and the nuclear accumulation of JMY, followed by exploring JMY-mediated transcriptional changes. Understanding the role of nuclear JMY during the DNA damage response would lead to clinical

opportunities to target key cellular pathways to modulate tumour cell fate in response to genotoxic stress.

Hypothesis

We hypothesise that nuclear JMY can act as a transcriptional regulator during DNA damage. Additionally, we hypothesise that nuclear actin and JMY's actin nucleation activity are required to exert JMY's role as a transcriptional regulator.

Aims

The work on this project aims to address the following research questions:

1. Investigate the role of nuclear JMY in transcriptional regulation during the DNA damage response using transcriptomic (RNA-seq) analysis (Chapter 3).

2. Characterise the role of nuclear JMY on p53-dependent DNA repair during DNA damage by analysing the expression of p53-dependent DNA repair targets and how these changes affect the accumulation of DNA lesions and subsequent tumour cell fate (Chapter 4).

3. Understand how nuclear JMY modulates the formation of paraspeckles during genotoxic stress by exploring the expression of lncRNA *NEAT1_2* and paraspeckle biogenesis by RNA-FISH (Chapter 5).

4. Investigate the influence of nuclear JMY in alternative splicing during DNA damage by exploring changes in the expression of core splicing factors and the expression of JMY-dependent alternatively spliced transcripts (Chapter 6).

# Chapter 2: Materials and methods

## 2.1. Materials

Cell lines

Five cell lines were used in this project. U2OS, MCF7 (Public Health England), Saos2 (gift from Dr Glen Kirkham, Nottingham Trent University), HAP1 parental and HAP1 JMY KO (Horizon Discovery) cells. HAP1 JMY KO cells present a 10bp deletion in the first coding exon of JMY generated by CRISPR-Cas9 gene editing using sgRNA: 5'-AGTGCGGGCCAAACCCATCC-3'.

Reagents and equipment

The complete list of materials, including compounds, plasmids, siRNA and primer sequences, antibodies, probes, plasticware, equipment and software used during the project are detailed in SI Tables 2.1-2.8.

## 2.2. Methods

Cell culture

Cells were cultured in complete growth media made of DMEM (4.5 g/L glucose with glutamax), supplemented with 5% FBS (v/v) in the absence of antibiotics and cultured under a humidified environment at 37ºC with 5% $CO_2$. Once the cells reached approximately 70-80% confluency, the media was removed; cells were washed once with 1x PBS to remove media traces and passaged by trypsinisation using 0.05% Trypsin-EDTA (5mg/L of trypsin and 2 mg/L of EDTA) for 3-5 minutes at 37ºC. Cell count was estimated using a hemacytometer, and cells were resuspended in growth media at different concentrations as required, using the following equations:

$$\frac{Cells}{mL} = Average\ cell\ count\ x\ 10^4\ x\ dilution\ factor$$

$$Volume\ of\ cells\ (mL) = \frac{Required\ cell\ number}{Cell\ concentration}$$

For preservation, cells were cultured and harvested in T75 flasks as described above and pelleted at 300 x *g* for 3 minutes. Pellets were resuspended in 1mL of pre-filtered freezing solution (90% FBS and 10% DMSO (v/v)), transferred to cryovials and frozen at -80ºC. Working cell stocks were kept at -80ºC whilst cryovials for long-term preservation were pre-cooled at -80ºC for 48h and transferred to liquid nitrogen.

As cultured cells can acquire genetic drifts over time including chromosomal duplications and rearrangements, accumulation of mutations and epigenetic changes, cells were replaced with fresh stocks every 3-4 months or after approximately 20 passages. Cryovials containing the frozen cells were quickly thawed at 37ºC (approximately 3-5 minutes) and the cell suspension was diluted in 8mL of complete growth media. Cells were transferred into T75 flasks and cultured as described above.

Mycoplasma contamination was routinely monitored using the EZ-PCR mycoplasma test kit following the manufacturer's instructions (Sartorius, #20-700-20). 1 mL of culture media was centrifuged at 300 x *g* for 5 minutes to eliminate cell debris. The supernatant was transferred to a clean tube and centrifuged at 15,000 x *g* for 10 minutes to sediment the mycoplasma. The pellet was

resuspended in 50 μL of buffer solution, heated at 95ºC for 5 minutes and stored at -20ºC. PCR reactions were prepared by mixing 2 μL of the sample, 2 μL of internal control primer mix, 0.5 μL of internal control DNA template, 4 μL of reaction mix and supplemented with nuclease-free water to a final 20 μL reaction. PCR amplification, including positive and negative controls, was conducted with the following cycling conditions as described in Table 2.1.

***Table 2.1. Mycoplasma test amplification cycling profile.***

| Cycles | Temperature (ºC) | Time (s) |
|---|---|---|
| 1x | 94 | 60 |
| 35x | 94 | 30 |
| | 60 | 120 |
| | 72 | 60 |
| 1x | 94 | 30 |
| | 60 | 120 |
| | 72 | 300 |

A 2% agarose gel (w/v) was prepared using 100 mL of TAE buffer (2 M Tris-HCl pH 8.0, 1 M acetic acid and 50 mM EDTA) and mixed with 2 μL of SYBR™ Safe. PCR amplicons were loaded in the agarose gel alongside a 50bp DNA ladder, and the gel electrophoresis was conducted at 100 V for 45 minutes. Bands were visualised using ChemiDoc™ XRS+ with Image Lab™ software, and a representative experiment is shown below (Fig. 2.1).

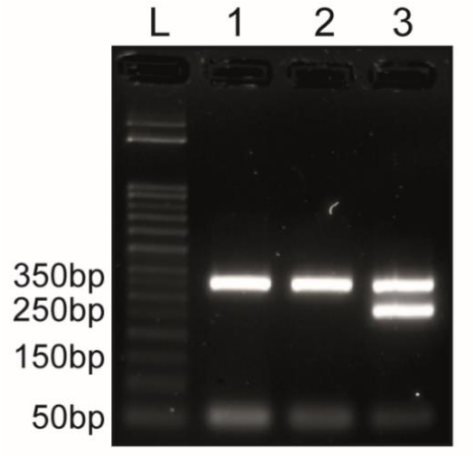


***Figure 2.1. Mycoplasma test results****. U2OS cells (lane 1) and the negative control (lane 2) show a band at 357bp amplified from the internal DNA template, whereas the positive control (lane 3) presents an additional band at 270bp obtained from the mycoplasma DNA. Primer dimers can be seen at approximately 50bp. L: DirectLoad™ 50bp DNA ladder (SigmaAldrich).*

Transfection and generation of stable cell lines:

Cells were seeded at 20-30% confluency in 6cm dishes before transfection was conducted for 48-72h. Plasmids (200 ng) or siRNA (25 nM) transfections were performed using 100 μL of Optimem and 1 μL of TransIT-X2 transfection reagent per 6 cm dish. Human JMY siRNA have been previously described [127], sequences for human *NEAT1_2* siRNA were obtained from [232], and siRNA AllStars (A*) was used as a non-targeting siRNA control [130]. siRNA sequences are described in SI Table 2.2.

Stable cell lines were generated by transfecting JMY constructs into U2OS cells for 72h and selection was performed using complete growth media supplemented with G418 (geneticin, 500 μg/mL) for 10-15 days until individual colonies started appearing. Cells expressing JMY derivatives were screened by immunoblotting before they were used for further experiments. Plasmid details are summarised in SI Table 2.3.

Single-cell alkaline comet assays and quantification:

Low melting agarose, CometSlide™ and pipette tips were pre-warmed at 37ºC before single-cell alkaline comet assays were performed following the manufacturer's instructions (R&D Systems, #4250-050-K). Cells were transfected and treated as described in the figure legends of Chapter 4, washed once with 1x PBS, and gently scrapped. The cell suspension was pelleted at 300 x *g* for 5 minutes and resuspended to $10^6$ cells/mL in 1x PBS. $10^4$ cells were diluted into 50 μL of low melting agarose and placed into the CometSlide™. Coverslips were cooled for 10 minutes at 4ºC to ensure the adherence of the agarose to the CometSlide™. Once the agarose was adhered, coverslips were immersed in lysis buffer (10 mM Tris-NaOH pH 10.0, 2.5 M NaCl, 100 mM EDTA, 1% Triton-X (v/v), 10% DMSO (v/v)) for 30 minutes at 4ºC allowing the lysis of the cell membrane. Coverslips were gently dried and immersed in alkaline unwinding solution (300 mM NaOH, 1 mM EDTA, pH ≥ 13.0) for 20 minutes at room temperature favouring DNA unwinding.

To separate DNA fragments, gel electrophoresis was conducted in cold alkaline electrophoresis solution (300 mM NaOH, 1 mM EDTA, pH ≥ 13.0) at 21 V for 30 minutes. Coverslips were drained and immersed twice in $dH_2O$ and once in 70% ethanol in $dH_2O$ (v/v) for 5 minutes each. The coverslips were left to completely dry at 37ºC (approximately 15 minutes), which brings the cells into a single plane to facilitate image acquisition. Samples were stained with Hoechst-33342 (2 μg/mL in nuclease-free $H_2O$) for 45 minutes before imaging. Images were obtained using a Leica DMi8 inverted fluorescence microscope with 20x or 40x dry lenses. Comet tails and the distribution of DNA content between the comet's tail and head [288] were quantified using the OpenComet plugin [289] from ImageJ/Fiji [290].

RNA isolation:

Cells were seeded into 6cm dishes before transfection and treatments were performed as required. For RNA extraction, cell pellets were resuspended in 300 μL of TRIzol reagent and 70 μL of chloroform, vortex for 10 s and incubated at room temperature for 2-3 minutes. Samples were centrifuged at 12,000 x *g* for 15 minutes at 4ºC allowing the RNA to separate from DNA and proteins and concentrate in the upper aqueous phase. The RNA was transferred to a clean tube, mixed with 175 μL of isopropanol and incubated for 10 minutes at room

temperature. RNA was pelleted by centrifugation at 12,000 x *g* for 10 minutes at 4ºC and the isopropanol was then discarded. RNA was washed with 70% ethanol in nuclease-free $H_2O$ (v/v), and it was recovered with a final spin at 7,500 x *g* for 5 minutes at 4ºC. RNA pellets were resuspended in 50 μL of nuclease-free $H_2O$ in the presence of RNase-free DNase I (0.1 U/mL) and incubated for 15 minutes at room temperature to ensure complete degradation of DNA contaminants. DNase I was heat inactivated at 75ºC for 5 minutes in the presence of EDTA (5 mM) before RNA samples were stored at -80ºC. RNA quality was assessed by spectrophotometry using NanoDrop™, and its yield was monitored by checking the integrity of the 28S and 18S rRNA in a 1% agarose gel (w/v) [291].

cDNA synthesis:

1 μg of RNA was denatured for 5 minutes at 65ºC and mixed with 4 μL of 5x RT buffer, 0.5 μL of RNase inhibitor (40 U/μL), 1 μL of dNTP mix (10 mM), 0.2 μL of oligod(T) primers or random hexamers (for *NEAT1* analysis only) (50 mM), 1 μL of MMLV-RT (100 U/μL) and supplemented with nuclease-free $H_2O$ as required to a final volume of 20 μL. cDNA was synthesised by incubating the mix for 60 minutes at 37ºC. cDNA samples were stored at -20ºC.

Reverse transcription polymerase chain reaction (RT-PCR) and gel electrophoresis:

RT-PCR was performed by mixing the 1 μL of cDNA with 10 μL of 2x Paq5000 PCR master mix, 1 μL of forward and reverse primers (10 μM) in the presence of 5% betaine (v/v) and supplemented with nuclease-free $H_2O$ to a final volume of 20 μL. PCR amplification was conducted with the cycling parameters described in Table 2.2, where Ta refers to the specific annealing temperature of each primer pair.

***Table 2.2. RT-PCR general cycling conditions.***

| Cycles | Temperature (ºC) | Time (s) |
|---|---|---|
| 1x | 95 | 180 |
| 30-40x | 95 | 30 |
| | Ta | 30 |
| | 72 | 30 |
| 1x | 72 | 180 |
| | 4 | - |

Samples were stored at -20ºC until PCR-amplified products were examined by agarose gel electrophoresis. A 1-2% agarose gel (w/v) was prepared using 100 mL of TAE buffer and mixed with 2 μL of SYBR™ Safe. PCR amplicons were loaded in the agarose gel alongside 1kb or 50bp DNA ladder, and the gel electrophoresis was conducted at 100 V for 45 minutes. Primers were designed using Primer3Plus (https://www.primer3plus.com/index.html) [292], and their characteristics, such as GC content, melting temperature, self- and pair-annealing and hairpin formation, were evaluated using PCR primer stats tool (http://www.bioinformatics.org/sms2/pcr_primer_stats.html). Primer sequence specificity was evaluated by predicting their interaction with the human genome using NCBI BLAST (https://blast.ncbi.nlm.nih.gov/Blast.cgi?PROGRAM=blastn&PAGE_TYPE=BlastSearch&LINK_LOC=blasthome) [293], and their activity was tested using the in-silico PCR tool from the UCSC Genome Browser (https://genome.ucsc.edu/cgi-bin/hgPcr) [294]. Primer sequences and their annealing temperatures are detailed in SI Table 2.4.

Reverse transcription quantitative real-time polymerase chain reaction (RT-qPCR):

RT-qPCR was conducted by mixing the 1 μL of cDNA with 2.5 μL of 2x Brilliant III Ultra-Fast SYBR Green qPCR master mix, 0.25 μL of forward and reverse primers (10 μM) and 1 μL of nuclease-free $H_2O$ in the presence of low ROX™ dye concentration (50 nM per well). RT-qPCR amplification was conducted in a QuantStudio5 RT-qPCR machine with the cycling parameters described in Table 2.3, where Ta refers to the specific annealing temperature of each primer pair. Changes in transcript expression were monitored using the $2^{-\Delta\Delta Ct}$ method [295], and

GAPDH was used as the internal control. Primer sequences and their annealing temperatures are detailed in SI Table 2.4.

***Table 2.3. RT-qPCR cycling conditions.***

| Cycles | Temperature (ºC) | Time (s) |
|---|---|---|
| 1x | 95 | 180 |
| 40x | 95 | 30 |
| | Ta | 30 |
| 1x | 95 | 30 |
| | 60 | 30 |
| | 95 | 30 |

Bacterial transformation:

*E. coli* DH5α competent bacteria were slowly thawed at room temperature and placed on ice for bacterial transformation to maintain stocks of the plasmids used in this project. 50 ng of purified plasmid DNA were aliquoted into a clean tube, diluted with 25 μL of competent bacteria and left on ice for 20 minutes. Then, samples were incubated for 45s at 42ºC to facilitate the entry of the plasmid into the bacteria and samples were put back on ice to recover after the heat shock. To each tube, 25 μL of sterile LB broth were added, and samples were incubated for 60 minutes at 37ºC. Bacteria were seeded onto LB agar plates containing the selective antibiotics and incubated overnight at 37ºC. The next day, a single colony was picked and diluted into 5 mL of liquid LB broth in the presence of antibiotic selection and incubated overnight at 37ºC. Then, bacterial stocks were prepared by mixing 500 μL of bacterial culture with an equal volume of 50% glycerol solution in PBS (v/v) and kept at -80ºC for long-term storage. The remaining volume of bacterial culture was centrifuged at 2,500 x *g* for 10 minutes at room temperature. Plasmids were extracted from the bacterial pellet using the Qiagen miniprep kit following the manufacturer's instructions (Qiagen, #27104). Briefly, bacterial pellets were resuspended in 250 μL of each P1 buffer in the presence of endonuclease-free RNase A (100 mg/mL), P2 buffer and N3 buffer, mixing vigorously between steps. Lysates were centrifuged at 17,900 x *g* for 10 minutes, and the supernatant was collected and added to a QIAprep column for plasmid purification. Columns were centrifuged and washed with 750 μL of PE buffer.

Plasmids were eluted from the columns in 50 μL of nuclease-free $H_2O$, and their concentration was measured using NanoDrop™.

Immunoblotting and quantification:

Cells were seeded into 6 cm dishes and transfected and treated as required before harvesting in TNN buffer (150 mM NaCl, 50 mM Tris-HCl pH 7.4, 5 mM EDTA, 0.5% NP40, 50 mM NaF, 0.2 mM $Na_3VO_4$, 10 μg/mL leupeptin, 10 μg/mL pepstatin and 5 μg/mL aprotinin). Lysates were kept on ice for 30 minutes before centrifugation at 15,000 x *g* for 10 minutes at 4ºC to sediment cell debris. Protein extracts were transferred to a clean tube, and protein quantification was performed using Bradford Reagent. A standard curve was generated using serial dilutions of BSA (initial stock at 10 mg/mL) diluted in TNN buffer generating the equation of the line of best fit that was used for quantifying unknown protein samples. 1 μL of protein extracts were diluted into 199 μL of Bradford Reagent, and absorbance was measured at 595nm after incubation for 5 minutes at room temperature.

Before SDS-PAGE gel electrophoresis and immunoblotting were conducted, SDS-PAGE gels were prepared at different concentrations, depending on the molecular weight of the protein of interest using Mini-PROTEAN® Electrophoresis System (BioRad, #1658003FC). For example, to prepare a 10% SDS-PAGE resolving gel (1 mm thick) the following reagents were mixed: 2 mL $H_2O$, 1.25 mL Tris-HCl (1.5 M) pH 8.8, 50 μL SDS solution (10% v/v in $H_2O$), 1.666 mL acrylamide/bisacrylamide (30:0.8), 25 μL APS solution (10% w/v in $H_2O$) and 5 μL of TEMED. Different resolving gel concentrations were prepared by adapting the volume of $H_2O$ and acrylamide/bisacrylamide mix while keeping the volume of the remaining reagents as well as the final volume of the gel mix. Resolving gels were left to polymerise for 30 minutes at room temperature before 4% SDS-PAGE stacking gel mix (1.55 mL $H_2O$, 625 μL Tris-HCl (0.5M) pH 6.8, 25 μL SDS solution (10% v/v in $H_2O$), 325 μL acrylamide/bisacrylamide (30:0.8), 12.5 μL APS solution (10% w/v in $H_2O$) and 5μL of TEMED) was poured on top of the resolving gel and left it to polymerise as described above.

Equal amounts of proteins (approximately 30 μg) were mixed with 7.5 μL of 4x loading dye (125 μL Tris-HCl (0.5 M) pH 6.8, 250 μL glycerol, 200 μL SDS solution (10% v/v in $H_2O$), 50 μL β-mercaptoethanol, 50 μL bromophenol blue (0.5% w/v in

$H_2O$) and supplemented with $H_2O$ to a final volume of 1 mL) and supplemented with TNN buffer to a final volume of 30 μL. Samples were denatured at 95ºC for 5 minutes before they were loaded into the SDS-PAGE gels. The electrophoresis was conducted using a Mini-PROTEAN® Tetra Cell and PowerPac™ (BioRad, #1658001FC) and gels were run in 1x gel running buffer (25 mM Tris, 192 mM glycine and 3 mM SDS) at 200 V for 40-45 minutes at room temperature. Meanwhile, a 9 cm x 6 cm piece of 0.2 μm-pore nitrocellulose membrane and six pieces of Whatman paper were pre-soaked in 1x gel transfer buffer (25 mM Tris, 192 mM glycine, 10% methanol (v/v) and 1% SDS (v/v), pH 8.3). After gel electrophoresis, proteins were transferred to the nitrocellulose membrane using a tank transfer where the transfer stack consisted of a sponge at the bottom, followed by three pieces of Whatman paper, the gel, the nitrocellulose membrane, three additional pieces of Whatman paper and a final sponge. The tank transfer was conducted in cold 1x gel transfer buffer at 400 mA for 90 minutes. Nitrocellulose membranes were stained with Ponceau S to ensure a correct protein transfer.

For immunoblotting, de-stained membranes were cut (when possible) depending on the molecular weight of the protein of interest and incubated with primary antibodies diluted in 5% skimmed milk (w/v) in 0.1% Tween-20 in PBS (v/v) solution. Incubation was carried out on a rocker overnight at 4ºC. After incubation, the membranes were washed three times for 5 minutes with 0.1% Tween-20 in PBS solution to remove unbound primary antibodies. The membranes were then incubated with secondary antibodies diluted in 5% skimmed milk in 0.1% Tween-20 in PBS solution on a rocker for 60 minutes at room temperature. A list of antibodies and their dilutions used in this project is detailed in SI Table 2.5. The membranes were washed three times in 0.1% Tween-20 in PBS solution before a final wash in $dH_2O$ to remove any traces of Tween-20. Protein detection was conducted by enhanced chemiluminescence (ECL). ECL solutions (solution A: 1 mL Tris-HCl (1 M) pH 8.8, 100 μL of luminol solution (250 mM in DMSO), 44 μL of coumaric acid solution (90 mM in DMSO) and supplemented with 9 mL $dH_2O$; and solution B: 1 mL Tris-HCl (1 M) pH 8.5, 6.2 μL of hydrogen peroxide (30% v/v) and supplemented with 9 mL $dH_2O$) were mixed at equal volumes and added to the membranes for 60s before visualisation. Images were obtained using a ChemiDoc™ XRS+ with Image Lab™ software.

If reprobing was required after visualisation, membranes were washed in 0.1% Tween-20 in PBS solution for 5 minutes, followed by a $dH_2O$ wash. Membranes were incubated in stripping buffer (200 mM glycine and 1% SDS (v/v), pH 2.5 with HCl) for a maximum of 60 minutes. Stripping efficiency was checked by ECL before reprobing with a primary antibody.

Band quantification was carried out using Fiji/ImageJ [290]. Briefly, images (as TIFF files) from the loading controls (GAPDH or actin) and the proteins of interest were loaded into the software. A region highlighting the first band of each image was selected using the rectangle tool. The rest of the bands were highlighted, maintaining the shape and size of the pre-defined rectangle. After selecting all bands, their intensity was plotted in a histogram, and the area under the curve was measured using the wand tool. Data was exported into Microsoft Excel for quantification. Each protein of interest was normalised against the loading control within its lane. Changes in protein expression were obtained after normalising with untreated controls unless otherwise specified in the figure legends.

Immunostaining and quantification:

Cells were seeded onto 13 mm glass coverslips and transfected and treated as required before immunofluorescence. Coverslips were washed once with 1x PBS before cells were fixed with 3.7% formaldehyde in PBS (v/v) for 10 minutes. Then, coverslips were washed once with 1x PBS to remove formaldehyde traces before the cells were permeabilised with 0.5% Triton X-100 in PBS (v/v) for 5 minutes. Coverslips were incubated with primary antibodies overnight at 4ºC in a humidified chamber. The next day, coverslips were extensively washed with 0.025% Tween-20 in PBS (v/v) to remove unbound antibodies. Secondary antibody incubation was performed at room temperature for 30 minutes. Finally, coverslips were washed with 0.025% Tween-20 in PBS and mounted on microscope slides using Vectashield with DAPI for nuclei visualisation. Images were obtained using a Leica DMi8 inverted fluorescence microscope. A list of antibodies and their dilutions used in this project is detailed in SI Table 2.5.

Quantification of JMY nuclear accumulation was measured using a modified version of the 'Human C-N translocation' CellProfiler pipeline [296]. Two folders containing the JMY signal (U2OS cells stably expressing HA-tag JMY derivatives detected with anti-HA antibody) and the nuclei (stained with DAPI) were used as

input. Nuclei masks were obtained using a global three-class Otsu threshold method to distinguish between the nuclei signal and the background. Nuclei cut at the image borders were discarded, and clumped nuclei were separated using a shape-smoothing function. Then, JMY signal was measured using the same module parameters described for the nuclei. The cytoplasmic signal was obtained by subtracting JMY fluorescence provided by the nuclear regions (defined by the nuclei masks obtained in the first step) from the total fluorescence. Results were exported to Microsoft Excel, and graphs and statistical analysis were conducted using GraphPad Prism 9.0.2.

DNA damage response foci were quantified using the FindFoci plugin [297] from ImageJ/Fiji [290]. Two different folders containing the foci signal (antibodies specified in the figure legends) and the nuclei (stained with DAPI) were used as input files. Nuclei masks were obtained using an auto-threshold (otsu_4_level) to distinguish between the nuclei signal and the background. Clumped nuclei were separated using the watershed function from ImageJ/Fiji, and the nuclei cut at the image borders were discarded. The number of foci per cell and their relative fluorescence were normalised with the number of cells per field using the nuclei masks obtained in the first step. Results were exported to Microsoft Excel, and graphs and statistical analysis were conducted using GraphPad Prism 9.0.2.

RNA-fluorescence *in situ* hybridization (RNA-FISH) and quantification:

Cells were seeded onto 13 mm glass coverslips, transfected, and treated as required before RNA-FISH. Coverslips were washed once with 1x PBS before cells were fixed with 3.7% formaldehyde in PBS (v/v) for 10 minutes. Then, coverslips were washed once with 1x PBS to remove formaldehyde traces before cells were permeabilised with 70% ethanol in $dH_2O$ (v/v) overnight at 4ºC. RNA-FISH was performed following the manufacturer's instructions (Biosearch Technologies) with some modifications. Initially, coverslips were washed once with freshly made wash buffer A (10% deionised formamide (v/v) and 20% Stellaris RNA-FISH wash buffer A (v/v)) for 5 minutes before incubation with human *NEAT1* middle segment or *GAPDH* probes overnight at 37ºC. The *NEAT1* middle segment probes recognise *NEAT1_2* isoform (Fig. 5.1b), whereas *GAPDH* was used as an internal control. Then, coverslips were washed twice with TE buffer (10 mM Tris-HCl pH 8.0, and 1 mM EDTA) followed by incubation in wash buffer A for 30 minutes at 37ºC. Finally,

coverslips were mounted on microscope slides using Vectashield with DAPI for nuclei visualisation. Probes characteristics are described in SI Table 2.5.

Images were obtained using a Leica THUNDER Imager Live Cell & 3D Assay inverted fluorescence microscope with 100x oil immersion lens. 3D images were taken where Z-stacks were performed using a logical size of 8 steps moving through a physical length of 6 μm. Images contained three channels set as i) DAPI staining (emission wavelength 440nm), ii) human *NEAT1* middle segment probe conjugated with Quasar® 570 dye (emission wavelength 594nm), and iii) human GAPDH probe conjugated with Quasar® 670 dye (emission wavelength 695nm). Following image acquisition, the Z-stacks from each channel were projected into a single image using the maximum intensity projection tool from LAS X software. Briefly, this processing consists of projecting into a 2D plane the voxels (pixels in 3D) that present the maximum intensity across all planes from the Z-stack. The 2D images were exported into individual folders to deposit the nuclei and paraspeckle signal.

Paraspeckle quantification was performed using a combination of CellProfiler 'Speckle counting' module [296] and *Python* scripts. These codes are stored on Dr Amanda S Coutts private repository and are available upon reasonable request. Briefly, nuclei masks were obtained using a global two-class Otsu threshold method to distinguish between the nuclei signal and the background. Clumped nuclei were separated using a shape-smoothing function, and those at the image borders were discarded. Then, the masks of the *NEAT1_2*-containing condensates were obtained as described for the nuclei but using a global three-class Otsu threshold method and by restricting the *NEAT1_2* signal to the nucleus area, using the nuclei masks obtained in the previous step. Each child *NEAT1_2* particle was linked to a parental nucleus using the CellProfiler particle analysis tool. Using the *AreaShape_Area* parameter from CellProfiler, paraspeckles were differentiated from single *NEAT1_2* molecules using a threshold size of 10 pixels (Fig. 2.2). This value was selected based on the average size of single *GAPDH* mRNA molecules obtained after measuring over 3,000 individual particles. Finally, the results were exported to Microsoft Excel files for data analysis and graphs and statistical analysis were conducted using GraphPad Prism 9.0.2.

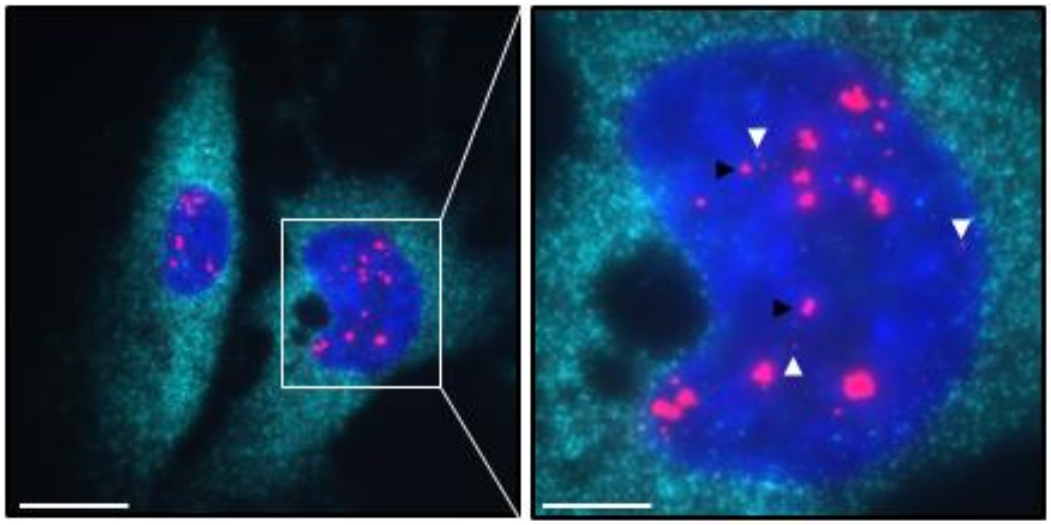

***Figure 2.2. Size classification of NEAT1_2-containing paraspeckles.*** *U2OS cells were cultured onto 13mm glass coverslips where paraspeckles were detected by RNA-FISH using NEAT1_2 middle probe (red). GAPDH probes (cyan) were included as control and nuclei were visualised using DAPI (blue). Paraspeckles were differentiated from single lncRNA NEAT1_2 molecules using a 10-pixel size cutoff based on the average GAPDH mRNA particle area. The right panel shows a magnified region of interest, with paraspeckles highlighted by black arrowheads and single NEAT1_2 molecules by white arrowheads. Scale bar = 20$\mu$m (left) and 2$\mu$m (right).*

Cell cycle analysis:

Cells were seeded into 6 cm dishes (in triplicates), transfected, and treated as required before harvesting for flow cytometry. Growth media was collected and centrifuged at 300 x *g* for 5 minutes at 4ºC to account for apoptotic and mitotic cells, and pellets were kept on ice. Then, adherent cells were incubated in Earle's EDTA (5.3 mM KCl, 117 mM NaCl, 26 mM $NaHCO_3$, 1 mM $NaH_2PO_4$ and 1 mM EDTA) for 10 minutes, pipetting once at 5 minutes to promote cell detachment. Adherent cells were combined with the previous pellet and recovered by centrifugation at 300 x *g* for 5 minutes at 4ºC. Pellets were washed once with cold 1x PBS before cells were fixed in ice-cold 70% ethanol in PBS (v/v) overnight at 4ºC. Fixed cells were washed once with 1x PBS and stained with 2% PI in PBS (v/v) in the presence of DNase-free RNase A (125 U/mL). Cell cycle analysis was performed using an Accuri C6 flow cytometer with the gating strategy described in Fig. 2.3.

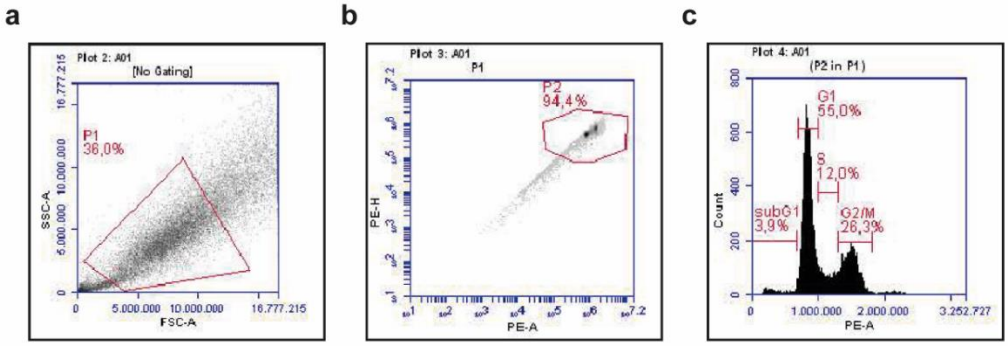


***Figure 2.3. Cell cycle analysis of PI-stained cells. a)*** *Density plot showing forward vs scatter area and gated with P1 to define single cells, eliminating cell debris and clumps,* ***b)*** *Density plot of P1-gated cells highlighting those stained with PI and gated in P2, and* ***c)*** *Histogram representation of the cell cycle profile from cells gated in P2, plotted as PI-stained cells vs cell count. Different phases of the cell cycle are marked as subG1, G1, S and G2/M.*

Apoptosis measurement:

HAP1 parental and JMY knockout cells were seeded into 6cm dishes (in duplicates) at a concentration of 2.5 x $10^5$ cells per dish 48h before treatment for 30h (unless otherwise specified). Growth media was collected and centrifuged at 300 x *g* for 5 minutes at 4ºC to account for apoptotic and mitotic cells, and pellets were kept on ice. Then, adherent cells were incubated in Earle's EDTA for 2-3 minutes at room temperature and combined with the previous pellet. Cells were recovered by centrifugation at 300 x *g* for 5 minutes at 4ºC. Then, pellets were washed once with 1x annexin-V binding buffer (10 mM HEPES, 140 mM NaCl and 2.5 mM $CaCl_2$) and resuspended to a final concentration of $10^6$ cells/mL. 100 μL of cells were stained with 5μL annexin V conjugated with FITC (25 μg/mL) and PI (1 μg/mL) in the presence of DNase-free RNase A (125 U/mL) for 30 minutes at room temperature. Single-stained and unstained controls were included in all experiments. Quantification of apoptotic cells was performed using an Accuri C6 flow cytometer following the gating strategy described in [298] (Fig. 2.4) and recently used in [283,299].

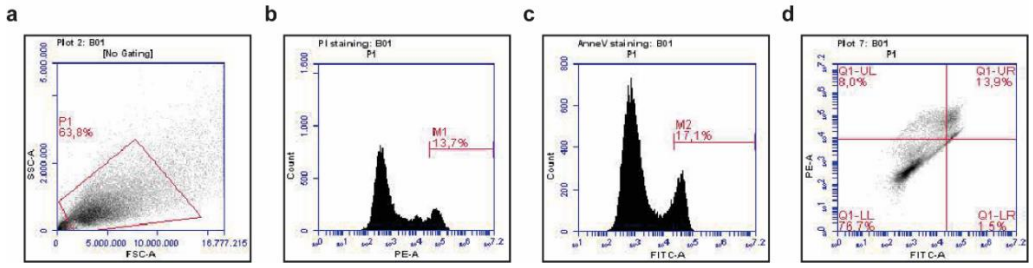


***Figure 2.4. Analysis of apoptosis. a)*** *Density plot showing forward vs scatter area and gated with P1 to define single cells eliminating cell debris and clumps,* ***b)*** *and* ***c)*** *Histograms representing P1-gated cells stained with PI (b) or Annexin V-FITC (c) to define the threshold fluorescence of single-stained cells compared with unstained controls (M1 and M2) and* ***d)*** *Density plot representing the percentage of apoptotic cells plotted as Annexin V-FITC vs PI double staining. The percentage of cells undergoing apoptosis was divided between living cells (Q1-LL) and early (Q1-LR) or late (Q1-UR) apoptosis using the minimum fluorescence obtained in* ***b)*** *and* ***c)****.*

Cell proliferation:

Cells were seeded into 96-well plates at 5,000 cells per well one day prior to performing cell proliferation assays using the IncuCyte S3 live-cell analysis system. Cells were treated as described in the figure legends, where treatments were performed in quadruplicate. Four phase contrast images were taken per well every 4h for 72h. Proliferation was quantified by masking the cell confluence after normalising against the first image (represented as fold over the initial scan) for each treatment set, using the IncuCyte live-cell analysis system. Masks were obtained from 16 photos per time point and treatment. Results were exported to Microsoft Excel, and graphs and statistical analysis were conducted using GraphPad Prism 9.0.2.

Chromatin immunoprecipitation (ChIP):

HAP1 parental and JMY knockout cells were seeded into 10 cm dishes (in triplicates) and treated with either vehicle control or etoposide (500 nM) for 6h. Growth media was removed, and cells were washed twice with 1x PBS to remove media traces. Then, cells were cross-linked with 1% formaldehyde in PBS (v/v) for 10 minutes before quenching for 2 minutes with glycine in PBS (125 mM). Cells were extensively washed with 1x PBS before they were harvested and pelleted at

300 x *g* for 5 minutes at 4ºC. Pellets were permeabilised in lysis buffer I (5 mM Tris-HCl pH 8, 85 mM KCl and 0.5% NP40 (v/v), 10 μg/mL leupeptin, 5 μg/mL aprotinin and 10 μg/mL pepstatin) for 20 minutes on ice and centrifuged at 300 x *g* for 5 minutes at 4ºC to sediment the nuclei. Then, nuclei were lysed using Farhnam's nuclei lysis buffer (50 mM Tris-HCl pH 8.1, 10 mM EDTA and 1% SDS (w/v), 10 μg/mL leupeptin, 5 μg/mL aprotinin and 10 μg/mL pepstatin) for a minimum of 10 minutes on ice before sonication. Sonication was performed on a Bioruptor® Pico for 10–20 cycles (30s on, 30s off) to shear the DNA. After sonication, lysates were centrifuged at 15,000 x *g* for 15 minutes at 4ºC to sediment cell debris, and chromatin was transferred to a clean tube.

Chromatin samples were stored at -20ºC until the sonication efficiency was checked. This was performed by reverse cross-linking 20 μL of sheared chromatin in the presence of proteinase K (40 μg/mL) and RNase A (20 μg/mL) for 3 hours at 55ºC, followed by overnight incubation at 65ºC. The next day, 5 μL of reverse cross-linked chromatin were mixed with 1 μL of 10x loading dye and supplemented with nuclease-free $H_2O$ to a final volume of 10 μL. Samples were run in a 1% agarose gel (w/v) at 100 V for 45 minutes. Chromatin fragments of approximately 200bp were monitored using a ChemiDoc™ XRS+ with Image Lab™ software. Before preclearing the chromatin, protein A/G Sepharose beads were blocked as follows. Beads were mixed with equal volumes of Farhnam's nuclei lysis buffer and resuspended in 1 mL of IP dilution buffer (0.01% SDS (v/v), 1% Triton X-100 (v/v), 1.2 mM EDTA, 16.7 mM Tris-HCl pH 8.1, 167 mM NaCl) in the presence of BSA (1mg/mL), sonicated salmon sperm DNA (400 μg/mL) and protease inhibitors. Beads were blocked in a rotator overnight at 4ºC.

After checking the sonication efficiency, chromatin samples were diluted in IP dilution buffer to a final volume of 1 mL. Samples were precleared by adding 30 μL of blocked beads and incubated in a rotator for 2h at 4ºC. Then, samples were centrifuged at 300 x *g* for 5 minutes at 4ºC. The supernatant containing the precleared chromatin was distributed into three tubes and incubated with: i) no antibody (inputs), ii) mouse anti-p53, or iii) mouse non-specific IgG antibodies (SI Table 2.5) in a rotator overnight at 4ºC. The next day, 30 μL of blocked beads were added to each tube and rotated for 2h at 4ºC. Beads retaining the chromatin were pelleted at 300 x *g* for 5 minutes at 4ºC. Then, the beads were extensively washed with low salt solution (0.1% SDS (v/v), 1% Triton X-100 (v/v), 20 mM Tris-HCl pH

8.1, 150 mM NaCl and 2 mM EDTA) and LiCl buffer (250 mM LiCl, 1% NP40 (v/v), 1% Na-deoxycholate (v/v), 1 mM EDTA and 10 mM Tris-HCl pH 8.1), followed by two final washes with TE solution (10 mM Tris-HCl pH 8.0, and 1 mM EDTA). Beads were resuspended in 250 μL of freshly made elution buffer (1% SDS (v/v) and 100 mM $NaHCO_3$) and rotated for 15 minutes at room temperature to recover the chromatin. Samples were centrifuged at 300 x *g* for 5 minutes, where supernatants (containing the chromatin) were collected, and the elution process was repeated on the pellets, combining the eluates at the end.

Eluates were mixed with 20 μL NaCl (5 M), 10 μL EDTA (500 mM), 20 μL Tris-HCl (1 M, pH = 6.5), 2 μL proteinase K (40 μg/mL) and 1 μL RNase A (20 μg/mL), except for the input chromatin controls (no antibody) where only proteinase K and RNase A were added. Samples were reverse cross-linked for 3 hours at 55ºC, followed by overnight incubation at 65ºC. DNA was purified using Qiaquick PCR purification kit following the manufacturer's instructions (Qiagen, #28104). Briefly, samples were mixed with five volumes of PB buffer and added to a QIAquick column (which captures the chromatin). Chromatin fragments were bound to the columns by centrifugation at 13,000 x *g* for 60s. Columns were washed with 750 μL of PE buffer and centrifuged twice, discarding the washing solution between centrifugations. DNA was eluted from the columns with 50 μL of nuclease-free $H_2O$. Then, 1 μL of chromatin was run on a 1% agarose gel (w/v), as mentioned above, to check the efficiency of the chromatin purification step. Bands were visualised using a ChemiDoc™ XRS+ with Image Lab™ software. Finally, chromatin immunoprecipitated samples were analysed by RT-qPCR as described before. Primer details are present in SI Table 2.4.

*In silico* clinical data analysis:

To investigate the role of JMY in human cancers, patients' data from the ICGC/TCGA pan-cancer cohort [300], including 2,922 samples from 2,583 patients, was explored using the cBioPortal for Cancer Genomics database (http://www.cbioportal.org/) [301]. Briefly, clinical outcomes were retrieved from the whole dataset or stratified into specific tumour types as described in the figure legends. Samples were manually grouped based on i) JMY expression levels (mRNA expression z-scores, high: EXP > 0.5 or low: EXP < -0.5) or JMY copy number (amplification: AMP or homozygous deletion: HOMDEL) as noted. Groups were further split based on p53 mutation status (wild-type: WT or mutant: mut)

using cBioportal Onco Query Language. Clinical data were retrieved, including relative transcript expression levels, Kaplan–Meier patient survival curves and mutational counts.

Transcriptomic RNA-sequencing (RNA-seq):

U2OS osteosarcoma cells were seeded into 10 cm dishes, transfected with 12.5 nM JMY or non-targeting siRNA for 72h and treated with etoposide (50 μM) for the last 6h before harvesting and storing at -80ºC (n = 3 independent biological repeats). RNA was isolated by Dr Amanda S Coutts using the ReliaPrep™ RNA Miniprep Systems kit following the manufacturer's instructions (Promega, #Z6011). Briefly, cell pellets were lysed in 500 μL of BL buffer in the presence of 7% isopropanol (v/v) before they were transferred into a ReliaPrep™ minicolumn. Columns were centrifuged at 12,000 x *g* for 30s at 4ºC to capture the RNA and incubated with RNase-free DNase I for 15 minutes at room temperature. Then, columns were washed once with column wash solution, followed by two additional washes with RNA wash buffer. Columns were transferred to a clean tube, and RNA was eluted in 50 μL of nuclease-free $H_2O$.

Using the services of Novogene Co., Ltd, RNA degradation was monitored by agarose gel electrophoresis, its purity was checked using a NanoPhotometer® spectrophotometer and its concentration was measured using Qubit® RNA Assay Kit in a Qubit® 2.0 flurometer. 3 μg of RNA were used for building the libraries according to NEBNext® Ultra™ RNA Library Prep Kit following the manufacturer's recommendations (New England Biolabs). Briefly, mRNA was enriched from total RNA using poly(T) oligo-attached magnetic beads and subsequently fragmented into small oligopeptides. RNA was reverse transcribed into double-strand cDNA, and blunt ends were obtained by partial treatment with exonucleases. Then, NEBNext Adaptors (5'- GATCGGAAGAGCACACGTCTGAACTCCAGTCA-3') were ligated to the cDNA, which was subsequently amplified and purified with an AMPure XP system. Libraries were sequenced on a HiSeq platform (Illumina), generating 30 million paired-end reads of 150bp length. Sequenced reads were recorded into FastQ files.

RNA-seq data were analysed using Galaxy [302]. First, the compressed version of the FastQ files were used as inputs for FastQC. This software evaluated each base pair sequencing quality, the AT/GC distribution across the read and the presence

of sequencing bias such as adaptors and long segments of uncertain nucleotides (N) generating a single-nucleotide quality score (Q). Then, Cutadapt [303] was set to trim adaptor sequences and eliminate low-quality reads based on the results from FastQC. Reads were removed when presenting untrimmed adaptor sequences, a significant number of uncertain nucleotides, if the overall quality of the read was low ($Q < 20$) or if the length of the read was less than 20nt or over 300nt (based on the read length at the library preparation step). After filtering, a collection of clean reads was obtained.

Next, clean reads were mapped to the reference human genome (hg38) using TopHat2 [304]. The mapping strategy discarded paired-reads presenting a conflicting alignment set to flag discordant (not matching) genomic coordinates between the reads of a pair. Furthermore, reads expanding exon-exon junctions were set to present a minimum of 10nt anchors between the flanking exons and the possibility to expand introns with a maximum length of $10^6$ nucleotides. In addition, reads with over 20 genomic alignment possibilities or when presenting more than 3 mismatches were removed. With these parameters, TopHat2 selected the reads with the highest mapping scores. The quality of the mapped reads was analysed using QualiMap RNA-Seq QC, which was set to remove alignments with low mapping scores ($Q \leq 30$). Finally, TopHat2 compressed the mapping information into BAM files, in which the reads were sorted by coordinates using SortSam.

Quantification of mapped reads was performed with HTSeq-count [305] using the reference transcriptome (v82) obtained from the Ensemble dataset (April 2020). From the reference transcriptome, two attributes were used for indexing: i) the 'featuring type' was set to use 'exon' to define the protein-coding sequences (exonic regions), and ii) the 'ID attribute' was set as 'gene_id' to retrieve the ENSEMBL identifier of each transcript. Alone, mapped reads cannot be used to quantify differences in gene expression and a normalisation step must be included to account for factors that impede direct sample comparison such as transcript length, the total number of reads, and sequencing biases [306].

Differential gene expression and normalisation were performed with DESeq2 [307]. Transcript counts were normalised using DESeq2's median of ratios method. Briefly, read counts (for each gene and sample) were divided by sample-specific size factors, which are determined by the median of the ratio between the number of reads (for each gene and sample) and the geometric mean of read counts (for

each gene) across all samples. Furthermore, DESeq2 'postcount' estimator was set to avoid complications arising from genes with zero values by calculating a modified geometric mean taking the n-th root of the product of the non-zero counts. A final list of differently expressed genes was obtained with a False Discovery Rate (FDR) adjusted p-value (q-value) < 0.05. Changes in gene expression were represented using heatmaps and volcano plots. The former were performed using ComplexHeatmap R Bioconductor package using default parameters and Euclidean clustering. The latter were created using EnhancedVolcano R Bioconductor package with default parameters.

To explore the molecular functions and pathways in which these targets are involved, a pathway enrichment analysis was performed following Reimand and colleagues' protocol [308]. Briefly, differentially expressed genes were used as input for the g:GOSt analysis function from gProfiler [309] with a significant threshold of q-value < 0.05. Enriched pathways and gene ontologies were obtained from the KEGG, REACTOME, and Gene Ontology Consortium databases, respectively. Enriched pathways were represented using Cytoscape [310] following Reimand and colleagues' protocol [308], where nodes and clusters were manually arranged for clarity.

Transcriptomic splicing analysis:

RNA-seq data was used to explore different transcript expression by monitoring changes in alternative splicing. Clean reads were obtained as described in the RNA-seq section and were mapped to the reference human genome (hg38, v100) using STAR [311]. Briefly, a 2-pass mapping model was used in which reads are pre-mapped with default parameters obtaining a 'reference' exon-exon junction profile. Then, these annotated junctions act as an index during the second round of mapping when the user-defined parameters are introduced. Furthermore, an *XS strand* tag was added to all alignments that contained exon-exon junctions in the BAM files. This tag is required for non-stranded RNA-seq data to be compatible for splicing analysis with EventPointer (package selected in this project to explore splicing events). Otherwise, the parameters used during the STAR mapping strategy were similar to the ones used with TopHat2. BAM files were sorted by coordinates and then separated into chromosomes (one BAM file per chromosome) using Sambamba [312].

The detection of alternative splicing events was performed with EventPointer [313] using the BAM files and human reference transcriptome (v100) as inputs. The analysis of splicing events was based on the SGSeq function [314] in which discrete gene sequences (exons and splice junctions) are predicted from the RNA-seq reads mapped to the reference genome and assembled into a splice graph. Splicing events (characterised by two or more splice variants) are identified when the reads are compared against the splice graph (designated as paths). Quantification of the relative transcript usage or percent spliced in index (ΔPSI) is obtained based on the number of reads spanning event boundaries (compatible reads that align with the start or end of the splice graph) when compared against the reference transcriptome. Splicing events were exported into Microsoft Excel files, whereas spliced graphs and paths were exported as GTF files for visualisation using the Integrative Genomics Viewer.

To ensure that the analysis described before was correctly developed, the pipeline was tested using the datasets from Vidaković and colleagues' work (accession number: GSE143542, RBP1 $K^{1268R}$ mutant and WT cells after 24h of UV radiation) [315]. Reads were mapped using STAR as described before using the human reference genome (hg38, v89). BAM files were sorted, split and analysed with EventPointer as described. The human reference transcriptome (v89) was used to quantify transcript usage. The reference genome and transcriptome versions were changed to mimic the original datasets [315]. The codes are stored on Dr Amanda S Coutts private repository and are available upon reasonable request.

Statistical analysis:

Statistical analysis was performed using GraphPad Prism 9.0.2. from at least three independent biological experiments. Results with error bars represent mean ± standard error of the mean (s.e.m.), and individual data points are shown in the graphs unless otherwise specified in the figure legends. Data were tested for normal distribution. The differences between two groups were analysed by unpaired two-tailed Student's t-test for normalised data and Mann–Whitney U test for non-normalised data, unless otherwise specified in the figure legends. Results were considered significant with a p-value $< 0.05$.

# Chapter 3: JMY-mediated transcriptomic changes in U2OS cells during etoposide-induced DNA damage.

## 3.1. Introduction

JMY is a multifunctional actin nucleator.

JMY is a member of the WASp (Wiskott-Aldrich Syndrome) family of actin nucleation-promoting factors [126]. It mainly localises in the cytosol, where JMY promotes cell motility and invasion by inducing the formation of actin filaments in an Arp2/3-dependent and independent manner [126,127]. Additionally, during metabolic stress, cytoplasmic JMY acts as a pro-survival factor where through its actin nucleation activity JMY promotes the formation and maturation of autophagosomes [125].

JMY is a DNA damage-responsive protein that undergoes nuclear accumulation upon specific genotoxic stress conditions [127,129,130]. JMY was discovered as a p300-interacting protein while exploring the impact of p300 on the activity of p53 during DNA damage [104]. Upon treatment with specific DNA damaging agents, JMY becomes nuclear, where it enhances p53 activity in *BAX*-luciferase reporter assays [104,127]. Notably, the ability of JMY to enhance the p53-driven expression of *BAX* was hindered upon inhibition of overall actin nucleation via latrunculin A treatment [127].

JMY possesses a unique function as a cytoplasmic actin nucleator and as a DNA damage-responsive protein that undergoes nuclear accumulation upon specific genotoxic stressors to enhance p53 transcriptional activity. However, the wider role of JMY in the transcriptional regulation within human tumours during DNA damage needs further investigation.

RNA-seq: the revolution in gene expression analysis.

High-throughput transcriptomics, such as RNA-seq, have become widely used technologies to explore changes in gene expression under specific experimental conditions (*e.g.* presence versus absence of a target of interest) [316]. The standard workflow consists of two main steps, including the sequencing strategy and the subsequent bioinformatic analysis.

A good experimental design depends on three factors: the type of cDNA library, sequencing depth and number of independent biological replicates [306,316]. Although RNA-specific targeted cDNA libraries are available, the most versatile option is using the whole transcriptome to prepare the libraries, which allows the detection of known and novel transcripts. Additionally, libraries could be explored at different depths, which refers to the total number of reads sequenced for a given sample. Deeper levels enable the identification of low-expressed transcripts; however, they may also result in higher detection of false positive targets, especially within the low-expressed genes [317]. Commonly, a library depth of 30 million reads will allow the recognition of a single transcript [318]. Lastly, the suitable number of biological replicates is determined by the technical noise, intragroup variance, and the desired power to detect low-expressed transcripts. Three biological replicates is the minimum requirement to monitor changes in transcript expression between conditions (using inferential analysis) with enough statistical power [306,316].

Predominantly, RNA-seq is used for analysing changes in transcript expression levels. Standard procedures start with the extraction of the RNA, followed by the enrichment of polyadenylated RNAs or removal of the highly abundant rRNAs [319]. Samples are then converted into a cDNA library, fragmented into smaller oligonucleotides and sequenced, with or without pre-amplification [316]. Once the quality of the sequencing step has been assessed, the reads that meet high-quality standards are mapped to a reference genome or transcriptome. Then, the aligned reads are normalised to account for differences in transcript length, total number of mapped reads and technical biases.

As the number of mapped reads is an estimator of gene expression, changes in transcript levels are calculated by measuring the number of mapped reads within a particular transcript and compared between samples to obtain a list of differentially expressed genes (DEG) [318]. Lastly, this list of DEG is compared with available functional annotation databases to characterise the molecular functions or pathways in which these targets are involved [316]. Given its versatility, RNA-seq has become a gold-standard approach to explore changes in transcript expression, providing a broad overview of which cellular processes are influenced under a specific experimental condition of interest.

Aim

The aim of this chapter was to investigate the role of JMY as a transcriptional regulator during DNA damage, in particular upon etoposide treatment, conditions where JMY is known to undergo nuclear accumulation and enhance the transcriptional activity of p53 [127,129]. This section summarises the JMY-mediated changes in gene expression in response to etoposide-induced DNA damage.

## 3.2. Summary of the methodology

U2OS osteosarcoma cells were cultured in complete growth media supplemented with 5% FBS (v/v) under a humidified environment at 37ºC with 5% $CO_2$. Cells were transfected with JMY or non-targeting (A*) siRNA (12.5nM) using Optimem and TransIT-X2 transfection reagent for 72h and treated with etoposide (50μM) for the last 6h.

RNA samples were isolated and sent to Novogene Co., Ltd, which performed the sequencing step on a HiSeq platform (Illumina), generating 30 million paired-end reads of 150bp length. RNA-seq data were analysed using Galaxy [320], and the output list of differentially expressed genes was obtained using DESeq2 [307].

To monitor JMY-mediated changes in gene expression, RNA was isolated and reverse-transcribed into cDNA. RT-qPCR was performed using Brilliant III Ultra-Fast SYBR qPCR and quantified using the $2^{-\Delta\Delta Ct}$ method [295]. Primers are detailed in SI Table 2.4. Statistical analysis was performed using unpaired two-tailed Student's t-test from at least three independent biological experiments (mean ± s.e.m.). Results were considered significant with a p-value < 0.05.

## 3.3. Results

RNA-seq experimental design and TopHat2 mapping strategy.

JMY is a cytoplasmic DNA damage-responsive actin nucleator that undergoes nuclear accumulation upon treatment with specific genotoxic stressors [119,121]. The localisation of JMY was monitored in U2OS cells, where JMY mainly accumulated in the cytosol under non-perturbed conditions. The induction of DNA damage via etoposide treatment led to JMY's nuclear accumulation (Fig. 3.1ai,ii), as previously described [127]. Under this etoposide-mediated genotoxic stress condition, a transcriptomic analysis was performed in U2OS cells transfected with non-targeting or JMY siRNA to understand the impact of JMY on gene expression during the DNA damage response (Fig. 3.1b, c).

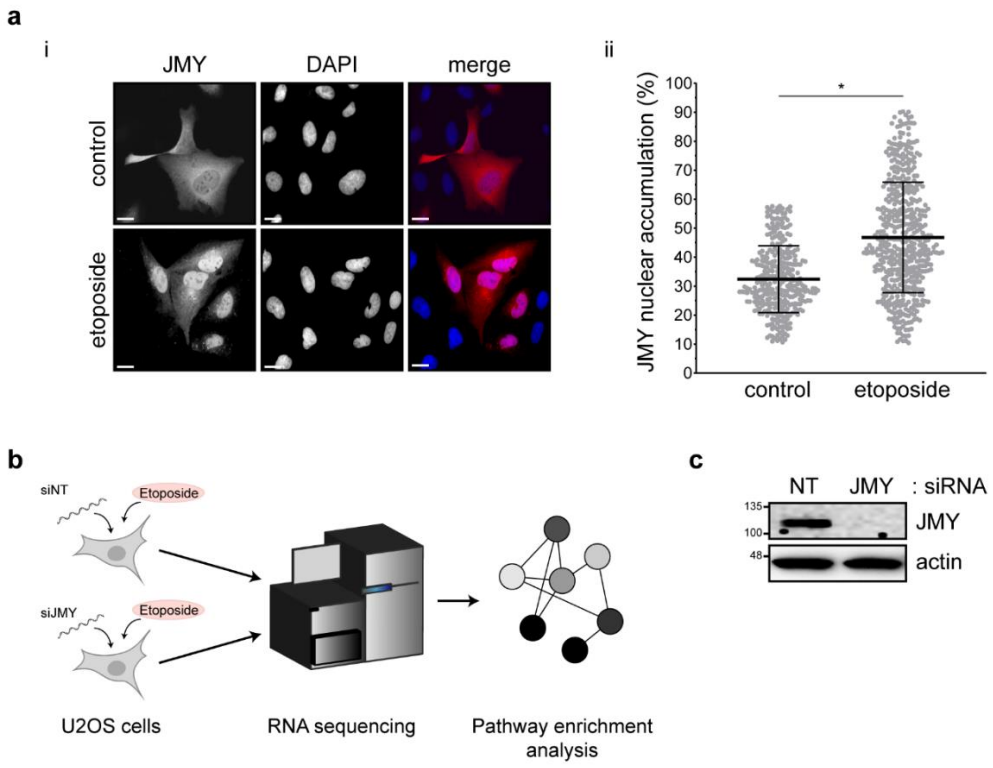


***Figure 3.1. RNA-seq experimental design.*** **a)** *U2OS cells expressing HA-tagged wild-type human JMY (JMY) were treated with DMSO vehicle (control) or etoposide (50μM) for 6h. JMY was detected using anti-HA antibody, and DAPI was used to visualise the nuclear DNA. Scale bar = 10μm. ii) Quantification of the nuclear accumulation of JMY (mean ± SD), n = 3 independent experiments each with N ≥ 100 cells per treatment, * p < 0.0001, Mann-Whitney test,* ***b)*** *Schematic*

*representation of the RNA-seq workflow, and* ***c)*** *JMY expression levels in U2OS cells after transfection with non-targeting (NT) or JMY siRNA for 72h.*

The sequencing step was performed by Novogene Co., Ltd, where input RNA samples were enriched in polyadenylated RNAs by using poly(T) oligo-attached magnetic beads, which efficiently depleted rRNA (data not shown). Enriched RNAs were then used to generate a cDNA library of 150bp paired-end reads with a sequencing depth of 30 million reads per sample, which grants identification and quantification of a single transcript [316,318].

The quality of the sequencing strategy was monitored by a two-step checkpoint control using FastQC and Cutadapt, which examined the overall quality of the reads after removing the adaptor sequences (necessary during the cDNA library preparation), obtaining single-nucleotide statistical scores. FastQC quality results showed an exceptional number of reads (97% of overall sequenced reads) overpassing the quality thresholds, presenting only 2% of total reads with remaining adaptor sequences and less than 1% with low overall sequencing quality scores (Fig 3.2a). Reads within the last two groups were removed before the mapping strategy.

Then, high-quality reads were aligned to the reference human genome using TopHat2, and the quality of the mapping step was assessed by quantifying the percentage of aligned reads. For well-annotated genomes such as the human genome, approximately 70-90% of reads should be mapped, with a significant fraction presenting a unique alignment [306]. Here, TopHat2 results retrieved that over 85% of reads were aligned to the reference human genome (Fig. 3.2b), from which the vast majority showed a unique mapping site (~96%). As the human genome harbours a large number of repetitive sequences, a common RNA-seq bias is the presence of multi-mapped reads which align with several genomic sites. These reads can represent up to 40% of total mapped reads [321].

Although the overall alignment of multi-mapped reads can lead to transcript overrepresentation during the quantification step, their complete removal can significantly reduce the sequencing coverage. To overcome this problem TopHat2 like several mapping algorithms (*e.g.* STAR [306]), sets a threshold of a maximum of 20 alignments within a specific read and ranks each individual alignment based on statistical information. Specifically, TopHat2 uses the information obtained from

unique-mapped reads and coverage of known splice junctions to align multi-mapped reads [304]. Here, default multi-mapped threshold parameter from TopHat2 was used, and results retrieved a small fraction of multi-mapped reads (~3%) showing less than 20 alignment sites (Fig. 3.2c). Reads overpassing this multi-mapped threshold (> 20 alignment sites) were considered to have a discordant alignment and were discarded for further analysis (Fig. 3.2c). In addition, an accumulation of reads covering the 3'-end of the transcript could indicate poor quality of the RNA used during the preparation of the cDNA library [306]. Here, the alignment step showed that read coverage was uniform across the transcript length reinforcing the high-quality RNA used during the cDNA library preparation (Fig. 3.2d).

TopHat2 is a spliced mapper that executes a two-step alignment in which a preliminary mapping step uses unspliced reads to define exonic regions. Then, unmapped reads are fragmented and re-aligned to identify exon-exon junctions [304]. The results of the alignment step showed that over 80% of mapped reads expanded transcript exonic regions (Fig. 3.2e). Surprisingly, 10%-15% of the reads were aligned exclusively with intronic regions (Fig. 3.2e), representing a higher proportion than conventional transcriptomic results performed in human tumour cells [322]. The remaining 5% of the reads expanded exon-exon junctions (Fig. 3.2e), showing that approximately 75% aligned to known or predicted splice sites, leaving 25% of reads reporting novel splicing junctions (Fig. 3.2f). Interestingly, it is observed that defects in the activity of the spliceosome often lead to a high proportion of reads aligned to intronic regions as well as the identification of novel exon-exon junctions during transcriptomic analysis [257]. These results may suggest that JMY could impact on the spliceosome activity during DNA damage (see Chapter 6).

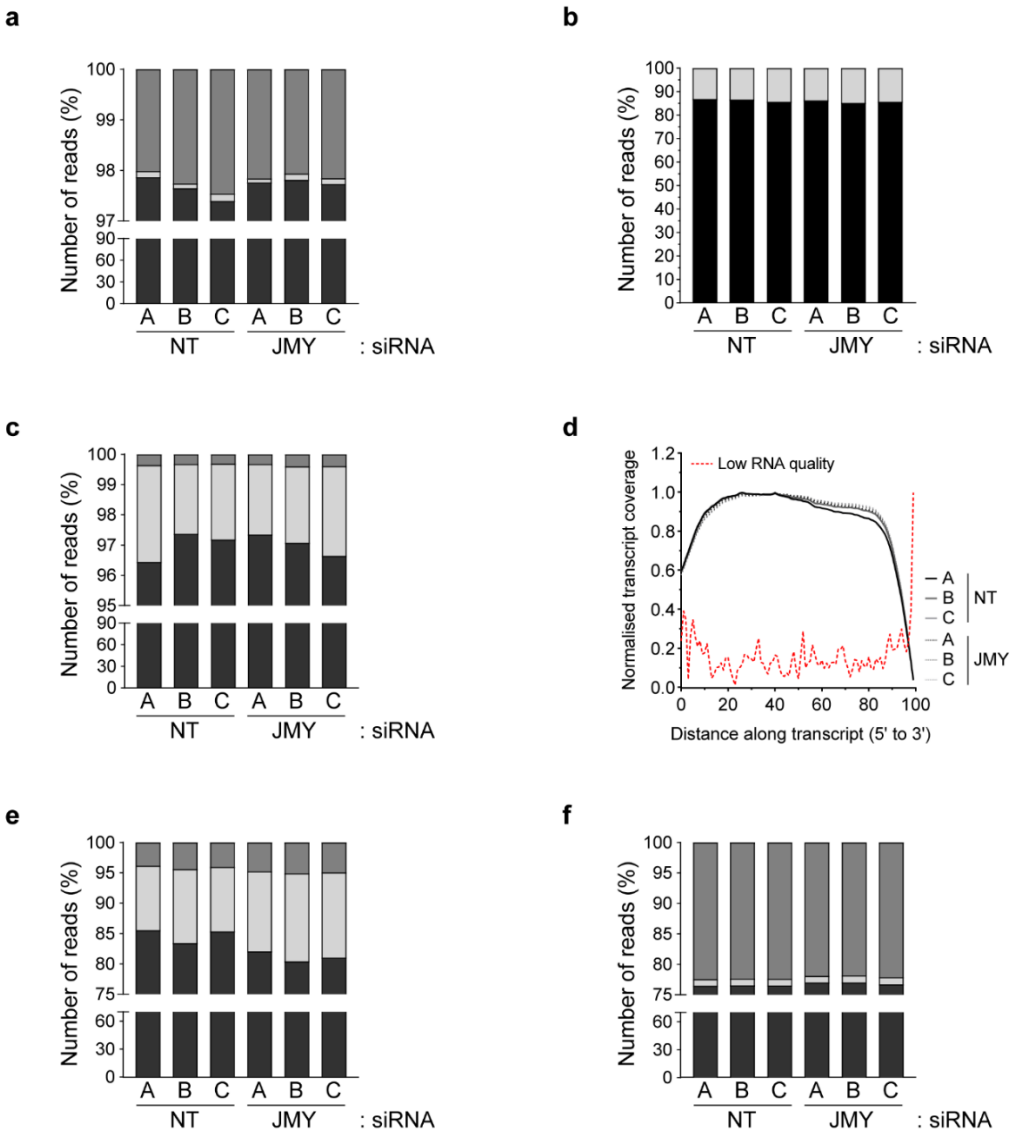


***Figure 3.2. TopHat2 alignment results. a)*** *Evaluation of the quality of reads after sequencing. Clean reads (black) were obtained after removing adaptor sequences. Reads with remaining adaptors (dark grey) or with an overall low quality (light grey) were removed before TopHat2 alignment,* ***b)*** *Quantification of reads mapped (black) or unmapped (light grey) against the reference genome using TopHat2,* ***c)*** *Distribution of mapped reads presenting a unique (black) or multiple (light grey) alignment regions. Paired-end reads presenting a conflicting alignment (dark grey) were discarded for further analysis.* ***d)*** *Uniform distribution of the read coverage across the transcript length. A red dotted line represents a theoretical example of low-quality RNA used to prepare the cDNA library.* ***e)*** *Mapping results showing the distribution of reads aligned with exonic (black), intergenic (dark grey) or intronic (light grey) regions.* ***f)*** *Distribution of reads*

*expanding exon-exon junctions presenting known (black), novel (dark grey) or predicted (light grey) splice sites. n = 3 independent biological repeats (A-C). RNA-seq was performed in U2OS cells transfected with JMY or non-targeting (NT) siRNA.*

JMY-mediated changes in gene expression during DNA damage

RNA-seq is predominantly used to measure changes in transcript expression levels as the number of aligned reads can be used as an estimator of gene expression [318]. This project focused on exploring the role of nuclear JMY in gene expression during the DNA damage response. If those changes in expression are expected to occur between experimental conditions, intrasample batch effects should be monitored during the analysis [306]. Here, the samples showed a high correlation within each experimental condition (Spearman $R^2 > 0.985$, Fig 3.3a), and two distinctive clusters between U2OS cells transfected with JMY or non-targeting siRNA were reported (Fig. 3.3b), indicating that these groups present different transcript expression profiles. Changes in gene expression were monitored using DESeq2 [307]. First, outliers were removed by monitoring gene-specific dispersion, where 69.3% of individual transcripts were selected (Fig. 3.3c). Then, these transcripts were used for DESeq2 independent gene filtering, retrieving a final list of 5,592 differentially expressed targets (Fig. 3.3d, normalised quantile $\theta = 0.6845 \pm SD$).

Specifically, the list of differentially expressed targets included 4,904 protein-coding genes and 688 ncRNAs (q-value < 0.05, Fig. 3.4a). As expected, the expression of *JMY* was downregulated ($log_2(FC) = -0.637$, q-value = 0.0001), reinforcing the accurate execution of the RNA-seq and bioinformatic analysis (Fig. 3.1b, c). To explore the molecular functions in which the JMY-mediated targets could be involved, pathway enrichment analysis was conducted using a more stringent target list (q-value < 0.001), including 2,169 protein-coding genes and 257 ncRNA (Fig. 3.4b, Table 3.1).

Enrichment results showed cellular processes in which JMY was previously described, such as autophagy [125] and regulation of actin cytoskeleton (Fig. 3.4c) [126,127]. However, results also suggested that JMY may regulate novel pathways such as splicing (Fig. 3.4c), expanding our understanding of the transcriptional role of nuclear JMY. Finally, several genes were monitored *in-vitro*, confirming that their

JMY-mediated changes in gene expression were similar to those obtained during the bioinformatic analysis (Fig. 3.4d). These results suggested that JMY can impact gene expression during the DNA damage response.

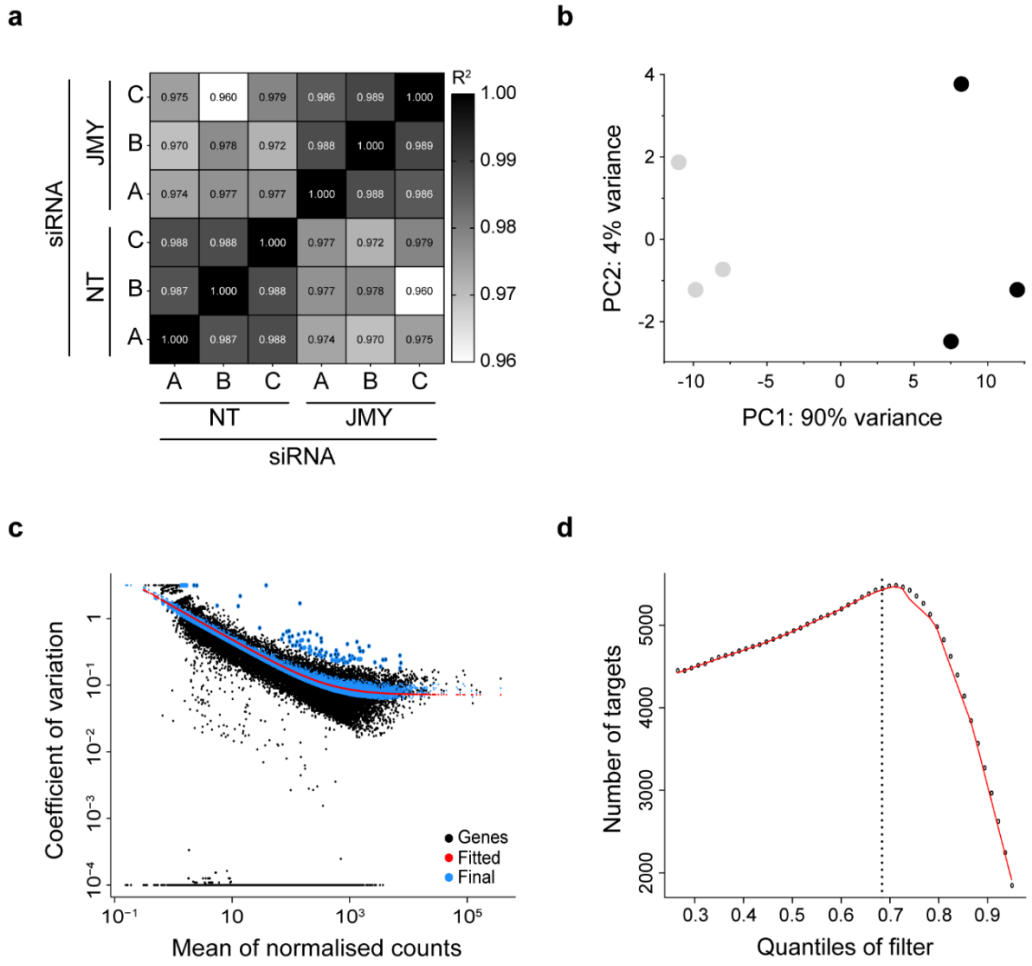


***Figure 3.3. Differential gene expression analysis. a)*** *Heatmap representing Pearson's correlation coefficients between U2OS cells transfected with JMY or non-targeting (NT) siRNA,* ***b)*** *Principal component analysis (PCA) of transcript expression profiles (DESeq2) from RNA-seq data. PCA plot shows independent clusters between U2OS cells transfected with non-targeting (light grey) or JMY siRNA (dark grey).* ***c)*** *Dispersion analysis showing gene-specific dispersion values (black) compared to the trend line obtained from the mean of the gene's normalised counts across all samples (red) and the corrected (log-normal fitted) dispersion values (blue). Outliers were defined using the 0.99 quantile of Cox Reid-adjusted profile likelihood maximisation for dispersion estimation (black dots surrounded in blue).* ***d)*** *Independent filtering analysis presents the quantile distribution of the mean of normalised counts and the number of targets with a q-value < 0.05 (FDR*

*adjusted p-value). The vertical dotted line shows the lowest quantile (θ = 0.6845 ± SD) with the maximum number of targets passing the threshold (q-value < 0.05). FDR: False Discovery Rate.*

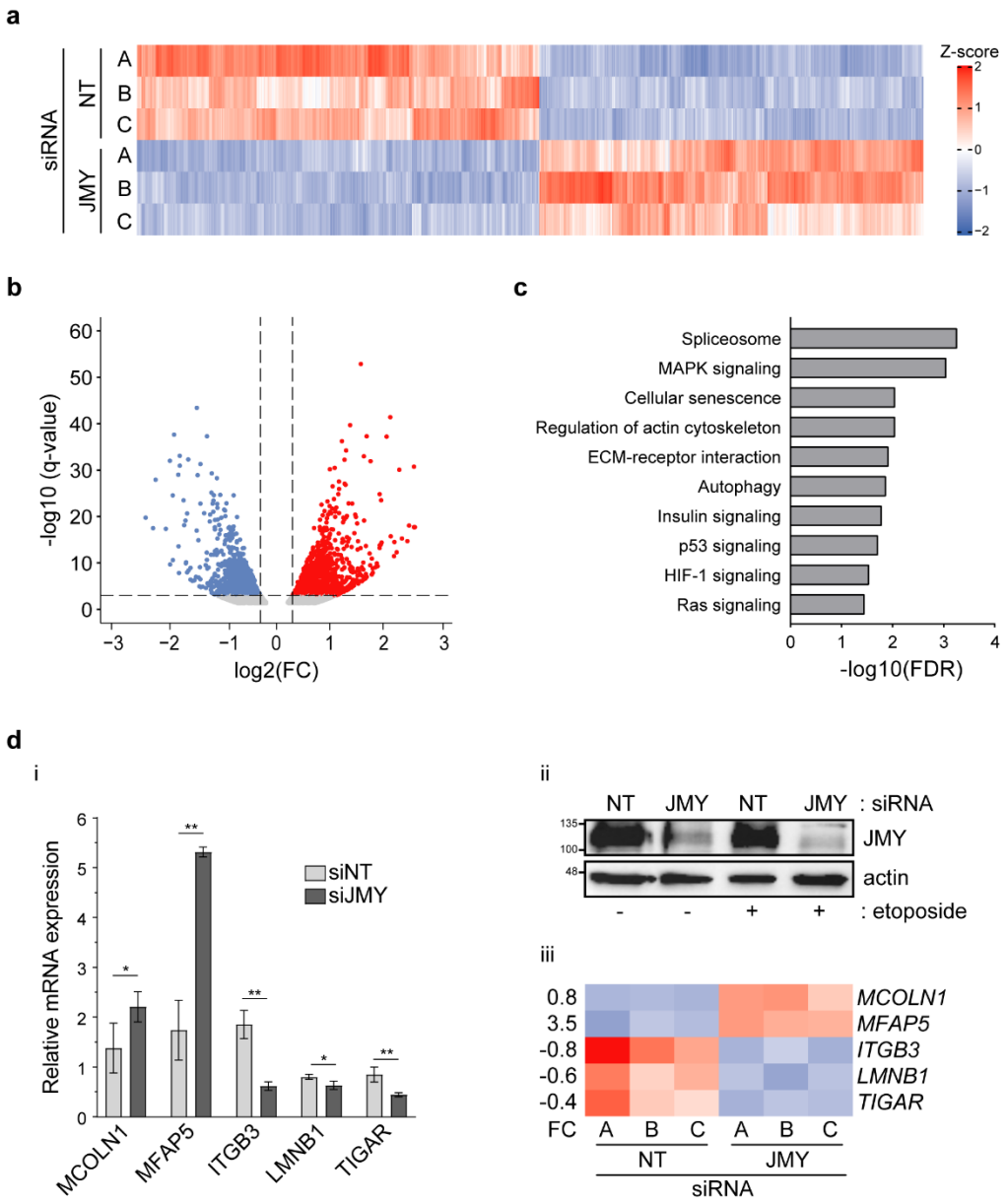


***Figure 3.4. JMY-mediated changes in gene expression. a)*** *JMY-mediated transcriptomic changes (Z-scores) for upregulated (red) or downregulated (blue) targets (q-value < 0.05),* ***b)*** *Volcano plot represents differentially expressed genes ($log_2$(FC)) influenced by JMY (q-value < 0.001). Red = upregulated, blue = downregulated and grey = not significant. For* ***(a-b)*** *no minimum threshold on gene expression was set and differentially expressed genes were considered using the significant cut-offs highlighted in* ***(a-b)****.* ***c)*** *Selected enriched KEGG pathways. The*

*threshold was set as q-value < 0.05, and* ***d)*** *U2OS cells were transfected with JMY or non-targeting (NT) siRNA for 72h and treated with vehicle (-, DMSO) or etoposide (+, 50*$\mu$*M) for the last 6h. i) Changes in gene expression are present as fold mRNA relative to vehicle-treated cells after normalising with GAPDH (mean ± s.e.m.). n = 3 independent experiments. ii) Western blot represents JMY knockdown and iii) Heatmap showing the relative expression of the validated targets in* ***(di)****. Changes in gene expression levels are represented as* $log_2$*(FC), and the colour code (z-scores) is noted in* ***(a)****. * p < 0.05, ** p < 0.01, unpaired two-tailed Student's t-test. FC: Fold-change.*

**Table 3.1. Selected JMY-mediated ncRNAs differentially expressed during DNA damage.**

| Gene name | $log_2$(FC)* | -$log_{10}$(q-value)# |
|---|---|---|
| *LINC00520* | 1.4 | 9.9 |
| *MALAT1* | 0.8 | 12.2 |
| *PKD1L2* | 1.5 | 20.4 |
| *PVT1* | 0.7 | 4.7 |
| *TINCR* | 0.7 | 1.4 |
| *LINC00511* | -1.0 | 14.0 |
| *MIAT* | -1.1 | 3.7 |
| *NEAT1* | -0.8 | 10.5 |
| *NKILA* | -1.4 | 22.8 |
| *ZEB1-AS1* | -0.6 | 2.7 |

** Changes in gene expression are represented as fold change and the quantification is explained in more detail in the Material and Methods section. # significant threshold was set as q-value < 0.05 (FDR adjusted p-value).*

## 3.4. Discussion

JMY is an actin nucleator and DNA damage-responsive protein that undergoes nuclear accumulation during specific genotoxic stress conditions, where it enhances p53 activity [104,127]. In this chapter, our transcriptomic results demonstrate a wider role for JMY as a transcriptional regulator during etoposide-induced DNA damage, conditions where JMY accumulates in the nucleus. Ultimately, we showed that JMY could influence the expression of a broad range of targets, including a significant number of ncRNAs, involved in several pathways, which expands our understanding of the transcriptional regulatory role of nuclear JMY.

JMY can localise in the cytosol, where it acts as an actin nucleation-promoting factor [126,127]. Although incompletely understood, different stressors can influence the subcellular localisation of JMY. For example, in response to metabolic stress (*e.g.* starvation), JMY remains cytoplasmic and associates with LC3-containing autophagosomes [125]. In contrast, specific genotoxic stressors result in JMY's nuclear accumulation (Fig. 3.1a) [129]. These results suggest that the subcellular localisation and activity of JMY may differ depending on the specific type of stress, as well as its duration and dose. It will be relevant for future studies to characterise how the temporal and dose-dependent effects of various genotoxic stressors may impact on JMY's cellular localisation and its activity during cell fate.

The findings present in this thesis expand our understanding of the role of nuclear JMY as a p53 transcriptional regulator during the DNA damage response. Interestingly, we observed basal levels of nuclear JMY under non-perturbed conditions (Fig. 3.1aii), in agreement with previous observations [127]. Monitoring the impact of JMY on the transcriptome of tumour cells in unperturbed conditions will be relevant as it provides insights into JMY´s role in core cellular pathways, like cell cycle regulation. Furthermore, the fact that JMY would likely be shuttling inside and outside of the nucleus at lower levels indicates that cytoplasmic JMY might also indirectly impact on gene expression (*e.g.* autophagy-mediated turnover of key proteins).

RNA-seq has become a gold standard technique to investigate changes in gene expression. Within the various stages of an RNA-seq workflow, the alignment of sequenced reads to a reference genome is crucial to identify which transcripts are differentially expressed [316]. Although there are several alignment algorithms,

TopHat2 is a widely used spliced mapper [304], and scores as one of the most efficient tools to align paired-end reads, reporting excellent mappability [319,323,324]. Despite the ability of TopHat2 to identify splice junctions, usually, only a small fraction of reads (< 10%) report novel exon-exon boundaries [323]. Unexpectedly, our transcriptomic results showed twice the amount of these unknown splice junctions, including a higher proportion of reads also aligned to intronic regions (Fig. 3.2e, f), which is commonly observed from defects in the activity of the spliceosome and an accumulation of unspliced pre-mRNAs [322]. These results suggest that JMY may impact on splicing during genotoxic stress, which is further supported by the fact that the spliceosome was reported as an enriched pathway (Fig. 3.4c). As splicing is crucial to expand transcript variability and can affect the cellular outcomes in response to genotoxic stress [325], the role of nuclear JMY in splicing has been explored in more detail, and the results are shown in Chapter 6.

Additionally, previous studies demonstrated that JMY enhances cell survival through both its nuclear transcriptional cofactor role and its cytoplasmic impact on promoting autophagy [125]. Our transcriptomic results demonstrate that, during DNA damage, JMY modulates the expression of autophagy-related targets. This suggests that, in addition to JMY's cytoplasmic role, it can also regulate autophagy at a transcriptional level during DNA damage, thus adding further complexity to the cytoplasmic versus nuclear roles of JMY. Given that etoposide has been described to enhance autophagy [64], it will be relevant for future studies to assess the impact of nuclear JMY in autophagy during DNA damage.

Collectively, this chapter demonstrates how JMY undergoes nuclear accumulation during etoposide-induced DNA damage and its impact on gene expression. This provides further insights into the transcriptional regulatory role of nuclear JMY, which could ultimately lead to the discovery of new JMY-mediated targets influencing tumour cell fate during the DNA damage response.

# Chapter 4: p53-dependent DNA repair during the DNA damage response requires actin nucleation by JMY.

## 4.1. Introduction

DNA damage activates the p53 response.

The human tumour suppressor p53 is a nuclear transcription factor that plays an essential role in the cellular response to various stressors, including DNA damage [95]. Functioning as a transcriptional regulator, p53 controls the expression of a wide variety of targets, impacting a myriad of cellular processes, including DNA repair, cell cycle arrest and induction of programmed cell death [80]. Although the regulatory mechanisms modulating the activity of p53 and how it may influence tumorigenesis are incompletely understood. A plethora of studies support a key role of p53 in tumour suppression via its regulation of DNA repair [65]. Cells exposed to DNA damaging agents initiate a tightly regulated response leading to the activation of DNA damage checkpoints and DNA repair mechanisms [3]. Recognition of DNA lesions and initiation of the DNA damage signalling response primarily occurs via ATM, ATR and DNA-PK, members of the phosphatidylinositol 3-kinase-related kinases (PIKK) family [48]. Upon activation, these kinases phosphorylate a wide range of targets, including p53 [59,60] and H2AX [326,327], leading to DNA repair, cell cycle arrest and apoptosis [48].

p53 exerts a direct impact on DNA repair mechanisms through transcriptionally activating various targets involved in DNA repair including, for example, *TP53I3* (PIG3), *XRCC5* (Ku80) and *XPC* [113]. The loss of p53 function can result in reduced expression of DNA repair genes leading to DNA damage accumulation, genomic instability and, ultimately, tumour development [4]. Interestingly, defects or reduced expression of DNA repair targets is often observed in tumour cells and can result in the loss of one or more DNA damage repair pathways [2], thus providing the molecular rationale for exploiting these vulnerabilities in cancer therapy through the use of small-molecule inhibitors targeting crucial players of the DNA damage response [2,4].

The role of JMY during the p53 transcriptional activity.

Upon induction of the DNA damage response, p53 is activated, leading to the transcriptional regulation of its target genes [80]. The p53 response to DNA damage is controlled by various cofactors, like JMY, that positively and negatively regulate p53 activity [74,108]. JMY is a DNA damage-responsive actin nucleator, member of the WASp protein family. JMY can localise in the cytoplasm and nucleus where cytoplasmic JMY promotes the formation of actin filaments both in an Arp2/3-dependent and independent manner, enhancing cell motility and invasion [126,127]. During metabolic stress like starvation, JMY increases cell survival due to its actin nucleation role been required for the formation and maturation of autophagosomes [125].

Under specific genotoxic stress conditions, JMY undergoes nuclear accumulation, where it enhances the p53-mediated transcriptional expression of *BAX* [104,127]. However, whether JMY could also modulate the expression of other p53 target genes requires further investigation. Interestingly, a growing body of evidence supports the presence of actin nucleation-promoting factors in the nucleus where actin can play a fundamental role in nuclear events such as transcriptional regulation [171] and DNA repair [176,178]. For example, several actin nucleators have been shown to enhance the repair of DNA strand breaks via their Arp2/3-mediated actin nucleation role, both by promoting the clustering of DNA strand breaks or through direct interaction with DNA repair components [178,181]. Nonetheless, the nuclear role of actin nucleators like JMY during the DNA damage response and how they might impact the transcriptional activity of p53 remains to be elucidated.

Aim

The overarching aim of this chapter was to investigate the role of JMY and its actin nucleation function during DNA damage and its impact on p53 transcriptional activity. This section summarises how nuclear JMY promotes DNA repair and overall cell survival during DNA damage through its Arp2/3-mediated actin nucleation by enhancing the expression of p53 target genes involved in DNA repair.

## 4.2. Summary of the methodology

U2OS, Saos2, MCF7 and HAP1 parental and JMY knockout cells were cultured in complete growth media supplemented with 5% FBS (v/v) under a humidified environment at 37ºC with 5% $CO_2$. U2OS, Saos2 and MCF7 cells were transfected with human JMY or non-targeting (A*) siRNA (25nM) for 72h before being treated, as described in the figure legends. The generation of stable U2OS cells expressing JMY derivatives was obtained after transfection with the appropriate construct. Selection was carried out by culturing U2OS cells in complete growth media supplemented with G418 at 500μg/mL. Transfections were performed using Optimem and TransIT-X2 transfection reagent. Plasmids and siRNA sequences are detailed in SI Table 2.2 and SI Table 2.3, respectively.

To monitor JMY-mediated changes in gene expression, RNA was isolated and reverse transcribed into cDNA using random hexamers and MMLV-RT. RT-qPCR was performed using Brilliant III Ultra-Fast SYBR qPCR and quantified using the $2^{-\Delta\Delta Ct}$ method [295]. Moreover, changes in protein levels were monitored by immunoblotting, where cells were lysed in TNN buffer before protein extracts were separated using mini SDS-PAGE gels. Proteins were then transferred to a nitrocellulose membrane, incubated with the appropriate antibodies as described in the figure legends, and bands were visualised by enhanced chemiluminescence (ECL) using a ChemiDoc™ XRS+ with Image LabTM software.

To monitor the accumulation of DNA damage, single-cell alkaline comet assays were performed following the manufacturer's instructions (R&D Systems). Before imaging, coverslips were stained with Hoechst-33342 (2μg/mL), and comets were quantified using OpenComet plugin [289] from ImageJ/Fiji [290].

Immunostaining was performed in cells seeded onto glass coverslips, fixed with 3.7% formaldehyde (v/v) and permeabilised with 0.5% Triton-X (v/v) before coverslips were incubated with the appropriate antibodies as detailed in the figure legends. Coverslips were then mounted on microscope slides using Vectashield with DAPI for nuclei visualisation. Unless otherwise specified, images were quantified using ImageJ/Fiji [290]. Foci were quantified using FindFoci plugin [297] from ImageJ/Fiji [290]. The description of the foci quantification protocol and parameters used during the analysis is detailed in the Materials and Methods section.

Cellular outcomes derived from the JMY-mediated p53-dependent expression of DNA repair proteins included cell proliferation, cell cycle analysis and apoptosis measurement. Briefly, for cell proliferation assays, cells were transfected and treated as described in the figure legends and imaged every 2h for 72h. Quantification was performed by masking the cell confluence (phase contrast images) after normalising against time zero images using the IncuCyte S3 live-cell analysis system. Cell cycle analysis was performed to measure the percentage of cells undergoing cell death (subG1 phase). Briefly, cells were transfected and treated as noted in the figure legends before growth media and adherent cells were collected, fixed and stained with 2% propidium iodide (v/v) in the presence of DNase-free RNase A (125U/mL) before the percentage of cells in subG1 phase was monitored using an Accuri C6 flow cytometer. Finally, for monitoring apoptosis, HAP1 parental and JMY knockout cells were treated as detailed in the figure legends before growth media and adherent cells were collected and resuspended to a final concentration of $10^6$ cells/mL. 100μL of cells were stained with 5μL of annexin-V conjugated with FITC (25μg/mL) and propidium iodide (1μg/mL) in the presence of DNase-free RNase A (125U/mL). Analysis of apoptosis was performed using an Accuri C6 flow cytometer.

## 4.3. Results

JMY-mediated expression of p53 targets involved in DNA repair.

To expand our understanding of how JMY can impact p53-mediated gene expression during DNA damage, a transcriptomic analysis was performed in U2OS cells upon etoposide treatment, conditions where JMY accumulated in the nucleus (Fig. 3.1a) [127]. Pathway enrichment analysis showed that the p53 signalling response was an enriched JMY-mediated cellular process (Fig. 3.4c), and the depletion of JMY resulted in reduced expression of p53 target genes, including *BAX* in support of previous studies [127]. Interestingly, the transcriptomic results showed that JMY depletion also led to reduced expression of additional p53 target genes like *BBC3* (*Puma), CDKN1A (p21)* and *TIGAR* (Table 4.1). Re-analysis of the p53 signalling response pathway indicated that while JMY impacted on the expression of a range of p53 target genes, there was an enrichment of DNA repair-related protein, with most of these targets presenting reduced expression upon JMY depletion (Fig. 4.1a, b; Table 4.1).

**Table 4.1. Selected p53 target genes influenced by JMY during DNA damage.**

| Gene name | $log_2$(FC)* | -$log_{10}$(q-value)# |
|---|---|---|
| *RRM2B*$ | -0.5 | 7.0 |
| *TP53I3*$ | -0.5 | 8.0 |
| *XPC*$ | -0.4 | 5.8 |
| *XRCC5*$ | -0.5 | 5.7 |
| *BBC3 (Puma)* | -0.7 | 21.9 |
| *NEAT1* | -0.8 | 10.5 |
| *TIGAR* | -0.4 | 3.7 |

*The list of p53-dependent targets was curated from [75]. * Changes in gene expression are represented as fold change and the quantification is explained in more detail in the Materials and Methods section, # significant threshold was set as q-value < 0.05 (False Discovery Rate adjusted p-value) and $ genes directly or indirectly involved in DNA repair.*

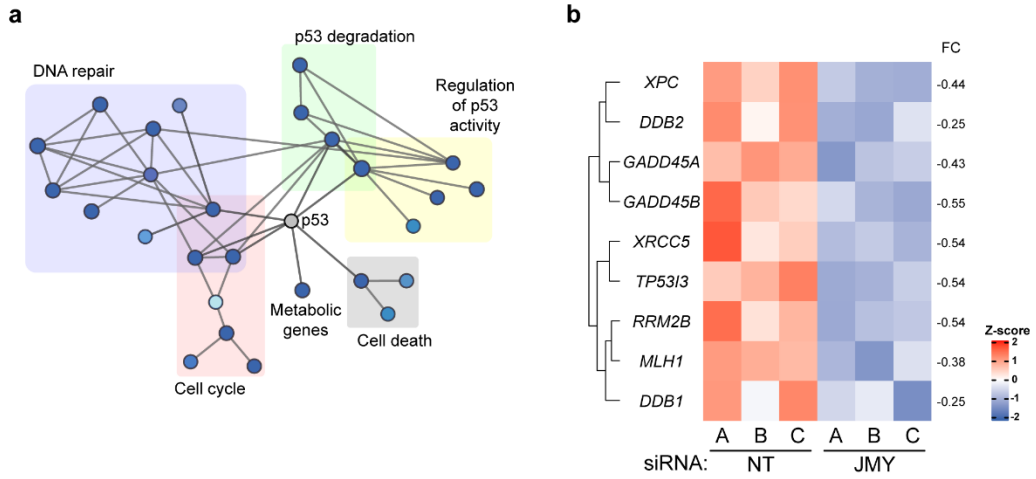


***Figure 4.1. JMY impacts on DNA repair via p53-dependent transcriptional regulation. a)*** *Enrichment map represents JMY-mediated p53-related and DNA repair pathways from Reactome database (q-value < 0.05). Nodes and clusters were obtained using Cytoscape and were manually arranged for clarity. Nodes colour represents normalised enrichment scores (blue = downregulated) .* ***b)*** *Heatmap shows the relative expression of p53 target genes involved in DNA repair when comparing U2OS cells transfected with JMY or non-targeting (NT) siRNA after being treated with etoposide (50$\mu$M) for 6h (q-value < 0.05). Independent biological replicates are represented with A-C. Changes in gene expression levels are represented as $log_2$(FC). Red = upregulated, blue = downregulated. q-value (FDR adjusted p-value) and FC: Fold-change expression.*

The JMY-mediated regulation of p53 targets involved in DNA repair was validated by RT-qPCR and demonstrated that in U2OS cells the depletion of JMY reduced the expression of *XPC* and *XRCC5* during etoposide treatment (Fig. 4.2a). Conversely, the impact of JMY's depletion on the expression of these targets was insignificant in p53 null Saos2 osteosarcoma cells (Fig. 4.2b). These results confirmed that JMY regulates the expression of *XPC* and *XRCC5*, in response to etoposide-induced DNA damage, via p53 transcriptional regulation. This was also reflected in changes in protein expression, as seen by a reduction in both XPC and XRCC5 levels upon siRNA-mediated JMY depletion (Fig. 4.2c, d). The impact of JMY on the expression of p53 targets involved in DNA repair was not restricted to a single cell type, as similar results were also observed in MCF7 breast cancer cells (Fig. 4.2e). The results were not limited to etoposide treatment as JMY also significantly accumulated in the nucleus of U2OS cells treated with 4NQO (Fig.

4.3a), conditions where the depletion of JMY also led to reduced expression of XPC and XRCC5 (Fig. 4.3b, c).

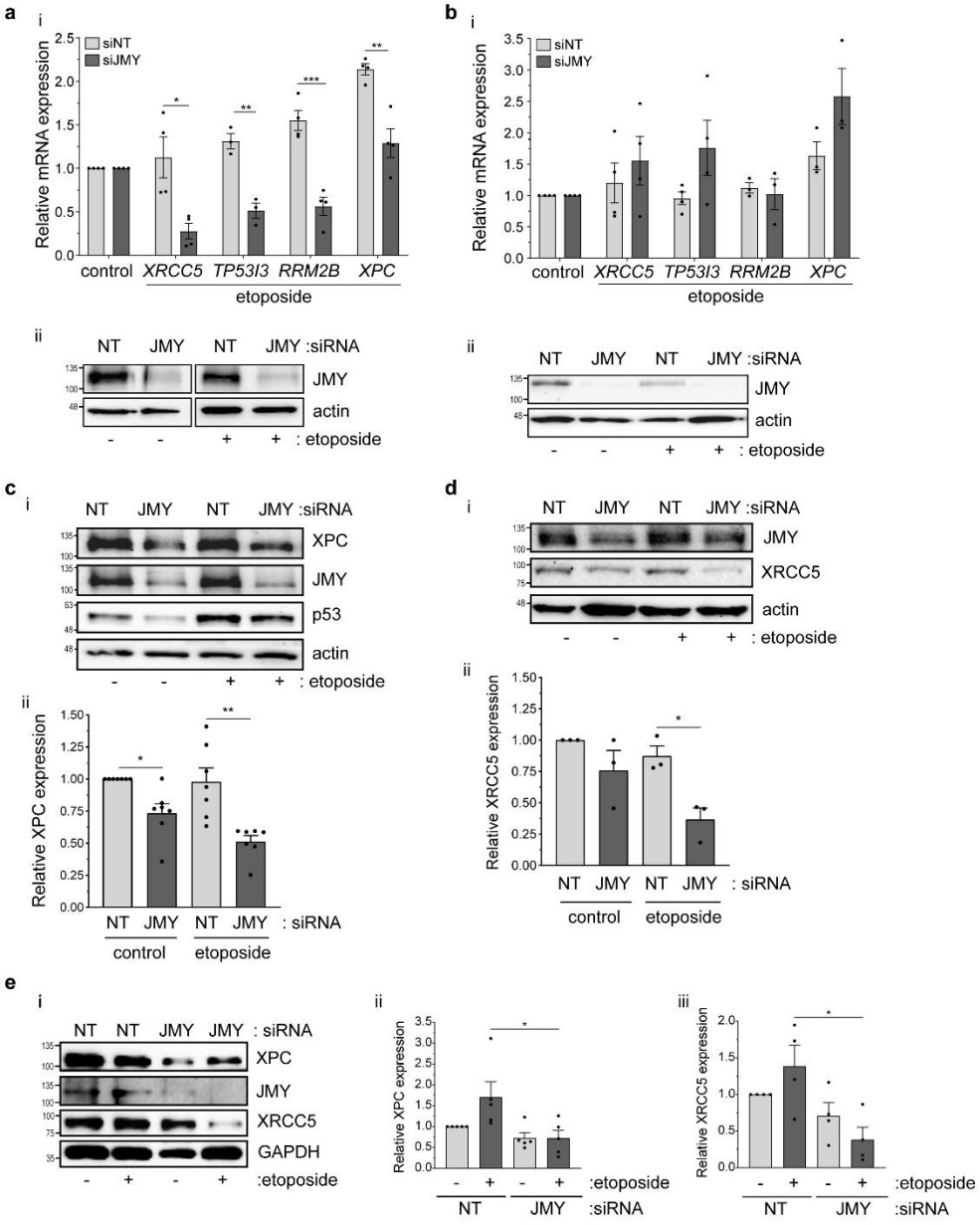


***Figure 4.2. JMY influences the expression of p53-dependent genes involved in DNA repair. a)*** *and* ***b)*** *U2OS* ***(a)*** *and Saos2* ***(b)*** *cells were transfected with JMY or non-targeting (NT) siRNA for 72h and treated with DMSO vehicle (-, control) or etoposide (+, 50*$\mu$*M) for the last 6h. i) Changes in gene expression are present as fold over vehicle-treated cells after normalising with GAPDH (mean ± s.e.m.), n = 3-4 independent experiments. ii) Western blot represents JMY knockdown.* ***c)*** *and* ***d)*** *i) U2OS cells were transfected and treated as in* ***(a)*** *before XPC* ***(c)*** *and XRCC5* ***(d)*** *protein expression levels were monitored. ii) Graph*

*represents protein expression after normalising with actin (mean ± s.e.m.). n = 3-7 independent experiments.* ***e)*** *i) MCF7 cells were transfected and treated as in* ***(a)*** *before XPC (ii) and XRCC5 (iii) protein expression levels were monitored as in* ***(c)*** *after normalising with GAPDH (mean ± s.e.m.). n = 4-5 independent experiments. * p < 0.05, ** p < 0.01, *** p < 0.001; unpaired two-tailed Student's t-test.*

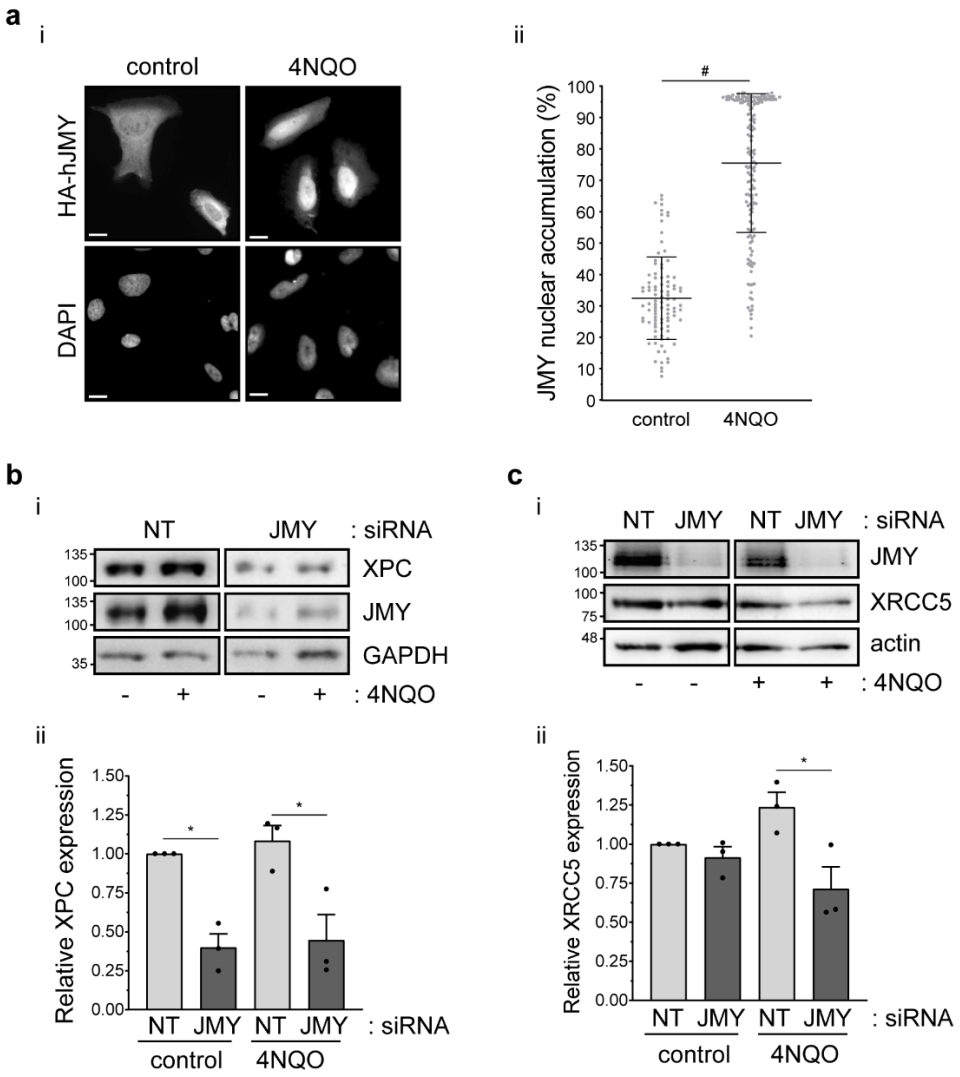


***Figure 4.3. JMY impacts the expression of DNA repair genes during 4NQO treatment. a)*** *i) U2OS cells expressing HA-tagged wild-type human JMY (HA-hJMY) were treated with DMSO vehicle (-, control) or 4NQO (100nM) for 16h. ii) Quantification of JMY nuclear versus cytoplasmic accumulation (mean ± SD). N ≥ 150 cells per treatment.* ***b)*** *and* ***c)*** *i) U2OS cells were transfected with JMY or non-targeting (NT) siRNA for 72h and treated as in* ***(a)*** *before XPC* ***(b)*** *or XRCC5* ***(c)*** *protein expression levels were monitored. ii) Graphs represent protein*

*expression after normalising with loading controls (mean ± s.e.m.), n = 3 independent replicates. Scale bar = 10$\mu$m. * p < 0.05; unpaired two-tailed Student's t-test. # p < 0.0001; Mann-Whitney test.*

Notably, a comparison between wild-type p53 HAP1 chronic myelogenous leukaemia-derived parental and JMY knockout cells (Fig. 4.4ai) revealed that JMY ablation also resulted in reduced expression of XPC and XRCC5 at both mRNA and protein levels (Fig. 4.4aii, b, c). To investigate whether the reduced *XPC* and *XRCC5* mRNA expression resulted from JMY's impact on the recruitment of p53 to the promoter of target genes, chromatin immunoprecipitation (ChIP) was performed in the HAP1 cell lines. HAP1 JMY knockout cells present compromised recruitment of p53 to target genes under etoposide treatment (Fig. 4.5). Collectively, these findings demonstrate that in response to DNA damage, JMY accumulates in the nucleus enhancing the p53 recruitment to target genes and its transcriptional activity, particularly promoting the expression of genes involved in DNA repair.

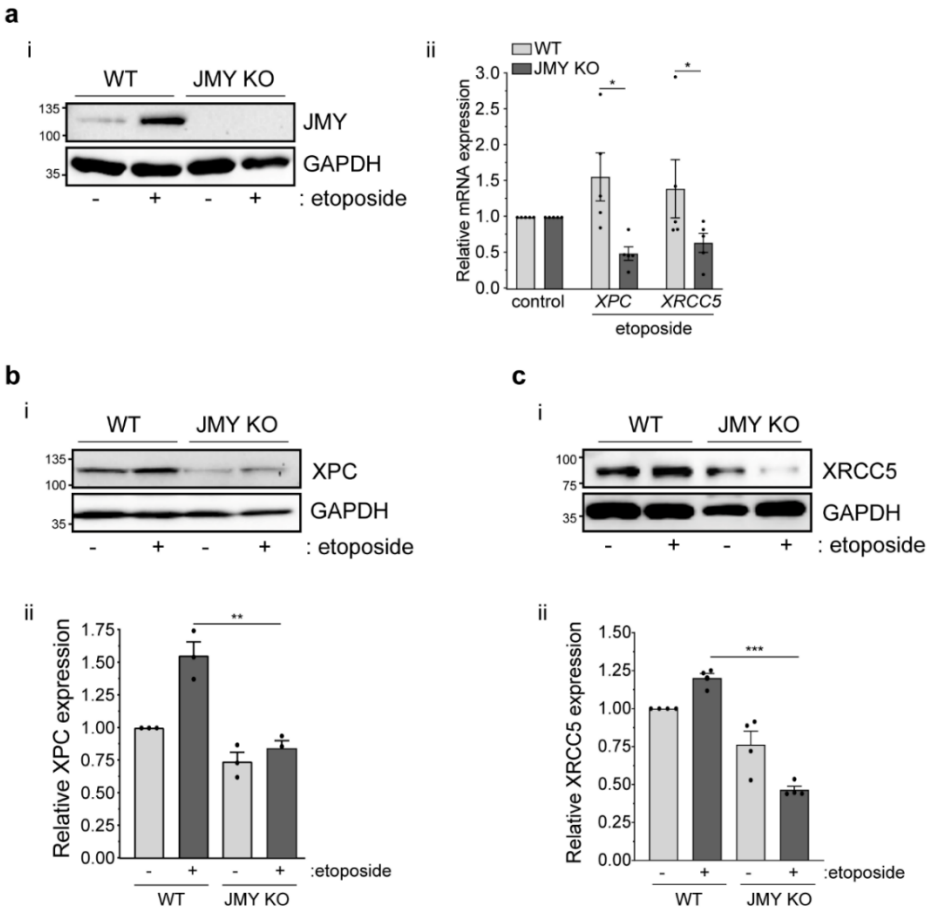


***Figure 4.4. JMY ablation reduces the expression of p53-dependent DNA repair genes. a)*** *HAP1 parental (WT) and JMY knockout (JMY KO) cells were treated with either DMSO vehicle (-, control) or etoposide (+, 500nM) for 6h. i) Western blot shows the absence of JMY in HAP1 JMY knockout but not in parental cells. ii) XPC and XRCC5 gene expression changes are represented as fold over vehicle-treated cells after normalising with GAPDH (mean ± s.e.m.). n = 5 independent experiments.* ***b)*** *and* ***c)*** *i) HAP1 parental (WT) and JMY knockout (JMY KO) cells were treated as in* ***(a)*** *before XPC* ***(b)*** *and XRCC5* ***(c)*** *protein expression were monitored. ii) Graphs represent protein expression after normalising with GAPDH (mean ± s.e.m.). n = 3-4 independents. * $p < 0.05$, ** $p < 0.01$, *** $p < 0.0001$; unpaired two-tailed Student's t-test.*

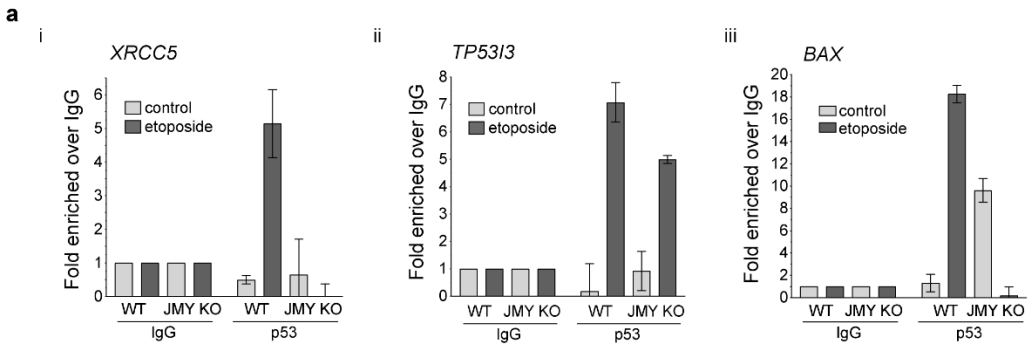


***Figure 4.5. JMY is required for the p53 recruitment to target genes. a)*** *HAP1 parental (WT) and JMY knockout (JMY KO) cells were treated with either DMSO vehicle (control) or etoposide (500nM) for 6h before ChIP. qPCR was performed on ChIP chromatin with results expressed as fold over IgG (mouse non-specific IgG) after normalising to input levels showing p53 recruitment to XRCC5 (i), TP53I3 (ii) and BAX (iii) promoters. (Fold ± SD), n = 2 independent experiments (one representative experiment is represented).*

Nuclear JMY reduces the accumulation of DNA damage.

Given the fact that the absence of JMY compromised the p53-driven expression of DNA repair targets suggested that JMY may be required for the repair of DNA strand breaks. Alkaline comet assays were employed to directly measure, at single-cell level, the impact of JMY on DNA damage accumulation [328]. As expected, the exposure to DNA-damaging agents like etoposide and 4NQO resulted in a marked accumulation of DNA breaks, as reflected by the elongation of comet tails and accumulation of DNA (increased fluorescence) within them (Fig. 4.6a). Although DNA damage was hardly detected in JMY-depleted U2OS cells under non-perturbed conditions, treatment with both etoposide and 4NQO led to a marked increase in the amount of detected DNA damage upon JMY depletion (Fig. 4.6a). The impact of JMY on DNA damage accumulation was not restricted to a single cell type as similar results were recapitulated upon treatment in both JMY-depleted MCF7 (Fig. 4.6b) and HAP1 JMY knockout cells (Fig. 4.6c). Interestingly, in p53 null Saos2 cells, the depletion of JMY had little impact on the amount of DNA damage accumulation (Fig. 4.6d). Based on these findings, it could be inferred that during genotoxic stress, the absence of nuclear JMY was compromising the ability to repair DNA lesions, and thus, augmenting the expression of nuclear JMY should have the opposite effect. To test this, nuclear

localised human JMY was overexpressed in U2OS cells (Fig. 4.7a, b), demonstrating that nuclear JMY was sufficient to reduce the accumulation of DNA damage during genotoxic stress (Fig. 4.7a). Together, these results suggest that nuclear JMY can enhance p53-mediated DNA repair in response to DNA damage.

DNA strand breaks lead to the accumulation of repair factors at the lesion sites that trigger the formation of DNA damage response foci, commonly defined by the presence of markers such as phosphorylated histone H2AX (γH2AX) and 53BP1 [329]. Surprisingly, the depletion of JMY reduced the number of γH2AX and 53BP1 foci during etoposide treatment (Fig. 4.8a, b) and decreased γH2AX cellular levels (Fig. 4.8c). The impact of JMY on the formation of DNA damage response foci was also observed in HAP1 JMY knockout cells, where ablation of JMY led to a marked reduction in both γH2AX foci and its cellular levels (Fig. 4.9a, b). Additionally, both the short-term depletion and ablation of JMY decreased ATM and ATR overall activity during etoposide treatment (Fig. 4.10a, b) as detected through immunofluorescence. Hence, these results suggest that JMY enables an efficient DNA damage response.

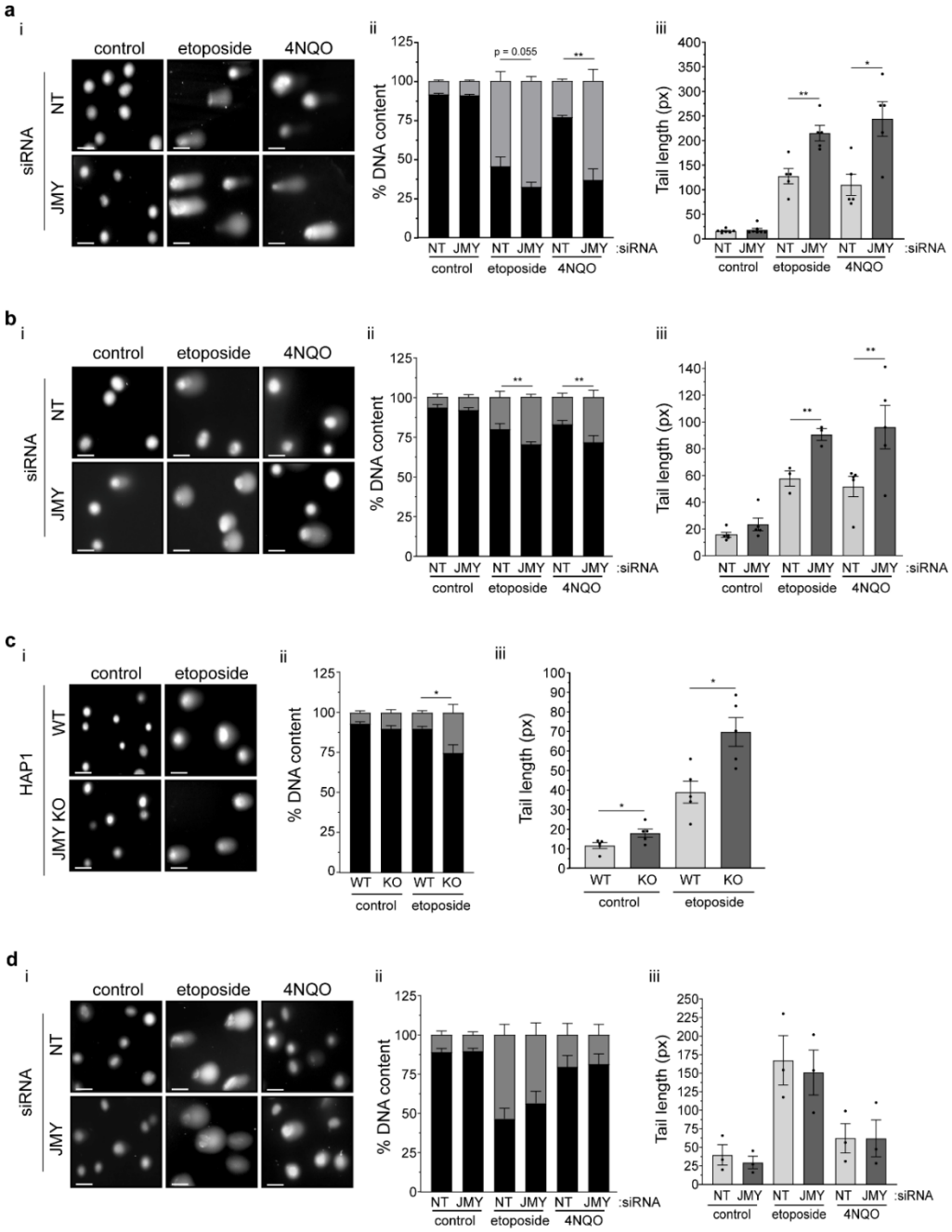


***Figure 4.6. The absence of JMY increases the accumulation DNA damage. a)*** *and* ***b)*** *i) U2OS* ***(a)*** *and MCF7* ***(b)*** *cells were transfected with JMY or non-targeting (NT) siRNA for 72h and treated with DMSO vehicle (control), etoposide (10*$\mu$*M) or 4NQO (100nM) for the last 16h. Quantification of the DNA content distributed between the head (black) and tail (grey) of the comet (ii) and the comet tail length (iii), (mean ± s.e.m), n = 3-5 independent experiments.* ***c)*** *HAP1 parental (WT) and JMY knockout (JMY KO, KO) cells were treated with DMSO vehicle (control) or etoposide (500nM) for 16h. Comet DNA distribution (ii) and tail length (iii) were calculated as in* ***(a)****, (mean ± s.e.m.), n = 5 independent experiments.* ***d)*** *Saos2*

*cells were transfected and treated as in **(a)**. Comet DNA distribution (ii) and tail length (iii) were calculated as in **(a)**, (mean ± s.e.m.), n = 3 independent experiments. Scale bar = 40μm. * p < 0.05, ** p < 0.01; unpaired two-tailed Student's t-test.*

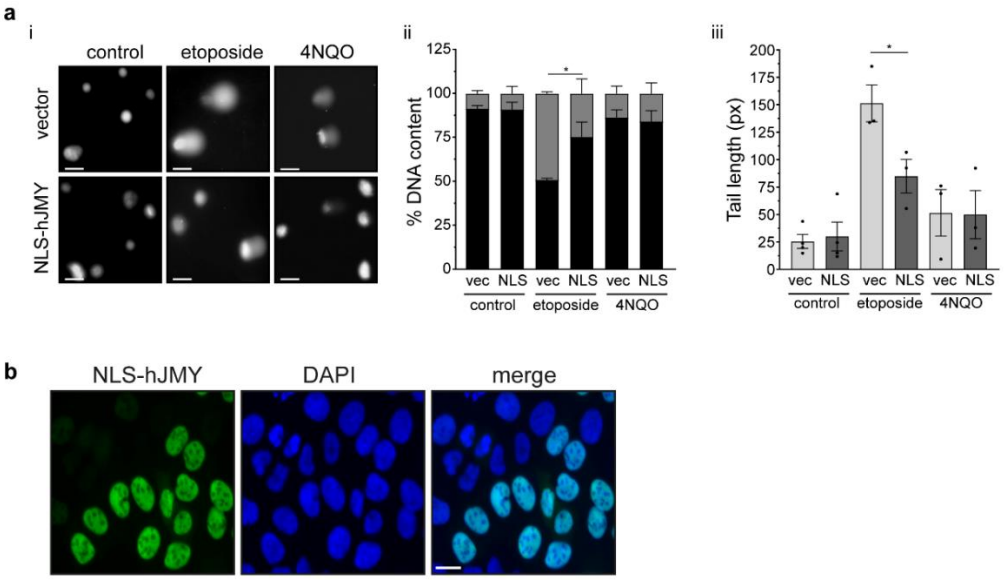


***Figure 4.7. Nuclear JMY reduces DNA damage accumulation in response to etoposide. a)** i) U2OS cells expressing FLAG-NLS-hJMY (NLS-hJMY, NLS) or vector control (vector, vec) were treated with DMSO vehicle (control), etoposide (10μM) or 4NQO (100nM) for 16h. ii) Quantification of the DNA content distributed between the head (black) and tail (grey) of the comet (ii) and the comet tail length (iii), (mean ± s.e.m), n = 3 independent experiments. Scale bar = 40μm. **b)** U2OS cells expressing FLAG-NLS-hJMY (NLS-hJMY). JMY was detected using anti-FLAG antibody, and DAPI was used to visualise the nuclear DNA. Data provided by Dr Amanda S Coutts. Scale bar = 10μm. * p < 0.05; unpaired two-tailed Student's t-test.*

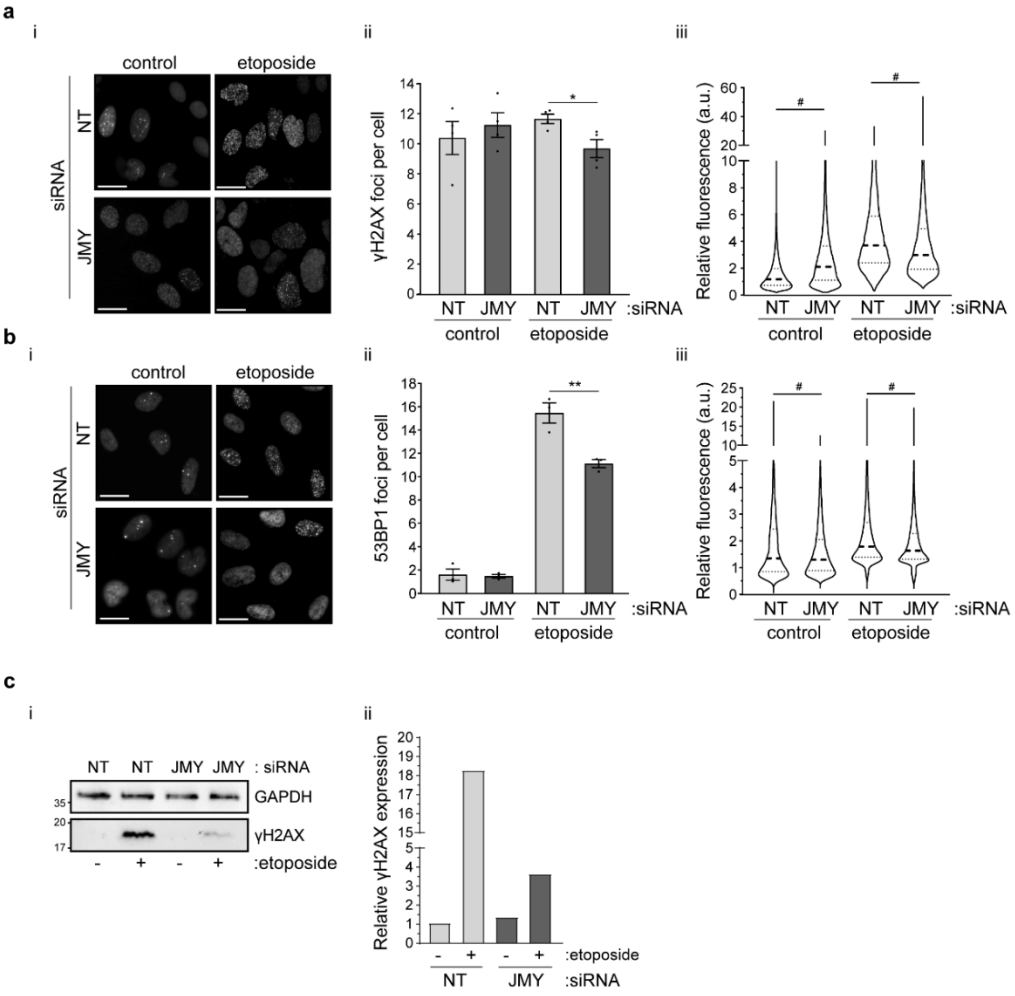


***Figure 4.8. JMY impacts the formation of DNA damage responsive foci. a)*** *and* ***b)*** *U2OS cells were transfected with JMY or non-targeting (NT) for 72h and treated with DMSO vehicle (control) or etoposide (50μM) for the last 6h. i) Foci were detected with anti-γH2AX* ***(a)*** *or anti-53BP1 antibodies* ***(b)****. ii) Graphs represent the mean number of foci per cell ± s.e.m. for γH2AX* ***(a)*** *or 53BP1* ***(b)****, n = 3-4 independent experiments, each with N ≥ 100 cells per condition, and iii) Violin plots represent relative fluorescence intensity for γH2AX* ***(a)*** *or 53BP1* ***(b)*** *(median and quartiles) N ≥ 300 cells per condition pooled from n = 3-4 independent experiments.* ***c)*** *i) U2OS cells were transfected as in* ***(a)*** *and treated with DMSO vehicle (-) or etoposide (+, 50μM) for the last 6h. ii) Graph represents quantification of cellular γH2AX levels after normalising with GAPDH, n = 3 independent experiments (representative experiment shown). Scale bars = 10μm. * p < 0.05 and ** p < 0.01; unpaired two-tailed Student's t-test. # p < 0.0001; Mann-Whitney U test.*

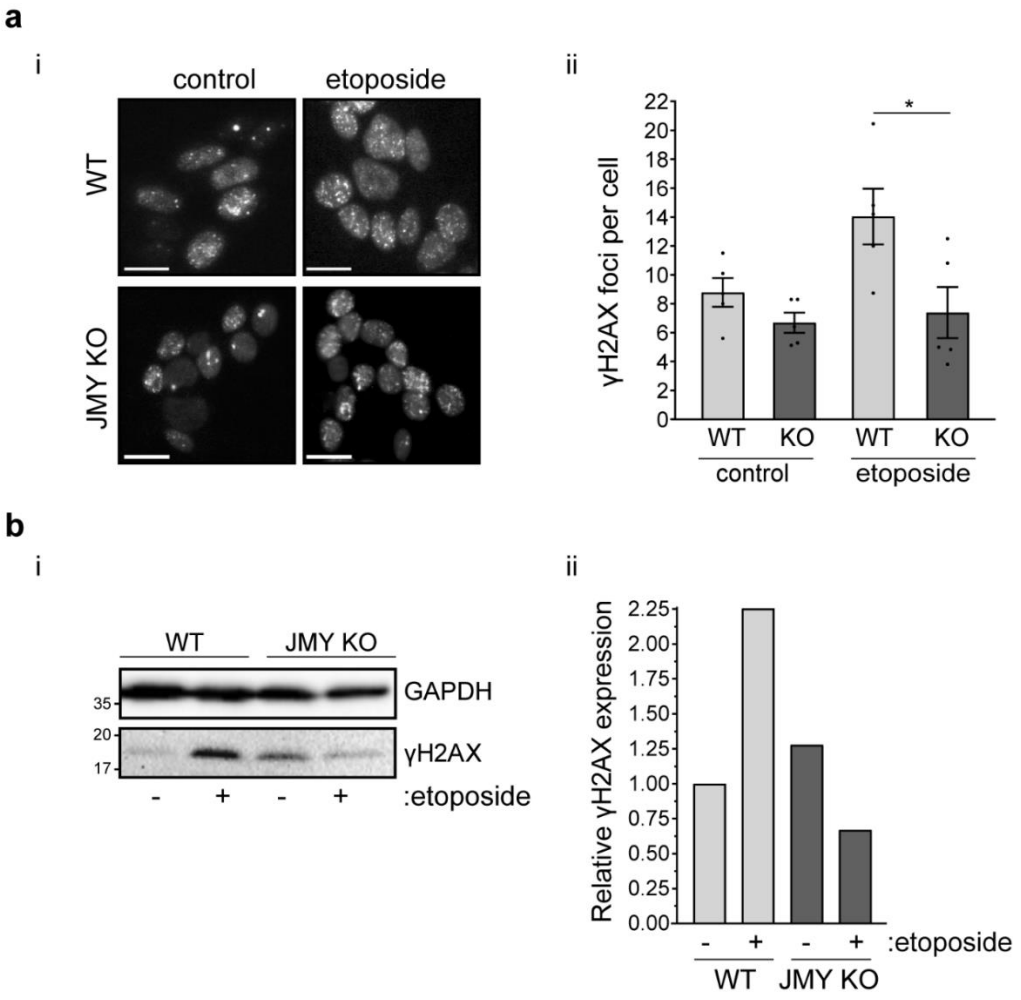


***Figure 4.9. The absence of JMY compromises the formation of γH2AX foci. a)*** *i) HAP1 parental (WT) and JMY knockout (JMY KO, KO) cells were treated with either DMSO vehicle (control) or etoposide (500nM) for 6h. ii) Quantification of γH2AX foci per cell (mean ± s.e.m.), n = 5 independent experiments each with N ≥ 100 cells per condition.* ***b)*** *i) HAP1 parental (WT) and JMY knockout (JMY KO) cells were treated with either DMSO vehicle (-) or etoposide (+, 500nM) for 6h. ii) Graph represents quantification of cellular γH2AX levels after normalising with GAPDH, n = 3 independent experiments (representative experiment shown). Scale bars = 10μm. * p < 0.05; unpaired two-tailed Student's t-test.*

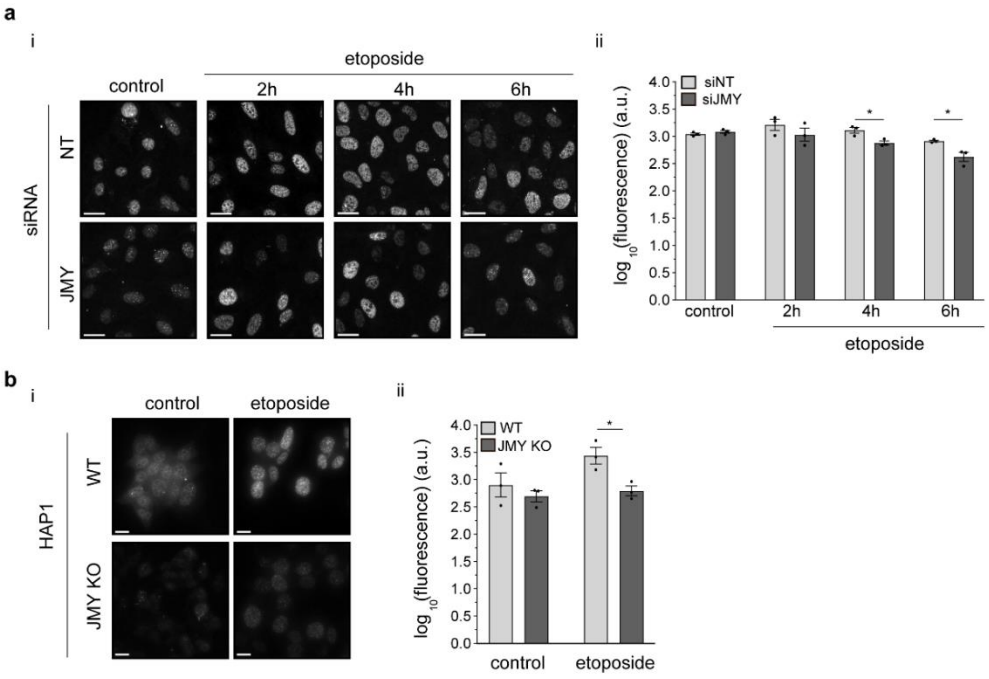


***Figure 4.10. The absence of JMY reduces activation of the DNA damage response. a)*** *i) U2OS cells were transfected with JMY or non-targeting (NT) siRNA for 72h and treated with DMSO vehicle (control) or etoposide (50$\mu$M) for the indicated time points before immunofluorescence was conducted with phospho-ATM/ATR substrate antibody.* ***b)*** *i) HAP1 parental (WT) and JMY knockout (JMY KO) cells were treated with DMSO vehicle (control) or etoposide (500nM) for 16h before immunofluorescence was conducted as in* ***(a)****. For* ***(a)*** *and* ***(b)*** *ii) Graph represents relative fluorescence (mean ± s.e.m.), n = 3 independent experiments, each with N $\geq$100 cells per condition. Scale bar = 10$\mu$m. * p < 0.05; unpaired two-tailed Student's t-test.*

DNA repair requires JMY's Arp2/3-dependent actin nucleation.

A growing body of evidence implicates nuclear actin in DNA repair [178], and previous work suggested that actin nucleation may be required for JMY's nuclear functions [127]. Therefore, the ability of JMY to nucleate actin may influence its role during DNA repair. To investigate this, nuclear JMY derivatives with and without Arp2/3-dependent and independent actin nucleation activity were overexpressed in U2OS cells (Fig. 4.11) [127]. Similar to the results observed with nuclear localised human JMY (Fig. 4.7a), overexpression of nuclear mouse JMY (NLS-mJMY) also decreased the accumulation of DNA damage detected during etoposide treatment (Fig. 4.12a). Interestingly, removal of JMY's entire WCA region (NLS-ΔWCA) or its

ability to mediate Arp2/3-dependent actin nucleation (NLS-W981A) resulted in increased accumulation of DNA damage when compared to cells overexpressing wild-type JMY (Fig. 4.12b). Hence, this suggested that the ability of JMY to nucleate actin via the Arp2/3 complex may influence JMY-mediated DNA repair. To further investigate this, Arp2/3 complex activity was inhibited using ck666 [330], in U2OS cells overexpressing nuclear localised JMY, where it was observed that inhibition of Arp2/3 activity had little impact on DNA damage accumulation under non-perturbed conditions (Fig. 4.12c). Conversely, during etoposide treatment, inhibition of Arp2/3 activity hindered the reduction in DNA damage accumulation that was observed upon overexpression of nuclear JMY (Fig. 4.12c). Moreover, when JMY's Arp2/3-dependent actin nucleation was compromised, a reduced expression of p53-dependent genes involved in DNA repair was observed (Fig. 4.12d). Together, these results suggest that the role of JMY in DNA repair involves its Arp2/3-mediated actin nucleation and this, in part, is through its influence of p53-dependent transcription.

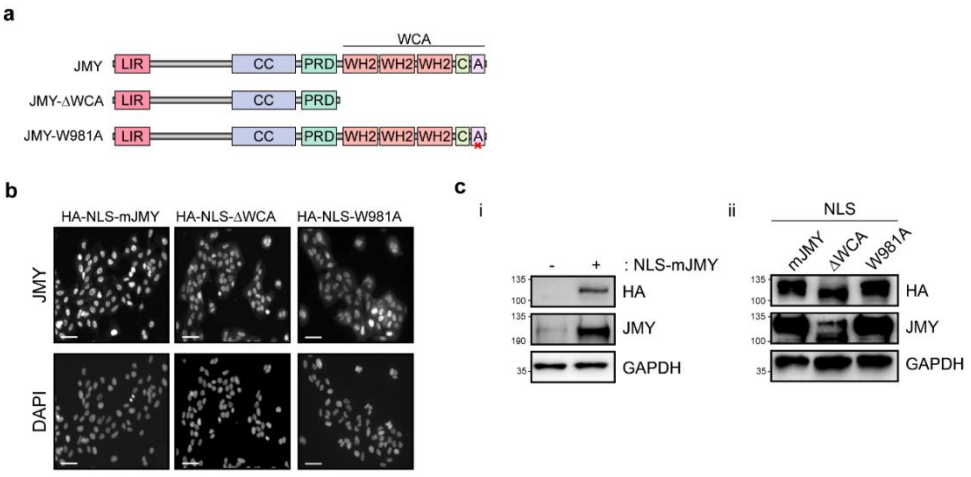


***Figure 4.11. Overexpression of nuclear JMY derivatives in U2OS cells. a)*** *Representation of JMY derivatives lacking the WCA actin nucleation domain (ΔWCA) or presenting a single mutation compromising the Arp2/3-dependent actin nucleation (W981A).* ***b)*** *U2OS cells expressing nuclear JMY and derivatives where ectopic JMY was detected by immunofluorescence using anti-HA antibody.* ***c)*** *i) and ii) Western blot of cell extracts from U2OS cells expressing nuclear JMY derivatives or non-transfected controls (-). Ectopic HA-tag JMY derivatives were detected as in* ***(b),*** *whereas both endogenous and ectopic JMY levels were detected using anti-JMY antibody.*

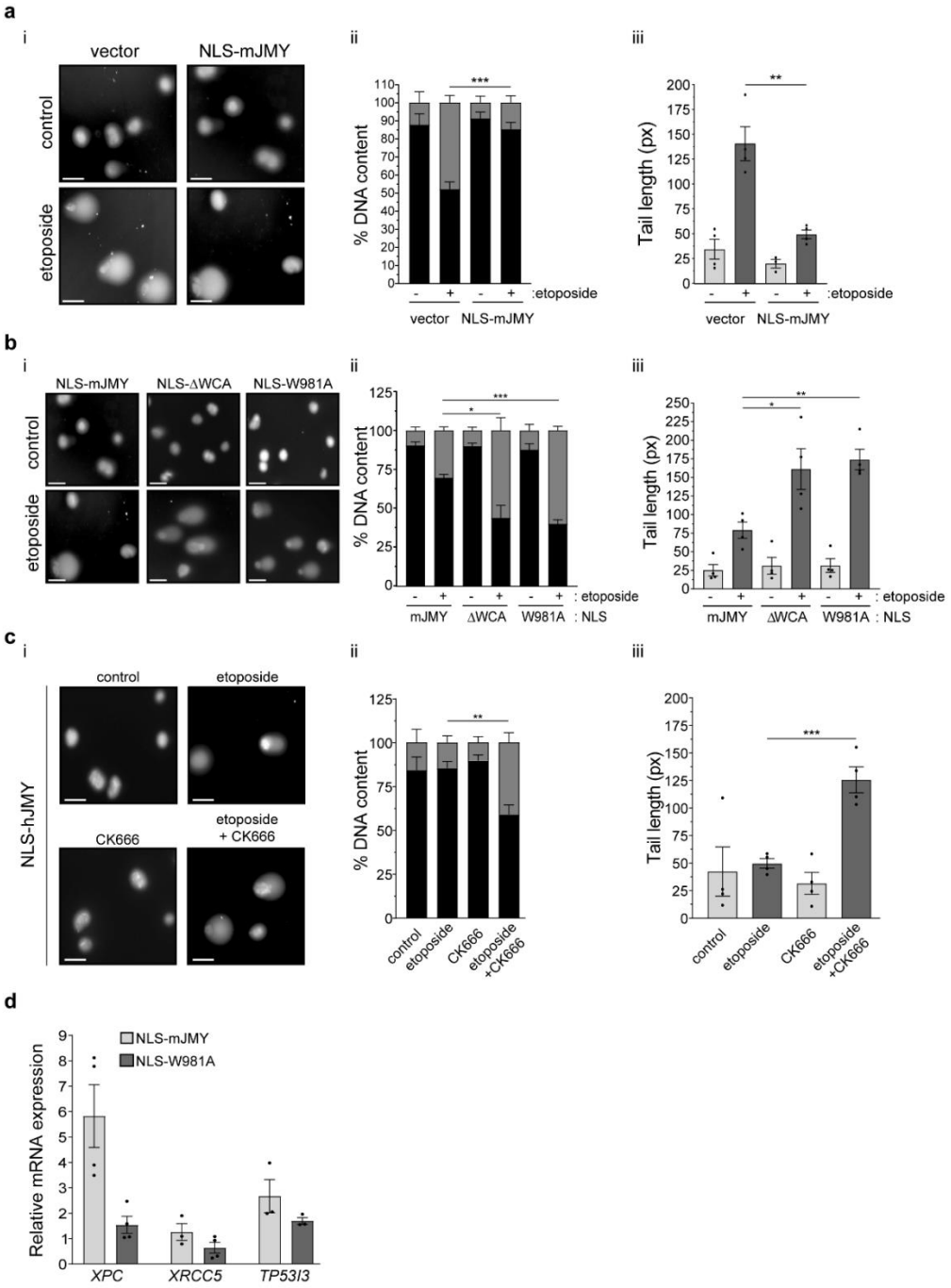


***Figure 4.12. JMY-mediated Arp2/3-dependent actin nucleation reduces DNA damage accumulation. a)*** *i) U2OS cells stably expressing nuclear wild-type mouse JMY (NLS-mJMY) or vector control were treated with DMSO vehicle (-, control) or etoposide (+, 10μM) for 16h. Quantification of the DNA content distributed between the head (black) and tail (grey) (ii) and tail length (iii) (mean ± s.e.m.), n = 4 independent experiments.* ***b)*** *U2OS stable cell lines expressing JMY derivatives were treated as in* ***(a)*** *before monitoring the distribution of DNA content between the head (black) and tail (grey) (ii) and tail length (iii), (mean ± s.e.m.), n*

*= 4 independent experiments.* ***c)*** *U2OS stable cells expressing NLS-hJMY were treated with either DMSO vehicle (control), etoposide (10μM), ck666 (100μM) or a combination as indicated for 16h. Comet DNA content distribution (ii) and tail length (iii) were calculated as in* ***(a)*** *(mean ± s.e.m.), n = 4 independent experiments.* ***d)*** *U2OS stable cell lines as in* ***(b)*** *were treated with vehicle (DMSO) or etoposide (50μM) for 6h, before XPC, XRCC5 and TP53I3 mRNA expression was monitored. Graph represents relative gene expression as fold over vehicle-treated cells after normalising with GAPDH (mean ± s.e.m.), n = 3-4 independent experiments. Scale bars = 40μm. * p < 0.05, ** p < 0.01 and *** p < 0.001; unpaired two-tailed Student's t-test.*

JMY promotes cell proliferation and survival during DNA damage.

Given that JMY can enhance DNA repair via the p53 response, the impact of JMY on cell fate during DNA damage was examined. The siRNA-mediated reduction of JMY expression in U2OS cells significantly decreased cell proliferation under non-perturbed conditions and had a moderate but significant effect upon etoposide treatment (Fig. 4.13a), while in HAP1 JMY knockout cells, a more dramatic decline in proliferation was observed during etoposide-induced DNA damage (Fig. 4.14a). This decrease in cell proliferation was reflected in increased cell death upon induction of genotoxic stress in both JMY knockdown and knockout cells (Fig. 4.13b; Fig. 4.14b). As the reduction in JMY levels was correlated with increased DNA damage and decreased ATM and ATR activity, it was reasoned that JMY might influence sensitivity to inhibitors of key targets involved in the DNA damage response. Indeed, the absence of JMY sensitised tumour cells to small-molecule inhibitors targeting ATM, ATR and DNA-PK under non-perturbed conditions (Fig. 4.13c; Fig. 4.14c), which was exacerbated upon etoposide treatment leading to increased cell death (Fig. 4.13d; Fig. 4.14d, e). These results indicate that the absence of JMY results in increased cellular sensitivity to DNA damaging agents and inhibitors targeting key factors of the DNA damage response, leading to decreased proliferation and increased cell death.

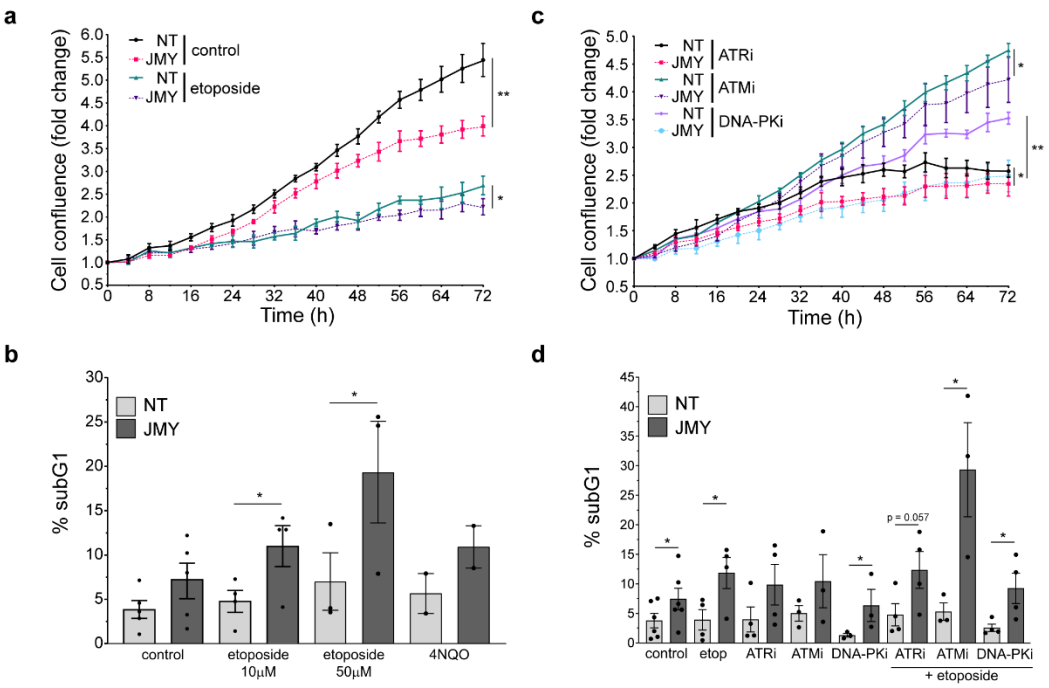


***Figure 4.13. JMY enhances cell proliferation and survival during genotoxic stress. a)*** *and* ***c)*** *U2OS cells were transfected with JMY or non-targeting (NT) siRNA for 72h and treated with either DMSO vehicle (control), etoposide (10μM)* ***(a)*** *and ATM (ATMi; KU60019 5μM), ATR (ATRi; AZD6738 5μM) or DNA-PK (DNA-PKi; M3814 5μM) inhibitors* ***(c)*** *as indicated. Graphs represent cell confluence after normalising with time zero images (mean ± SD), n = 3 independent experiments (representative experiment shown).* ***b)*** *and* ***d)*** *U2OS cells were transfected as in* ***(a)*** *and treated with DMSO vehicle (control), etoposide (as indicated) or 4NQO (500nM)* ***(b)*** *or ATM (ATMi, 10μM), ATR (ATRi; 10μM) and DNA-PK (DNA-PKi; 1μM) inhibitors in the presence or absence of etoposide (10μM)* ***(d)****. Graphs represent percentage subG1 (mean ± s.e.m.), n = 3-5 independent experiments. * p < 0.05 and ** p < 0.001; unpaired two-tailed Student's t-test.*

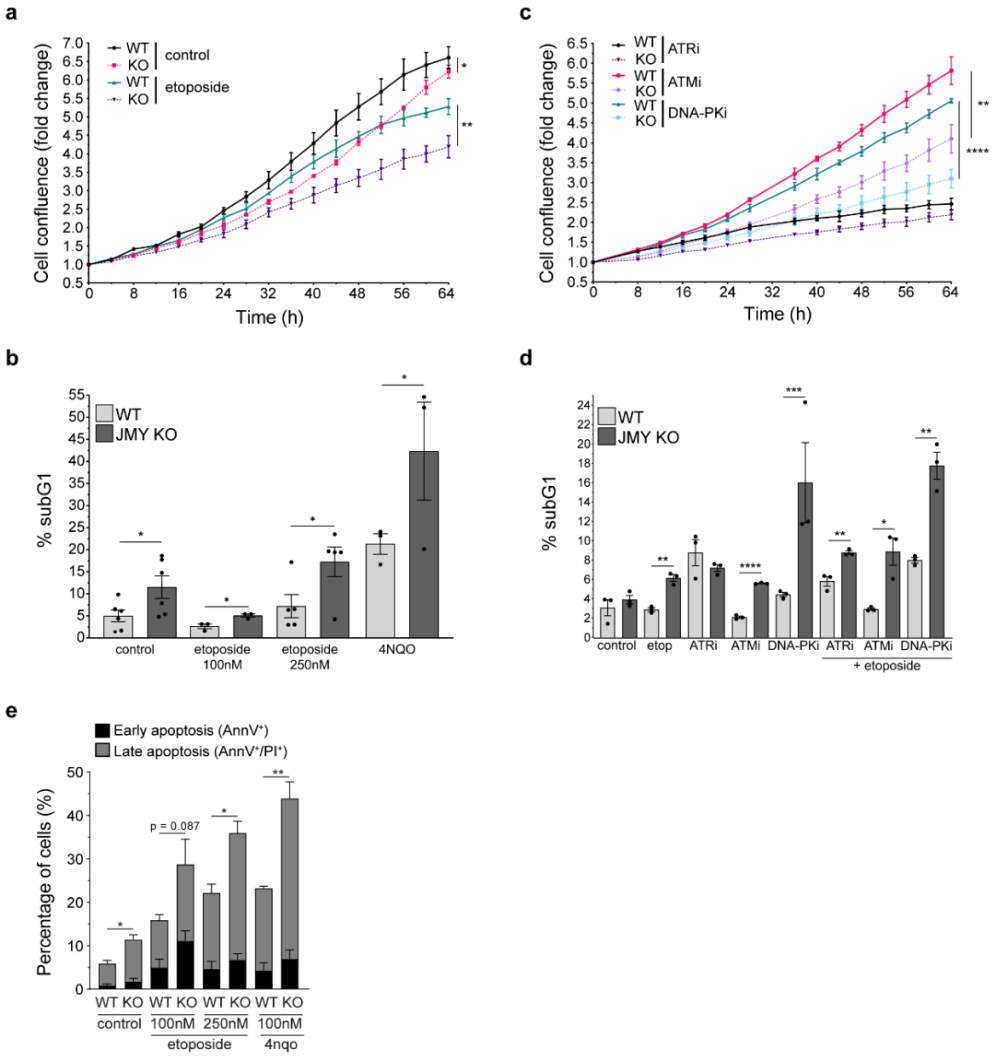


***Figure 4.14. The absence of JMY reduces cell proliferation and increases cell death during genotoxic stress. a)*** *and* ***c)*** *HAP1 parental (WT) and JMY knockout (JMY KO, KO) cells were treated with DMSO vehicle (control) or etoposide (100nM)* ***(a)*** *and ATM (ATMi; KU60019, 500nM), ATR (ATRi; AZD6738, 500nM) or DNA-PK (DNA-PKi; M3814, 1*$\mu$*M) inhibitors* ***(c)*** *as indicated. Graphs represent cell confluence after normalising with time zero images (mean ± SD), n = 3 independent experiments (representative experiment shown).* ***b)*** *and* ***d)*** *HAP1 parental (WT) and JMY knockout (JMY KO) cells were treated with DMSO vehicle (control), etoposide (as indicated) or 4NQO (100nM)* ***(b)****, or ATM (ATMi; 500nM), ATR (ATRi; 500nM) and DNA-PK (DNA-PKi; 1*$\mu$*M) inhibitors in the presence or absence of etoposide (100nM)* ***(d)****. Graphs represent percentage subG1 (mean ± s.e.m.), n = 3-6 independent experiments.* ***e)*** *HAP1 parental (WT) and JMY knockout (JMY KO) cells were treated as in* ***(b)****. Graphs represent the percentage of cells undergoing early (black) or late (grey) apoptosis (mean ± s.e.m.), n = 3*

*independent experiments. * p < 0.05, ** p < 0.01, *** p < 0.001 and **** p < 0.0001; unpaired two-tailed Student's t-test.*

Given the essential role of nuclear JMY in promoting tumour cell survival during stress, it was hypothesised that alterations in *JMY* levels may impact patient outcomes. Due to the lack of transcriptomic data specific for osteosarcoma models and to improve our mechanistic understanding of JMY's role in tumour cells, we conducted a pan-cancer analysis using the data from the TCGA cohort [300]. Interestingly, analysis across all cancer types, indicated that patients whose tumours had lower *JMY* mRNA expression or homozygous deletion present higher mutation count (Fig. 4.15a). Further stratification based on *p53* (TP53) mutation status also indicated that tumours with lower *JMY* levels and expression of mutant p53 had a significantly higher mutation count (Fig. 4.15b). Since JMY can reduce the accumulation of DNA damage, increase resistance to DNA damaging agents and reduce overall mutation count, it was reasoned that tumours with higher *JMY* expression levels might lead to poorer patient outcomes due to a more aggressive phenotype. As expected, patients whose tumours present higher *JMY* mRNA expression showed significantly lower overall survival (Fig. 4.15c). Together, these results suggest that JMY can promote cell survival during DNA damage by its impact on p53-mediated gene expression and DNA repair, which is reflected in patient outcomes.

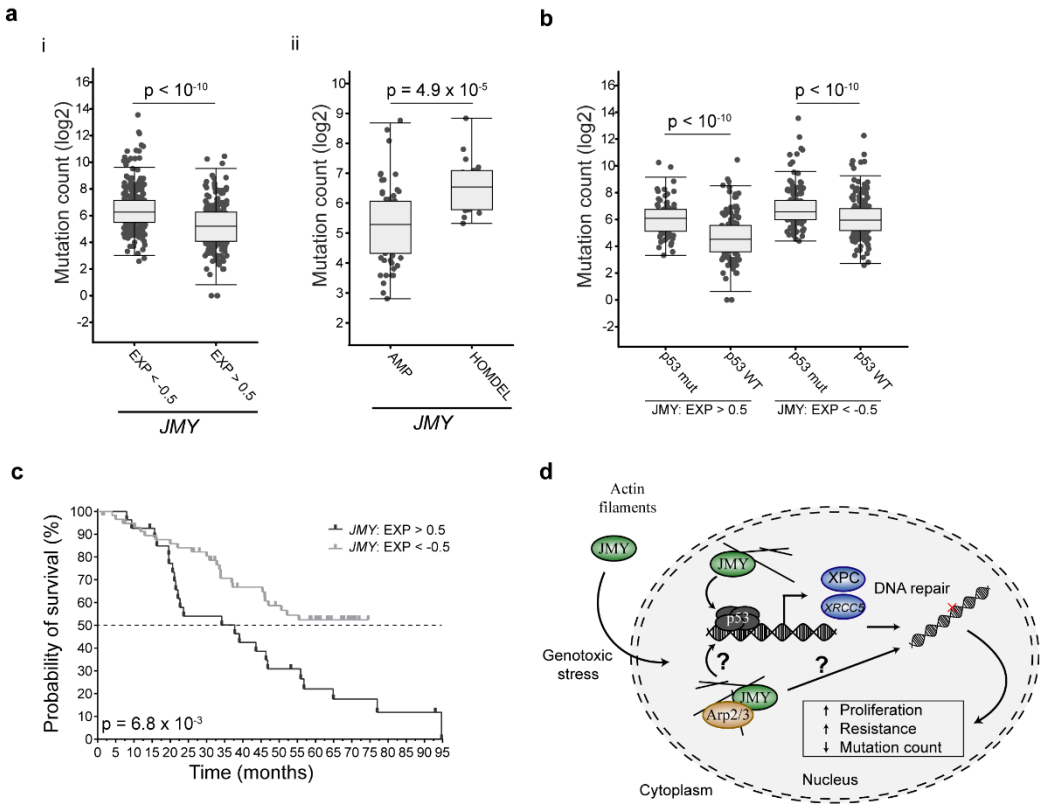


***Figure 4.15. Lower JMY expression is correlated with improved overall patient survival. a)*** *and* ***b)*** *Mutation count of tumours stratified by JMY mRNA expression levels, low (EXP < -0.5) versus high (EXP > 0.5) (i), JMY amplification versus deletion (ii) or further grouped based on p53 (TP53) mutation status* ***(b)****.* ***c)*** *Kaplan–Meier survival curve for patients whose tumours express low (light grey) or high (dark grey) JMY mRNA levels. For* ***(a-c)*** *data was obtained from the TCGA pan-cancer dataset* [300]*.* ***d)*** *During DNA damage, JMY promotes the p53-driven expression of DNA repair proteins, and through its Arp2/3-dependent actin nucleation, JMY impacts the accumulation of DNA lesions and affects overall cell survival.*

## 4.4. Discussion

The tumour suppressor p53 plays a crucial role during the DNA damage response through activating a myriad of targets, including the expression of DNA repair factors. In this chapter, our results demonstrate that the absence of JMY compromises the expression of p53 target genes involved in DNA repair and hinders the DNA damage signalling response leading to an accumulation of DNA damage. JMY's Arp2/3-mediated actin nucleation activity is required for the p53 expression of target genes and it impacts on DNA repair. Ultimately, the absence of JMY sensitises tumour cells to DNA damaging agents and inhibitors of crucial targets involved in the DNA damage response and impacts on cell survival which is reflected in human tumours where reduced expression of *JMY* mRNA results in increased patient survival (Fig. 4.15d).

JMY is a DNA damage-responsive actin nucleator that can localise in the cytoplasm and nucleus, where cytoplasmic JMY enhances cell migration and invasion through promoting both Arp2/3-dependent and independent actin nucleation [126,127]. Upon treatment with specific genotoxic stressors, JMY undergoes nuclear accumulation, where previous studies demonstrated that it could enhance the p53-driven expression of *BAX* [104,127]. However, the broader role of JMY as a p53 transcriptional cofactor is incompletely understood. The results in this chapter expand our knowledge of transcriptional function of nuclear JMY and its ability to modulate the expression of p53 targets, in particular genes involved in DNA repair.

Multiple stressors, including DNA damage, can induce the activation of p53 and depending on the stress response, p53 can promote the expression of specific genes, leading to cell cycle arrest or DNA repair [65]. Several factors meticulously regulate the p53 response, including its stability and activation, which is mainly influenced by post-translational modifications and interaction with cofactors such as JMY [108,127]. Upon genotoxic stress, p53 is activated by all three PIKK (ATM, ATR and DNA-PK), resulting in p53 stabilisation and nuclear accumulation [80]. Here, we observe that JMY influences the recruitment of p53 to target genes during etoposide-induced DNA damage (Fig. 4.5). It is likely that JMY's impact on the p53-driven expression of DNA repair genes will also influence critical downstream steps of the DNA damage response. Interestingly, we observed that in JMY-depleted U2OS and HAP1 JMY KO cells, there is a reduced or delayed DDR signalling (Fig.

4.10). We suggest that the absence of JMY can compromise the initial recognition of DNA lesions both under non-perturbed and genotoxic stress conditions. Therefore, the absence of JMY may blunt the activation of PIKKs (*e.g.* ATM and ATR), resulting in a decreased activation of p53 activity and downstream repair of DNA lesions. Given that U2OS and HAP1 cells present different sensitivity to DNA damaging agents and PIKK inhibitors, it will be relevant to further explore the role of JMY in the initial recognition of DNA lesions and activation of the DDR in different tumour cells, improving our mechanistic understanding of the role of JMY during DNA damage recognition.

For example, XRCC5 (Ku80) through its interaction with XRCC6 (Ku70) form the Ku heterodimeric complex that recognises double-strand DNA breaks initiating the NHEJ repair pathway and prompting the recruitment of other repair factors such as DNA-PK [121]. Defects in the recruitment of DNA-PK to the damaged sites in the absence of JMY could explain the sensitivity of JMY knockout cells to DNA-PK inhibition (Fig 4.14d). In comparison to the Ku complex, XPC plays an important role in recognising DNA lesions such as destabilised DNA base pairs (*e.g.* DNA adducts induced by 4NQO [16]), where XPC initiates the NER response [28]. Defects in XPC expression in the absence of JMY could also explain the increased sensitivity of JMY knockout cells to 4NQO treatment (Fig 4.14d, e). Moreover, our results demonstrate that nuclear JMY is required for the correct clearance of DNA lesions in multiple tumour cells, including osteosarcoma, breast and chronic lymphocytic leukaemia cell models. Given the substantial heterogeneity among tumour cells, comprehensive pan-cancer studies, including analysis of corresponding non-neoplastic tissues, are crucial to fully exploit the potential of a therapeutic target [331–334]. Future studies should explore JMY's expression patterns across various tumours and their non-neoplastic counterparts, expanding our comprehension of JMY's role in cellular fate, as well as its potential as a target for therapeutic interventions. Together, the results present in this chapter show how JMY positively regulates the activation of the DNA damage response as well as p53 activity, reducing the accumulation of DNA damage. These findings expand our understanding of the role of nuclear JMY during DNA damage.

It is known that different stressors can influence the cellular localisation of JMY, although the mechanisms that control this process are still incompletely understood. For example, in response to specific genotoxic stressors, JMY undergoes nuclear accumulation (Fig. 3.1a, Fig. 4.3a) [129], whereas during

starvation, JMY associates with cytoplasmic autophagosomes [125]. Recently, cytoplasmic JMY was described to influence several steps of the intrinsic mitochondrial-mediated apoptotic pathway, including the formation of the apoptosome through its actin nucleation role [145], thus adding further complexity to JMY's cytoplasmic function as well as its overall impact on cell fate. The cellular localisation of JMY will likely be determined by the duration and dose and the type of stress response, which can influence JMY's activity in the cell. Interestingly, previous studies have described that the duration and type of stressor affect p53 activity and its downstream cellular outcomes. For example, pulsating p53 levels induced via γ-irradiation promote the transient expression of cell cycle arrest and DNA repair genes [335,336], whilst a more prolonged p53 activation via ultraviolet radiation leads to the expression of pro-apoptotic genes [335]. Thus, for p53 activity to shift between the transient expression of DNA repair genes to a more sustained apoptotic target expression, the levels of p53 must likely exceed a time-dependent threshold. Therefore, future studies need to assess how the duration and dose of different stressors influence JMY's impact on p53 activity, particularly upon treatment with DNA damaging agents, and how this can module gene expression leading to different cellular outcomes.

Furthermore, our results indicate that JMY's actin nucleation activity is important in both DNA repair and p53-dependent transcriptional regulation (Fig. 4.12). Previous work demonstrated that the inhibition of overall cellular actin nucleation via latrunculin A treatment hindered JMY's capacity to enhance the p53-dependent activity on *BAX*-luciferase reporter assays, whilst the impairment of JMY's Arp2/3-dependent actin nucleation had no effect [127]. It may be that JMY's role could be gene-specific, leading to different recruitment of p53 or actin to the promoter of DNA repair versus apoptotic targets. It will be relevant to future studies to assess how JMY can modulate actin recruitment to target genes, its influence on gene expression and how this contributes to cell survival during stress.

Importantly, a growing body of evidence supports the role of actin nucleators in different aspects of DNA repair. For example, the clustering of double-strand DNA breaks via WASP-mediated Arp2/3-driven actin nucleation facilitates homology-directed repair [178]. More recently, WASP through its Arp2/3-dependent actin nucleation role has been shown to promote chromosomal rearrangement, which is required for the clustering and compartmentalisation of distal DNA strand breaks and their end-joining repair via DNA-PK [337]. Furthermore, WASH (another member

of the WASp protein family) is recruited to DNA lesions via its interaction with the Ku heterodimer and through the WASH-meadited Arp2/3-driven actin nucleation activity, WASH promotes NHEJ repair directly at the DNA damage site [181]. Overall, for the efficient repair of DNA strand breaks, data supports that cells require actin polymerisation and recruitment of actin nucleators directly at the DNA lesions [176]. Further studies are needed to expand our understanding of the role of nuclear JMY, specifically regarding whether JMY is also directly recruited to DNA breaks to enhance their repair. Nonetheless, the data present in this chapter contributes to the existing body of evidence describing that actin polymerisation mediated by nuclear actin nucleators is crucial in determining the cellular outcomes during DNA damage.

Together, these results suggest a broader role for JMY during the p53-driven expression of DNA repair targets, and through its Arp2/3-dependent actin nucleation, JMY impacts the accumulation of DNA damage and overall cell survival (Fig. 4.15d). As tumour cells often rely on less efficient DNA repair pathways due to common defects or reduced expression of DNA repair factors [2], these vulnerabilities can be exploited in cancer therapy. The results present in this chapter provide further evidence of the regulation of p53 activity during the DNA damage signalling response and could open new clinical opportunities to manipulate these pathways to benefit patient outcomes.

# Chapter 5: Paraspeckle formation during DNA damage requires p53 cofactor JMY.

## 5.1. Introduction

p53 regulates the expression of lncRNA *NEAT1_2* during DNA damage.

Tumour suppressor p53 is an essential transcription factor required during the response to cellular stressors like DNA damage, during which it mainly promotes the activation of protein-coding genes leading to DNA repair, cell cycle arrest or apoptosis [80]. However, p53 not only enhances the expression of protein-coding genes, as several long non-coding RNAs (lncRNAs) have also been identified as p53 targets activated in response to DNA damage (Table 5.1), like the lncRNA *NEAT1* [207,217].

**Table 5.1 Selected p53 target lncRNAs from** [338]

| Target | Principal role | Reference |
|---|---|---|
| *NEAT1** | Formation of paraspeckles | [207] |
| *TUG1** | Promotes cell proliferation | [339] |
| *GUARDIN* | Maintains genomic stability | [340] |
| *lincRNA-p21* | Controls *CDKN1A* expression | [341] |

**Targets differentially expressed during etoposide-induced DNA damage upon JMY depletion in U2OS cells extracted from the transcriptomic results (Fig. 3.4a).*

The human *NEAT1* locus produces two isoforms, the longer *NEAT1_2* transcript (22.7kb) stabilised by a triple helix structure [213] and the shorter polyadenylated *NEAT1_1* isoform (3.7kb) produced through alternative 3'-end processing from *NEAT1_2* [212]. This alternative 3'-end processing is mainly controlled by the CFIm (NUDT21 and CPSF6) and Integrator (INTS11) complexes. The former recognises a tandem of five UGUA sequences upstream of a canonical polyadenylation signal (PAS) promoting *NEAT1_1* expression [212]. The latter interacts with the 3'-end segment, and it is suggested to increase *NEAT1_1* levels by impairing the recruitment of other remodelling complexes [214]; for example, HNRNPK. HNRNPK recognises a pyrimidine-rich region adjacent to the PAS sequence competing for the recruitment of both the CFIm and Integrator complexes to the *NEAT1* transcript, promoting the expression of *NEAT1_2* [212]. p53 is recruited to the *NEAT1* promoter in response to several genotoxic stressors such as DNA damaging agents, reactive

oxygen species accumulation or hypoxia, where it drives the expression of both *NEAT1* isoforms [207,220]. Although DNA damage is described as the primary stressor to induce the p53-driven expression of *NEAT1*, other signalling responses like proteotoxic stress via inhibition of the proteasome can also enhance *NEAT1* expression due to prolonged recruitment of RNA polymerase II and p53 to the *NEAT1* promoter [222].

*NEAT1_2* is a crucial scaffold during the formation of paraspeckles.

Whereas the function of *NEAT1_1* is incompletely understood, *NEAT1_2* is a known architectural scaffold of paraspeckles [188,189]. Paraspeckles are stress-responsive non-membranous subnuclear bodies composed of approximately 50 RNA-binding proteins arranged throughout the *NEAT1_2* transcript. Paraspeckle biogenesis proceeds in two different steps. First, core paraspeckle-associated RNA-binding proteins (*e.g.* NONO and SFPQ) interact with *NEAT1_2* forming an intermediate ribonucleoprotein that favours the aggregation of other *NEAT1_2* molecules. Then, although it is still not well described, additional RNA-binding proteins are recruited to the pre-formed ribonucleoprotein through liquid-phase separation. This, changes the conformation of *NEAT1_2* molecules into a U-shape, leading to the formation of organised liquid-liquid structures presenting an exterior (shell) and interior (core) compartment [208]. The essential role of *NEAT1_2* isoform in paraspeckle biogenesis is shown as *NEAT1* knockout cells fail to form these subnuclear bodies and only the overexpression of *NEAT1_2* isoform can rescue the formation of paraspeckles [212].

Further structural studies using CRISPR/Cas9-mediated genome editing identified several *NEAT1_2* domains required for paraspeckle biogenesis. For example, the complete deletion of the 5'-end domain (0-4.5kb) leads to a reduced number of paraspeckles. Surprisingly, a smaller truncation lacking the first 0-2.8kb abolishes the expression of *NEAT1* (both isoforms) and paraspeckle biogenesis. Additionally, deletion of the 3'-end domain containing the triple helix structure that stabilises *NEAT1_2* leads to its degradation and reduction in paraspeckle detection. Contrarily, the deletion of the *NEAT1* PAS sequence promotes the expression of *NEAT1_2* isoform increasing paraspeckle biogenesis [188,189]. Together, these results suggest that the 5'- and 3'-ends of *NEAT1_2* transcript are required for its expression and stability whereas the *NEAT1* central domain is essential for

promoting the specific expression of *NEAT1_2* and its interaction with paraspeckle-associated components and thus paraspeckle biogenesis [208].

Disruption of paraspeckles modulates tumour response to stress.

Although not completely understood, paraspeckles have an important role in tumour cell fate during stress. For example, the formation of paraspeckles via p53-driven expression of *NEAT1_2* enhances tumour cell survival during genotoxic stress due to decreased cell sensitivity to DNA damaging agents and hypoxic conditions [207,220]. Despite this, the mechanisms by how paraspeckles can reduce cell death upon genotoxic stress remain to be elucidated.

Several studies have proposed that the role of paraspeckles during the DNA damage response may occur through their ability to regulate gene expression [210]. These subnuclear bodies are mainly constructed co-transcriptionally and can interact with active chromatin regions promoting their relaxation leading to increased gene expression [199]. Moreover, during paraspeckle biogenesis, components like SFPQ are sequestered, limiting their availability. This retention has been shown to restrict the transcriptional role of SFPQ either by favouring the expression of *IL-8* in response to immune activation [232] or by hindering the expression of pro-apoptotic targets during proteotoxic stress [222]. Paraspeckles have also been described to retain specific mRNAs presenting inverted Alu (IRAlus) repeats in their 3'-UTR region, which reduces their cytoplasmic translocation and further translation [236]. Lastly, a recent study has proposed that paraspeckles may impact tumour cell fate by modulating alternative splicing both indirectly by sequestering splicing factors and directly via transcriptional activation of spliceosome components [198]. Together, these studies suggest that, during stress conditions, paraspeckles may play an important role in cell fate by controlling gene expression.

Overall, these studies describe the p53-driven expression of *NEAT1_2*, its architectural role in paraspeckle formation and how these subnuclear bodies may modulate tumour cell fate in response to stress. However, further investigation is needed to characterise the regulatory mechanisms that control the p53-mediated activation of *NEAT1_2* during DNA damage, how this may affect paraspeckle biogenesis and whether the formation of these subnuclear bodies can impact the cellular response to stress.

Aim

The overarching aim of this chapter was to investigate the role of JMY in the p53-dependent transcriptional regulation of *NEAT1* and its impact on paraspeckle formation during DNA damage. This section summarises how JMY enhances the recruitment of p53 to the *NEAT1* promoter, leading to the expression of *NEAT1_2* and paraspeckle formation and how disruption of these subnuclear bodies increases cell death in response to genotoxic stress.

## 5.2. Summary of the methodology

U2OS, Saos2 and HAP1 parental and JMY KO cells were cultured in complete growth media supplemented with 5% FBS (v/v) under a humidified environment at 37ºC with 5% $CO_2$. Cells were transfected with JMY, *NEAT1_2* or non-targeting (A*) siRNA (25nM) using Optimem and TransIT-X2 (U2OS cells) or X-tremeGENE (HAP1 cells) transfection reagent for 72h.

To monitor JMY-mediated changes in *NEAT1* expression, RNA was isolated and reverse-transcribed into cDNA using random hexamers and MMLV-RT. RT-qPCR was performed using Brilliant III Ultra-Fast SYBR qPCR and quantified using the $2^{-\Delta\Delta Ct}$ method [295]. Primers to detect total *NEAT1* or specifically *NEAT1_2* are detailed in SI Table 2.4 (Fig. 5.1b).

Paraspeckles were detected by RNA fluorescence *in situ* hybridisation (RNA-FISH) using human *NEAT1* middle segment probes (Fig. 5. 1b). Images were obtained using a Leica Thunder inverted fluorescence microscope with 100x oil immersion lens. Paraspeckles were quantified using CellProfiler [296], data was analysed using *Python* and figures and statistical analysis were performed in GraphPad Prizm 9.0.2. The codes are stored on Dr Amanda S Coutts private repository and are available upon reasonable request.

Cell cycle analysis was performed to measure the percentage of cells undergoing cell death (subG1 phase). Cells were transfected and treated as noted in the figure legends before growth media and adherent cells were collected, fixed and stained with 2% propidium iodide (v/v) in the presence of DNase-free RNase A (125U/mL) before the percentage of cells in subG1 phase was monitored using an Accuri C6 flow cytometer.

## 5.3. Results

JMY influences the p53-mediated expression of lncRNA *NEAT1_2*.

JMY is a cytoplasmic DNA damage-responsive actin nucleator that undergoes nuclear accumulation under specific genotoxic stressors [129,130]. In the nucleus, JMY acts as a transcriptional cofactor enhancing the p53-driven expression of DNA repair genes (Fig. 4.2a) [130]. To explore whether JMY may influence the expression of other p53-dependent targets, a closer inspection of the RNA-seq results (as presented in Fig. 3.4b, c) revealed that the lncRNA *NEAT1* was also differentially expressed (Fig. 5.1a).

The human *NEAT1* locus can express two different transcripts, *NEAT1_2* (22.7kb) or *NEAT1_1* (3.7kb). The latter is produced from *NEAT1_2* through an alternative 3'-end procession, so both isoforms share an identical 5'-end region (3.7kb) [212]. In response to DNA damage, p53 induces the transcriptional expression of both *NEAT1* isoforms [207]. To assess whether JMY influenced the expression of both *NEAT1* transcripts, two primer sets were used, expanding either the region uniquely expressed in *NEAT1_2* (Fig. 5.1b, N1_2) or the section shared between both isoforms (Fig. 5.1b, N1_1).

JMY deficiency reduced the expression of both *NEAT1* isoforms in U2OS cells upon etoposide-induced DNA damage with a marked reduction in the expression of *NEAT1_2* isoform (Fig. 5.1c). These results were recapitulated using HAP1 cells, where the ablation of JMY also resulted in a significant decrease in the expression of *NEAT1_2* transcript (Fig. 5.2a). Conversely, in p53-null Saos2 cells, JMY had little impact on the expression of *NEAT1* transcripts (Fig. 5.1d), suggesting that JMY can modulate the expression of both *NEAT1* isoforms via the p53 response. As described in Chapter 4, to expand our knowledge of the role of nuclear JMY in tumour cells and given the absence of transcriptomic data specific for osteosarcoma models, we conducted a pan-cancer analysis using the data from the TCGA cohort [300]. We identified that patients whose tumours had lower *JMY* mRNA levels presented a marked reduction in the expression of lncRNA *NEAT1* (Fig. 5.1e). Further stratification based on *p53 (TP53)* mutation status revealed that those tumours with reduced *JMY* mRNA levels along with mutant *p53* expression exhibited the lowest *NEAT1* levels (Fig. 5.1e), supporting the role for JMY in the p53-driven expression of *NEAT1*.

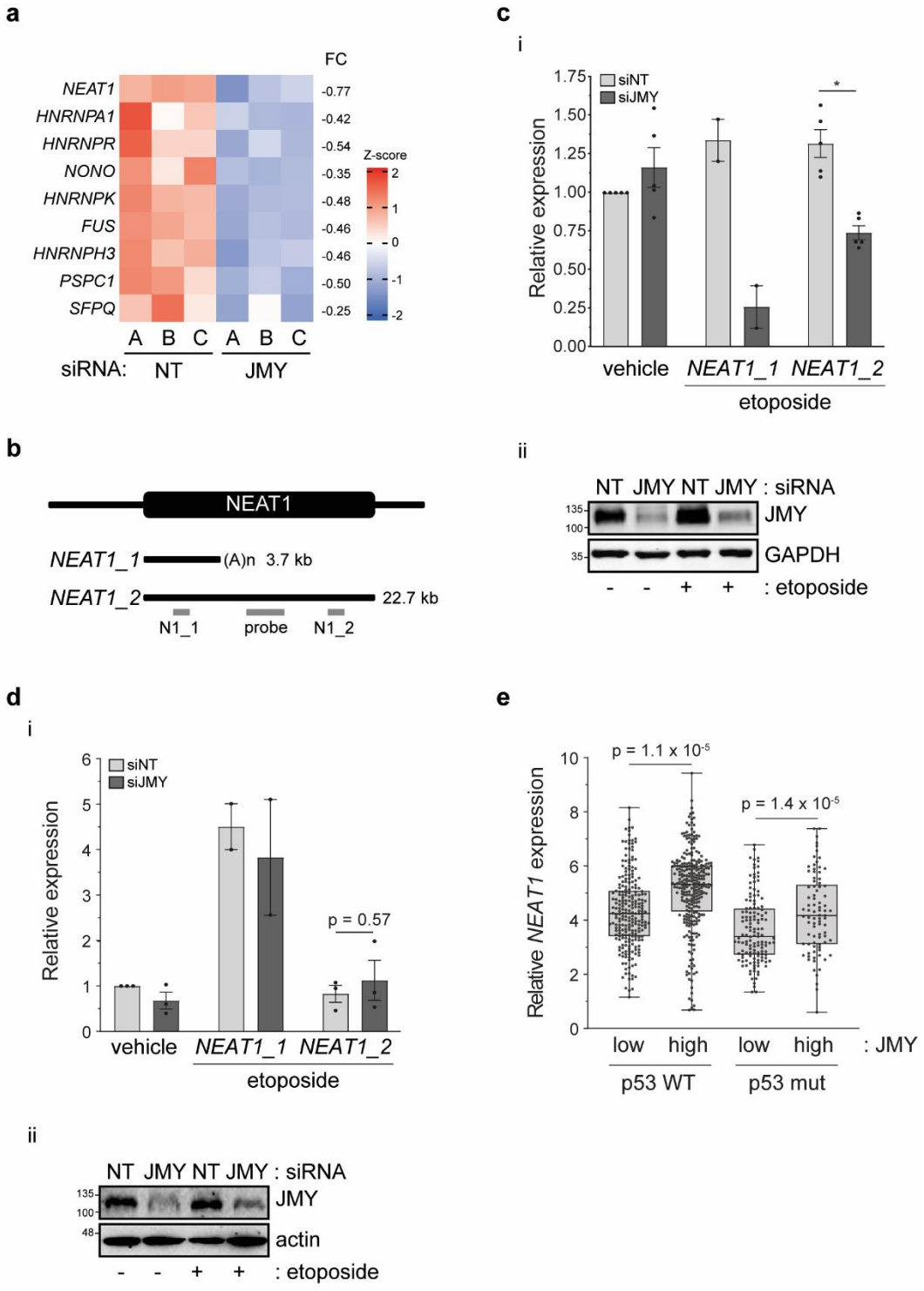


***Figure 5.1. JMY influences the p53-driven expression of NEAT1 transcripts during DNA damage. a)*** *Heatmap represents the relative expression of paraspeckle-associated components from U2OS cells transfected with JMY or non-targeting (NT) siRNA and treated with etoposide (50μM) for 6h. Independent biological replicates are represented with A-C. Changes in gene expression levels*

*are represented as $log_2$(FC). Red = upregulated, blue = downregulated. FDR < 0.05 (False Discovery Rate), FC: Fold-change expression.* ***b)*** *Schematic representation of the NEAT1 locus and the differences between both isoforms. The localisation of the RNA-FISH probe and RT-qPCR primers (N1_1 for NEAT1_1 and N1_2 for NEAT1_2) are shown below.* ***c-d)*** *U2OS* ***(c)*** *and Saos2* ***(d)*** *cells were transfected with JMY or non-targeting (NT) siRNA for 72h and treated with vehicle (-, DMSO) or etoposide (+, 50$\mu$M) for the last 6h. i) Changes in NEAT1 isoform expression are present as fold over vehicle-treated non-targeting transfected cells after normalising with GAPDH (mean ± s.e.m). n = 2-5 independent experiments, and ii) Western blot represents JMY knockdowns.* ***e)*** *Relative NEAT1 expression in tumours stratified by low (EXP < -0.5) versus high (EXP > 0.5) JMY mRNA expression levels and further grouped based on p53 (TP53) mutation status obtained from the TCGA pan-cancer dataset* [300]*. * p < 0.001; unpaired two-tailed Student's t-test. q: q-value (FDR corrected p-value).*

To determine whether the reduced expression of *NEAT1* was derived from JMY's influence on p53 recruitment to *NEAT1* promoter, chromatin immunoprecipitation (ChIP) was performed in the HAP1 cell lines. Our previous work showed that the absence of JMY reduces p53 recruitment to target genes during DNA damage (Fig. 4.5) [130]. Here, HAP1 JMY knockout cells present a significant reduction in p53 recruitment to the *NEAT1* promoter under etoposide treatment conditions (Fig. 5.2b). Together, these results demonstrate that nuclear JMY enhances p53 activity and its recruitment to the *NEAT1* promoter during etoposide-induced DNA damage, and it positively influences the expression of *NEAT1* transcripts.

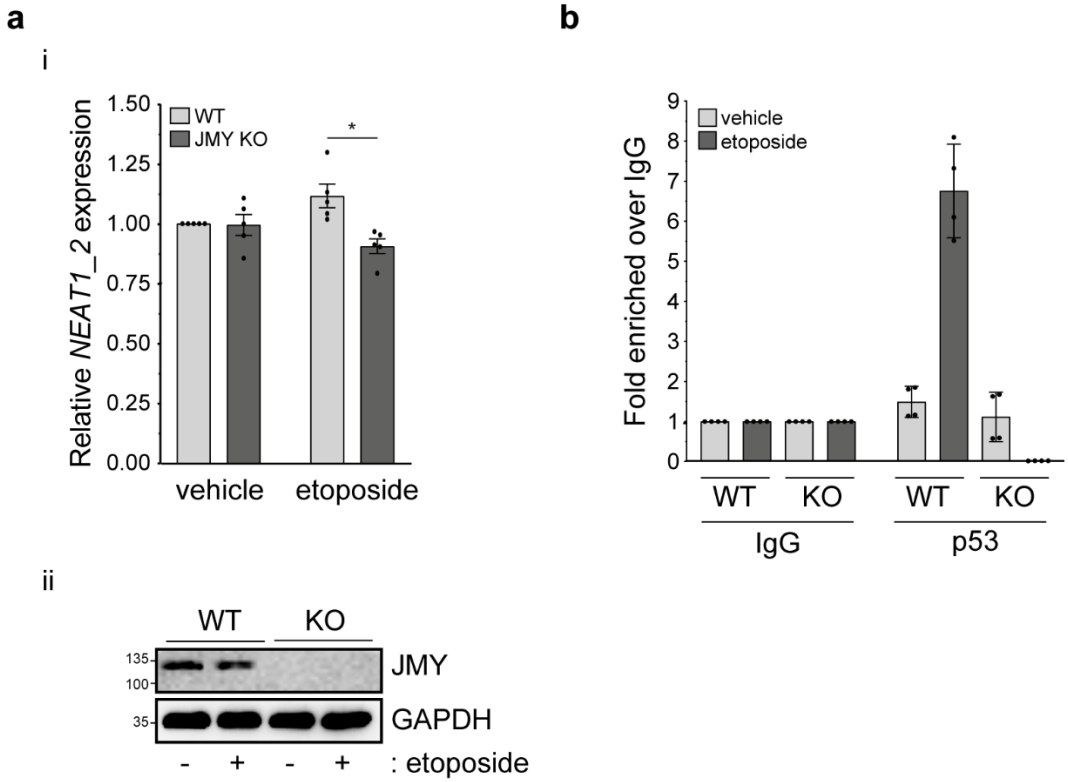


***Figure 5.2. JMY influences the recruitment of p53 to NEAT1 promoter during DNA damage. a)*** *i) HAP1 parental (WT) and JMY knockout (JMY KO) cells were treated with vehicle (-, DMSO) or etoposide (+, 500nM) for 6h. i) Changes in NEAT1_2 expression levels are present as fold over vehicle-treated cells after normalising with GAPDH (mean ± s.e.m). n = 5 independent experiments, and ii) Western blot represents the absence of JMY in HAP1 JMY knockout cells.* ***b)*** *HAP1 parental (WT) and JMY knockout (KO) cells were treated as in* ***(a)*** *before ChIP. qPCR was performed on ChIP chromatin, and results are expressed as fold over IgG (mouse non-specific IgG) after normalising to input levels showing p53 recruitment to NEAT1 promoter (mean ± SD), n = 2 independent experiments, each with quadruplicates (one representative experiment showed). * $p < 0.05$; unpaired two-tailed Student's t-test.*

JMY impacts the formation of paraspeckles during DNA damage.

Although the function of *NEAT1_1* is incompletely understood, the longer *NEAT1_2* isoform is a known architectural scaffold of paraspeckles [188,189]. Paraspeckles are non-membranous subnuclear bodies composed of multiple RNA-binding proteins assembled around *NEAT1_2* [342]. Interestingly, JMY depletion in U2OS cells resulted in a reduced expression of core paraspeckle

components upon etoposide treatment (Fig. 5.1a). Given the fact that the lack of JMY significantly compromised the expression of *NEAT1_2* and paraspeckle-associated proteins suggested that JMY may influence the formation of paraspeckles.

To investigate if JMY could impact paraspeckle biogenesis, RNA-FISH was employed using a probe detecting the middle segment of *NEAT1_2* (3.8-11.7kb, but not *NEAT1_1*) (Fig. 5.1b). As paraspeckles liquid-liquid phase-separated structures [342], to validate their detection, cells were treated with 1,6-hexanediol (1,6-HD), a small molecule that disrupts the multivalent hydrophobic interactions that confine non-membranous bodies [188]. As expected, treatment with 5% 1,6-HD (w/v) severely compromised the detection of paraspeckles (Fig. 5.3), as previously described [188].

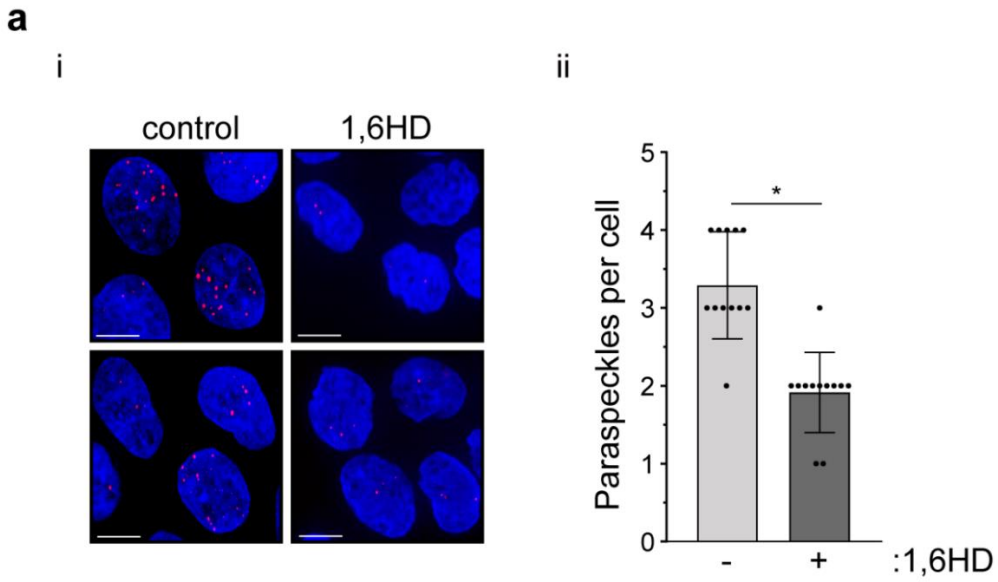


***Figure 5.3. Paraspeckles are phase-separated subnuclear bodies. a)*** *i) HAP1 parental cells were treated 1,6-hexanediol (1,6-HD, 5% w/v) for 5 minutes at room temperature before paraspeckles were detected by RNA-FISH. ii) Graphs represent the number of paraspeckles per cell (mean ± SD) from N ≥ 10 images (N ≥ 100 cells per condition). Scale bar = 10μm. * p < 0.0001; unpaired two-tailed Student's t-test.*

In response to DNA damage, p53 drives the expression of *NEAT1_2* and thus promotes the formation of paraspeckles [207]. Because our results suggested that JMY could modulate the p53-driven expression of *NEAT1_2* (Fig. 5.1c, d; Fig. 5.2a) it was reasoned that the lack of JMY may compromise paraspeckle biogenesis

during etoposide-induced DNA damage. Indeed, siRNA-mediated JMY depletion in U2OS cells decreased the number of paraspeckles upon etoposide treatment (Fig. 5.4a). An increase in the formation of these subnuclear bodies was still visible in non-targeting transfected cells (Fig. 5.4a), supporting previous evidence that paraspeckles are stress-responsive organelles [207]. Similar results were also observed in HAP1 JMY knockout cells, where the absence of JMY reduced the number of paraspeckles (Fig. 5.4b). Surprisingly, paraspeckles biogenesis was also compromised under non-perturbed conditions in these cells (Fig. 5.4b). Moreover, in the absence of p53, JMY depletion had little impact on paraspeckle biogenesis during DNA damage (Fig. 5.4c), providing further evidence of the p53-driven *NEAT1_2*-dependent formation of paraspeckles in response to stress [207]. Together, these results suggest that JMY promotes paraspeckle biogenesis via p53 during etoposide-induced DNA damage.

Paraspeckles promote tumour cell survival during genotoxic stress.

Because paraspeckles can modulate tumour cell sensitivity to genotoxic stressors [207] and given the evidence that JMY could enhance paraspeckle formation upon etoposide treatment (Fig. 5.4), further investigation was conducted to explore the impact of paraspeckles on tumour cell survival in response to genotoxic stress. To explore this, paraspeckles were disrupted via *NEAT1_2* depletion, as previously described [232]. Transfection with *NEAT1_2* siRNA significantly reduced its expression (Fig. 5.5a) and perturbed paraspeckle biogenesis (Fig. 5.5b). Interestingly, short-term *NEAT1_2* depletion decreased cell survival upon treatment with DNA damaging agents like etoposide and 4NQO in both U2OS (Fig. 5.5c) and HAP1 (Fig. 5.5d) cells. Thus, these results provide further evidence that paraspeckles may impact tumour cell survival during genotoxic stress.

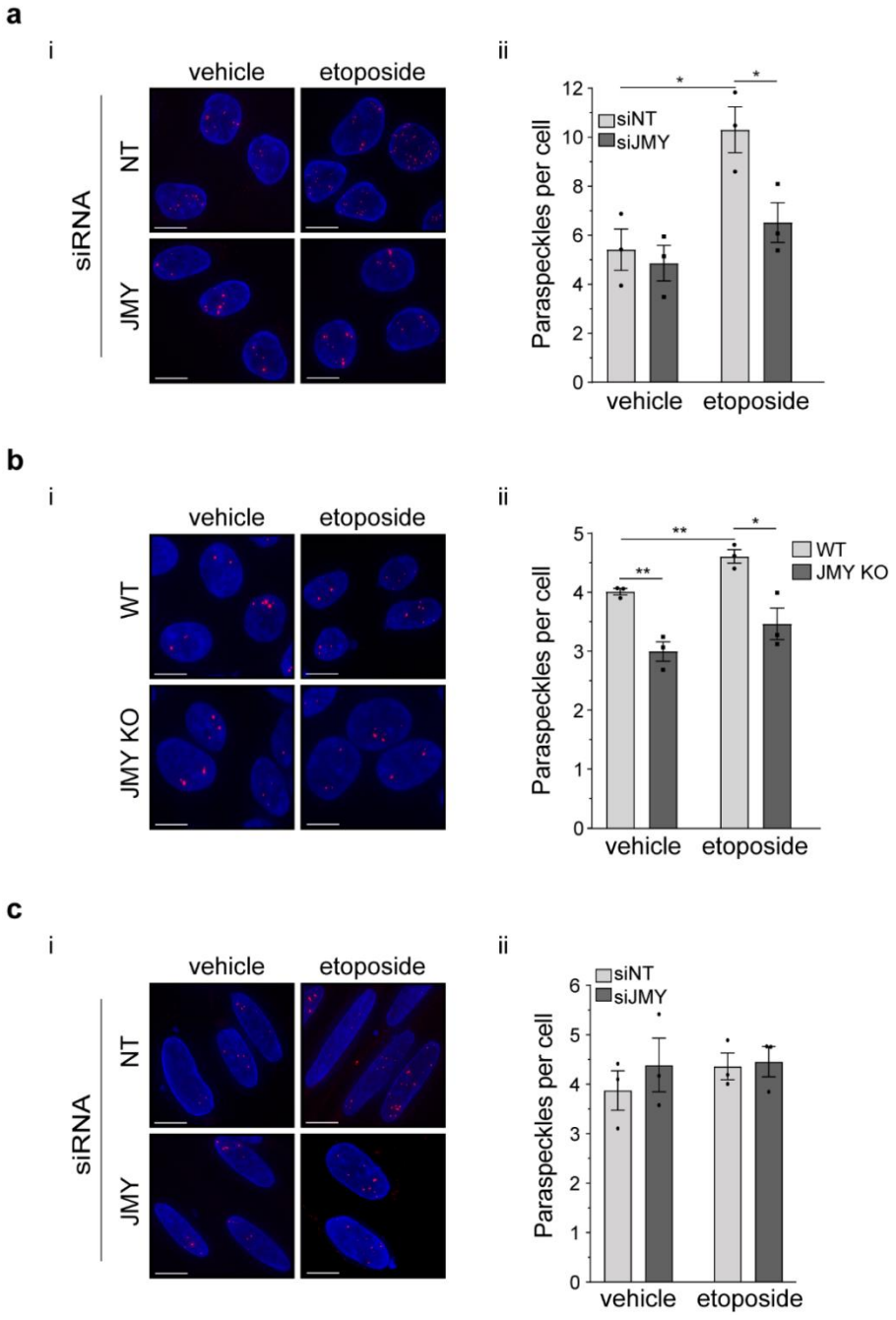


***Figure 5.4. JMY enhances the p53-medited formation of paraspeckles. a)*** *and* ***c)*** *i) U2OS* ***(a)*** *and Saos2* ***(c)*** *cells were transfected with JMY or non-targeting (NT) siRNA for 72h and treated with vehicle (DMSO) or etoposide (50$\mu$M) for the last 6h before paraspeckles were detected by RNA-FISH.* ***b)*** *HAP1 parental (WT) and JMY knockout (JMY KO) cells were treated with vehicle (DMSO) or etoposide (500nM) before paraspeckles were monitored as in* ***(a)****. For* ***a-c)*** (ii) *Graphs represent the number of paraspeckles per cell (mean ± s.e.m), n = 3 independent experiments, each with N ≥ 100 cells per treatment. Scale bar = 10$\mu$m. * p < 0.05, ** p < 0.01; unpaired two-tailed Student's t-test.*

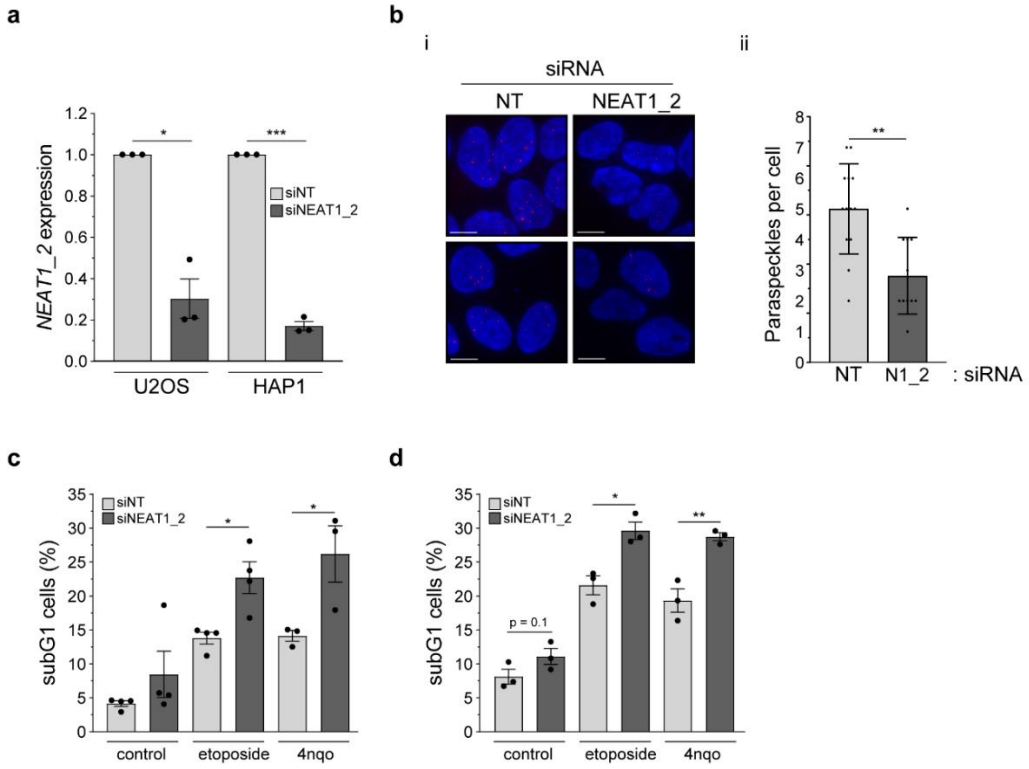


***Figure 5.5. Paraspeckle disruption decreases tumour cell survival during genotoxic stress. a)*** *i) U2OS and HAP1 parental cells were transfected with NEAT1_2 or non-targeting (NT) siRNA for 72h. Changes in NEAT1_2 expression are represented as fold over non-targeting transfected cells after normalising with GAPDH (mean ± s.e.m). n = 3 independent experiments.* ***b)*** *i) U2OS cells were transfected with NEAT1_2 (N1_2) or non-targeting (NT) siRNA for 72h before quantification of paraspeckles. ii) Graphs represent the number of paraspeckles per cell (mean ± SD) from N ≥ 10 individual images (N ≥ 100 cells per condition).* ***c)*** *U2OS cells were transfected with NEAT1_2 or non-targeting (NT) siRNA for 72h and treated with DMSO vehicle (control), etoposide (10μM) or 4nqo (100nM) for the last 30h before collecting for flow cytometry. Graphs represent the percentage of cells in subG1 (mean ± s.e.m.), n = 3-4 independent experiments.* ***d)*** *HAP1 parental cells were transfected as in* ***(c)*** *and treated with DMSO vehicle (control), etoposide (500nM) or 4nqo (50nM) before the percentage of cells in subG1 was monitored as in* ***(c)*** *(mean ± s.e.m.), n = 3 independent experiments. Scale bar = 10μM. * p < 0.05, ** p < 0.01, *** p < 0.001; unpaired two-tailed Student's t-test.*

**Table 5.2. Selected genes that are differentially expressed by both JMY depletion and paraspeckle disruption [198].**

| Gene name | $log_2$(FC)* | -$log_{10}$(q-value)# |
|---|---|---|
| *FUS*$ | -0.5 | 7.5 |
| *HNRNPM*$ | -0.4 | 5.2 |
| *LSM3*$ | -0.4 | 2.4 |
| *GALNT5* | 1.7 | 37.3 |
| *GPNMB* | 1.6 | 52.9 |
| *MYOF* | 1.4 | 22.8 |
| *HR* | -1.8 | 29.0 |
| *STMN3* | -1.0 | 10.3 |
| *SYP* | -1.2 | 4.1 |
| *VGF* | -1.5 | 43.4 |

** Changes in gene expression are represented as fold change and the quantification is explained in more detail in the Material and Methods section. # significant threshold was set as q-value < 0.05 (False Discovery Rate adjusted p-value). $ genes directly involved in splicing.*

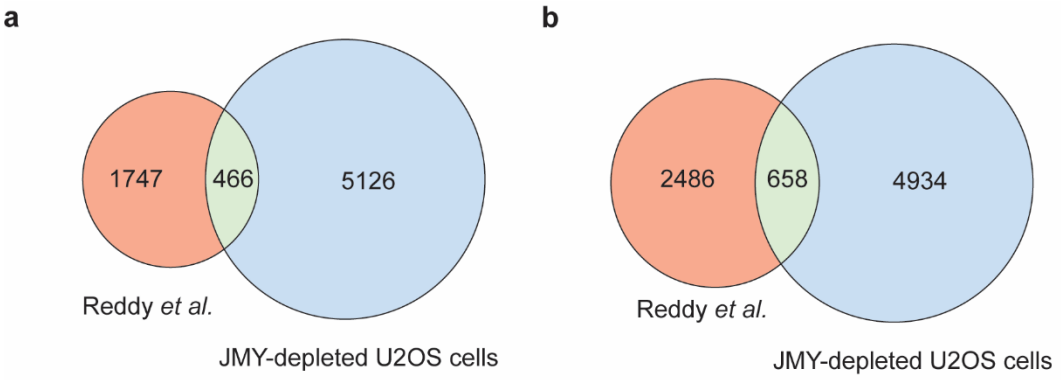


***Figure 5.6. Shared differentially expressed genes deregulated by NEAT1 or JMY depletion in tumour cells.*** *Venn diagrams represent the number of differentially expressed genes overlapping between Reddy and colleagues´ work (NEAT1-depleted cells) [198] and this project (JMY-depleted cells) obtained after comparing RNA-seq **(a)** or CHART-seq datasets **(b)** from [198].*

## 5.4. Discussion

The tumour suppressor p53 plays an important role in paraspeckle biogenesis by promoting the expression of lncRNA *NEAT1_2* [207,217]*.* In this chapter, our results demonstrate that the lack of JMY compromises the formation of paraspeckles by hindering the p53-driven expression of *NEAT1_2* during etoposide-induced DNA damage. Ultimately, the disruption of paraspeckles via *NEAT1_2* depletion decreases tumour cell survival upon genotoxic stress.

JMY is a DNA damage-responsive protein that undergoes nuclear accumulation under specific genotoxic stress conditions [129,130]. Previous studies demonstrated that in the nucleus, JMY could enhance the p53-mediated expression of *BAX* [127] and DNA repair genes (Chapter 4) [130]. Our findings expand the transcriptional cofactor role of nuclear JMY and reveal a novel function during the p53-driven expression of lncRNA *NEAT1*. Notably, p53 induces *NEAT1* expression in response to several stressors. For example, treatment with DNA-damaging agents or hypoxic conditions enhance p53 activation, thus leading to the expression of *NEAT1* transcripts [207,220]. Additionally, other factors such as proteasomal inhibition or Nutlin-3a treatment (blocks the interaction between MDM2 and p53) also stimulate *NEAT1* expression due to prolonged recruitment of p53 to the *NEAT1* promoter [207,222]. Our previous results demonstrated that JMY is required for the recruitment of p53 to target genes (Fig. 4.5) [130], and impairment of JMY's actin nucleation activity could hinder p53-dependent transcription of target genes [127,130]. Interestingly, a growing body of evidence supports the key role of actin in transcriptional regulation [171]; however, we still need to fully understand how actin nucleators like JMY can impact p53 activity and whether changes in actin recruitment or actin nucleation can modulate p53-dependent transcription at *NEAT1* promoter.

The human *NEAT1* locus produces two isoforms, *NEAT1_1* (3.7kb) and *NEAT1_2* (22.7kb), where the former is obtained through alternative 3'-end processing from *NEAT1_2* [212]. While p53 stimulates the expression of both *NEAT1* isoforms upon various forms of stress, including DNA damage [207], *NEAT1_2* transcriptional levels are typically higher than *NEAT1_1* [207,214,217]. Although incompletely understood, several factors are involved in the alternative 3'-end processing of *NEAT1_2* balancing the expression of *NEAT1* isoforms. For example, the CFIm and Integrator complexes and TDP-43 can interact with *NEAT1* polyadenylation signal

(PAS), leading to transcriptional termination promoting the expression of *NEAT1_1* [212,214,215]. Contrarily, HNRNPK and HRNRPM can interact with the PAS flanking regions competing with *NEAT1_1* promoting factors leading to the expression of *NEAT1_2* [212]. Although these factors can modulate *NEAT1* isoform-specific expression, their functionality during DNA damage (conditions where *NEAT1_2* expression is favoured) has not been fully characterised. Our transcriptomic results indicated that during etoposide-induced genotoxic stress, JMY depletion in U2OS cells compromises the expression of several of these factors, including CFIm complex catalytic subunits (NUDT21, CPSF6), TDP-43 and both HNRNPK and HNRNPM (Fig. 3.4a, b). These results might suggest that during DNA damage, JMY could also modulate the expression of specific *NEAT1* isoforms via transcriptional regulation of these isoform-specific promoting factors. It will be relevant to future studies to explore the regulatory mechanisms by which JMY can control the expression of these targets and whether their balance impacts the expression of *NEAT1* isoforms, contributing to our understanding of *NEAT1* isoform-specific expression during stress and its impact on cellular outcomes.

While the function of *NEAT1_1* remains unclear, *NEAT1_2* is an established architectural scaffold of paraspeckles [188,189]. Paraspeckles are stress-responsive non-membranous subnuclear bodies constituted by multiple RNA-binding proteins attached throughout *NEAT1_2* [208]. A growing body of evidence showed that paraspeckles form in response to different stressors via transcriptional expression of *NEAT1_2*, and it has also been suggested that these subnuclear bodies can promote tumour cell survival during genotoxic stress [207]. However, the precise molecular mechanisms underlying how paraspeckle formation leads to increased cell viability during genotoxic stress remain to be elucidated. Our data supported a role for JMY in the *NEAT1_2*-dependent formation of paraspeckles in response to DNA damage (Fig. 5.4) and suggested a key role for these subnuclear bodies in promoting cell survival (Fig. 5.5). However, further studies are required to provide an improved mechanistic understanding of JMY's role in paraspeckle biogenesis and its implication in cell survival during DNA damage.

Recently, paraspeckles were shown to play an important role in alternative splicing both indirectly by sequestering splicing factors and directly via transcriptional activation of spliceosome components [198]. Even though previous work demonstrated that DNA damage promotes paraspeckle biogenesis [207] and impacts alternative splicing [325], whether these two processes are connected has yet to be

described. It is likely that these two processes modulate each other as paraspeckles are localised in close proximity to splicing speckles [209], which may suggest that splicing factors can be exchanged between these non-membranous bodies. Additionally, both the formation of paraspeckles and the spliceosome assembly mainly occur co-transcriptionally and are conditioned by the transcriptional rate of RNA polymerase II [199,343]. Further research is required to determine whether there is a link between alternative splicing and paraspeckles and if these structures must colocalise maybe within transcriptional hubs. Our results indicate that JMY can influence the expression of several paraspeckle-associated (Fig. 5.1a) and core spliceosome (Fig. 6.2a) components as well as genes that have been previously proposed to be transcriptionally regulated by paraspeckles (Table 5.2; Fig. 5.6) [198]. Interestingly, our transcriptomic data also supported a role for JMY in modulating splicing (Chapter 6) leading to the formation of alternatively spliced transcripts that were also described when paraspeckle biogenesis was compromised via *NEAT1_2* depletion (Table 6.1; Fig. 6.7) [198]. However, whether the JMY-mediated formation of paraspeckles influences splicing remains to be elucidated. Together, these findings further exacerbate the complexity of JMY's nuclear regulatory network and suggest that paraspeckles and splicing could be intricately connected through JMY.

Together, the results present in this chapter suggest a novel role for JMY in the formation of paraspeckles through impacting the p53-dependent transcriptional regulation of *NEAT1_2*. Our data also indicate that paraspeckle disruption via *NEAT1_2* depletion increases tumour cell death during DNA damage. Tumour cells commonly induce the formation of paraspeckles in response to genotoxic stress, which, although incompletely understood, increases resistance to the DNA damaging agent [207]. Thus, our results provide further insights into the nuclear regulatory network of JMY and p53, which could lead to clinical opportunities to manipulate the p53-dependent formation of paraspeckles and its impact on cellular outcomes.

# Chapter 6: JMY modulates alternative splicing during DNA damage.

## 6.1. Introduction

The spliceosome orchestrates alternative splicing.

Splicing is an essential posttranscriptional modification in which the introns (non-coding sequences) of pre-mRNAs are removed, leading to the formation of mature mRNA transcripts retaining the collection of exons (coding sequences) [238]. Splicing is a constitutive cellular process orchestrated by the spliceosome, a multiprotein complex composed of five small nuclear ribonucleoproteins (snRNPs: U1, U2, U4, U5 and U6) and a broad collection of regulatory factors [238]. In eukaryotic cells, there are two spliceosomal complexes: the U2-dependent spliceosome, which is responsible for 99% of intron removals and the U12-mediated machinery which controls the remaining splicing events [239]. In order for the spliceosome to recognise and remove non-coding regions, introns are defined by short conserved motifs at the flanking edges called splice sites (5'SS and 3'SS), a conserved adenosine branch point (BS) and a polypyrimidine tract (PPT) located towards the end of the intron [240].

Splicing is a stepwise process and, as mentioned above, is controlled by the spliceosome. The assembly of the spliceosome is initiated by the recruitment of the U1 snRNP to the 5'SS, followed by recognition of the BS-PPT and 3'SS by SF1 and U2AF subunits, respectively (E complex, Fig. 1.9a). The interaction of SF1 and U2AF directs the U2 snRNP to the BS leading to the release of SF1 and U2AF (A complex, Fig. 1.9b). Then, the pre-assembled U4/U6.U5 tri-snRNPs is recruited to the spliceosomal machinery (pre-B complex, Fig. 1.9c), where the 5'SS is transferred to the U5/U6 complex leading to the disassociation of U1/U4 snRNPs forming the catalytically active spliceosome ($B^{act}$ complex). Intron removal is then conducted in a two-step transesterification reaction (B* and C complexes, Fig. 1.9d). First, there is a nucleophilic attack of the 5′SS by the adenosine BS that results in the formation of an intron lariat and the release of the upstream exon (Fig. 1.9e). Second, the released exon attacks the 3'SS connecting the upstream and downstream exons and liberating the intron lariat with attached spliceosomal components (post-spliceosomal complex, Fig. 1.9f). Finally, U2, U5 and U6

snRNPs and the remaining auxiliary factors are detached and recycled for a new splicing cycle (reviewed in [238]).

The aforementioned splicing process is referred to as canonical splicing and consists of the processing of all transcribed introns and exons from a particular pre-mRNA [240]. Besides, the spliceosome can also modulate different exon rearrangements, intron retentions and the use of non-conventional 5'SS and 3'SS, which increases the diversity of mRNA isoforms. This non-canonical processing is known as alternative splicing and can occur in over 95% of human genes [252].

RNA splicing deregulation as a tumour hallmark.

Alternative splicing is a tightly controlled process; hence its deregulation has been associated with human disorders like tumour formation and progression [251]. Interestingly, most human cancers exhibit widespread splicing abnormalities, which commonly leads to the use of variable exonic regions or frequent retention of introns. These abnormal splicing events can alter the expression of specific transcript isoforms and can lead to the reduced expression of tumour suppressors or enhanced expression of oncogenes [258]. Typically, tumour-related splicing deregulation arises from the aberrant expression of spliceosomal components (*trans*-acting factors) or due to mutations in the conserved splice sites from the pre-mRNA molecule being processed (*cis*-acting factors) [251].

Interestingly, across several human tumours, mutations often occur in core spliceosomal components related with early steps of the spliceosome assembly, like within the U2 snRNP subunit [259]. SF3B1 (factor within the U2 snRNP) is the most frequently mutated splicing factor in human cancers, where most of the mutations affect its ability to recognise the adenosine BS required for the A complex assembly resulting in widespread splicing alterations [260]. Mechanistically, mutations in SF3B1 generally lead to intron retention events which impact on the expression of genes involved in the DNA damage response and cell proliferation [261]. In addition, altered expression of other U2 snRNP-related factors (*e.g.* PHF5A and SF3B6) in human tumours can induce deregulation in alternative splicing [344]. Due to this aberrant alternative splicing processing, tumour cells present a more varied transcript repertoire than non-malignant cells, and these tumour-specific transcripts can provide an advantage to tumour cells, enhancing their development and progression [258].

Therapeutic strategies to target the spliceosome in human cancers.

Interestingly, the vast majority of the mutations in *trans*-activating splicing factors are heterozygous and mutually exclusive; thus, at least one wild-type allele is necessary to support tumour cell survival. This makes the spliceosome a good therapeutic candidate for treating human tumours [270]. The most common approach is to target core spliceosome subunits, and SF3B1 has become the primary focus due to its crucial role in the early assembly of the spliceosome [243].

Several small molecule inhibitors targeting the spliceosome have been developed, including pladienolide B (plad B) and its derivatives [271]. Mechanistically, plad B intercalates in the tunnel-shape region between the HEAT domain of SF3B1 and two residues from PHF5A ($Y^{36}$ and $R^{38}$) within the U2 snRNP. In particular, the interaction of plad B stalls SF3B1 into an 'open' conformation which impedes further conformation changes required to enclose the HEAT domain of SF3B1 and subsequent recognition of the adenosine BS [272]. Interestingly, the inhibition of SF3B1 through plad B has been shown to induce widespread intron retention [273], impair cell proliferation and increase cell death [276,278]. However, resistance to plad B and its derivatives have already been described in tumours, specifically in those presenting SF3B1 and PHF5A mutations (*e.g.* $SF3B1^{R1074H}$ or $PHF5A^{Y36C}$ ) [280]. To overcome tumour resistance towards SF3B1 inhibition, new splicing inhibitors have been developed, such as isoginkgetin. This *Ginkgo biloba* derivative presents a broader spliceosomal inhibitory action by impeding the recruitment of the U4/U6.U5 tri-snRNP to the A complex [282]. Interestingly, isoginkgetin is able to reduce tumour cell proliferation and survival [278,345], lessen cell invasion [346] and increase cell sensitivity to metabolic stress [285]. Despite this, isoginkgetin is highly cytotoxic and presents restricted delivery due to its high hydrophobicity, which limits its use in clinical studies [287].

In summary, several studies started to characterise the tumour-specific deregulation of alternative splicing. However, the regulatory mechanisms that govern spliceosome assembly or the functions of the spliced products remain to be elucidated.

Aim

The overarching aim of this chapter was to investigate JMY-mediated changes in the expression of spliceosome components and their impact on alternative splicing during DNA damage. This section summarises the role of JMY during the expression of U2 snRNP-related components, its impact on alternative splicing during DNA damage and the role of nuclear JMY on tumour cell fate during treatment with spliceosome inhibitors.

## 6.2. Summary of the methodology

U2OS and HAP1 parental and JMY KO cells were cultured in complete growth media supplemented with 5% FBS (v/v) under a humidified environment at 37ºC with 5% $CO_2$. U2OS cells were transfected with JMY or non-targeting (A*) siRNA (25nM) using Optimem and TransIT-X2 transfection reagent for 72h before being treated, as noted in the figure legends.

To monitor JMY-mediated changes in transcript expression, RNA was isolated and reverse transcribed into cDNA using oligo (dT) primers and MMLV-RT. RT-qPCR was performed using Brilliant III Ultra-Fast SYBR qPCR and quantified using the $2^{-\Delta\Delta Ct}$ method [295]. In addition, changes in protein levels were monitored by western blotting, where cells were lysed in TNN buffer before protein extracts were separated using mini SDS-PAGE gels. Then, proteins were transferred into a nitrocellulose membrane, incubated with the appropriate antibodies as required and bands were visualised by enhanced chemiluminescence (ECL).

Cellular outcomes derived from the JMY-mediated decrease in spliceosomal components included cell proliferation assays. Briefly, cells were transfected and treated as noted and imaged every 2-4h for 72h. Quantification was performed by masking the phase contrast cell confluence after normalising against time zero images using the IncuCyte S3 live-cell analysis system.

To explore JMY-derived changes in splicing, RNA-seq samples were prepared as described in Chapter 3 and analysed using Galaxy [320]. Paired-end reads were mapped against the reference genome using 2-pass STAR [311] and output BAM files were used to monitor differentially spliced events using EventPoint [313,347]. Alternative splicing events were validated *in-vitro,* where RNA was extracted and

reverse transcribed into cDNA as described before. RT-PCR amplified samples were separated using a 1-2% agarose gel stained with SYBR™ Safe. Finally, bands were visualised and quantified using a ChemiDocTM XRS+ and Fiji/ImageJ [290], respectively.

## 6.3. Results

JMY influences the expression of U2 snRNP-related spliceosomal components.

The results present in Chapter 3 indicated that splicing could be affected upon JMY depletion during DNA damage (Fig. 3.4c). JMY is a DNA damage-responsive actin nucleator that significantly undergoes nuclear accumulation under specific genotoxic stress conditions [127,130]. Other actin nucleators have also been described to accumulate in the nucleus like WASP, a close family member of JMY, where it impairs the expression of several splicing factors through its association with chromatin [269]. As described in Chapter 3, JMY could modulate the expression of a wide range of spliceosomal components (Fig. 3.4c). Closer inspection revealed that there was an enrichment of genes related to the U2 snRNP subunit with the vast majority of targets being downregulated with JMY depletion (Fig. 6.1a).

These RNA-seq results were validated showing that JMY-depleted U2OS cells present reduced expression of *PHF5A*, *SF3B6* and *SF3A3*, which are core spliceosomal components of the U2 snRNP subunit. In contrast, JMY depletion had a minor impact on the expression of the auxiliary factor *SF3B2* (Fig. 6.1b). Interestingly, this was also reflected in changes in protein expression, as seen by a reduction in both PHF5A and SF3B6 levels upon siRNA-mediated JMY depletion (Fig. 6.1c, d). The impact of JMY on the expression of U2 snRNP-related splicing factors was not restricted to a single cell type, as similar results were observed when comparing HAP1 parental and JMY knockout cells. The ablation of JMY resulted in decreased transcript expression of U2 snRNP factors (Fig. 6.1e), which was reflected in lowered PHF5A and SF3B6 protein levels (Fig. 6.1f). Together, these results suggest that JMY is required for the expression of U2 snRNP-related splicing factors during DNA damage.

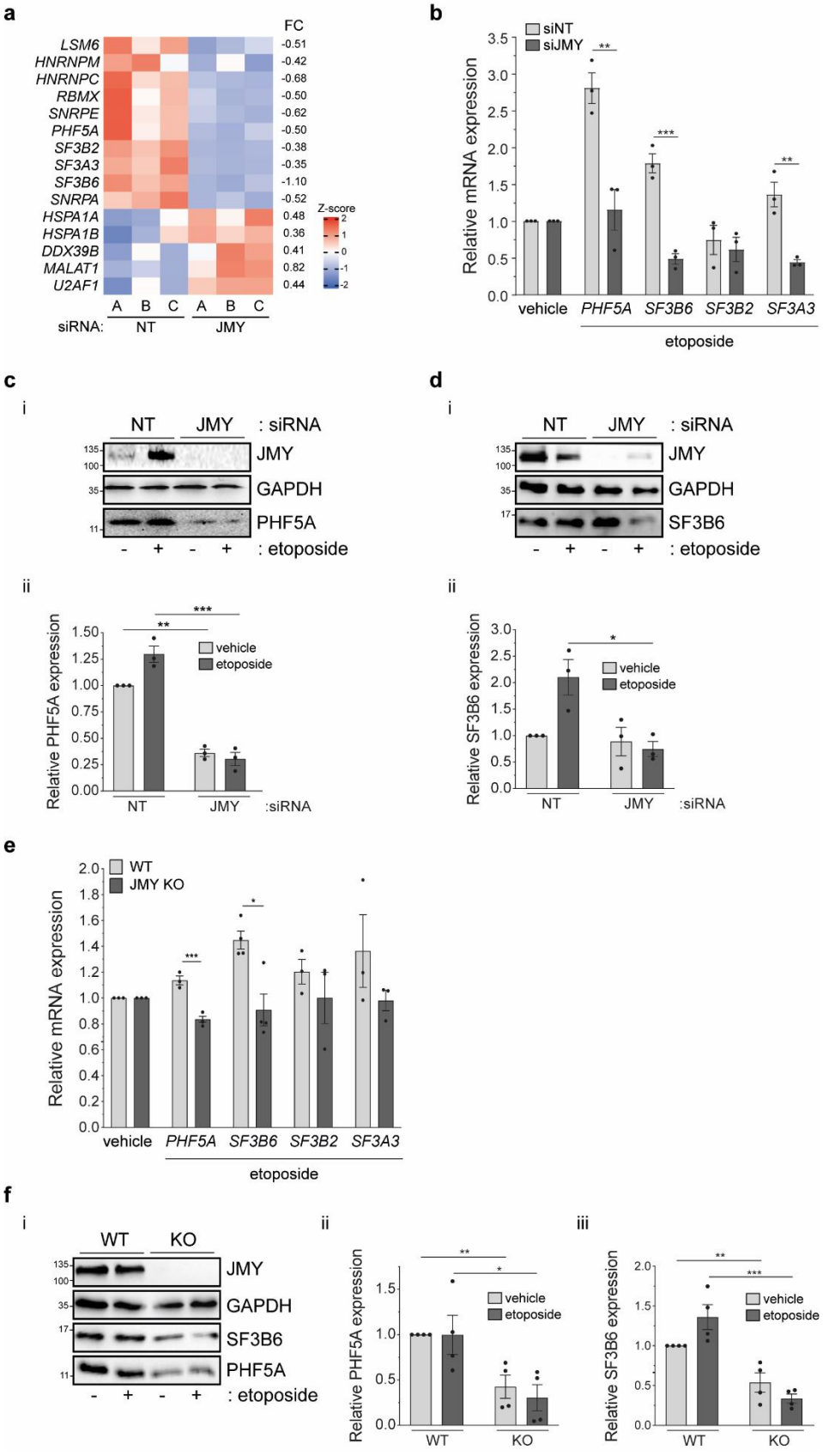


***Figure 6.1. JMY-mediated expression of U2 snRNP-related spliceosomal factors. a)*** *Heatmap showing the relative expression of spliceosome components*

*when comparing U2OS cells transfected with JMY or non-targeting (NT) siRNA after treatment with etoposide (50μM) for 6h. Independent biological replicates are represented with A-C. Changes in gene expression levels are represented as $log_2$(FC). Red = upregulated, blue = downregulated. FDR < 0.05 (False Discovery Rate), FC: fold-change expression.* ***b)*** *U2OS cells were transfected with JMY or non-targeting (NT) siRNA for 72h and treated with vehicle (DMSO) or etoposide (50μM) for the last 6h. Changes in gene expression are present as fold over vehicle-treated cells after normalising with GAPDH (mean ± s.e.m). n = 3 independent experiments.* ***c)*** *and* ***d)*** *i) U2OS cells were transfected and treated with vehicle (-, DMSO) or etoposide (+, 50μM) for 6h and ii) protein expression of PHF5A* ***(c)*** *and SF3B6* ***(d)*** *were monitored. Graph represents expression levels after normalising with GAPDH (mean ± s.e.m). n = 3 independent experiments.* ***e)*** *HAP1 parental (WT) and JMY knockout (JMY KO) cells were treated with vehicle (DMSO) or etoposide (500nM) for 6h. Changes in gene expression are present as fold over vehicle-treated cells after normalising with GAPDH (mean ± s.e.m). n = 3-4 independent experiments.* ***f)*** *i) HAP1 parental and JMY knockout (KO) cells were treated vehicle (DMSO) or etoposide (500nM) for 6h before protein expression of PHF5A (ii) and SF3B6 (iii) were monitored. Graphs represent expression levels after normalising with GAPDH (mean ± s.e.m). n = 4 independent experiments. * p < 0.05, ** p < 0.01, *** p < 0.001; unpaired two-tailed Student's t-test.*

<u>EventPointer detection of alternative splicing events</u>

Deregulated expression of SF3B6 and PHF5A in tumour cells has been described to modulate alternative splicing [263,267]. Given that JMY impacted on the expression of U2 snRNP factors, it was hypothesised that JMY may modulate overall alternative splicing. To investigate this, the RNA-seq samples obtained in Chapter 3 (Fig. 3.2a) were aligned to the human reference genome using 2-pass STAR [311]. The quality of the mapping strategy was assessed, showing that over 80% of reads were aligned to the genome (Fig. 6.2a), from which the vast majority present a unique mapping site (~75%). These results were comparable to those obtained using TopHat2 (Fig. 3.2b, c) and showed a large proportion of aligned reads as expected from well-annotated genomes [306]. Interestingly, this mapping results also showed a uniform read coverage across the transcript length (Fig. 6.2b), reemphasising the high-quality RNA used during the cDNA library preparation.

Like TopHat2, STAR executes a two-pass mapping strategy in which a preliminary alignment step defines the reads mapped with exonic regions. Then, using this 'reference' annotation, STAR maps the remaining reads to identify exon-exon junctions [311]. Interestingly, the alignment results showed that over 80% of reads mapped with exonic regions, whereas 5% of those reads expanded exon-exon junctions (Fig. 6.2c). From the latter, approximately 75% reported known or predicted splice sites leaving an outstanding 25% of reads presenting non-canonical junctions (Fig. 6.2d). Interestingly, these results were similar to those reported when using TopHat2 (Fig. 3.2e). Surprisingly, the remaining 10-15% of reads were exclusively identified at introns (Fig. 6.2c). The higher proportion of reads covering intronic regions and presenting novel exon-exon junctions when compared with typical transcriptomic results performed in human tumour cells [322], supported the idea that JMY-mediated changes in splicing factors could be modulating splicing during DNA damage.

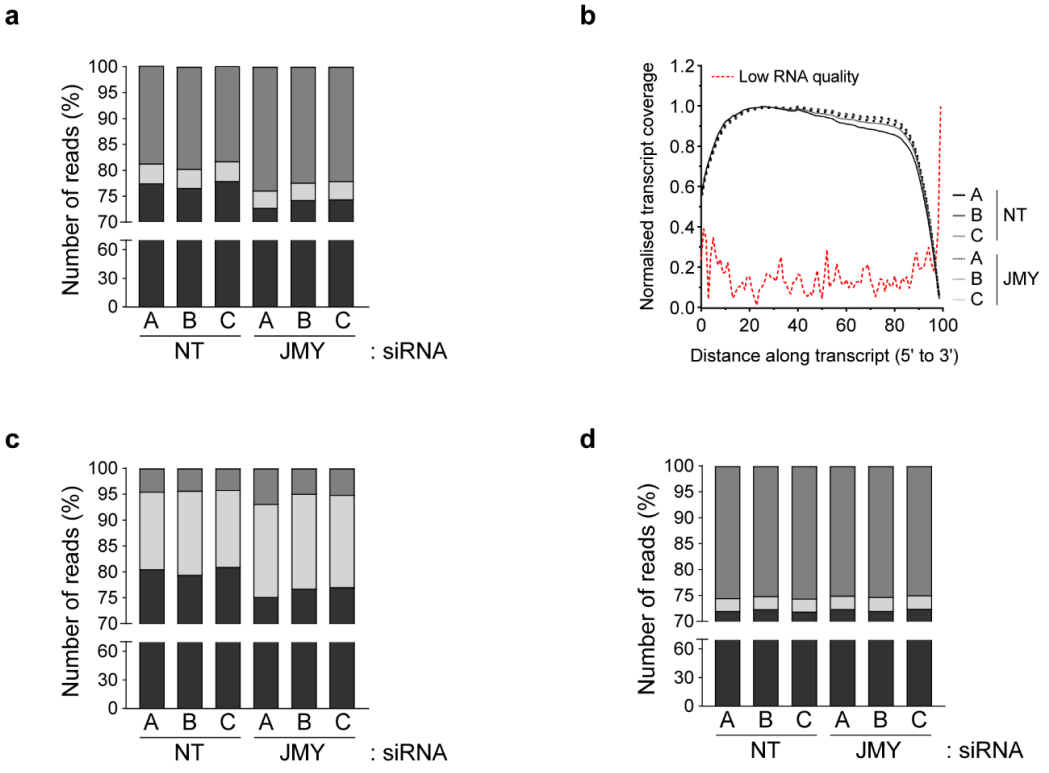


***Figure 6.2. 2-pass STAR alignment results. a)*** *Distribution of mapped reads presenting a unique (black) or multiple (light grey) alignment regions. Paired-end reads presenting a conflicting alignment (dark grey) were discarded for further analysis.* ***b)*** *Uniform distribution of reads' coverage across the transcript length. A red dotted line represents a theoretical example of low-quality RNA used to prepare*

*the cDNA library.* ***c)*** *Mapping results showing the distribution of reads aligned with exonic (black), intergenic (dark grey) or intronic (light grey) regions.* ***d)*** *Distribution of reads expanding exon-exon junctions presenting known (black), novel (dark grey) or predicted (light grey) splice sites. RNA-seq was performed in U2OS cells transfected with JMY or non-targeting (NT) siRNA after treatment with etoposide (50*$\mu$*M) for 6h. n = 3 independent biological repeats (A-C).*

JMY modulates alternative splicing during DNA damage.

A bioinformatic pipeline using EventPointer R package [313] was developed to monitor JMY-derived changes in alternative splicing (Fig. 6.3a). First, the workflow was benchmarked using Vidaković and colleagues' dataset (GSE143542: 24h UV-treatment results) [315]. Their original sequencing files were mapped to the reference genome using 2-pass STAR, and the output BAM files were then run through our script. As in their original work, our bioinformatic pipeline also identified the top three alternative splicing events induced by UV radiation, including *CHMP2B, DHPS* and *ARL5A* (Fig. 6.3b), validating the script developed in this project.

Our pipeline was then used to explore JMY-mediated changes in alternative splicing. Surprisingly, the siRNA-mediated JMY depletion in U2OS cells resulted in 633 alternatively spliced events (q-value < 0.01) (Fig. 6.3c), of which approximately half of them were reported as complex events (Fig. 6.3c). The complex event results could arise due to EventPointer functionality, as when two or more events occur nearby, the algorithm is not able to individually distinguish them, categorising the whole segment as a 'complex event' [347]. Pathway enrichment analysis was conducted using the JMY-mediated alternatively spliced events to explore the molecular functions in which these targets could be involved. Interestingly, enrichment analysis showed defects in RNA processing pathways, including mRNA surveillance and the spliceosome itself (Fig. 6.3d), suggesting that JMY might have a dual regulatory mechanism over splicing both by controlling the transcriptional expression of spliceosomal components (Fig. 3.4c; Fig. 6.1) as well as modulating the expression of different splicing factor isoforms which can alter their functionality (Fig. 6.3d). These results increase the complexity of JMY's nuclear role during DNA damage further from its original p53 cofactor role [104,127].

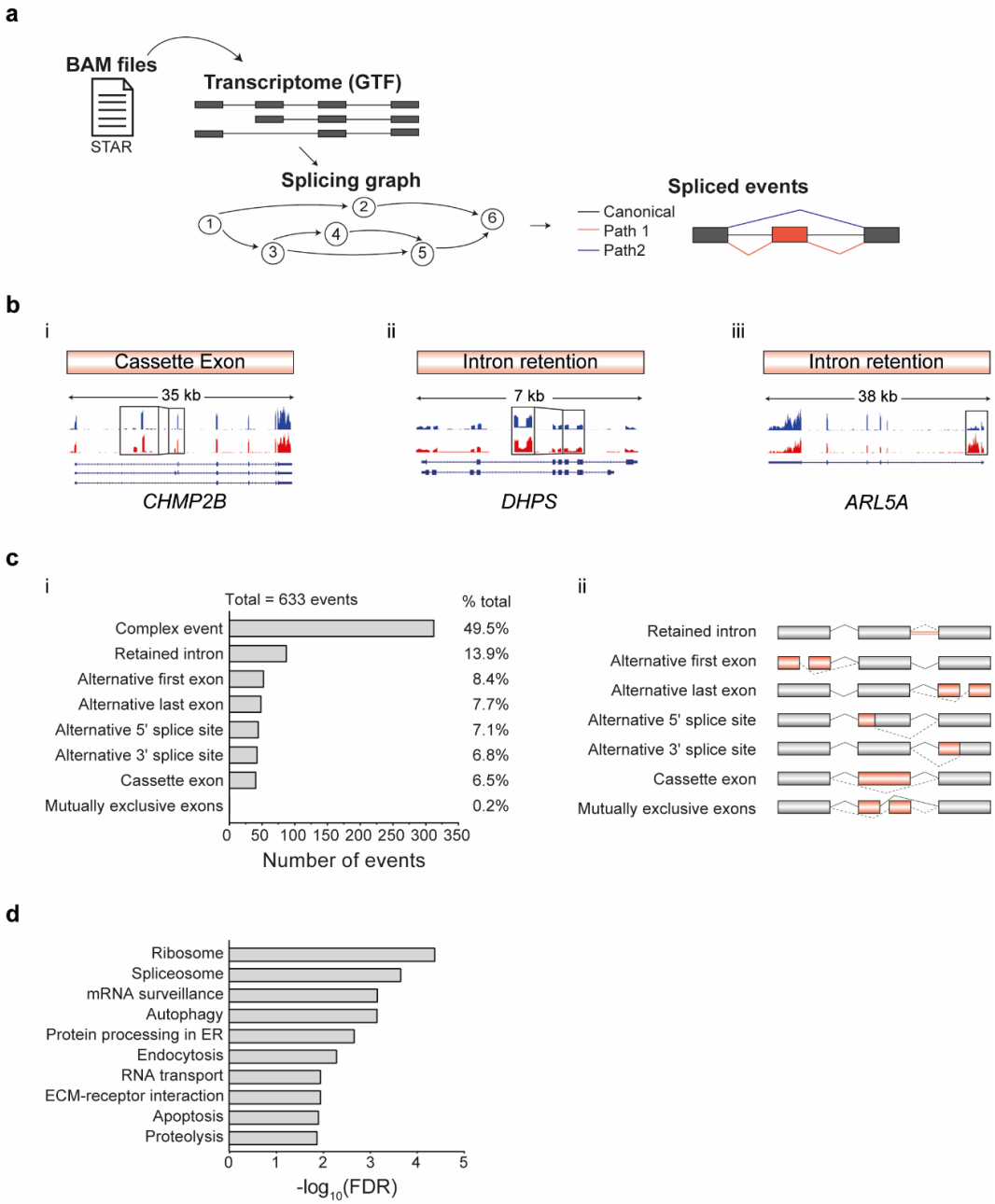


***Figure 6.3. EventPointer alternative splicing results. a)*** *Schematic representation of the EventPointer script developed in this project. Briefly, BAM files obtained from 2-pass STAR were compared against a reference transcriptome obtaining a splice graph which defines different paths (splicing events) compared with the canonical isoform.* ***b)*** *Alternative splicing events from Vidaković and colleagues' work* [315] *were validated with the script developed in this project. Results show a cassette exon event at CHMP2B sixth exon (i) or retained intron events in DHPS second intron (ii) and ARL5A first intron (iii) as reported the original work* [315]*.* ***c)*** *i) JMY-mediated alternatively spliced events occurring in U2OS cells transfected*

*with JMY or non-targeting siRNA and treated with etoposide (50μM) for 6h. Results were obtained using EventPointer from n = 3 independent experiments (q-value < 0.01). ii) Schematic representation of the most common splicing events where coloured rectangles represent spliced exons or introns and dotted lines represent the splicing event.* ***d)*** *Selected enriched KEGG pathways obtained from the list of alternatively spliced targets (ci). The threshold was set as Benjamini-Hochberg FDR < 0.05.*

Because the results present in this section suggested that JMY could modulate alternative splicing, several of these alternatively splicing events were investigated. Interestingly, the depletion of JMY in U2OS cells caused a marked increase in the removal of exon 6 and exon 36 in *TNFSF12* and *MED12L* (Fig. 6.4a, b), respectively, and promoted the partial retention of intron 1 in *DIABLO* (Fig. 6.4c). These events present a positive percent spliced in index (ΔPSI) indicating that the ratio between reads including or excluding the event were higher in JMY-depleted cells. To ensure that the pipeline developed in this project was also correctly measuring events with ΔPSI < 0 (higher proportion in non-targeting transfected cells), splicing events in *MACF1* and *MDM4* were monitored. Interestingly, isoform analysis showed a lower retention of exon 53 in *MACF1* and a higher exon 6 retention in *MDM4*, indicating that the pipeline was also correctly recognising ΔPSI < 0 events (Fig. 6.5a, b). The impact of JMY on these splicing events was not restricted to a single cell type, as similar results were also observed in HAP1 JMY knockout cells (Fig. 6.4d-f and Fig. 6.5c, d). Together, these results suggest that JMY is able to modulate splicing during DNA damage.

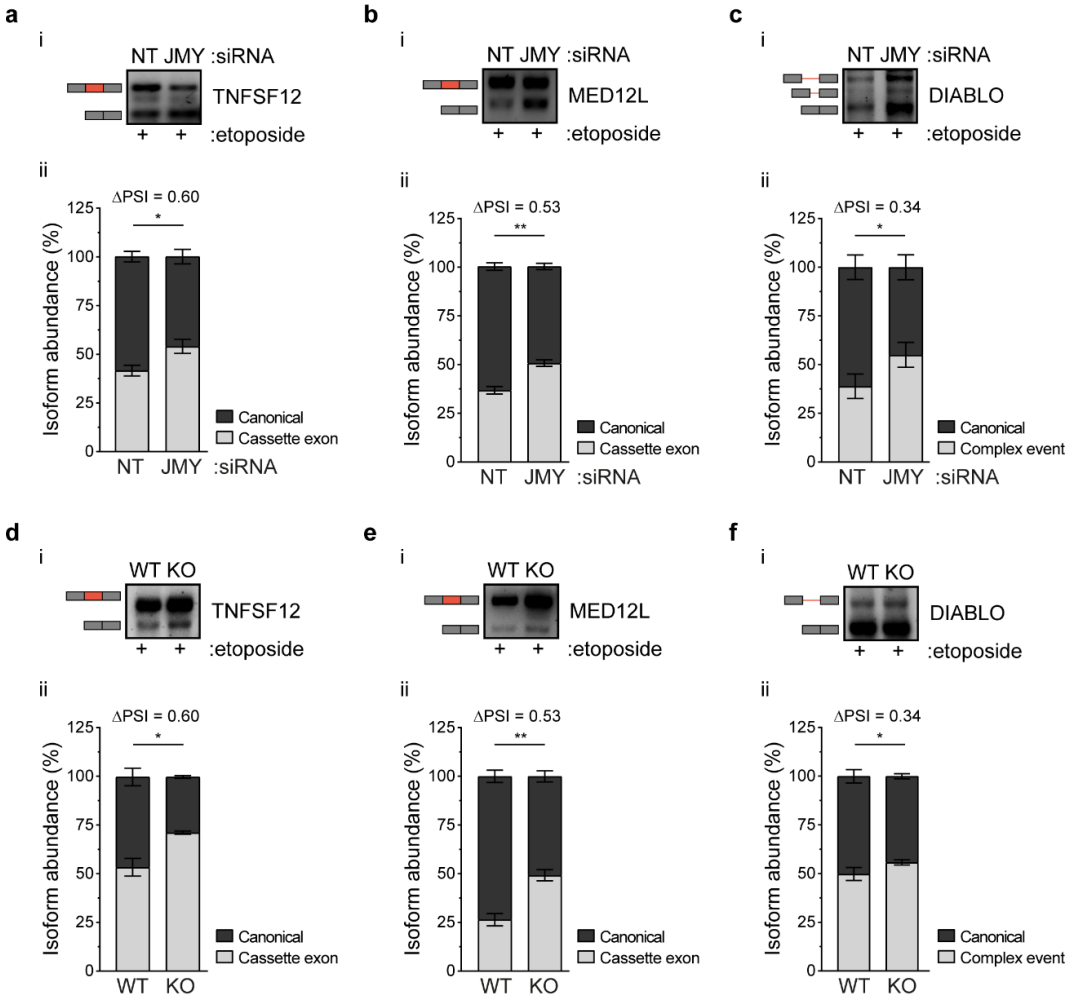


***Figure 6.4. The absence or depletion of JMY results in the enrichment of certain alternative splicing events during DNA damage. a-c)*** *i) U2OS cells were transfected with JMY or non-targeting (NT) siRNA for 72h and treated with etoposide (+, 50$\mu$M) for the last 6h before alternative splicing events were monitored in TNFSF12 (a, cassette exon), MED12L (b, cassette exon) and DIABLO (c, intron retention), ii) Isoform abundance was calculated after normalising for total isoform expression (mean ± s.e.m), n = 3 independent experiments.* ***d-f)*** *HAP1 parental and JMY KO (KO) cells were treated with etoposide (+, 500nM) for 6h before alternative splicing events were monitored and isoform abundance was calculated as in* ***(a-c)*** *(mean ± s.e.m), n = 3 independent experiments. * p < 0.05, ** p < 0.01, unpaired two-tailed Student's t-test.*

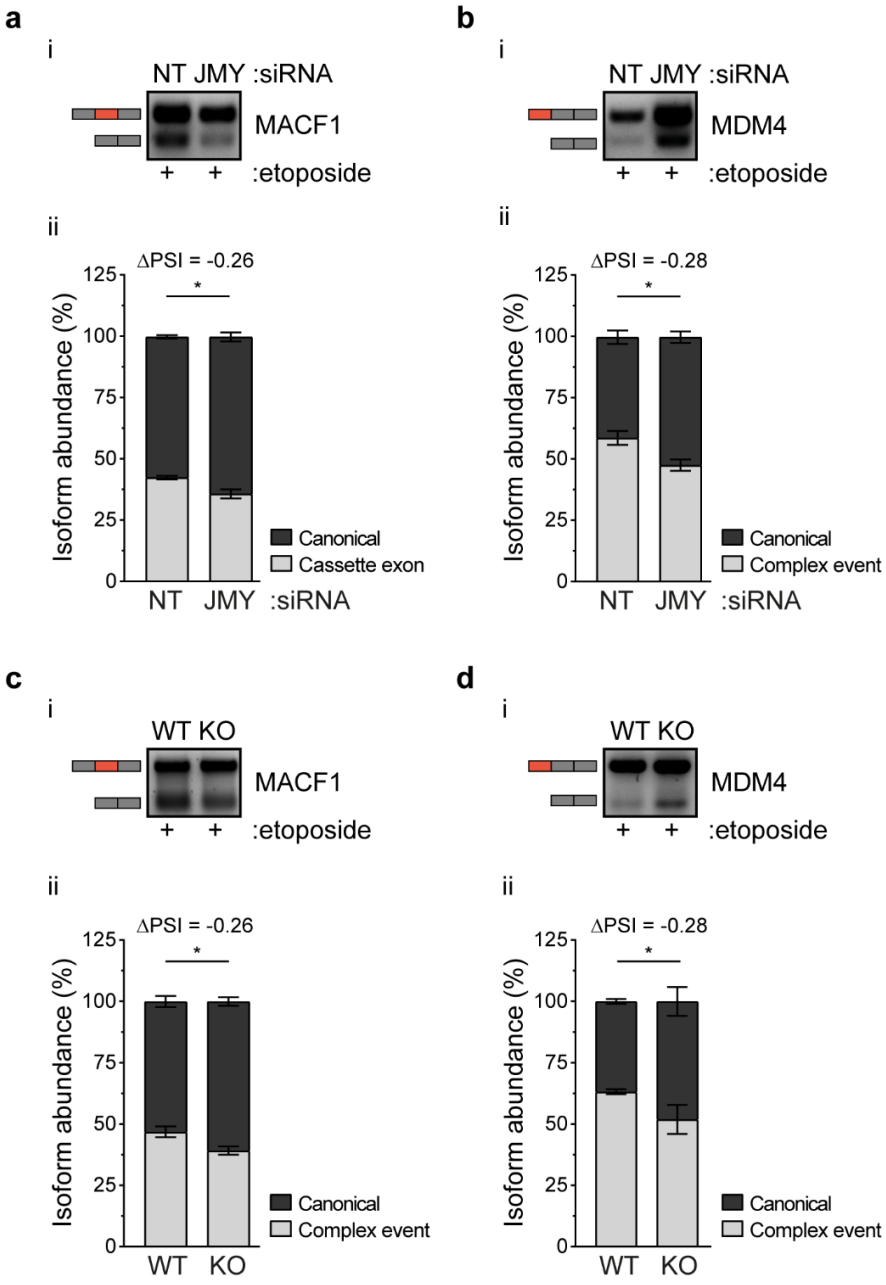


***Figure 6.5. JMY depletion can also suppress the expression of specific alternative splicing during DNA damage. a-b)*** *i) U2OS cells were transfected with JMY or non-targeting (NT) siRNA for 72h and treated with etoposide (+, 50μM) for the last 6h before alternative splicing events were monitored in MACF1 (a, cassette exon) and MDM4 (b, exon retention) ii) Isoform abundance was calculated after normalising for total isoform expression (mean ± s.e.m), n = 3 independent experiments.* ***c-d)*** *HAP1 parental and JMY KO (KO) cells were treated with etoposide (+, 500nM) for 6h before alternative splicing events were monitored and isoform abundance was calculated as in* ***(a-b)*** *expression (mean ± s.e.m), n = 3 independent experiments. * p < 0.05, unpaired two-tailed Student's t-test.*

JMY modulates tumour cell sensitivity to spliceosome inhibitors.

Given that JMY enhanced the expression of U2 snRNP components and modulated alternative splicing, the role of JMY in tumour cell fate during treatment with spliceosome inhibitors was explored. Isoginkgetin is a spliceosome inhibitor that impedes the recruitment of the U4/U6.U5 tri-snRNP to the A complex [282]. The short-term JMY depletion in U2OS cells had a marked effect on cell proliferation both under non-perturbed conditions and upon isoginkgetin treatment (Fig. 6.6ai). These results were not restricted to a single cell type as the ablation of JMY in HAP1 cells also led to reduced cell proliferation upon treatment with isoginkgetin (Fig. 6.6aii). To ensure that these results were not restricted to isoginkgetin, cells were also treated with plad B. Plad B inhibits the recognition of the adenosine BS by SF3B1 which blocks the spliceosome into the A complex [272]. Treatment with plad B also impaired cell proliferation both in the knockdown (Fig. 6.6bi) and knockout (Fig. 6.6bii) models; however, the results were modest compared with the isoginkgetin-mediated reduction in cell proliferation. These results suggested that the absence of JMY can increase tumour cell sensitivity to spliceosome inhibitors and it may be particularly relevant for targeting the spliceosome assembly after the formation of the A complex.

To determine if the reduction in cell proliferation upon treatment with spliceosome inhibitors was due to an increase in cell death, cell cycle analysis was performed in the HAP1 cell lines. The absence of JMY resulted in increased cell death upon treatment with both isoginkgetin and plad B (Fig. 6.6c). Interestingly, plad B has also been described to induce cell cycle arrest in the G2-M phase [278]. Treatment with plad B seemed to arrest HAP1 parental but not JMY knockout cells (Fig. 6.6d). These results were specific upon plad B treatment as no significant changes in the cell cycle profile were observed with isoginkgetin (Fig. 6.6d). Whether the decrease in cell proliferation and increase in cell death observed in JMY knockout cells may be a result of inefficient cell cycle arrest leading to DNA damage accumulation, require further characterisation. Together, these results suggest that tumour cells presenting lower JMY levels are more sensitive to spliceosome inhibitors, leading to compromised cell proliferation and enhanced cell death.

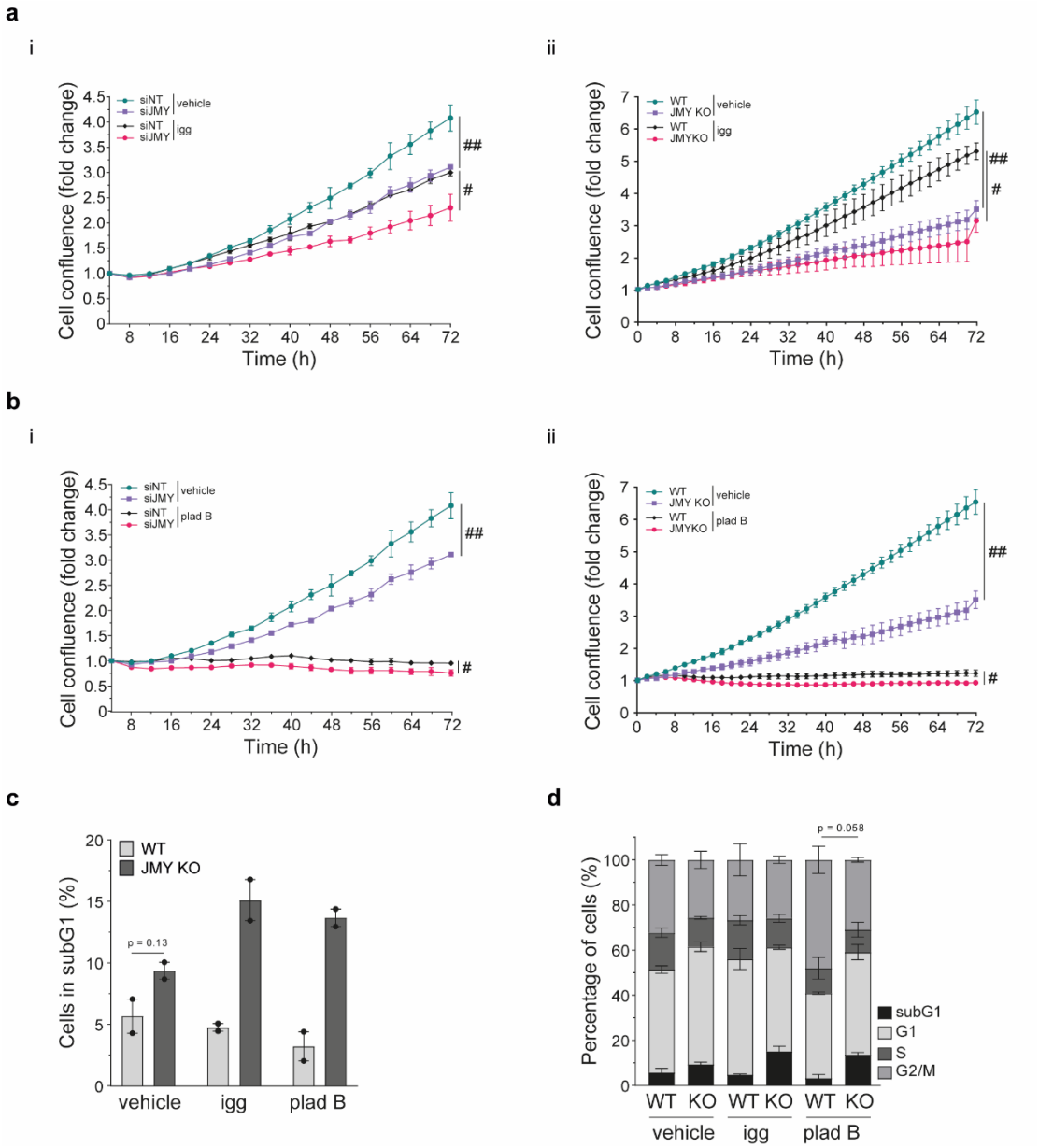


***Figure 6.6. JMY enhances tumour cell survival during spliceosome inhibition. a)*** *Cell confluence of U2OS cells transfected with JMY or non-targeting (NT) siRNA (i) or HAP1 parental (WT) and JMY KO cells (ii) after treatment with vehicle (DMSO) or isoginkgetin (igg, 15$\mu$M) for the indicated timepoints.* ***b)*** *Cell confluence of U2OS cells transfected as in* ***(a)*** *(i) or HAP1 parental (WT) and JMY KO cells (ii) after treatment with vehicle (DMSO) or pladienolide B (plad B, 5nM) for the indicated timepoints. Graphs represent cell confluence after normalising to time zero (mean ± s.e.m.), n = 3 independent experiments, except for U2OS cells where one representative experiment is shown (mean ± SD). # p < 0.01, ## p < 0.0001; two-way repeated measures ANOVA.* ***c-d)*** *HAP1 parental and JMY KO cells were treated as in* ***(a, b)*** *for 30h before collecting for flow cytometry. Graphs*

*represent the percentage of cells in subG1 phase* ***(c)*** *or complete cell cycle profiles* ***(d)*** *(mean ± s.e.m.), n = 2 independent experiments.*

**Table 6.1. JMY-mediated spliced events shared with** [198]

| Target | Alternative splicing events | q-value* | ΔPSI# |
|---|---|---|---|
| *DVL2* | Retained Intron | 4.5e-4 | 0.4 |
| *SF3A2* | Retained Intron | 3.5e-3 | 0.3 |
| *SF3B1* | Complex Event | 1.0e-3 | 0.2 |
| *MEN1* | Retained Intron | 3.7e-3 | 0.3 |
| *UBE2G2* | Retained Intron | 7.9e-3 | 0.2 |
| *ARFGAP1* | Retained Intron | 7.9e-3 | -0.3 |
| *MACF1* | Cassette Exon | 2.3e-3 | -0.3 |
| *RPL10* | Retained Intron | 9.6e-3 | -0.3 |
| *RPS3* | Retained Intron | 3.1e-3 | -0.5 |
| *RPS11* | Retained Intron | 3.3e-3 | -0.3 |

** Significant threshold was set as q-value < 0.01 (FDR corrected p-value); # ΔPSI: percent spliced in index. The quantification of the ΔPSI is explained in more detail in the Material and Methods section.*

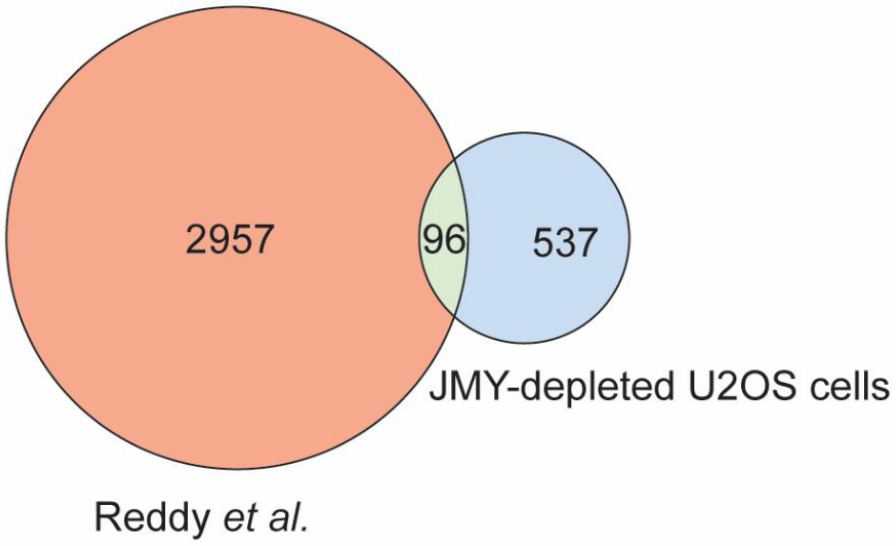


***Figure 6.7. Shared alternative splicing events obtained after NEAT1 or JMY depletion in tumour cells.*** *The Venn diagram represents the number of alternative splicing events overlapping between Reddy and colleagues´ work (NEAT1-depleted cells)* [198] *and this project (JMY-depleted cells).*

## 6.4. Discussion

JMY is a DNA damage-responsive actin nucleator that undergoes nuclear accumulation upon treatment with specific genotoxic stressors, where it can enhance the p53-driven expression of DNA repair genes (Chapter 4) [130], *BAX* [104,127] and *NEAT1_2* (Chapter 5). In this chapter, our results demonstrate a wider role for JMY in transcriptional regulation modulating the expression of U2 snRNP-related splicing factors. Ultimately, we showed that JMY impacts alternative splicing during DNA damage and sensitises tumour cells to spliceosome inhibitors suggesting that JMY could be a novel target to modulate tumour-specific alternative splicing.

Our data support a role for JMY in the transcriptional regulation of splicing factors and modulation of alternative splicing in response to etoposide-induced DNA damage, conditions where JMY accumulates in the nucleus [129,130]. The vast majority of mammalian genes are alternatively spliced in a process where the spliceosome differentially retains or excludes intronic and exonic regions, leading to a diverse pool of transcripts [252]. Interestingly, a growing body of evidence indicates that induction of genotoxic stress causes changes in the spliceosome activity leading to DNA damage-specific alternative splicing events [325]. For example, induction of DNA damage triggers changes in the spliceosome organisation which modulate the recognition of exons leading to frequent exon skipping events [348,349]. Most of these splicing events can occur co-transcriptionally, where defects in RNA polymerase II elongation rates or changes in the interaction between the spliceosome and the transcriptional machinery lead to an inadequate intron removal [273,350]. Further studies are required to refine our understanding of how JMY regulates the expression of splicing factors and how this can impact JMY-mediated changes in alternative splicing. Additionally, as most of the JMY-mediated splicing factors described here are not previously known p53 targets [268], it will be of great interest to explore the interactome of nuclear JMY to expand our knowledge of JMY's regulatory network during genotoxic stress.

Although incompletely understood, our results suggest that JMY influences splicing during etoposide-induced DNA damage leading to the expression of specific alternatively spliced isoforms (Fig. 6.4, 6.5). As tumour cells commonly exhibit splicing abnormalities, this deregulation is being used for cancer therapy ranging from broad spliceosome inhibitors to the modulation and targeting of specific alternatively spliced transcripts. However, the vast majority of these therapeutical

strategies present high cytotoxicity, partial inhibitory responses and challenges of delivery to the target tissue [251]. As our results suggest that non-conventional splicing regulators like JMY can modulate alternative splicing and influence the expression of tumour-specific isoforms, it will be of great interest to further investigate the role of JMY in alternative splicing during DNA damage and the role of these JMY-mediated spliced events in tumour cell fate. For example, our splicing analysis identified autophagy as an altered pathway during DNA damage (Fig. 6.3e) [286], which in combination with the enrichment results present in Chapter 3 (Fig. 3.4c), suggest that JMY might promote cell survival through its influence on nuclear activities as well as through its cytoplasmic impact on autophagy [125]. Thus, our work opens the possibility to explore non-canonical spliceosomal components to understand their role in the regulation of tumour-specific splicing.

As described in Chapter 5, the absence of JMY hinders the p53-driven expression of lncRNA *NEAT1_2*, thus compromising paraspeckle biogenesis. A recent study described that paraspeckles modulate the expression of splicing factors as well as their retention within these subnuclear bodies which impact overall alternative splicing [198]. Interestingly, several of the alternatively spliced variants obtained from our transcriptomic results were also reported when paraspeckle formation was compromised via *NEAT1_2* depletion (Table 6.1; Fig. 6.7) [198]. These results may suggest a link between paraspeckles and alternative splicing as discussed in Chapter 5.

JMY is an actin nucleator, and its ability to promote actin polymerisation is required to enhance the p53-mediated transcriptional expression of *BAX* [127], whereas JMY requires its Arp2/3-driven actin nucleation to reduce the accumulation of DNA damage through its transcriptional regulation of p53-dependent DNA repair genes [130]. Notably, a growing body of evidence implicates nuclear actin and actin-promoting factors in important nuclear events like DNA repair [178] and transcription [171]; however, their role during splicing is still poorly characterised. Recently, WASP was shown to hinder the expression of splicing factors proposing a transcriptional inhibitory role that was linked with the aberrant formation of splicing speckles leading to compromised widespread alternative splicing [269]. In addition, actin was described to interact with core and auxiliary splicing factors and changes in nuclear actin levels were correlated with aberrant splice site recognition in minigene reporter assays suggesting splicing deregulation [166]. Whether JMY also modulates splicing via direct interaction with the spliceosome and if its actin nucleation activity

is required to control alternative splicing requires further investigation. Nonetheless, our results expand the evidence that nuclear actin nucleators play a key role in splicing dynamics.

Together, the results present in this chapter suggest that JMY is able to modulate alternative splicing during DNA damage through its impact on the expression of splicing factors (maybe in combination with its influence on paraspeckle biogenesis) and its role during tumour cell fate upon spliceosome inhibition. This provides further evidence of the complexity of JMY's nuclear regulatory network and open new possibilities to source JMY as a target to modulate splicing and tumour outcomes in response to stress.

# Chapter 7: Discussion and conclusions.

In this project, the role of JMY in the regulation of gene expression within human tumour cells during DNA damage was investigated. Transcriptomic analysis was performed in U2OS osteosarcoma cells where JMY was depleted, and DNA damage was induced via etoposide treatment. Pathway enrichment analysis demonstrated that JMY plays a crucial role in various cellular processes, including the p53 signalling response, paraspeckle biogenesis and alternative splicing. This project presented a novel role for nuclear JMY in DNA repair during the DDR. The absence of JMY hinders the p53-dependent expression of DNA repair genes and compromises the activation of the DNA damage response, leading to the accumulation of DNA lesions. Also, the JMY-mediated Arp2/3-driven actin nucleation is required for DNA repair and p53 transcriptional activation of DNA repair factors. Moreover, the absence of JMY sensitises tumour cells to chemotherapeutic agents and impacts cell survival, which is reflected in human tumours where lower *JMY* levels correlate with increased overall patient survival.

Additionally, a new role for nuclear JMY in paraspeckle biogenesis during DNA damage was described. The absence of JMY hinders the p53-dependent expression of lncRNA *NEAT1_2,* resulting in decreased paraspeckle formation. Although incompletely understood, the disruption of these subnuclear bodies sensitises tumour cells to DNA damaging agents. Lastly, this project also demonstrated a new role for JMY in alternative splicing during DNA damage. The absence of JMY compromises the expression of U2 snRNP-related splicing factors and impacts on alternative splicing during etoposide-induced genotoxic stress. Although the detailed mechanisms remain to be characterised, the absence of JMY sensitises tumour cells to spliceosome inhibitors. Collectively, these findings demonstrate the broad role of nuclear JMY in transcriptional regulation, suggest a role for actin in JMY's nuclear activity and highlight the impact of JMY on cell fate during the genotoxic stress.

JMY is a DNA damage-responsive protein that localises in the cytoplasm and nucleus. In the former, JMY acts as an actin nucleator and promotes the formation of actin filaments both in an Arp2/3-dependent and independent manner, enhancing cell motility and invasion [126,127]. In response to metabolic stress (*e.g.* starvation), JMY acts as a pro-survival factor by promoting the formation and

maturation of cytoplasmic autophagosomes [125]. Under specific DNA damaging conditions, JMY translocates to the nucleus, where it enhances p53 transcriptional activity [127,130]. These results indicate that the type of stressor may influence the cellular localisation of JMY and therefore its activity.

A previous study has proposed a mechanism to explain how JMY undergoes nuclear accumulation during DNA damage [147]. According to this model, during genotoxic stress, the formation of cytoplasmic actin filaments can decrease the availability of cytoplasmic G-actin, reducing its interaction with JMY's C-terminal region (WH2 domains). This, in turn, can expose the second NLS within JMY, enabling its recognition by importin β and facilitating the accumulation of JMY in the nucleus [147]. However, recent findings have questioned the previously proposed model, where it was observed that under certain etoposide treatment conditions, JMY exhibited a perinuclear localisation forming F-actin structures [145]. Nevertheless, several studies demonstrated that during specific genotoxic stress conditions (including etoposide treatment), JMY undergoes nuclear accumulation [127,129,130]. Collectively, these findings suggest that the subcellular localisation of JMY may be regulated by various factors such as the type of stressor, its duration and dose.

Interestingly, earlier studies demonstrated that the nuclear accumulation of WASP could occur independently of cytoplasmic F-actin formation [159,160]. Like JMY, WASP can localise in both the cytoplasm and nucleus [159,160], where cytoplasmic WASP has been described to present an inactive conformation that is released through the phosphorylation of a tandem of three conserved tyrosines ($Y^{253}$, $Y^{256}$, $Y^{291}$) located closely to the WCA region [351,352]. These residues can be phosphorylated by several kinases from the Scr family (*e.g.* FYN, BTK, SCR and HCK) [160,351–355]. The phosphorylation of these residues induces conformational changes in WASP, exposing its NLS, which is subsequently recognised by both importin β and importin α , promoting the nuclear accumulation of WASP [159,160]. It is possible that JMY may present similar regulatory mechanisms. Additionally, extensive research describes that genotoxic stress activates the Scr family of kinases [356,357]. Notably, a recent study demonstrated that the different temporal and dose-dependent exposure to etoposide results in changes in the activation of SCR kinase [358]. Mechanistically, lower doses of etoposide led to prolonged activation of this kinase, while higher doses negatively regulated SCR activation [358]. Interestingly, the shift in SCR's activity was also correlated with a change from senescence to apoptosis

in human immortalised fibroblast [358]. These findings demonstrate that differences in the duration and dose-dependent exposure to etoposide result in differential activation of SCR kinase. Since several Scr kinases regulate the cellular localisation of WASP, it would be worth exploring if this family of kinases could impact on JMY. Thus this regulatory mechanism may explain the differences in the nuclear accumulation of JMY upon exposure to specific genotoxic stressors.

Even though the mechanisms remain to be elucidated, JMY is known to undergo nuclear accumulation under specific genotoxic stress conditions [127,130]. Previous work demonstrated that nuclear JMY enhances the p53-dependent transcriptional activation of *BAX* [104,127]. Our results show that the absence of JMY negatively impacts the p53-dependent expression of target genes involved in DNA repair. These findings indicate that JMY promotes the p53-dependent transcriptional activation of both pro-apoptotic and DNA repair factors. Notably, using *BAX*-luciferase reporter assays, it was demonstrated that JMY's ability to promote p53-dependent activity was hindered upon inhibition of overall actin nucleation via latrunculin A treatment. However, JMY's Arp2/3-dependent nucleation had no effect [127]. In contrast, we observed that the expression of a JMY derivative unable to mediate Arp2/3-dependent actin nucleation reduces the p53-dependent expression of DNA repair genes and increases the accumulation of DNA damage [130]. Since the presence of nuclear JMY plays a crucial role in the p53-dependent activation of genes involved in both programmed cell death and DNA repair [104,127,130], it is likely that JMY's activity at target genes will be promoter specific. Therefore, it is possible that the complete absence of JMY may hinder the overall recruitment of p53 to target gene promoters. However, in the presence of nuclear JMY, its actin nucleation activity may lead to distinct recruitment of both p53 and actin to the promoters of specific target genes. Based on this hypothesis, it is likely that JMY's actin nucleation activity may be required directly at the chromatin to enhance the recruitment of p53. To investigate this future studies should focus on using nuclear JMY derivatives with and without Arp2/3-dependent and independent actin nucleation activities or specific inhibitors of the Arp2/3 complex (*e.g.* ck666)[330]. This approach will avoid off-target effects associated with inhibiting overall cellular actin nucleation, unlike latrunculin derivatives [359].

Under non-perturbed conditions, p53 levels are tightly controlled by its interacting with MDM2, which promotes the polyubiquitination and proteasomal-dependent degradation of p53 [85,8990]. However, ATM, ATR, and DNA-PK promote the

phosphorylation and activation of p53 during DNA damage [59,60,63,64]. These PIKKs can both directly and indirectly phosphorylate p53 at $S^{15}$ and $S^{20}$ leading to the dissociation of p53 from MDM2, resulting in increased p53 stability and transcriptional activity [96]. Interestingly, we also observed that JMY enhances the activity of ATM and ATR in response to DNA damage and promotes the activation of p53 through phosphorylation at $S^{15}$ (data not shown). Notably, MDM2 also interacts with and negatively regulates JMY through polyubiquitination, which leads to the proteasomal degradation of JMY [129], similar to what has been extensively described for p53 [85]. Therefore, it is likely that, during DNA damage, nuclear JMY may impact the stability and activation of p53, thereby influencing its transcriptional activity.

Notably, a growing body of research supports the role of nuclear actin and actin nucleation-promoting factors during DNA repair [155]. Two independent studies demonstrated the role of WASp family of proteins and the Arp2/3 complex during the resolution of DBSs via homology-directed repair. Initially, WASH-mediated Arp2/3-driven formation of nuclear actin filaments promote the translocation of chromatin segments containing the DSBs to the nuclear periphery. Then, the formation of nuclear F-actin by WASP (mediated via the Arp2/3 complex) promotes the clustering of DSBs, recruitment of DNA repair factors and DNA end resection, ultimately leading to homology-directed repair [178,179]. Additionally, WASH was recently described to enhance the repair of DSBs through NHEJ. Nuclear WASH interacts with the Ku heterodimeric complex directly at the DSB, where its ability to mediate Arp2/3-dependent actin nucleation promotes chromatin relaxation and recruitment of repair factors, thus, leading to the activation of the NHEJ repair pathway [181]. Collectively, these findings support the role of nuclear F-actin and actin nucleators during the repair of DSBs. During DNA damage, nuclear JMY can incorporate nuclear G-actin [127], and JMY's actin nucleation activity influences its transcriptional cofactor role [127,130]. It is likely that JMY may also be recruited and directly involved in DNA lesion repair during DNA damage. However, the detailed mechanisms underlying these interactions remain to be elucidated.

The results presented in this thesis also expand our understanding of the role of JMY in transcriptional regulation and demonstrate a novel role for nuclear JMY during the p53-dependent expression of lncRNA *NEAT1.* The human *NEAT1* locus encodes two isoforms, *NEAT1_2* (22.7kb) and *NEAT1_1* (2.7kb), where the latter

is obtained through alternative 3'-end processing from *NEAT1_2* [212]. Notably, p53 induces the expression of both *NEAT1* transcripts in response to various stress conditions, including DNA damage, hypoxic conditions or proteotoxic stress [207,220,222]. However, *NEAT1_2* is generally expressed at higher levels than *NEAT1_1* [207,214,217].

Although the mechanisms underlying the alternative 3'-end processing are incompletely understood, the balance between *NEAT1* isoforms is regulated by several factors. Integrator and CFIm (CPSF6 and NUDT21) complexes as well as TDP-43 interact with the PAS, leading to transcriptional termination and expression of *NEAT1_1* [212,214,215]. Contrarily, HNRNPK and HNRNPM bind to regions flanking the PAS, preventing the binding of *NEAT1_1*-promoting factors and thereby enhancing *NEAT1_2* expression [212]. However, the specific mechanisms by which these factors regulate the *NEAT1* isoform-specific expression during DNA damage, conditions that favour *NEAT1_2* expression, are yet to be determined. Our results suggest that during genotoxic stress, JMY can impact on the expression of multiple factors that promote specific *NEAT1* isoform expression, including *CPSF6*, *TDP-43*, *HNRNPK*, and *HNRNPM*. Interestingly, JMY seems to enhance the expression of factors that specifically promote *NEAT1_2* (*e.g. HNRNPK* and *HNRNPM*) over those involved in *NEAT1_1*. This suggests that nuclear JMY may hinder the alternative 3'-end processing, enhancing *NEAT1_2* expression. Previous studies indicated that MYC acts as a transcriptional regulator for both *HNRNPK* and *HNRNPM* [268,360,361]. Therefore, during DNA damage, nuclear JMY may influence the MYC-dependent transcriptional expression of *HNRNPK* and *HNRNPM*. These findings, combined with the observations that JMY influences the p53-driven expression of *NEAT1*, will further contribute to the upregulation of *NEAT1_2* expression.

While the function of *NEAT1_1* is incompletely understood, *NEAT1_2* acts as an architectural scaffold during the formation of paraspeckles [188,189]. Paraspeckles are stress-responsive subnuclear bodies composed of approximately 50 RNA-binding proteins distributed along *NEAT1_2* [208]. Paraspeckle biogenesis occurs in two steps and is enhanced in response to various stressors, including DNA damage [207]. However, the detailed mechanisms underlying this process are not fully understood. During DNA damage, JMY seems to influence the expression of class 1B paraspeckle-associated proteins, suggesting that nuclear JMY may play a role during the liquid-phase separation process required for the recruitment of these

proteins during paraspeckle biogenesis [208]. Notably, several studies have suggested that changes in nuclear actin dynamics influenced by cellular confinement and reduced cell motility can increase liquid-phase separation processes and promote paraspeckle biogenesis [185–187]. Remarkably, these studies also reported that these changes in paraspeckle formation are independent of the expression of *NEAT1_2* [185,186], which was previously reported as the only limiting factor for paraspeckle biogenesis [207]. Collectively, these studies suggest that nuclear actin dynamics may influence the formation of paraspeckles. Moreover, recent findings revealed the presence of actin and multiple subunits of the Arp2/3 complex (*e.g.* ARPC2 and ARPC3) within *NEAT1_2*-containing paraspeckles [199,362,363]. Considering that genotoxic stress induces the formation of various nuclear actin structures [177,178], and as the actin nucleation of JMY is required for its nuclear role during DNA damage [127,130], it is possible to propose that nuclear JMY may also be physically involved in the formation of paraspeckles.

Paraspeckles are proposed to play an important role in promoting tumour cell survival during genotoxic stress [207,220]. Three main regulatory mechanisms have been suggested, including transcriptional activation (through the interaction between paraspeckles and actively transcribed genes) and the retention of both IRAlus-containing mRNAs and paraspeckle-associated components [199,222,233]. Notably, two JMY-regulated targets, namely *HSPA5* and *MTDH*, are known to be IRAlus-containing mRNAs that are retained within paraspeckles [364]. Increased expression of these targets has been associated with enhanced tumour cell death [365,366]. For instance, elevated *HSPA5* expression in human mesothelioma cells reduces tumour cell survival during the unfolded protein response related to endoplasmic reticulum stress [365]. Similarly, in prostate tumour cells that develop resistance to nutrient starvation, the increased expression of *HSPA5* abolishes this survival advantage [367]. Furthermore, increased levels of *MTDH* have been suggested to sensitise endometrial and triple-negative breast cancer cells to ferroptosis [366]. Therefore, by retaining these pro-apoptotic targets within paraspeckles, JMY may influence tumour cell survival in response to genotoxic stress. This suggests a novel regulatory mechanism by which nuclear JMY can modulate tumour cell fate.

Recently, paraspeckles have also been proposed to modulate alternative splicing and thus gene expression both indirectly by sequestering splicing factors and

directly via transcriptional activation of auxiliary spliceosome components [198]. Although DNA damage has been described to promote paraspeckle biogenesis and impact on alternative splicing [207,325], whether there is a link between these two processes remains to be elucidated. Given that paraspeckles localise close to splicing speckles [209], it is likely that paraspeckles can modulate alternative splicing by controlling the exchange of splicing factors between both non-membranous subnuclear bodies. Our findings demonstrated that during DNA damage, the absence of JMY leads to changes in alternative splicing, resulting in the expression of specific spliced isoforms. Several of these spliced targets have also been described when paraspeckle biogenesis is compromised via *NEAT1_2* depletion [198]. For example, these events include the retention of the second intron in both *BAP1* and *DVL2*. Notably, previous results demonstrated that this intron retention event in *BAP1* reduces its ubiquitination activity, resulting in increased tumour cell sensitivity to PARP (olaparib) and mTOR (GDC0980) inhibitors [368]. This effect can be partially explained by an increase in apoptosis due to the negative regulation of pro-survival targets *BCL2* and *MCL1* by BAP1 [369]. Additionally, the reduction in BAP1 activity, derived from the retained intron, leads to increased monoubiquitination of H2AK119, resulting in the epigenetic downregulation of metabolic-related genes like *SLC7A11* and induction of tumour cell death via ferroptosis [370,371]. Moreover, in colorectal tumour cells the retention of the second intron of *DVL2* causes increased degradation of its mRNA, which results in the decreased stability of β-catenin and inactivation of the Wnt signalling pathway, leading to reduced cell survival [372]. These results suggest that JMY, through its role in paraspeckle biogenesis, can modulate the alternative splicing of specific targets that may influence cell survival. These findings expand our understanding of the regulatory network of nuclear JMY and its potential impact on tumour cell fate.

Alternative splicing is frequently deregulated in human tumours and occurs due to the abnormal expression of spliceosome components [251]. This leads to the presence of cancer-specific transcripts, which have been described to both impair the expression of tumour suppressors and enhance the activity of oncogenes [257]. Notably, several studies demonstrated that MYC acts as a central transcriptional regulator of spliceosome components, particularly within the U2 snRNP subunit [268,361]. Recent evidence suggests that MYC promotes the expression of U2 snRNP-related splicing factors such as *SF3B6* and *SF3A3* [373]*.* Hence, nuclear JMY may influence the MYC-mediated transcriptional regulation of U2 snRNP-related splicing factors during DNA damage. Moreover, nuclear actin has been recently

described as an interactor of a wide range of splicing factors [166]. More recently, WASP was described to modulate alternative splicing both by the transcriptional regulation of splicing factors as well as through the formation of splicing speckles [269]. These studies suggest a role for actin and actin nucleators in alternative splicing. Therefore, it is likely that nuclear JMY, through its actin nucleation activity, may modulate the expression of splicing factors via MYC transcriptional regulation and thus the formation of nuclear splicing speckles, which can ultimately impact alternative splicing.

It is known that defects in splicing factors within human tumours are primarily heterozygous and mutually exclusive, highlighting the reliance of cancer cells on the presence of at least one functional wild-type allele. Consequently, the spliceosome has emerged as a promising therapeutic target for the treatment of human cancers [256]. Although several small molecule inhibitors have been developed to target different stages of the spliceosome assembly and thus alternative splicing, the vast majority of these therapeutical strategies present high cytotoxicity, restricted delivery and partial inhibitory responses [251]. Furthermore, the emergence of resistance to spliceosome inhibitors in human tumours has posed challenges to their clinical usage [256]. Remarkably, MYC-active tumours present increased sensitivity to spliceosome inhibitors [361,374]. In MYC-driven tumours, including triple-negative breast cancer and glioblastomas, the inhibition of the spliceosome leads to decreased cell proliferation and increased cell death [375,376]. These MYC-dependent tumours appear to be particularly susceptible to the inhibition of U2 snRNP factors such as SF3B1 [377]. Mechanistically, it has been proposed that the inhibition of the spliceosome (targeting SF3B1 within the U2 snRNP) leads to the retention of intronic segments in MYC-dependent targets, resulting in the formation of dsRNAs and their accumulation in the cytoplasm. These dsRNAs can activate the antiviral immune signalling response, triggering the activation of caspase-3, caspase-7 and caspase-8, ultimately inducing apoptosis [376]. Additionally, a wide range of solid tumours harbouring MYC amplification exhibit increased sensitivity to T-025, an SR-protein inhibitor, highlighting that MYC-driven tumours present a widespread sensitivity for spliceosome inhibitors [378]. Collectively, these findings suggest that MYC-dependent tumours rely on the spliceosome. Considering that JMY regulates the expression of U2 snRNP-related factors which are known MYC targets [268,361], it is possible that the increased sensitivity to spliceosome inhibitors observed in the absence of JMY may be linked to its possible role as a nuclear MYC regulator.

These findings suggest that JMY could be a clinically relevant target for manipulating the spliceosome, particularly in the context of MYC-driven tumours.

Our understanding of JMY's cellular functions shows that it mainly localises in the cytoplasm, promoting cell motility and invasion through its actin nucleation activity [126,127]. However, under different stress conditions, JMY accumulates in distinct cellular compartments. For example, during metabolic stress, JMY acts as a pro-survival factor as it localises to cytoplasmic autophagosomes, promoting their formation and maturation [125]. In contrast, specific genotoxic stress conditions lead to JMY's nuclear accumulation, where it enhances p53 activity [127,130]. Nuclear JMY contributes to the repair of DNA lesions and increases cellular resistance to several chemotherapeutic agents [130]. Additionally, JMY plays an important role in the p53-dependent transcriptional regulation of *NEAT1_2* and thus paraspeckle biogenesis upon DNA damage. Nuclear JMY is also required for the transcriptional expression of splicing factors, whereas its absence results in overall changes in alternative splicing during genotoxic stress (Fig. 7.1). This project provides further insights into JMY's transcriptional regulatory role in human tumours and can lead to clinical opportunities to target key cellular pathways like the p53 signalling response and alternative splicing.

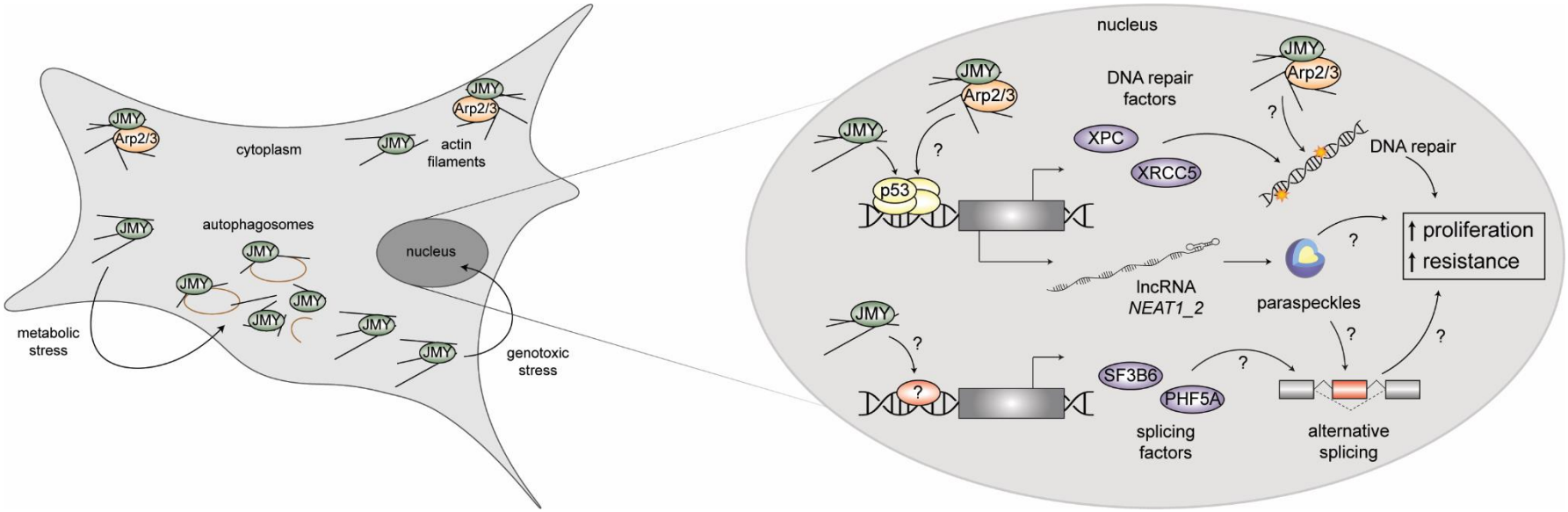


***Figure 7.1. The cellular functions of JMY.*** *Cytoplasmic JMY is an actin nucleator that enhances cell motility and invasion by regulating actin filament formation. Different stress conditions result in distinct JMY's cellular localisation and outcomes. During metabolic stress, JMY acts as a pro-survival factor by facilitating the formation and maturation of cytoplasmic autophagosomes. In response to specific genotoxic stress conditions, JMY undergoes nuclear accumulation. Nuclear JMY enhances the p53 transcriptional activation of DNA repair factors (e.g. XPC and XRCC5), and, through its Arp2/3-dependent actin nucleation activity, impacts on the accumulation of DNA lesions and overall cell survival during DNA damage. Moreover, JMY promotes the p53-dependent expression of lncRNA NEAT1_2 and thus modulates paraspeckle biogenesis, which could sensitise cells to DNA damaging agents. Lastly, JMY is required for the expression of splicing factors (e.g. SF3B6 and PHF5A) and can impact on alternative splicing during DNA damage.*

# References


1 Moon J, Kitty I, Renata K, Qin S, Zhao F, Kim W. DNA Damage and Its Role in Cancer Therapeutics. *Int J Mol Sci* 2023; **24**: 1–19.

2 Tubbs A, Nussenzweig A. Endogenous DNA Damage as a Source of Genomic Instability in Cancer. *Cell* 2017; **168**: 644–656.

3 Jackson SP, Bartek J. The DNA-damage response in human biology and disease. *Nature* 2009; **461**: 1071–1078.

4 Knijnenburg TA, Wang L, Zimmermann MT, Chambwe N, Gao GF, Cherniack AD *et al.* Genomic and Molecular Landscape of DNA Damage Repair Deficiency across The Cancer Genome Atlas. *Cell Rep* 2018; **23**: 239–254.

5 Hanahan D. Hallmarks of Cancer: New Dimensions. *Cancer Discov* 2022; **12**: 31–46.

6 Groelly FJ, Fawkes M, Dagg RA, Blackford AN, Tarsounas M. Targeting DNA damage response pathways in cancer. *Nat Rev Cancer* 2022; **23**: 78–94.

7 Kluska M, Woźniak K. Natural Polyphenols as Modulators of Etoposide Anti-Cancer Activity. *Int J Mol Sci* 2021; **22**: 6602-6612.

8 Urvalek AM, Osei-Sarfo K, Tang XH, Zhang T, Scognamiglio T, Gudas LJ. Identification of Ethanol and 4-Nitroquinoline-1-Oxide Induced Epigenetic and Oxidative Stress Markers During Oral Cavity Carcinogenesis. *Clin Exp Res* 2015; **39**: 1360–1372.

9 Mckie SJ, Neuman KC, Maxwell A. DNA topoisomerases: Advances in understanding of cellular roles and multi-protein complexes via structure-function analysis. *BioEssays* 2021; **43**: 1–35.

10 Riccio AA, Schellenberg MJ, Williams RS. Molecular Mechanisms of Topoisomerase 2 DNA-Protein Crosslink Resolution. *Cell Mol Life Sci* 2020; **77**: 81–91.

11 Chen SF, Huang NL, Lin JH, Wu CC, Wang YR, Yu YJ *et al.* Structural insights into the gating of DNA passage by the topoisomerase II DNA-gate. *Nat Commun* 2018; **9**: 1–13.

12 Schmidt BH, Osheroff N, Berger JM. Structure of a topoisomerase II-DNA-nucleotide complex reveals a new control mechanism for ATPase activity. *Nat Struct Mol Biol* 2012; **19**: 1147–1154.

13 Le TT, Wu M, Lee JH, Bhatt N, Inman JT, Berger JM *et al.* Etoposide

promotes DNA loop trapping and barrier formation by topoisomerase II. *Nat Chem Biol* 2023; **19**: 641–650.

14 Wu CC, Li TK, Farh L, Lin LY, Lin TS, Yu YJ *et al.* Structural basis of type II topoisomerase inhibition by the anticancer drug etoposide. *Science* 2011; **333**: 459–462.

15 Downes DJ, Chonofsky M, Tan K, Pfannenstiel BT, Reck-Peterson SL, Todd RB. Characterization of the mutagenic spectrum of 4-nitroquinoline 1-oxide (4-NQO) in Aspergillus nidulans by whole genome sequencing. *G3 Genes, Genomes, Genet* 2014; **4**: 2483–2492.

16 Arima Y, Nishigori C, Takeuchi T, Oka S, Morimoto K, Utani A *et al.* 4-Nitroquinoline 1-Oxide Forms 8-Hydroxydeoxyguanosine in Human Fibroblasts through Reactive Oxygen Species. *Toxicol Sci* 2006; **91**: 382–392.

17 Brüsehafer K, Manshian BB, Doherty AT, Zaïr ZM, Johnson GE, Doak SH *et al.* The clastogenicity of 4NQO is cell-type dependent and linked to cytotoxicity, length of exposure and p53 proficiency. *Mutagenesis* 2016; **31**: 171–180.

18 Bailleul B, Daubersies P, Galiègue-Zouitina S, Loucheux-Lefebvre M -H. Molecular Basis of 4-Nitroquinoline 1-Oxide Carcinogenesis. Jpn. J. Cancer. 1989; **80**: 691–697.

19 Di Paolo C, Müller Y, Thalmann B, Hollert H, Seiler TB. P53 Induction and Cell Viability Modulation By Genotoxic Individual Chemicals and Mixtures. *Environ Sci Pollut Res* 2018; **25**: 4012–4022.

20 Nimrat Chatterjee, Walker GC. Mechanisms of DNA damage, repair and mutagenesis. *Environ Mol Mutagen* 2017; **58**: 235–263.

21 Kuper J, Kisker C. At the core of nucleotide excision repair. *Curr Opin Struct Biol* 2023; **80**: 4982–4994.

22 Scully R, Panday A, Elango R, Willis NA. DNA double-strand break pathway choice in somatic mammalian cells. *Nat Rev Mol Cell Biol* 2019; **20**: 1–17.

23 Jacobs AL, Schär P. DNA glycosylases: In DNA repair and beyond. *Chromosoma* 2012; **121**: 1–20.

24 Mol CD, Izumi T, Mitra S, Tainer JA, Talner JA. DNA-bound structures and mutants reveal abasic DNA binding by APE1 and DNA repair coordination. *Nature* 2000; **403**: 451–456.

25 Demin AA, Hirota K, Tsuda M, Adamowicz M, Hailstone R, Brazina J *et al.* XRCC1 prevents toxic PARP1 trapping during DNA base excision repair. *Mol Cell* 2021; **81**: 3018–3030.

26 Caldecott KW. Mammalian DNA base excision repair : Dancing in the moonlight. *DNA Repair (Amst)* 2020; **93**: 85–92.

27 Mengwasser K, Adeyemi R, Leng Y, Choi MY, Clairmont C, D'andrea A *et al.* Genetic Screens Reveal FEN1 and APEX2 as BRCA2 Synthetic Lethal Targets. *Mol Cell* 2019; **75**: 885–899.

28 Kusakabe M, Onishi Y, Tada H, Kurihara F, Kusao K, Furukawa M *et al.* Mechanism and regulation of DNA damage recognition in nucleotide excision repair. *Genes Environ* 2019; **41**: 1–6.

29 Kusakabe M, Kakumu E, Kurihara F, Tsuchida K, Maeda T, Tada H *et al.* Histone deacetylation regulates nucleotide excision repair through an interaction with the XPC protein. *iScience* 2022; **25**: 99–138.

30 Kokic G, Chernev A, Tegunov D, Dienemann C, Urlaub H, Cramer P. Structural basis of TFIIH activation for nucleotide excision repair. *Nat Commun* 2019; **10**: 1–9.

31 Kim J, Li C-L, Chen X, Cui Y, Golebiowski FM, Wang H *et al.* Lesion recognition by XPC, TFIIH and XPA in DNA excision repair. *Nature* 2023; **617**: 170–175.

32 Chen S, Lee L, Naila T, Fishbain S, Wang A, Tomkinson AE *et al.* Structural basis of long-range to short-range synaptic transition in NHEJ. *Nature* 2021; **593**: 294–298.

33 Chen X, Xu X, Chen Y, Cheung JC, Wang H, Jiang J *et al.* Structure of an activated DNA-PK and its implications for NHEJ. *Mol Cell* 2021; **81**: 801–810.

34 Yue X, Bai C, Xie D, Ma T, Zhou P-K. DNA-PKcs: A Multi-Faceted Player in DNA Damage Response. *Front Genet* 2020; **11**: 739–74.

35 Wang JL, Duboc C, Wu Q, Ochi T, Liang S, Tsutakawa SE *et al.* Dissection of DNA double-strand-break repair using novel single-molecule forceps. *Nat Struct Mol Biol* 2018; **25**: 482–487.

36 Whelan DR, Rothenberg E. Super-resolution mapping of cellular double-strand break resection complexes during homologous recombination. *Proc Natl Acad Sci U S A* 2021; **118**: 1–12.

37 Cejka P, Symington LS. DNA End Resection: Mechanism and Control. Annu. Rev. Genet. 2021; **55**: 285–307.

38 Whelan DR, Lee WTC, Yin Y, Ofri DM, Bermudez-Hernandez K, Keegan S *et al.* Spatiotemporal dynamics of homologous recombination repair at single collapsed replication forks. *Nat Commun* 2018; **9**: 699–713.

39 Tarsounas M, Sung P. The antitumorigenic roles of BRCA1–BARD1 in DNA

repair and replication. *Nat Rev Mol Cell Biol* 2020; **21**: 284–299.

40 Punatar RS, Martin MJ, Wyatt HDM, Chan YW, West SC. Resolution of single and double Holliday junction recombination intermediates by GEN 1. *Proc Natl Acad Sci U S A* 2017; **114**: 443–450.

41 Ranjha L, Howard SM, Cejka P. Main steps in DNA double-strand break repair: an introduction to homologous recombination and related processes. *Chromosoma* 2018; **127**: 187–214.

42 Li Q, Qian W, Zhang Y, Hu L, Chen S, Xia Y. A new wave of innovations within the DNA damage response. *Signal Transduct Target Ther* 2023; **8**: 1–26.

43 Pearl LH, Schierz AC, Ward SE, Al-Lazikani B, Pearl FMG. Therapeutic opportunities within the DNA damage response. *Nat Rev Cancer* 2015; **15**: 166–180.

44 O'Connor MJ. Targeting the DNA Damage Response in Cancer. *Mol Cell* 2015; **60**: 547–560.

45 Wang M, Chen S, Ao D. Targeting DNA repair pathway in cancer: Mechanisms and clinical application. *MedComm* 2021; **2**: 654–691.

46 Baxter JS, Zatreanu D, Pettitt SJ, Lord CJ. Resistance to DNA repair inhibitors in cancer. *Mol Oncol* 2022; **16**: 3811–3827.

47 Groelly FJ, Fawkes M, Dagg RA, Blackford AN, Tarsounas M. Targeting DNA damage response pathways in cancer. *Nat Rev Cancer* 2022; **23**: 78–94.

48 Blackford AN, Jackson SP. ATM, ATR, and DNA-PK: The Trinity at the Heart of the DNA Damage Response. *Mol Cell* 2017; **66**: 801–817.

49 Baretić D, Williams RL. PIKKs - the solenoid nest where partners and kinases meet. *Curr Opin Struct Biol* 2014; **29**: 134–142.

50 Jiang X, Sun Y, Chen S, Roy K, Price BD. The FATC domains of PIKK proteins are functionally equivalent and participate in the Tip60-dependent activation of DNA-PKcs and ATM. *J Biol Chem* 2006; **281**: 15741–15746.

51 Bosotti R, Isacchi A, Sonnhammer ELL. FAT: A novel domain in PIK-related kinases. *Trends Biochem Sci* 2000; **25**: 225–227.

52 Burger K, Ketley RF, Gullerova M. Beyond the Trinity of ATM, ATR, and DNA-PK: Multiple Kinases Shape the DNA Damage Response in Concert With RNA Metabolism. *Front Mol Biosci* 2019; **6**: 801–817.

53 So S, Davis AJ, Chen DJ. Autophosphorylation at serine 1981 stabilizes ATM at DNA damage sites. *J Cell Biol* 2009; **187**: 977–990.

54 Haahr P, Hoffmann S, Tollenaere MAX, Ho T, Toledo LI, Mann M *et al.*

Activation of the ATR kinase by the RPA-binding protein ETAA1. *Nat Cell Biol* 2016; **18**: 1196–1207.

55 Lee JH, Paull TT. Cellular functions of the protein kinase ATM and their relevance to human disease. *Nat Rev Mol Cell Biol* 2021; **22**: 796–814.

56 Paull TT, Rogakou EP, Yamazaki V, Kirchgessner CU, Gellert M, Bonner WM. A critical role for histone H2AX in recruitment of repair factors to nuclear foci after DNA damage. *Curr Biol* 2000; **10**: 886–895.

57 Kieffer SR, Lowndes NF. Immediate-Early , Early , and Late Responses to DNA Double Stranded Breaks. *Front Genet* 2022; **13**: 1–24.

58 Melchionna R, Chen XB, Blasina A, McGowan CH. Threonine 68 is required for radiation-induced phosphorylation and activation of Cds1. *Nat Cell Biol* 2000; **2**: 762–765.

59 Banin S, Moyal L, Shieh SY, Taya Y, Anderson CW, Chessa L *et al.* Enhanced phosphorylation of p53 by ATM in response to DNA damage. *Science* 1998; **281**: 1674–1677.

60 Canman CE, Lim DS, Cimprich KA, Taya Y, Tamai K, Sakaguchi K *et al.* Activation of the ATM kinase by ionizing radiation and phosphorylation of p53. *Science* 1998; **281**: 1677–1679.

61 Stewart-Ornstein J, Lahav G. Dynamics of p53 in response to DNA damage vary across cell lines and are shaped by efficiency of DNA repair and activity of the kinase ATM. *Sci Signal* 2018; **476**: 1658–1669.

62 Sur S, Agrawal DK. Phosphatases and kinases regulating CDC25 activity in the cell cycle: clinical implications of CDC25 overexpression and potential treatment strategies. Mol. Cell. Biochem. 2016; **416**: 33–46.

63 Tibbetts RS, Brumbaugh KM, Williams JM, Sarkaria JN, Cliby WA, Shieh SY *et al.* A role for ATR in the DNA damage-induced phosphorylation of p53. *Genes Dev* 1999; **13**: 152–157.

64 Chen TY, Huang BM, Tang TK, Chao YY, Xiao XY, Lee PR *et al.* Genotoxic stress-activated DNA-PK-p53 cascade and autophagy cooperatively induce ciliogenesis to maintain the DNA damage response. *Cell Death Differ* 2021; **28**: 1865–1879.

65 Thomas AF, Kelly GL, Strasser A. Of the many cellular responses activated by TP53, which ones are critical for tumour suppression? *Cell Death Differ* 2022; **29**: 961–971.

66 Wang H, Guo M, Wei H, Chen Y. Targeting p53 pathways: mechanisms, structures, and advances in therapy. *Signal Transduct Target Ther* 2023; **8**: 1–35.

67 Linzer DIH, Levine AJ. Characterization of a 54K dalton cellular SV40 tumor antigen present in SV40-transformed cells and uninfected embryonal carcinoma cells. *Cell* 1979; **17**: 43–52.

68 Lane DP, Crawford L V. T antigen is bound to a host protein in SV40-transformed cells. *Nature* 1979; **278**: 261–263.

69 Eliyahu D, Michalovitz D, Oren M. Overproduction of p53 antigen makes established cells highly tumorigenic. *Nature* 1985; **316**: 158–160.

70 Isobe M, Emanuel BS, Givol D, Oren M, Croce CM. Localization of gene for human p53 tumour antigen to band 17p13. *Nature* 1986; **320**: 84–85.

71 Ghosh M, Saha S, Li J, Montrose DC, Martinez LA. p53 engages the cGAS/STING cytosolic DNA sensing pathway for tumor suppression. *Mol Cell* 2023; **83**: 266–280.

72 Nishimura M, Takizawa Y, Nozawa K, Kurumizaka H. Structural basis for p53 binding to its nucleosomal target DNA sequence. *PNAS Nexus* 2022; **1**: 1–9.

73 El-Deiry WS, Kern SE, Pietenpol JA, Kinzler KW, Vogelstein B. Definition of a consensus binding site for p53. *Nat Genet* 1992; **1**: 45–49.

74 Hafner A, Bulyk ML, Jambhekar A, Lahav G. The multiple mechanisms that regulate p53 activity and cell fate. *Nat Rev Mol Cell Biol* 2019; **20**: 199–210.

75 Fischer M. Census and evaluation of p53 target genes. *Oncogene 2017 3628* 2017; **36**: 3943–3956.

76 Gencel-Augusto J, Lozano G. p53 tetramerization: at the center of the dominant-negative effect of mutant p53. *Genes Dev* 2020; **34**: 1128–1146.

77 Hernández Borrero LJ, El-Deiry WS. Tumor suppressor p53: Biology, signaling pathways, and therapeutic targeting. *Biochim Biophys - Rev Cancer* 2021; **1876**: 188556–188556.

78 Wells M, Tidow H, Rutherford TJ, Markwick P, Jensen MR, Mylonas E *et al.* Structure of tumor suppressor p53 and its intrinsically disordered N-terminal transactivation domain. *Proc Natl Acad Sci U S A* 2008; **105**: 5762–5767.

79 Jumper J, Evans R, Pritzel A, Green T, Figurnov M, Ronneberger O *et al.* Highly accurate protein structure prediction with AlphaFold. *Nature* 2021; **596**: 583–589.

80 Levine AJ. p53: 800 million years of evolution and 40 years of discovery. *Nat Rev Cancer* 2020; **20**: 471–480.

81 Kotler E, Shani O, Goldfeld G, Lotan-Pompan M, Tarcic O, Gershoni A *et al.* A Systematic p53 Mutation Library Links Differential Functional Impact to Cancer Mutation Pattern and Evolutionary Conservation. *Mol Cell* 2018; **71**:

178–190.

82 Wang Z, Strasser A, Kelly GL. Should mutant TP53 be targeted for cancer therapy? *Cell Death Differ* 2022; **29**: 911–920.

83 Schulz-Heddergott R, Moll UM. Gain-of-function (GOF) mutant p53 as actionable therapeutic target. *Cancers (Basel)* 2018; **10**: 1–16.

84 Boettcher S, Miller PG, Sharma R, McConkey M, Leventhal M, Krivtsov A V. *et al.* A dominant-negative effect drives selection of TP53 missense mutations in myeloid malignancies. *Science* 2019; **365**: 599–604.

85 Liu Y, Tavana O, Gu W. P53 modifications: Exquisite decorations of the powerful guardian. *J Mol Cell Biol* 2019; **11**: 564–577.

86 Kussie PH, Gorina S, Marechal V, Elenbaas B, Moreau J, Levine AJ *et al.* Structure of the MDM2 Oncoprotein Bound to the p53 Tumor Suppressor Transactivation Domain. *Science* 1996; **274**: 948–953.

87 Lee JM, Hammarén HM, Savitski MM, Baek SH. Control of protein stability by post-translational modifications. *Nat Commun* 2023; **14**: 1–16.

88 Coutts AS, Adams CJ, La Thangue NB. p53 ubiquitination by Mdm2: A never ending tail? *DNA Repair (Amst)* 2009; **8**: 483–490.

89 Li M, Brooks CL, Wu-Baer F, Chen D, Baer R, Gu W. Mono- Versus Polyubiquitination: Differential Control of p53 Fate by Mdm2. *Science* 2003; **302**: 1972–1975.

90 Haupt Y, Mayat R, Kazazt A, Orent M. Mdm2 promotes the rapid degradation of p53. *Nature* 1997; **387**: 296–299.

91 Lohrum MAE, Woods DB, Ludwig RL, Bálint É, Vousden KH. C-Terminal Ubiquitination of p53 Contributes to Nuclear Export. *Mol Cell Biol* 2001; **21**: 8521–8532.

92 Gu J, Nie L, Wiederschain D, Yuan Z-M. Identification of p53 Sequence Elements That Are Required for MDM2-Mediated Nuclear Export. *Mol Cell Biol* 2001; **21**: 8533–8546.

93 Yu DH, Xu ZY, Mo S, Yuan L, Cheng XD, Qin JJ. Targeting MDMX for Cancer Therapy: Rationale, Strategies, and Challenges. *Front Oncol* 2020; **10**: 1–14.

94 Wang X, Li Y, Yan X, Yang Q, Zhang B, Zhang Y *et al.* Recognition of an Ala-rich C-degron by the E3 ligase Pirh2. *Nat Commun* 2023; **14**: 1–12.

95 Vaddavalli PL, Schumacher B. The p53 network: cellular and systemic DNA damage responses in cancer and aging. *Trends Genet* 2022; **38**: 598–612.

96 Teufel DP, Bycroft M, Fersht AR. Regulation by phosphorylation of the relative affinities of the N- terminal transactivation domains of p53 for p300

domains and Mdm2. *Oncogene* 2009; **28**: 2112–2118.

97 Kapoor M, Lozano G. Functional activation of p53 via phosphorylation following DNA damage by UV but not γ radiation. *Proc Natl Acad Sci U S A* 1998; **95**: 2834–2837.

98 Hua LU, Taya Y, Ikeda M, Levine AJ. Ultraviolet radiation, but not γ radiation or etoposide-induced DNA damage, results in the phosphorylation of the murine p53 protein at serine-389. *Proc Natl Acad Sci U S A* 1998; **95**: 6399–6402.

99 Xia Z, Kon N, Gu AP, Tavana O, Gu W. Deciphering the acetylation code of p53 in transcription regulation and tumor suppression. *Oncogene* 2022; **41**: 3039–3050.

100 Tang Z, Chen WY, Shimada M, Nguyen UTT, Kim J, Sun XJ *et al.* SET1 and p300 Act Synergistically, through Coupled Histone Modifications, in Transcriptional Activation by p53. *Cell* 2013; **154**: 297–310.

101 Gu W, Roeder RG. Activation of p53 sequence-specific DNA binding by acetylation of the p53 C-terminal domain. *Cell* 1997; **90**: 595–606.

102 Tang Y, Luo J, Zhang W, Gu W. Tip60-Dependent Acetylation of p53 Modulates the Decision between Cell-Cycle Arrest and Apoptosis. *Mol Cell* 2006; **24**: 827–839.

103 Ito A, Kawaguchi Y, Lai CH, Kovacs JJ, Higashimoto Y, Appella E *et al.* MDM2-HDAC1-mediated deacetylation of p53 is required for its degradation. *EMBO J* 2002; **21**: 6236–6245.

104 Shikama N, Lee CW, France S, Delavaine L, Lyon J, Krstic-Demonacos M *et al.* A novel cofactor for p300 that regulates the p53 response. *Mol Cell* 1999; **4**: 365–376.

105 Demonacos C, Krstic-Demonacos M, La Thangue NB. A TPR motif cofactor contributes to p300 activity in the p53 response. *Mol Cell* 2001; **8**: 71–84.

106 Demonacos C, Krstic-Demonacos M, Smith L, Xu D, O'Connor DP, Jansson M *et al.* A new effector pathway links ATM kinase with the DNA damage response. *Nat Cell Biol* 2004; **6**: 968–976.

107 Adams CJ, Graham AL, Jansson M, Coutts AS, Edelmann M, Smith L *et al.* ATM and Chk2 kinase target the p53 cofactor Strap. *EMBO Rep* 2008; **9**: 1222–1229.

108 Coutts AS, La Thangue NB. The p53 response: Emerging levels of co-factor complexity. *Biochem Biophys Res Commun* 2005; **331**: 778–785.

109 Trigiante G, Lu X. ASPPs and cancer. *Nat Rev Cancer* 2006; **6**: 217–226.

110 Chen S, Wu J, Zhong S, Li Y, Zhang P, Ma J *et al.* iASPP mediates p53

selectivity through a modular mechanism fine-tuning DNA recognition. *Proc Natl Acad Sci U S A* 2019; **116**: 17470–17479.

111 Liebl MC, Hofmann TG. Regulating the p53 Tumor Suppressor Network at PML Biomolecular Condensates. *Cancers (Basel)* 2022; **14**: 3156–3164.

112 Cuella-Martin R, Oliveira C, Lockstone HE, Snellenberg S, Grolmusova N, Chapman JR. 53BP1 Integrates DNA Repair and p53-Dependent Cell Fate Decisions via Distinct Mechanisms. *Mol Cell* 2016; **64**: 51–64.

113 Williams AB, Schumacher B. p53 in the DNA-damage-repair process. *Cold Spring Harb Perspect Med* 2016; **6**: 851–860.

114 Tan T, Chu G. p53 Binds and Activates the Xeroderma Pigmentosum DDB2 Gene in Humans but Not Mice. *Mol Cell Biol* 2002; **22**: 3247.

115 Shivakumar C V, Brown DR, Deb S, Deb SP. Wild-type human p53 transactivates the human proliferating cell nuclear antigen promoter. *Mol Cell Biol* 1995; **15**: 6785–6793.

116 Adimoolam S, Ford JM. p53 and DNA damage-inducible expression of the xeroderma pigmentosum group C gene. *Proc Natl Acad Sci U S A* 2002; **99**: 12985–12990.

117 Krasikova Y, Rechkunova N, Lavrik O. Nucleotide excision repair: From molecular defects to neurological abnormalities. *Int J Mol Sci* 2021; **22**: 1707–1718.

118 Wang QE, Zhu Q, Wani MA, Wani G, Chen J, Wani AA. Tumor suppressor p53 dependent recruitment of nucleotide excision repair factors XPC and TFIIH to DNA damage. *DNA Repair (Amst)* 2003; **2**: 483–499.

119 Wang YH, Ho TLF, Hariharan A, Goh HC, Wong YL, Verkaik NS *et al.* Rapid recruitment of p53 to DNA damage sites directs DNA repair choice and integrity. *Proc Natl Acad Sci U S A* 2022; **119**: 1–12.

120 Braastad CD, Leguia M, Hendrickson EA. Ku86 autoantigen related protein-1 transcription initiates from a CpG island and is induced by p53 through a nearby p53 response element. *Nucleic Acids Res* 2002; **30**: 1713–1724.

121 Chang H, Pannunzio NR, Adachi N, Lieber MR. Non-homologous DNA end joining and alternative pathways to double-strand break repair. *Nat Rev Mol Cell Biol* 2017; **18**: 495–506.

122 Arias-Lopez C, Lazaro-Trueba I, Kerr P, Lord CJ, Dexter T, Iravani M *et al.* p53 modulates homologous recombination by transcriptional regulation of the RAD51 gene. *EMBO Rep* 2006; **7**: 219–224.

123 Rieckmann T, Kriegs M, Nitsch L, Hoffer K, Rohaly G, Kocher S *et al.* P53 modulates homologous recombination at I-SceI-induced double-strand

breaks through cell-cycle regulation. *Oncogene* 2013; **32**: 968–975.

124 Sirbu BM, Lachmayer SJ, Wülfing V, Marten LM, Clarkson KE, Lee LW *et al.* ATR-p53 restricts homologous recombination in response to replicative stress but does not limit DNA interstrand crosslink repair in lung cancer cells. *PLoS One* 2011; **6**: 1070–1085.

125 Coutts AS, La Thangue NB. Actin nucleation by WH2 domains at the autophagosome. *Nat Commun* 2015; **6**: 1–9.

126 Zuchero JB, Coutts AS, Quinlan ME, La Thangue NB, Mullins RD. p53-cofactor JMY is a multifunctional actin nucleation factor. *Nat Cell Biol* 2009; **11**: 451–459.

127 Coutts AS, Weston L, La Thangue NB. A transcription co-factor integrates cell adhesion and motility with the p53 response. *Proc Natl Acad Sci U S A* 2009; **106**: 19872–19877.

128 Kramer DA, Piper HK, Chen B. WASP family proteins: Molecular mechanisms and implications in human disease. *Eur J Cell Biol* 2022; **101**: 151244–151264.

129 Coutts AS, Boulahbel H, Graham A, La Thangue NB. Mdm2 targets the p53 transcription cofactor JMY for degradation. *EMBO Rep* 2007; **8**: 84–90.

130 Rodriguez-Pastrana I, Birli E, Coutts AS. p53-dependent DNA repair during the DNA damage response requires actin nucleation by JMY. *Cell Death Differ* 2023; : 1–12.

131 Coutts AS, Pires IM, Weston L, Buffa FM, Milani M, Li JL *et al.* Hypoxia-driven cell motility reflects the interplay between JMY and HIF-1α. *Oncogene* 2011; **30**: 4835–4842.

132 Muz B, de la Puente P, Azab F, Azab AK. The role of hypoxia in cancer progression, angiogenesis, metastasis, and resistance to therapy. *Hypoxia* 2015; **15**: 83–92.

133 Semenza GL. Defining the role of hypoxia-inducible factor 1 in cancer biology and therapeutics. *Oncogene* 2010; **29**: 625–634.

134 Luo Z, Tian M, Yang G, Tan Q, Chen Y, Li G *et al.* Hypoxia signaling in human health and diseases: implications and prospects for therapeutics. *Signal Transduct Target Ther* 2022; **7**: 1–30.

135 Maxwell PH, Wlesener MS, Chang GW, Clifford SC, Vaux EC, Cockman ME *et al.* The tumour suppressor protein VHL targets hypoxia-inducible factors for oxygen-dependent proteolysis. *Nature* 1999; **399**: 271–275.

136 Wang GL, Jiang BH, Rue EA, Semenza GL. Hypoxia-inducible factor 1 is a basic-helix-loop-helix-PAS heterodimer regulated by cellular O2 tension.

*Proc Natl Acad Sci U S A* 1995; **92**: 5514.

137 Hershko T, Chaussepied M, Oren M, Ginsberg D. Novel link between E2F and p53: Proapoptotic cofactors of p53 are transcriptionally upregulated by E2F. *Cell Death Differ* 2005; **12**: 377–383.

138 Nomura K, Klejnot M, Kowalczyk D, Hock AK, Sibbet GJ, Vousden KH *et al.* Structural analysis of MDM2 RING separates degradation from regulation of p53 transcription activity. *Nat Struct Mol Biol* 2017; **24**: 578–587.

139 Sitar T, Gallinger J, Ducka AM, Ikonen TP, Wohlhoefler M, Schmoller KM *et al.* Molecular architecture of the Spire-actin nucleus and its implication for actin filament assembly. *Proc Natl Acad Sci U S A* 2011; **108**: 19575–19580.

140 Quinlan ME, Heuser JE, Kerkhoff E, Mullins RD. Drosophila Spire is an actin nucleation factor. *Nature* 2005; **433**: 382–388.

141 Debnath J, Gammoh N, Ryan KM. Autophagy and autophagy-related pathways in cancer. *Nat Rev Mol Cell Biol* 2023; : 1–16.

142 Coutts AS, La Thangue NB. Regulation of actin nucleation and autophagosome formation. *Cell Mol Life Sci* 2016; **73**: 3249–3263.

143 Hu X, Mullins RD. LC3 and STRAP regulate actin filament assembly by JMY during autophagosome formation. *J Cell Biol* 2019; **218**: 251–266.

144 Johansen T, Lamark T. Selective Autophagy: ATG8 Family Proteins, LIR Motifs and Cargo Receptors. *J Mol Biol* 2020; **432**: 80–103.

145 King VL, Campellone KG. F-actin-rich territories coordinate apoptosome assembly and caspase activation during DNA damage-induced intrinsic apoptosis. *Mol Biol Cell* 2023; **34**: 1106–1121.

146 King VL, Leclair NK, Coulter AM, Campellone KG. The actin nucleation factors JMY and WHAMM enable a rapid Arp2/3 complex-mediated intrinsic pathway of apoptosis. *PLOS Genet* 2021; **17**: 242–255.

147 Zuchero JB, Belin B, Mullins RD. Actin binding to WH2 domains regulates nuclear import of the multifunctional actin regulator JMY. *Mol Biol Cell* 2012; **23**: 853–863.

148 Lappalainen P, Kotila T, Jégou A, Romet-Lemonne G. Biochemical and mechanical regulation of actin dynamics. *Nat Rev Mol Cell Biol* 2022; **23**: 836–852.

149 Ali R, Zahm JA, Rosen MK. Bound nucleotide can control the dynamic architecture of monomeric actin. *Nat Struct Mol Biol* 2022; **29**: 320–328.

150 Meenakshi S I, Rao M, Mayor S, Sowdhamini R. A census of actin-associated proteins in humans. *Front Cell Dev Biol* 2023; **11**: 1–13.

151 Alekhina O, Burstein E, Billadeau DD. Cellular functions of WASP family

proteins at a glance. *J Cell Sci* 2017; **130**: 2235–2241.

152 Campellone KG, Lebek NM, King VL. Branching out in different directions : Emerging cellular functions for the Arp2 / 3 complex and WASP-family actin nucleation factors. *Eur J Cell Biol* 2023; **102**: 151301–151324.

153 Courtemanche N. Mechanisms of formin-mediated actin assembly and dynamics. *Biophys Rev* 2018; **10**: 1553–1569.

154 Ahuja R, Pinyol R, Reichenbach N, Custer L, Klingensmith J, Kessels MM *et al.* Cordon-Bleu Is an Actin Nucleation Factor and Controls Neuronal Morphology. *Cell* 2007; **131**: 337–350.

155 Ulferts S, Prajapati B, Grosse R, Vartiainen MK. Emerging properties and functions of actin and actin filaments inside the nucleus. *Cold Spring Harb Perspect Biol* 2021; **13**: 1–16.

156 Kyheröinen S, Vartiainen MK. Nuclear actin dynamics in gene expression and genome organization. *Semin Cell Dev Biol* 2020; **102**: 105–112.

157 Dopie J, Skarp KP, Rajakylä EK, Tanhuanpää K, Vartiainen MK. Active maintenance of nuclear actin by importin 9 supports transcription. *Proc Natl Acad Sci U S A* 2012; **109**: 544–552.

158 Stüven T, Hartmann E, Görlich D. Exportin 6: A novel nuclear export receptor that is specific for profilin-actin complexes. *EMBO J* 2003; **22**: 5928–5940.

159 Sadhukhan S, Sarkar K, Taylor M, Candotti F, Vyas YM. Nuclear Role of WASp in Gene Transcription is Uncoupled from its ARP2/3-Dependent Cytoplasmic Role in Actin Polymerization. *J Immunol* 2014; **193**: 150–160.

160 Wu X, Suetsugu S, Cooper LA, Takenawa T, Guan JL. Focal Adhesion Kinase Regulation of N-WASP Subcellular Localization and Function. *J Biol Chem* 2004; **279**: 9565–9576.

161 Girbig M, Misiaszek AD, Müller CW. Structural insights into nuclear transcription by eukaryotic DNA-dependent RNA polymerases. *Nat Rev Mol Cell Biol* 2022; **23**: 603–622.

162 Almuzzaini B, Sarshad AA, Rahmanto AS, Hansson ML, Von Euler A, Sangfelt O *et al.* In β-actin knockouts, epigenetic reprogramming and rDNA transcription inactivation lead to growth and proliferation defects. *FASEB J* 2016; **30**: 2860–2873.

163 Ye J, Zhao J, Hoffmann-Rohrer U, Grummt I. Nuclear myosin I acts in concert with polymeric actin to drive RNA polymerase I transcription. *Genes Dev* 2008; **22**: 322–330.

164 Philimonenko V V., Zhao J, Iben S, Dingová H, Kyselá K, Kahle M *et al.*

Nuclear actin and myosin I are required for RNA polymerase I transcription. *Nat Cell Biol* 2004; **6**: 1165–1172.

165 Hu P, Wu S, Hernandez N. A role for β-actin in RNA polymerase III transcription. *Genes Dev* 2004; **18**: 3010–3015.

166 Viita T, Kyheröinen S, Prajapati B, Virtanen J, Frilander MJ, Varjosalo M *et al.* Nuclear actin interactome analysis links actin to KAT14 histone acetyl transferase and mRNA splicing. *J Cell Sci* 2019; **132**: 1–16.

167 Hofmann WA, Stojiljkovic L, Fuchsova B, Vargas GM, Mavrommatis E, Philimonenko V *et al.* Actin is part of pre-initiation complexes and is necessary for transcription by RNA polymerase II. *Nat Cell Biol* 2004; **6**: 1094–1101.

168 Sokolova M, Moore HM, Prajapati B, Dopie J, Meriläinen L, Honkanen M *et al.* Nuclear Actin Is Required for Transcription during Drosophila Oogenesis. *iScience* 2018; **9**: 63–70.

169 Qi T, Tang W, Wang L, Zhai L, Guo L, Zeng X. G-actin participates in RNA polymerase II-dependent transcription elongation by recruiting positive transcription elongation factor b (P-TEFb). *J Biol Chem* 2011; **286**: 15171–15181.

170 Spencer VA, Costes S, Inman JL, Xu R, Chen J, Hendzel MJ *et al.* Depletion of nuclear actin is a key mediator of quiescence in epithelial cells. *J Cell Sci* 2011; **124**: 123–132.

171 Wei M, Fan X, Ding M, Li R, Shao S, Hou Y *et al.* Nuclear actin regulates inducible transcription by enhancing RNA polymerase II clustering. *Sci Adv* 2020; **6**: 3412–3425.

172 Huang Y, Zhang S, Park J Il. Nuclear Actin Dynamics in Gene Expression, DNA Repair, and Cancer. *Results Probl. Cell Differ* 2022; **70**: 625–663.

173 Mouilleron S, Langer CA, Guettler S, McDonald NQ, Treisman R. Structure of a pentavalent G-actin•MRTF-A complex reveals how G-actin controls nucleocytoplasmic shuttling of a transcriptional coactivator. *Sci Signal* 2011; **4**: 1–11.

174 Vartiainen MK, Guettler S, Larijani B, Treisman R. Nuclear actin regulates dynamic subcellular localization and activity of the SRF cofactor MAL. *Science* 2007; **316**: 1749–1752.

175 Pawłowski R, Rajakylä EK, Vartiainen MK, Treisman R. An actin-regulated importin α/β-dependent extended bipartite NLS directs nuclear import of MRTF-A. *EMBO J* 2010; **29**: 3448–3458.

176 Caridi CP, Plessner M, Grosse R, Chiolo I. Nuclear actin filaments in DNA

repair dynamics. *Nat Cell Biol* 2019; **21**: 1068–1077.

177 Belin BJ, Lee T, Mullins RD. DNA damage induces nuclear actin filament assembly by formin-2 and spire-1/2 that promotes efficient DNA repair. *Elife* 2015; **4**: 1–21.

178 Schrank BR, Aparicio T, Li Y, Chang W, Chait BT, Gundersen GG *et al.* Nuclear ARP2/3 drives DNA break clustering for homology-directed repair. *Nature* 2018; **559**: 61–66.

179 Caridi CP, D'agostino C, Ryu T, Zapotoczny G, Delabaere L, Li X *et al.* Nuclear F-actin and myosins drive relocalization of heterochromatic breaks. *Nature* 2018; **559**: 54–60.

180 Andrin C, Mcdonald D, Attwood KM, Rodrigue A, Ghosh S, Mirzayans R *et al.* A requirement for polymerized actin in DNA double-strand break repair. *Nucleus* 2012; **3**: 384–395.

181 Wang T, Du XH, Hong Y, Hong X, Fan L, Zhou JW *et al.* WASH interacts with Ku to regulate DNA double-stranded break repair. *iScience* 2022; **25**: 103676–103694.

182 Feric M, Brangwynne CP. A nuclear F-actin scaffold stabilizes RNP droplets against gravity in large cells. *Nat Cell Biol* 2013; **15**: 1253–1259.

183 Feric M, Vaidya N, Harmon TS, Mitrea DM, Zhu L, Richardson TM *et al.* Coexisting liquid phases underlie nucleolar sub-compartments. *Cell* 2016; **165**: 1686–1696.

184 Lafontaine DLJ, Riback JA, Bascetin R, Brangwynne CP. The nucleolus as a multiphase liquid condensate. *Nat Rev Mol Cell Biol* 2020; **22**: 165–182.

185 Todorovski V, Fox AH, Choi YS. Matrix stiffness-sensitive long noncoding RNA NEAT1 seeded paraspeckles in cancer cells. *Mol Biol Cell* 2020; **31**: 1654–1662.

186 Todorovski V, McCluggage F, Li Y, Meid A, Spatz JP, Holle AW *et al.* Confined environments induce polarized paraspeckle condensates. *Commun Biol* 2023; **6**: 1–6.

187 Liu C, Gao X, Li Y, Sun W, Xu Y, Tan Y *et al.* The mechanosensitive lncRNA Neat1 promotes osteoblast function through paraspeckle-dependent Smurf1 mRNA retention. *Bone Res 2022 101* 2022; **10**: 1–16.

188 Yamazaki T, Souquere S, Chujo T, Kobelke S, Chong YS, Fox AH *et al.* Functional Domains of NEAT1 Architectural lncRNA Induce Paraspeckle Assembly through Phase Separation. *Mol Cell* 2018; **70**: 1038–1053.

189 Yamazaki T, Yamamoto T, Yoshino H, Souquere S, Nakagawa S, Pierron G *et al.* Paraspeckles are constructed as block copolymer micelles. *EMBO*

*J* 2021; **40**: 107270–107289.

190 Nojima T, Proudfoot NJ. Mechanisms of lncRNA biogenesis as revealed by nascent transcriptomics. *Nat Rev Mol Cell Biol* 2022; **23**: 389–406.

191 Slack FJ, Chinnaiyan AM. The Role of Non-coding RNAs in Oncology. *Cell* 2019; **179**: 1033–1055.

192 Mattick JS, Amaral PP, Carninci P, Carpenter S, Chang HY, Chen LL *et al.* Long non-coding RNAs: definitions, functions, challenges and recommendations. *Nat Rev Mol Cell Biol* 2023; **24**: 430–447.

193 Deveson IW, Hardwick SA, Mercer TR, Mattick JS. The Dimensions, Dynamics, and Relevance of the Mammalian Noncoding Transcriptome. *Trends Genet* 2017; **33**: 464–478.

194 Iyer MK, Niknafs YS, Malik R, Singhal U, Sahu A, Hosono Y *et al.* The landscape of long noncoding RNAs in the human transcriptome. *Nat Genet* 2015; **47**: 199–208.

195 Hon CC, Ramilowski JA, Harshbarger J, Bertin N, Rackham OJL, Gough J *et al.* An atlas of human long non-coding RNAs with accurate 5' ends. *Nature* 2017; **543**: 199–204.

196 Kopp F, Mendell JT. Functional Classification and Experimental Dissection of Long Noncoding RNAs. *Cell* 2018; **172**: 393–407.

197 Gil N, Ulitsky I. Regulation of gene expression by cis-acting long non-coding RNAs. *Nat Rev Genet* 2019; **21**: 102–117.

198 Reddy D, Bhattacharya S, Levy M, Zhang Y, Gogol M, Li H *et al.* Paraspeckles interact with SWI/SNF subunit ARID1B to regulate transcription and splicing. *EMBO Rep* 2023; **24**: 22–29.

199 West JA, Davis CP, Sunwoo H, Simon MD, Sadreyev RI, Wang PI *et al.* The Long Noncoding RNAs NEAT1 and MALAT1 Bind Active Chromatin Sites. *Mol Cell* 2014; **55**: 791–802.

200 Roden C, Gladfelter AS. RNA contributions to the form and function of biomolecular condensates. *Nat Rev Mol Cell Biol* 2020; **22**: 183–195.

201 Tripathi V, Ellis JD, Shen Z, Song DY, Pan Q, Watt AT *et al.* The Nuclear-Retained Noncoding RNA MALAT1 Regulates Alternative Splicing by Modulating SR Splicing Factor Phosphorylation. *Mol Cell* 2010; **39**: 925–935.

202 Liu SJ, Dang HX, Lim DA, Feng FY, Maher CA. Long noncoding RNAs in cancer metastasis. *Nat Rev Cancer* 2021; **21**: 446–460.

203 Gao Y, Wang P, Wang Y, Ma X, Zhi H, Zhou D *et al.* Lnc2Cancer v2.0: updated database of experimentally supported long non-coding RNAs in

human cancers. *Nucleic Acids Res* 2019; **47**: 1028–1033.

204 Carlevaro-Fita J, Lanzós A, Feuerbach L, Hong C, Mas-Ponte D, Pedersen JS *et al.* Cancer LncRNA Census reveals evidence for deep functional conservation of long noncoding RNAs in tumorigenesis. *Commun Biol* 2020; **3**: 1–16.

205 Esposito R, Bosch N, Lanzós A, Polidori T, Pulido-Quetglas C, Johnson R. Hacking the Cancer Genome: Profiling Therapeutically Actionable Long Non-coding RNAs Using CRISPR-Cas9 Screening. *Cancer Cell* 2019; **35**: 545–557.

206 Huarte M, Guttman M, Feldser D, Garber M, Koziol MJ, Kenzelmann-Broz D *et al.* A large intergenic noncoding RNA induced by p53 mediates global gene repression in the p53 response. *Cell* 2010; **142**: 409–419.

207 Adriaens C, Standaert L, Barra J, Latil M, Verfaillie A, Kalev P *et al.* P53 induces formation of NEAT1 lncRNA-containing paraspeckles that modulate replication stress response and chemosensitivity. *Nat Med* 2016; **22**: 861–868.

208 Hirose T, Yamazaki T, Nakagawa S. Molecular anatomy of the architectural NEAT1 noncoding RNA: The domains, interactors, and biogenesis pathway required to build phase-separated nuclear paraspeckles. *Wiley Interdiscip Rev RNA* 2019; **10**: 124–135.

209 Fox AH, Lam YW, Leung AKL, Lyon CE, Andersen J, Mann M *et al.* Paraspeckles : A Novel Nuclear Domain. *Curr Biol* 2002; **12**: 13–25.

210 Fox AH, Nakagawa S, Hirose T, Bond CS. Paraspeckles: Where Long Noncoding RNA Meets Phase Separation. *Trends Biochem Sci* 2018; **43**: 124–135.

211 Jain AK. Emerging roles of long non-coding RNAs in the p53 network. *RNA Biol* 2020; **17**: 1648.

212 Naganuma T, Nakagawa S, Tanigawa A, Sasaki YF, Goshima N, Hirose T. Alternative 3′-end processing of long noncoding RNA initiates construction of nuclear paraspeckles. *EMBO J* 2012; **31**: 4020–4034.

213 Sunwoo H, Dinger ME, Wilusz JE, Amaral PP, Mattick JS, Spector DL. Men ε/β nuclear-retained non-coding RNAs are up-regulated upon muscle differentiation and are essential components of paraspeckles. *Genome Res* 2009; **19**: 347–359.

214 Barra J, Gaidos GS, Blumenthal E, Beckedorff F, Tayar MM, Kirstein N *et al.* Integrator restrains paraspeckles assembly by promoting isoform switching of the lncRNA NEAT1. *Sci Adv* 2020; **6**: 1–17.

215 Modic M, Grosch M, Rot G, Schirge S, Lepko T, Yamazaki T *et al.* Cross-Regulation between TDP-43 and Paraspeckles Promotes Pluripotency-Differentiation Transition. *Mol Cell* 2019; **74**: 951–965.

216 McCluggage F, Fox AH. Paraspeckle nuclear condensates: Global sensors of cell stress? *BioEssays* 2021; **43**: 2121–2132.

217 Blume CJ, Hotz-Wagenblatt A, Hüllein J, Sellner L, Jethwa A, Stolz T *et al.* P53-dependent non-coding RNA networks in chronic lymphocytic leukemia. *Leukemia* 2015; **29**: 2015–2023.

218 Mello SS, Sinow C, Raj N, Mazur PK, Bieging-Rolett K, Broz DK *et al.* Neat1 is a p53-inducible lincRNA essential for transformation suppression. *Genes Dev* 2017; **31**: 1095–1108.

219 Adriaens C, Rambow F, Bervoets G, Silla T, Mito M, Chiba T *et al.* The long noncoding RNA NEAT1_1 is seemingly dispensable for normal tissue homeostasis and cancer cell growth. *RNA* 2019; **25**: 1681–1695.

220 Godet AC, Roussel E, David F, Hantelys F, Morfoisse F, Alves J *et al.* Long non-coding RNA Neat1 and paraspeckle components are translational regulators in hypoxia. *Elife* 2022; **11**: 69162–69199.

221 Choudhry H, Albukhari A, Morotti M, Haider S, Moralli D, Smythies J *et al.* Tumor hypoxia induces nuclear paraspeckle formation through HIF-2α dependent transcriptional activation of NEAT1 leading to cancer cell survival. *Oncogene* 2015; **34**: 4482–4490.

222 Hirose T, Virnicchi G, Tanigawa A, Naganuma T, Li R, Kimura H *et al.* NEAT1 long noncoding RNA regulates transcription via protein sequestration within subnuclear bodies. *Mol Biol Cell* 2014; **25**: 169–183.

223 Wang Y, Hu S Bin, Wang MR, Yao RW, Wu D, Yang L *et al.* Genome-wide screening of NEAT1 regulators reveals cross-regulation between paraspeckles and mitochondria. *Nat Cell Biol* 2018; **20**: 1145–1158.

224 Zhang M, Zheng Y, Sun Y, Li S, Chen L, Jin X *et al.* Knockdown of NEAT1 induces tolerogenic phenotype in dendritic cells by inhibiting activation of NLRP3 inflammasome. *Theranostics* 2019; **9**: 3425–3442.

225 Zeng C, Liu S, Lu S, Yu X, Lai J, Wu Y *et al.* The c-Myc-regulated lncRNA NEAT1 and paraspeckles modulate imatinib-induced apoptosis in CML cells. *Mol Cancer* 2018; **17**: 1–6.

226 Souquere S, Beauclair G, Harper F, Fox A, Pierron G. Highly ordered spatial organization of the structural long noncoding NEAT1 RNAs within paraspeckle nuclear bodies. *Mol Biol Cell* 2010; **21**: 4020–4027.

227 Hennig S, Kong G, Mannen T, Sadowska A, Kobelke S, Blythe A *et al.* Prion-

like domains in RNA binding proteins are essential for building subnuclear paraspeckles. *J Cell Biol* 2015; **210**: 529–539.

228 Nakagawa S, Yamazaki T, Hirose T. Molecular dissection of nuclear paraspeckles: Towards understanding the emerging world of the RNP milieu. *Open Biol* 2018; **8**: 180150–180163.

229 Li R, Harvey AR, Hodgetts SI, Fox AH. Functional dissection of NEAT1 using genome editing reveals substantial localization of the NEAT1_1 isoform outside paraspeckles. *RNA* 2017; **23**: 872–881.

230 West JA, Mito M, Kurosaka S, Takumi T, Tanegashima C, Chujo T *et al.* Structural, super-resolution microscopy analysis of paraspeckle nuclear body organization. *J Cell Biol* 2016; **214**: 817–830.

231 Wang Z, Zhao Y, Xu N, Zhang S, Wang S, Mao Y *et al.* NEAT1 regulates neuroglial cell mediating Aβ clearance via the epigenetic regulation of endocytosis-related genes expression. *Cell Mol Life Sci* 2019; **76**: 3005–3018.

232 Imamura K, Imamachi N, Akizuki G, Kumakura M, Kawaguchi A, Nagata K *et al.* Long Noncoding RNA NEAT1-Dependent SFPQ Relocation from Promoter Region to Paraspeckle Mediates IL8 Expression upon Immune Stimuli. *Mol Cell* 2014; **53**: 393–406.

233 Wang Z, Li K, Huang W. Long non-coding RNA NEAT1-centric gene regulation. *Cell Mol Life Sci* 2020; **77**: 3769–3779.

234 Prasanth K V., Prasanth SG, Xuan Z, Hearn S, Freier SM, Bennett CF *et al.* Regulating gene expression through RNA nuclear retention. *Cell* 2005; **123**: 249–263.

235 Ben-Zvi M, Amariglio N, Paret G, Nevo-Caspi Y. F11R Expression upon Hypoxia Is Regulated by RNA Editing. *PLoS One* 2013; **8**: 1–12.

236 Chen LL, Carmichael GG. Altered Nuclear Retention of mRNAs Containing Inverted Repeats in Human Embryonic Stem Cells: Functional Role of a Nuclear Noncoding RNA. *Mol Cell* 2009; **35**: 467–478.

237 Matera AG, Wang Z. A day in the life of the spliceosome. *Nat Rev Mol Cell Biol* 2014; **15**: 108–121.

238 Wilkinson ME, Charenton C, Nagai K. RNA Splicing by the Spliceosome. *Annu Rev Biochem* 2020; **89**: 359–388.

239 Akinyi M V., Frilander MJ. At the Intersection of Major and Minor Spliceosomes: Crosstalk Mechanisms and Their Impact on Gene Expression. *Front Genet* 2021; **12**: 61–76.

240 Kretova M, Selicky T, Cipakova I, Cipak L. Regulation of Pre-mRNA

Splicing: Indispensable Role of Post-Translational Modifications of Splicing Factors. *Life* 2023; **13**: 604–629.

241 Pomeranz Krummel DA, Oubridge C, Leung AKW, Li J, Nagai K. Crystal structure of human spliceosomal U1 snRNP at 5.5Å resolution. *Nature* 2009; **458**: 475–480.

242 Selenko P, Gregorovic G, Sprangers R, Stier G, Rhani Z, Krä A. Structural Basis for the Molecular Recognition between Human Splicing Factors U2AF 65 and SF1/mBBP protein/protein interactions to align the 5 and 3 splice sites. The spliceosome is assembled in a stepwise manner. *Mol Cell* 2003; **11**: 965–976.

243 Schmitzová J, Cretu C, Dienemann C, Urlaub H, Pena V. Structural basis of catalytic activation in human splicing. *Nature* 2023; **1**: 1–9.

244 Cretu C, Schmitzová J, Ponce-Salvatierra A, Dybkov O, De Laurentiis EI, Sharma K *et al.* Molecular Architecture of SF3b and Structural Consequences of Its Cancer-Related Mutations. *Mol Cell* 2016; **64**: 307–319.

245 Zhang Z, Rigo N, Dybkov O, Fourmann JB, Will CL, Kumar V *et al.* Structural insights into how Prp5 proofreads the pre-mRNA branch site. *Nature* 2021; **596**: 296–300.

246 Boesler C, Rigo N, Anokhina MM, Tauchert MJ, Agafonov DE, Kastner B *et al.* A spliceosome intermediate with loosely associated tri-snRNP accumulates in the absence of Prp28 ATPase activity. *Nat Commun* 2016; **7**: 46–60.

247 Bertram K, Agafonov DE, Dybkov O, Haselbach D, Leelaram MN, Will CL *et al.* Cryo-EM Structure of a Pre-catalytic Human Spliceosome Primed for Activation. *Cell* 2017; **170**: 701–713.

248 Townsend C, Leelaram MN, Agafonov DE, Dybkov O, Will CL, Bertram K *et al.* Mechanism of protein-guided folding of the active site U2/U6 RNA during spliceosome activation. *Science* 2020; **370**: 3753–3766.

249 Pacheco-Fiallos B, Vorländer MK, Riabov-Bassat D, O FJ, Ayala FI, Schellhaas U *et al.* Nuclear mRNA recognition and packaging by the human transcription-export complex. *Nature* 2023; **616**: 828–839.

250 Fica SM, Oubridge C, Wilkinson ME, Newman AJ, Nagai K. A human postcatalytic spliceosome structure reveals essential roles of metazoan factors for exon ligation. *Science* 2019; **363**: 710–714.

251 Bradley RK, Anczuków O. RNA splicing dysregulation and the hallmarks of cancer. *Nat Rev Cancer* 2023; **1**: 1–21.

252 Pan Q, Shai O, Lee LJ, Frey BJ, Blencowe BJ. Deep surveying of alternative splicing complexity in the human transcriptome by high-throughput sequencing. *Nat Genet* 2008; **40**: 1413–1415.

253 Wang Y, Liu J, Huang B, Xu Y-M, Li J, Huang L-F *et al.* Mechanism of alternative splicing and its regulation. *Biomed Reports* 2015; **3**: 152–158.

254 Warren CFA, Wong-Brown MW, Bowden NA. BCL-2 family isoforms in apoptosis and cancer. *Cell Death Dis* 2019; **10**: 176–188.

255 Li Z, Li Q, Han L, Tian N, Liang Q, Li Y *et al.* Pro-apoptotic effects of splice-switching oligonucleotides targeting Bcl-x pre-mRNA in human glioma cell lines. *Oncol Rep* 2016; **35**: 1013–1019.

256 Stanley RF, Abdel-Wahab O. Dysregulation and therapeutic targeting of RNA splicing in cancer. *Nat Cancer* 2022; **3**: 536–546.

257 Wright CJ, Smith CWJ, Jiggins CD. Alternative splicing as a source of phenotypic diversity. *Nat Rev Genet* 2022; **23**: 697–710.

258 Kahles A, Lehmann K Van, Toussaint NC, Hüser M, Stark SG, Sachsenberg T *et al.* Comprehensive Analysis of Alternative Splicing Across Tumors from 8,705 Patients. *Cancer Cell* 2018; **34**: 211–224.

259 Seiler M, Peng S, Agrawal AA, Palacino J, Teng T, Zhu P *et al.* Somatic Mutational Landscape of Splicing Factor Genes and Their Functional Consequences across 33 Cancer Types. *Cell Rep* 2018; **23**: 282–296.

260 Alsafadi S, Houy A, Battistella A, Popova T, Wassef M, Henry E *et al.* Cancer-associated SF3B1 mutations affect alternative splicing by promoting alternative branchpoint usage. *Nat Commun* 2016; **7**: 10615–10627.

261 Wang L, Brooks AN, Fan J, Wan Y, Gambe R, Li S *et al.* Transcriptomic characterization of SF3B1 mutation reveals its pleiotropic effects in chronic lymphocytic leukemia. *Cancer Cell* 2016; **30**: 750–763.

262 Zhang J, Ali AM, Lieu YK, Liu Z, Gao J, Rabadan R *et al.* Disease-Causing Mutations in SF3B1 Alter Splicing by Disrupting Interaction with SUGP1. *Mol Cell* 2019; **76**: 82–95.

263 Chang Y, Zhao Y, Wang L, Wu M, He C, Huang M *et al.* PHF5A promotes colorectal cancerprogression by alternative splicing of TEAD2. *Mol Ther - Nucleic Acids* 2021; **26**: 1215–1227.

264 Wang Z, Yang X, Liu C, Li X, Zhang B, Wang B *et al.* Acetylation of PHF5A Modulates Stress Responses and Colorectal Carcinogenesis through Alternative Splicing-Mediated Upregulation of KDM3A. *Mol Cell* 2019; **74**: 1250–1263.

265 Zheng YZ, Xue MZ, Shen HJ, Li XG, Ma D, Gong Y *et al.* PHF5A

epigenetically inhibits apoptosis to promote breast cancer progression. *Cancer Res* 2018; **78**: 3190–3206.

266 Siebring-Van Olst E, Blijlevens M, de Menezes RX, van der Meulen-Muileman IH, Smit EF, van Beusechem VW. A genome-wide siRNA screen for regulators of tumor suppressor p53 activity in human non-small cell lung cancer cells identifies components of the RNA splicing machinery as targets for anticancer treatment. *Mol Oncol* 2017; **11**: 534–551.

267 Kato K, Udagawa R, Hayashi Y, Maki M, Yanagida M, Higashiura S *et al.* SF3B14 is involved in the centrosome regulation trough splicing of TUBGCP6 pre-mRNA. *Biochem Biophys Res Commun* 2022; **588**: 133–139.

268 Urbanski L, Brugiolo M, Park SH, Angarola BL, Leclair NK, Yurieva M *et al.* MYC regulates a pan-cancer network of co-expressed oncogenic splicing factors. *Cell Rep* 2022; **41**: 1–8.

269 Yuan B, Zhou X, Suzuki K, Ramos-Mandujano G, Wang M, Tehseen M *et al.* Wiskott-Aldrich syndrome protein forms nuclear condensates and regulates alternative splicing. *Nat Commun* 2022; **13**: 3646–3666.

270 Bonnal SC, López-Oreja I, Valcárcel J. Roles and mechanisms of alternative splicing in cancer — implications for care. *Nat Rev Clin Oncol* 2020; **17**: 457–474.

271 Kotake Y, Sagane K, Owa T, Mimori-Kiyosue Y, Shimizu H, Uesugi M *et al.* Splicing factor SF3b as a target of the antitumor natural product pladienolide. *Nat Chem Biol* 2007; **3**: 570–575.

272 Cretu C, Agrawal AA, Cook A, Will CL, Fekkes P, Smith PG *et al.* Structural Basis of Splicing Modulation by Antitumor Macrolide Compounds. *Mol Cell* 2018; **70**: 265–273.

273 Caizzi L, Monteiro-Martins S, Schwalb B, Lysakovskaia K, Schmitzova J, Sawicka A *et al.* Efficient RNA polymerase II pause release requires U2 snRNP function. *Mol Cell* 2021; **81**: 1920–1934.

274 Kashyap MK, Kumar D, Villa R, La Clair JJ, Benner C, Sasik R *et al.* Targeting the spliceosome in chronic lymphocytic leukemia with the macrolides FD-895 and pladienolide-B. *Haematologica* 2015; **100**: 945–954.

275 Arrest PCG, Kaida D, Satoh T, Ishida K, Yoshimoto R. A Truncated Form of the p27 Cyclin-Dependent Kinase Inhibitor Translated from Pre-mRNA Causes G2-Phase Arrest. *Mol Cell Biol* 2022; **42**: 1–17.

276 Zhang Y, Yuan Z, Jiang Y, Shen R, Gu M, Xu W *et al.* Inhibition of splicing

factor 3b subunit 1 (SF3B1) reduced cell proliferation, induced apoptosis and resulted in cell cycle arrest by regulating homeobox A10 (HOXA10) splicing in AGS and MKN28 human gastric cancer cells. *Med Sci Monit* 2020; **26**: 1–10.

277 Popli P, Richters MM, Chadchan SB, Kim TH, Tycksen E, Griffith O *et al.* Splicing factor SF3B1 promotes endometrial cancer progression via regulating KSR2 RNA maturation. *Cell Death Dis* 2020; **11**: 842–855.

278 Vanzyl EJ, Rick KRC, Blackmore AB, MacFarlane EM, McKay BC. Flow cytometric analysis identifies changes in S and M phases as novel cell cycle alterations induced by the splicing inhibitor isoginkgetin. *PLoS One* 2018; **13**: 1–13.

279 Vanzyl EJ, Sayed H, Blackmore AB, Rick KRC, Fernando P, McKay BC. The spliceosome inhibitors isoginkgetin and pladienolide B induce ATF3-dependent cell death. *PLoS One* 2020; **15**: 224953–224965.

280 Teng T, Tsai JH, Puyang X, Seiler M, Peng S, Prajapati S *et al.* Splicing modulators act at the branch point adenosine binding pocket defined by the PHF5A-SF3b complex. *Nat Commun* 2017; **8**: 1–16.

281 Yokoi A, Kotake Y, Takahashi K, Kadowaki T, Matsumoto Y, Minoshima Y *et al.* Biological validation that SF3b is a target of the antitumor macrolide pladienolide. *FEBS J* 2011; **278**: 4870–4880.

282 O'Brien K, Matlin AJ, Lowell AM, Moore MJ. The biflavonoid isoginkgetin is a general inhibitor of pre-mRNA splicing. *J Biol Chem* 2008; **283**: 33147–33154.

283 Wang Z, Wang S, Qin J, Zhang X, Lu G, Liu H *et al.* Splicing factor BUD31 promotes ovarian cancer progression through sustaining the expression of anti-apoptotic BCL2L12. *Nat Commun* 2022; **13**: 6246–6264.

284 Heinhuis B, Plantinga TS, Semango G, Küsters B, Netea MG, Dinarello CA *et al.* Alternatively spliced isoforms of IL-32 differentially influence cell death pathways in cancer cell lines. *Carcinogenesis* 2015; **37**: 197–205.

285 Tsalikis J, Abdel-Nour M, Farahvash A, Sorbara MT, Poon S, Philpott DJ *et al.* Isoginkgetin, a Natural Biflavonoid Proteasome Inhibitor, Sensitizes Cancer Cells to Apoptosis via Disruption of Lysosomal Homeostasis and Impaired Protein Clearance. *Mol Cell Biol* 2019; **39**: 18–35.

286 González-Rodríguez P, Klionsky DJ, Joseph B. Autophagy regulation by RNA alternative splicing and implications in human diseases. *Nat Commun* 2022; **13**: 1–17.

287 Darrigrand R, Pierson A, Rouillon M, Renko D, Boulpicante M, Bouyssié D

*et al.* Isoginkgetin derivative IP2 enhances the adaptive immune response against tumor antigens. *Commun Biol* 2021; **4**: 269–283.

288 Møller P, Azqueta A, Boutet-Robinet E, Koppen G, Bonassi S, Milić M *et al.* Minimum Information for Reporting on the Comet Assay (MIRCA): recommendations for describing comet assay procedures and results. *Nat Protoc* 2020; **15**: 3817–3826.

289 Gyori BM, Venkatachalam G, Thiagarajan PS, Hsu D, Clement MV. OpenComet: an automated tool for comet assay image analysis. *Redox Biol* 2014; **2**: 457–465.

290 Schindelin J, Arganda-Carreras I, Frise E, Kaynig V, Longair M, Pietzsch T *et al.* Fiji: An open-source platform for biological-image analysis. *Nat Methods* 2012; **9**: 676–682.

291 Schroeder A, Mueller O, Stocker S, Salowsky R, Leiber M, Gassmann M *et al.* The RIN: An RNA integrity number for assigning integrity values to RNA measurements. *BMC Mol Biol* 2006; **7**: 1–12.

292 Untergasser A, Nijveen H, Rao X, Bisseling T, Geurts R, Leunissen JAM. Primer3Plus, an enhanced web interface to Primer3. *Nucleic Acids Res* 2007; **35**: 71–74.

293 Altschul SF, Gish W, Miller W, Myers EW, Lipman DJ. Basic local alignment search tool. *J Mol Biol* 1990; **215**: 403–410.

294 Kuhn RM, Haussler D, James Kent W. The UCSC genome browser and associated tools. *Brief Bioinform* 2013; **14**: 144–161.

295 Rao X, Huang X, Zhou Z, Lin X. An improvement of the 2ˆ(-delta delta CT) method for quantitative real-time polymerase chain reaction data analysis. *Biostat Bioinforma Biomath* 2013; **3**: 71–85.

296 Stirling DR, Swain-Bowden MJ, Lucas AM, Carpenter AE, Cimini BA, Goodman A. CellProfiler 4: improvements in speed, utility and usability. *BMC Bioinformatics* 2021; **22**: 433–444.

297 Herbert AD, Carr AM, Hoffmann E, Lichten M. FindFoci: A focus detection algorithm with automated parameter training that closely matches human assignments, reduces human inconsistencies and increases speed of analysis. *PLoS One* 2014; **9**: 114749–114782.

298 Rieger AM, Nelson KL, Konowalchuk JD, Barreda DR. Modified annexin V/propidium iodide apoptosis assay for accurate assessment of cell death. *J Vis Exp* 2011; **50**: 2597–2601.

299 Mahale S, Setia M, Prajapati B, Subhash S, Yadav MP, Thankaswamy Kosalai S *et al.* HnRNPK maintains single strand RNA through controlling

double-strand RNA in mammalian cells. *Nat Commun* 2022; **13**.

300 Consortium TIP-CA of WG. Pan-cancer analysis of whole genomes. *Nature* 2020; **578**: 82–93.

301 Cerami E, Gao J, Dogrusoz U, Gross BE, Sumer SO, Aksoy BA *et al.* The cBio Cancer Genomics Portal: An open platform for exploring multidimensional cancer genomics data. *Cancer Discov* 2012; **2**: 401–404.

302 The Galaxy Community. The Galaxy platform for accessible, reproducible and collaborative biomedical analyses: 2022 update. *Nucleic Acids Res* 2022; **50**: 345–351.

303 Martin M. Cutadapt removes adapter sequences from high-throughput sequencing reads. *EMBnet.journal* 2011; **17**: 10.

304 Kim D, Pertea G, Trapnell C, Pimentel H, Kelley R, Salzberg SL. TopHat2: Accurate alignment of transcriptomes in the presence of insertions, deletions and gene fusions. *Genome Biol* 2013; **14**: 1–13.

305 Anders S, Pyl PT, Huber W. HTSeq-A Python framework to work with high-throughput sequencing data. *Bioinformatics* 2015; **31**: 166–169.

306 Conesa A, Madrigal P, Tarazona S, Gomez-Cabrero D, Cervera A, McPherson A *et al.* A survey of best practices for RNA-seq data analysis. *Genome Biol* 2016; **17**: 1–19.

307 Love MI, Huber W, Anders S. Moderated estimation of fold change and dispersion for RNA-seq data with DESeq2. *Genome Biol* 2014; **15**: 1–21.

308 Reimand J, Isserlin R, Voisin V, Kucera M, Tannus-Lopes C, Rostamianfar A *et al.* Pathway enrichment analysis and visualization of omics data using g:Profiler, GSEA, Cytoscape and EnrichmentMap. *Nat Protoc* 2019; **14**: 482–517.

309 Raudvere U, Kolberg L, Kuzmin I, Arak T, Adler P, Peterson H *et al.* G:Profiler: A web server for functional enrichment analysis and conversions of gene lists (2019 update). *Nucleic Acids Res* 2019; **47**: 191–198.

310 Shannon P, Markiel A, Ozier O, Baliga NS, Wang JT, Ramage D *et al.* Cytoscape: A Software Environment for Integrated Models of Biomolecular Interaction Networks. *Genome Res* 2003; **13**: 2498.

311 Dobin A, Davis CA, Schlesinger F, Drenkow J, Zaleski C, Jha S *et al.* STAR: Ultrafast universal RNA-seq aligner. *Bioinformatics* 2013; **29**: 15–21.

312 Tarasov A, Vilella AJ, Cuppen E, Nijman IJ, Prins P. Sambamba: Fast processing of NGS alignment formats. *Bioinformatics* 2015; **31**: 2032–2034.

313 Ferrer-Bonsoms JA, Gimeno M, Olaverri D, Sacristan P, Lobato C, Castilla C *et al.* EventPointer 3.0: flexible and accurate splicing analysis that

includes studying the differential usage of protein-domains. *NAR Genomics Bioinforma* 2022; **4**: 1–16.

314 Goldstein LD, Cao Y, Pau G, Lawrence M, Wu TD, Seshagiri S *et al.* Prediction and quantification of splice events from RNA-seq data. *PLoS One* 2016; **11**: 1–18.

315 Tufegdžić Vidaković A, Mitter R, Kelly GP, Neumann M, Harreman M, Rodríguez-Martínez M *et al.* Regulation of the RNAPII Pool Is Integral to the DNA Damage Response. *Cell* 2020; **180**: 1245–1261.

316 Stark R, Grzelak M. RNA sequencing: the teenage years. *Nat Rev Genet* 2019; **20**: 631–656.

317 Tarazona S, García-Alcalde F, Dopazo J, Ferrer A, Conesa A. Differential expression in RNA-seq: A matter of depth. *Genome Res* 2011; **21**: 2213–2223.

318 Mortazavi A, Williams BA, McCue K, Schaeffer L, Wold B. Mapping and quantifying mammalian transcriptomes by RNA-Seq. *Nat Methods* 2008; **5**: 621–628.

319 Zhao S, Zhang Y, Gamini R, Zhang B, Von Schack D. Evaluation of two main RNA-seq approaches for gene quantification in clinical RNA sequencing: PolyA+ selection versus rRNA depletion. *Sci Rep* 2018; **8**: 1–12.

320 Afgan E, Baker D, Batut B, Van Den Beek M, Bouvier D, Ech M *et al.* The Galaxy platform for accessible, reproducible and collaborative biomedical analyses: 2018 update. *Nucleic Acids Res* 2018; **46**: 537–544.

321 Deschamps-Francoeur G, Simoneau J, Scott MS. Handling multi-mapped reads in RNA-seq. *Comput Struct Biotechnol J* 2020; **18**: 1569–1576.

322 Lee S, Zhang AY, Su S, Ng AP, Holik AZ, Asselin-Labat M-L *et al.* Covering all your bases: incorporating intron signal from RNA-seq data. *NAR Genomics Bioinforma* 2020; **2**: 1010752–1010764.

323 Engström PG, Steijger T, Sipos B, Grant GR, Kahles A, Consortium TR *et al.* Systematic evaluation of spliced alignment programs for RNA-seq data. *Nat Methods* 2013; **10**: 1185-1191.

324 Corchete LA, Rojas EA, Alonso-López D, De Las Rivas J, Gutiérrez NC, Burguillo FJ. Systematic comparison and assessment of RNA-seq procedures for gene expression quantitative analysis. *Sci Rep* 2020; **10**: 1–15.

325 Shkreta L, Chabot B. The RNA Splicing Response to DNA Damage. *Biomolecules* 2015; **5**: 2935–2977.

326 Burma S, Chen BP, Murphy M, Kurimasa A, Chen DJ. ATM Phosphorylates Histone H2AX in Response to DNA Double-strand Breaks. *J Biol Chem* 2001; **276**: 42462–42467.

327 Ward IM, Chen J. Histone H2AX Is Phosphorylated in an ATR-dependent Manner in Response to Replicational Stress. *J Biol Chem* 2001; **276**: 47759–47762.

328 Singh NP. The comet assay: Reflections on its development, evolution and applications. *Mutat Res Mutat Res* 2016; **767**: 23–30.

329 Martinez-Pastor B, Silveira GG, Clarke TL, Chung D, Gu Y, Cosentino C *et al.* Assessing kinetics and recruitment of DNA repair factors using high content screens. *Cell Rep* 2021; **37**: 110176–110201.

330 Nolen BJ, Tomasevic N, Russell A, Pierce DW, Jia Z, McCormick CD *et al.* Characterization of two classes of small molecule inhibitors of Arp2/3 complex. *Nature* 2009; **460**: 1031–1034.

331 Campbell PJ, Getz G, Korbel JO, Stuart JM, Jennings JL, Stein LD *et al.* Pan-cancer analysis of whole genomes. *Nature* 2020; **578**: 82–93.

332 Alexandrov LB, Kim J, Haradhvala NJ, Huang MN, Tian Ng AW, Wu Y *et al.* The repertoire of mutational signatures in human cancer. *Nature* 2020; **578**: 94–101.

333 Reyna MA, Haan D, Paczkowska M, Verbeke LPC, Vazquez M, Kahraman A *et al.* Pathway and network analysis of more than 2500 whole cancer genomes. *Nat Commun* 2020; **11**: 1–17.

334 Zhang Y, Chen F, Fonseca NA, He Y, Fujita M, Nakagawa H *et al.* High-coverage whole-genome analysis of 1220 cancers reveals hundreds of genes deregulated by rearrangement-mediated cis-regulatory alterations. *Nat Commun* 2020; **11**: 1–14.

335 Hafner A, Stewart-Ornstein J, Purvis JE, Forrester WC, Bulyk ML, Lahav G. P53 pulses lead to distinct patterns of gene expression albeit similar DNA-binding dynamics. *Nat Struct Mol Biol* 2017; **24**: 840–847.

336 Purvis JE, Karhohs KW, Mock C, Batchelor E, Loewer A, Lahav G. p53 dynamics control cell fate. *Science* 2012; **336**: 1440–1444.

337 Zagelbaum J, Schooley A, Zhao J, Schrank BR, Callen E, Zha S *et al.* Multiscale reorganization of the genome following DNA damage facilitates chromosome translocations via nuclear actin polymerization. *Nat Struct Mol Biol* 2022; **30**: 1–8.

338 Chaudhary R, Lal A. Long noncoding RNAs in the p53 network. *Wiley Interdiscip Rev RNA* 2017; **8**: 1–24.

339 Zhang E, Yin D, Sun M, Kong R, Liu X, You L *et al.* P53-regulated long non-coding RNA TUG1 affects cell proliferation in human non-small cell lung cancer , partly through epigenetically regulating HOXB7 expression. *Cell Death Dis* 2014; **5**: 1–12.

340 Hu WL, Jin L, Xu A, Wang YF, Thorne RF, Zhang XD *et al.* GUARDIN is a p53-responsive long non-coding RNA that is essential for genomic stability. *Nat Cell Biol* 2018; **20**: 492–502.

341 Winkler L, Jimenez M, Zimmer JT, Williams A, Simon MD, Dimitrova N. Functional elements of the cis-regulatory lincRNA-p21. *Cell Rep* 2022; **39**: 110687–11105.

342 Hirose T, Ninomiya K, Nakagawa S, Yamazaki T. A guide to membraneless organelles and their various roles in gene regulation. *Nat Rev Mol Cell Biol* 2023; **24**: 288–304.

343 Herzel L, Ottoz DSM, Alpert T, Neugebauer KM. Splicing and transcription touch base: co-transcriptional spliceosome assembly and function. *Nat Rev Mol Cell Biol 2017 1810* 2017; **18**: 637–650.

344 Urbanski L, Leclair N, Anczuków O. Alternative-splicing defects in cancer: Splicing regulators and their downstream targets, guiding the way to novel cancer therapeutics. *Wiley Interdiscip Rev RNA* 2018; **9**: 1476–1532.

345 Parkhitko AA, Singh A, Hsieh S, Hu Y, Binari R, Lord CJ *et al.* Cross-species identification of PIP5K1-, splicing- And ubiquitin-related pathways as potential targets for RB1-deficient cells. *PLoS Genet* 2021; **17**: 1–31.

346 Yoon SO, Shin S, Lee HJ, Chun HK, Chung AS. Isoginkgetin inhibits tumor cell invasion by regulating phosphatidylinositol 3-kinase/Akt-dependent matrix metalloproteinase-9 expression. *Mol Cancer Ther* 2006; **5**: 2666–2675.

347 Romero JP, Muniategui A, De Miguel FJ, Aramburu A, Montuenga L, Pio R *et al.* EventPointer: An effective identification of alternative splicing events using junction arrays. *BMC Genomics* 2016; **17**: 467–493.

348 Dutertre M, Sanchez G, De Cian MC, Barbier J, Dardenne E, Gratadou L *et al.* Cotranscriptional exon skipping in the genotoxic stress response. *Nat Struct Mol Biol* 2010; **17**: 1358–1366.

349 Tresini M, Warmerdam DO, Kolovos P, Snijder L, Vrouwe MG, Demmers JAA *et al.* The core spliceosome as target and effector of non-canonical ATM signalling. *Nature* 2015; **523**: 53–58.

350 Muñoz MJ, Santangelo MSP, Paronetto MP, de la Mata M, Pelisch F, Boireau S *et al.* DNA Damage Regulates Alternative Splicing through

Inhibition of RNA Polymerase II Elongation. *Cell* 2009; **137**: 708–720.

351 Looi CY, Sasahara Y, Watanabe Y, Satoh M, Hakozaki I, Uchiyama M *et al.* The open conformation of WASP regulates its nuclear localization and gene transcription in myeloid cells. *Int Immunol* 2014; **26**: 341–352.

352 Miki H, Miura K, Takenawa T. N-WASP, a novel actin-depolymerizing protein, regulates the cortical cytoskeletal rearrangement in a PIP2-dependent manner downstream of tyrosine kinases. *EMBO J* 1996; **15**: 5326–5335.

353 Torres E, Rosen MK. Protein-tyrosine kinase and GTPase signals cooperate to phosphorylate and activate Wiskott-Aldrich syndrome protein (WASP)/neuronal WASP. *J Biol Chem* 2006; **281**: 3513–3520.

354 Cory GOC, Garg R, Cramer R, Ridley AJ. Phosphorylation of tyrosine 291 enhances the ability of WASp to stimulate actin polymerization and filopodium formation. *J Biol Chem* 2002; **277**: 45115–45121.

355 Suetsugu S, Hattori M, Miki H, Tezuka T, Yamamoto T, Mikoshiba K *et al.* Sustained activation of N-WASP through phosphorylation is essential for neurite extension. *Dev Cell* 2002; **3**: 645–658.

356 Fukumoto Y, Morii M, Miura T, Kubota S, Ishibashi K, Honda T *et al.* Src family kinases promote silencing of atr-chk1 signaling in termination of DNA damage checkpoint. *J Biol Chem* 2014; **289**: 12313–12329.

357 Dandoulaki M, Petsalaki E, Sumpton D, Zanivan S, Zachos G. Src activation by Chk1 promotes actin patch formation and prevents chromatin bridge breakage in cytokinesis. *J Cell Biol* 2018; **217**: 3071–3089.

358 Anerillas C, Herman AB, Rossi M, Munk R, Lehrmann E, Martindale JL *et al.* Early SRC activation skews cell fate from apoptosis to senescence. *Sci Adv* 2022; **8**: 1–17.

359 Fujiwara I, Zweifel ME, Courtemanche N, Pollard TD. Latrunculin A Accelerates Actin Filament Depolymerization in Addition to Sequestering Actin Monomers. *Curr Biol* 2018; **28**: 3183–3192.

360 David CJ, Chen M, Assanah M, Canoll P, Manley JL. HnRNP proteins controlled by c-Myc deregulate pyruvate kinase mRNA splicing in cancer. *Nature* 2010; **463**: 364–368.

361 Koh CM, Bezzi M, Low DHP, Ang WX, Teo SX, Gay FPH *et al.* MYC regulates the core pre-mRNA splicing machinery as an essential step in lymphomagenesis. *Nature* 2015; **523**: 96–100.

362 Chen B, Deng S, Ge T, Ye M, Yu J, Lin S *et al.* Live cell imaging and proteomic profiling of endogenous NEAT1 lncRNA by CRISPR/Cas9-

mediated knock-in. *Protein Cell* 2020; **11**: 641–660.

363 Yap K, Chung TH, Makeyev E V. Hybridization-proximity labeling reveals spatially ordered interactions of nuclear RNA compartments. *Mol Cell* 2022; **82**: 463–478.

364 Chen LL, DeCerbo JN, Carmichael GG. Alu element-mediated gene silencing. *EMBO J* 2008; **27**: 1694–1705.

365 Xu D, Liang SQ, Yang H, Lüthi U, Riether C, Berezowska S *et al.* Increased sensitivity to apoptosis upon endoplasmic reticulum stress-induced activation of the unfolded protein response in chemotherapy-resistant malignant pleural mesothelioma. *Br J Cancer* 2018; **119**: 65–75.

366 Bi J, Yang S, Li L, Dai Q, Borcherding N, Wagner BA *et al.* Metadherin enhances vulnerability of cancer cells to ferroptosis. *Cell Death Dis* 2019; **10**: 682–706.

367 Bennett HL, Fleming JT, O'Prey J, Ryan KM, Leung HY. Androgens modulate autophagy and cell death via regulation of the endoplasmic reticulum chaperone glucose-regulated protein 78/BiP in prostate cancer cells. *Cell Death Dis* 2010; **1**: 1–12.

368 Parrotta R, Okonska A, Ronner M, Weder W, Stahel R, Penengo L *et al.* A Novel BRCA1-Associated Protein-1 Isoform Affects Response of Mesothelioma Cells to Drugs Impairing BRCA1-Mediated DNA Repair. *J Thorac Oncol* 2017; **12**: 1309–1319.

369 He M, Chaurushiya MS, Webster JD, Kummerfeld S, Reja R, Chaudhuri S *et al.* Intrinsic apoptosis shapes the tumor spectrum linked to inactivation of the deubiquitinase BAP1. *Science* 2019; **364**: 283–285.

370 Yuan J, Ma Y, Huang T, Chen Y, Peng Y, Li B *et al.* Genetic Modulation of RNA Splicing with a CRISPR-Guided Cytidine Deaminase. *Mol Cell* 2018; **72**: 380–394.

371 Zhang Y, Shi J, Liu X, Feng L, Gong Z, Koppula P *et al.* BAP1 links metabolic regulation of ferroptosis to tumour suppression. *Nat Cell Biol* 2018; **20**: 1181–1192.

372 Yuan H, Li N, Fu D, Ren J, Hui J, Peng J *et al.* Histone methyltransferase SETD2 modulates alternative splicing to inhibit intestinal tumorigenesis. *J Clin Invest* 2017; **127**: 3375–3391.

373 Cieśla M, Ngoc PCT, Cordero E, Martinez ÁS, Morsing M, Muthukumar S *et al.* Oncogenic translation directs spliceosome dynamics revealing an integral role for SF3A3 in breast cancer. *Mol Cell* 2021; **81**: 1453–1468.

374 Lee SCW, Abdel-Wahab O. Therapeutic targeting of splicing in cancer. *Nat*

*Med* 2016; **22**: 976–986.

375 Hsu TY, Simon LM, Neill N, Marcotte R, Bland CS, Echeverria G V *et al.* The spliceosome is a therapeutic vulnerability in MYC-driven cancer. *Nature* 2015; **525**: 384–388.

376 Bowling EA, Wang JH, Gong F, Wu W, Neill NJ, Kim IS *et al.* Spliceosome-targeted therapies trigger an antiviral immune response in triple-negative breast cancer. *Cell* 2021; **184**: 384–403.

377 Hubert CG, Bradley RK, Ding Y, Toledo CM, Herman J, Skutt-Kakaria K *et al.* Genome-wide RNAi screens in human brain tumor isolates reveal a novel viability requirement for PHF5A. *Genes Dev* 2013; **27**: 1032–1045.

378 Iwai K, Yaguchi M, Nishimura K, Yamamoto Y, Tamura T, Nakata D *et al.* Anti-tumor efficacy of a novel CLK inhibitor via targeting RNA splicing and MYC-dependent vulnerability. *EMBO Mol Med* 2018; **10**: 1–15.

## Supplementary information.

**SI Table 1.1. List of general abbreviations.**

| Abbreviation | Full name |
|---|---|
| 4NQO | 4-nitroquinoline-1-oxide |
| A | Adenine |
| ADP | Adenosine 5'-diphosphate |
| Alu | *Arthrobacter luteus* (DNA segments) |
| ATP | Adenosine triphosphate |
| BAM | Binary alignment map |
| BER | Base excision repair |
| BH | Benjamini and Hochberg |
| bp | Base pair |
| BS | Branch site |
| ºC | Celsius |
| C | Cytosine |
| C- | Carboxyl (terminus end) |
| C (Cys) | Cysteine |
| CA | Central-acid domain |
| Cas | CRISPR-associated endonuclease |
| cDNA | Complementary DNA |
| ChIP | Chromatin immunoprecipitation |
| $CO_2$ | Carbon dioxide |
| CRISPR | Clustered regularly interspaced short palindromic repeats |
| Ct | Cycle threshold |
| CTD | C-terminus domain (p53) |
| DDR | DNA damage response |
| DEG | Differently expressed gene |
| DN | Dominant-negative |
| DNA | Deoxyribonucleic acid |
| DSB | Double strand break |
| DSBR | Double strand break repair |
| dsDNA | Double stranded DNA |
| ECL | Enhanced chemiluminescence |
| EJC/TREX | Exon junction and transcription-export |
| ESE | Exonic splicing enhancers |
| ESS | Exonic splicing silencers |
| EXP | Expression |
| F (Phe) | Phenylalanine |
| F-actin | Filamentous actin |
| FC | Fold-change |
| FDR | False discovery rate |
| FISH | Fluorescence *in situ* hybridization |
| FPKM | Fragments per kilobase of exon model per million reads |
| g | Grams |
| G | Guanine |
| *g* | Gravitational field |
| G-actin | Globular actin (monomeric) |
| GFF | General feature format |
| GFP | Green fluorescent protein |
| GO | Gene ontology |
| GOF | Gain-of-function |
| GSEA | Gene set enrichment analysis |
| GTF | Gene transfer format |
| GTP | Guanosine-5'-triphosphate |
| h | Hours |
| H (His) | Histidine |

| Abbreviation | Full name |
|---|---|
| HAP1 | Huntingtin associated protein 1 |
| HEAT | Huntingtin, elongation factor 3, phosphatase 2A, and TOR1 repeats. |
| hJMY | Human JMY |
| hnRNPs | Heterogeneous nuclear ribonucleoproteins |
| HR | Homologous recombination |
| HRE | Hypoxia response elements |
| HRP | Horse radish peroxidase |
| IAP | Inhibitor of apoptosis |
| Ig | Immunoglobulin |
| IGV | Integrative genomics viewer |
| IRAlus | Inverted Alu repeats |
| ISE | Intronic splicing enhancers |
| ISS | Intronic splicing silencers |
| K (Lys) | Lysine |
| KD | Knockdown |
| kDa | Kilo Dalton |
| KEGG | Kyoto encyclopaedia of genes and genomes |
| KO | Knockout |
| L | Litre |
| lincRNA | Long intergenic non-coding RNA |

| Abbreviation | Full name |
|---|---|
| LINE1 | Long interspersed nuclear element 1 |
| LIR | LC3-interacting motif |
| lncRNA | Long non-coding RNA |
| LOF | Loss-of-function |
| log | logarithm |
| M | Molar |
| m/v | Mass/volume ratio |
| MAPK | Mitogen-Activated Protein Kinases |
| MBL | Monomer binding linker |
| MCF7 | Michigan cancer foundation-7 |
| mJMY | Mouse JMY |
| mL | Millilitre |
| mM | Millimolar |
| mRNA | Messenger ribonucleic acid |
| mut | Mutant |
| N- | Amino (terminus end) |
| NER | Nucleotide excision repair |
| NGS | Next generation sequencing |
| NHEJ | Non-homologous end joining |
| NLS | Nuclear location signal |
| NPF | Nucleation-promoting factors |

| Abbreviation | Full name |
|---|---|
| nt | Nucleotide |
| OB | Oligonucleotide/oligosaccharide-binding |
| P (Pro) | Proline |
| PAGE | Polymerase acrylamide gel electrophoresis |
| PAS | Polyadenylation signal |
| PC | Principal component |
| PCA | Principal component analysis |
| PCR | Polymerase chain reaction |
| PI | Propidium iodide |
| PIKK | Phosphatidylinositol 3-kinase-related kinases |
| Plad B | Pladienolide B |
| poly(A) | Poly-adenine |
| poly(T) | Poly-thymidine |
| PPT | Poly-pyrimidine tract |
| PRD | Proline-rich region |
| pre-mRNA | Premature messenger ribonucleic acid |
| PSI | Percent spliced in index |
| PTM | Post-translational modifications |
| px | Pixels |
| R (Arg) | Arginine |

| Abbreviation | Full name |
|---|---|
| RI | Retained intron |
| RNA | Ribonucleic acid |
| RNA-FISH | RNA-fluorescence *in situ* hybridization |
| RNA-seq | Ribonucleic acid sequencing |
| RNP | Ribonucleoprotein |
| ROS | Reactive oxygen species |
| RPKM | Reads per kilobase of exon model per million reads |
| rRNA | Ribosomal RNA |
| RT | Reverse transcriptase or retrotranscriptase |
| RT-PCR | Reverse transcription polymerase chain reaction |
| RT-qPCR | Quantitative reverse transcription polymerase chain reaction |
| s | Seconds |
| S (Ser) | Serine |
| s.e.m. | Standard error of the mean |
| SAM | Sequencing alignment map |
| Saos2 | Sarcoma osteogenic |
| SBS | Single strand break |

| Abbreviation | Full name |
|---|---|
| SBS | Single strand break |
| SD | Standard deviation |
| SDSA | Single strand break repair |
| SE | Skipped exon or exon skipping |
| sgRNA | Single guide RNA |
| SI | Supplementary information |
| siRNA | Small interfering ribonucleic acid |
| SNP | Single nucleotide polymorphism |
| snRNP | Small nuclear ribonucleoprotein |
| SR | Serine-arginine proteins |
| SRF | Serum response transcription factor |
| SS | Splice site |
| SSA | Single strand annealing |
| ssDNA | Single stranded DNA |
| STAR | Spliced Transcripts Alignment to a Reference |
| T | Thymine |
| TAD | Transactivation domain |

| Abbreviation | Full name |
|---|---|
| TCGA | The cancer genome atlas |
| TPM | Transcripts per million |
| TPR | Tetratricopeptide |
| tRNA | Transfer RNA |
| U | Units |
| U | Uracil (nucleotide) |
| U2OS | U2 osteosarcoma |
| UCSC | University of California Santa Cruz |
| UTR | Untranslated region |
| UV | Ultraviolet |
| V (Val) | Valine |
| v/v | Volume/volume ratio |
| w/v | Weight/volume ratio |
| WASP | Wiskott-Aldrich syndrome protein |
| WH2 | Wiskott-Aldrich syndrome protein homology 2 |
| WT | Wild type |
| Y (Tyr) | Tyrosine |
| µg | Micrograms |
| µL | Microlitre |
| µM | Micromolar |

**SI Table 1.2. List of gene and protein names.**

| Symbol | Full name |
|---|---|
| 53BP1 | p53-binding protein 1 |
| ACTB | Actin beta |
| AKT | Alpha serine/threonine protein kinase |
| APTX | Aprataxin |
| ARFGAP1 | ADP ribosylation factor GTPase activating protein 1 |
| ARL5A | ADP Ribosylation Factor Like GTPase 5A |
| ARP2/3 (ARPC2-ARPC3) | Actin related protein 2/3 complex (subunits 2 and 3) |
| ASPP1 | Apoptosis-stimulating protein of p53 protein 1 |
| ASPP2 | Apoptosis-stimulating protein of p53 protein 2 |
| ATF2 | Activating transcription factor 2 |
| ATM | Ataxia telangiectasia mutated |
| ATR | Ataxia telangiectasia and Rad3-related protein |
| BAP1 | BRCA1 associated protein-1 |
| BAX | Bcl-2 Associated X-protein |
| BBC3/Puma | Bcl-2 binding component 3 |
| BCL-2 | B-cell lymphoma-2 |
| BCL2L1 | Bcl-2-like protein 1 |
| BCL2L12 | Bcl-2-like protein 12 |
| BLM | Bloom syndrome protein |
| BRCA1 | Breast cancer type 1 |
| BRCA2 | Breast cancer type 2 |
| BTK | Bruton's tyrosine kinase |
| CAT-2 | Catalase 2 |
| CBP | cAMP response element-binding protein |
| CBP | CREB binding protein |
| CDK2 | Checkpoint kinase 2 |
| CDK9 | Cyclin-dependent kinase 9 |
| CDKN1A/p21 | Cyclin dependent kinase inhibitor 1A / protein 21 |
| CDKN1B/p27 | Cyclin Dependent Kinase Inhibitor 1B |
| CHK1 | Checkpoint kinase 1 |
| CHK2 | Checkpoint kinase 2 |
| CHMP2B | Charged multivesicular body protein 2B |
| CPSF6 | Cleavage polyadenylation specificity factor 6 |
| CREB | cAMP-response element binding protein |
| DAZAP1 | DAZ-associated protein 1 |
| DDX39B | DExD-box helicase 39B |
| DHPS | Deoxyhypusine synthase |
| DIABLO | Diablo IAP-binding mitochondrial protein |
| DNA2 | DNA replication helicase/nuclease 2 |
| DNAJB1 | DnaJ homolog subfamily B member 1 |
| DNA-PK | DNA-dependent protein kinase |
| DVL2 | Dishevelled Segment Polarity Protein 2 |
| EGFR | Epidermal growth factor receptor |
| EP300/p300 | Adenovirus early region 1A-associated protein 300 / protein 300 |
| ERCC1 | Excision repair cross complementation group 1 |
| EXO1 | Exonuclease 1 |

| Symbol | Full name |
|---|---|
| F11R | F11 junction adhesion molecule |
| FASTK | Fas-activated serine/threonine kinase |
| FEN1 | Flap endonuclease 1 |
| FUS | Fused In Sarcoma |
| GADD45A | Growth arrest and DNA-damage-inducible protein 45 alpha |
| GALNT5 | Polypeptide N-acetylgalacto-saminyltransferase 5 |
| GAPDH | Glyceraldehyde 3-phosphate dehydrogenase |
| GPNMB | Glycoprotein non-metastatic b |
| H2AX | H2A histone family member X |
| H3K27 | Histone 3 lysine 27 |
| HCK | Hematopoietic cell kinase |
| HDAC1 | Deacetylases like deacetylase-1 |
| HIF-1 | Hypoxia-inducible factor 1 |
| HIF2a | Hypoxia-inducible factor-2 alpha |

| Symbol | Full name |
|---|---|
| HNRNPA | Heterogeneous nuclear ribonucleoprotein A |
| HNRNPF | Heterogeneous nuclear ribonucleoprotein F |
| HNRNPH | Heterogeneous nuclear ribonucleoprotein H |
| HNRNPH3 | Heterogeneous nuclear ribonucleoprotein H subunit 3 |
| HNRNPK | Heterogeneous nuclear ribonucleoprotein K |
| HNRNPM | Heterogeneous nuclear ribonucleoprotein M |
| HR | HR lysine demethylase and nuclear receptor corepressor |
| HSPA5 | Heat Shock Protein Family A (Hsp70) Member 5 |
| iASPP | Inhibitor of apoptosis-stimulating protein of p53 |
| IL-32 | Interleukin 32 |
| IL-8 | Interleukin-8 |
| Imp α/β | Importin alpha/beta |
| INTS11 | Integrator complex subunit 11 |
| IPO9 | Importin 9 |

| Symbol | Full name |
|---|---|
| JMY | Junction mediating and regulatory protein |
| KDM3A | Lysine demethylase 3A |
| LC3/MAP1L C3B | Microtubule-associated proteins 1A/1B light chain 3B |
| LIG1 | Ligase 1 |
| LIG3 | Ligase 3 |
| LIG4 | Ligase 4 |
| LSM3 | U6 small nuclear RNA and mRNA degradation associated protein. |
| MACF1 | Microtubule-actin cross-linking factor 1 |
| MCL-1 | Myeloid leukaemia 1 |
| MDM2 | Murine double minute 2 |
| MDM4 | Murine double minute 4 |
| MED12L | Mediator of RNA polymerase II transcription subunit 12-like protein |
| MEN1 | Multiple endocrine neoplasia link type 1 |
| MMP9 | Matrix Metallopeptidase 9 |
| MOF | Males absent on the first |
| MOZ | Monocytic leukaemia zing finger |

| Symbol | Full name |
|---|---|
| MRE11 | Meiotic recombination 11 homolog |
| MRTF-A | Myocardin-related transcription factor A |
| MTDH | Metadherin |
| MTOR | Mammalian target of rapamycin |
| MYC | BHLH transcription factor (proto-oncogene) |
| NBS1 | Nibrin |
| NEAT1 | Nuclear paraspeckle assembly transcript 1 |
| NM1 | Nuclear myosin 1 |
| NONO | Non-POU domain-containing octamer-binding protein |
| NUDT21 | Nudix Hydrolase 21 |
| PARP | Poly-ADP-Ribose Polymerase |
| PCNA | Proliferating cell nuclear antigen |
| PHF5A | PHD finger-like domain-containing protein 5A |
| PI3K | Phosphatidylinositol 3-kinase |

| Symbol | Full name |
|---|---|
| PIRH2 | p53-induced protein with a RING-H2 domain |
| PML | Promyelocytic leukaemia |
| POLB | DNA polymerase subunit beta |
| POLE | DNA polymerase subunit epsilon |
| POLG | DNA polymerase subunit gamma |
| POLL | DNA polymerase subunit lambda |
| POLM | DNA Polymerase mu |
| POLR3C | RNA Polymerase III Subunit C |
| Prp19 | pre-mRNA-splicing ATP-dependent RNA helicase 19 |
| Prp2 | pre-mRNA-splicing ATP-dependent RNA helicase 2 |
| Prp28 | pre-mRNA-splicing ATP-dependent RNA helicase 28 |
| PSF/SFPQ | Splicing factor proline- and glutamine-rich |
| PSPC1 | Paraspeckle component 1 |
| PTB | Polypyrimidine-tract-binding protein |

| Symbol | Full name |
|---|---|
| P-TEFb | Positive transcription elongation factor b |
| RAD23B | UV excision repair protein RAD23 homolog B |
| RAD50 | RAD50 double strand break repair |
| RAD51 | DNA repair protein recA homolog 1 |
| RBBP8/CtIP | Retinoblastoma-binding protein 8 |
| RBM14 | RNA binding motif protein 14 |
| RPA | Replication protein A |
| RPL10 | Ribosomal protein large 10 |
| RPS11 | Ribosomal protein small 11 |
| RPS3 | Ribosomal protein small 3 |
| RRM2B | Ribonucleotide reductase regulatory TP53 inducible subunit M2B |
| SCAR | Sequence characterized amplified region |
| SCR | S locus cysteine-rich gene |
| SF1 | Splicing factor 1 |
| SF3A3 | Splicing factor 3A subunit 3 |
| SF3B1 | Splicing factor 3B subunit 1 |
| SF3B3 | Splicing factor 3B subunit 3 |

| Symbol | Full name |
|---|---|
| SF3B6 | Splicing factor 3B subunit 6 |
| SIRT1 | Sirtuin, silent mating type information regulation 2 homolog 1 |
| SLC7A11 | Solute carrier family 7 member 11 |
| SMARCA4 | SWI/SNF related, matrix associated, actin dependent regulator of chromatin, subfamily a, member 4 |
| SNRPA | Small nuclear ribonucleoprotein polypeptide A |
| SRSF2 | Serine/arginine-rich splicing factor 2 |
| STMN3 | Stathmin 3 |
| STRAP | Serine/threonine kinase receptor associated protein |
| SV40 | Simian virus 40 |
| SWI/SNF | Switch/Sucrose non fermentable |
| SYP | Synaptophysin |
| TDP-43 | Transactive response DNA binding protein 43 |
| TEAD2 | TEA Domain Transcription Factor 2 |

| Symbol | Full name |
|---|---|
| TFIIH | Transcription factor II H |
| TIGAR | TP53 induced glycolysis regulatory phosphatase |
| TIMP1 | Tissue inhibitors of metalloproteinase 1 |
| TIP60 | Tat-interactive protein 60 |
| TNFSF12 | Tumour necrosis factor ligand superfamily member 12 |
| TP53/p53 | Tumour protein p53 |
| TP53I3/PIG3 | Tumour protein p53 inducible protein 3 |
| TUBB | Tubulin Beta Class I |
| TUBGCP6 | Tubulin gamma complex associated protein 6 |
| TUG1 | Taurine upregulated gene 1 |
| U2AF | U2 auxiliary factor |
| UBE2G2 | Ubiquitin-conjugating enzyme E2 G2 |
| UNC45 | Unc-45 myosin chaperone B |
| VGF | VGF nerve growth factor inducible |
| WASP | Wiskott-Aldrich syndrome protein |
| WAVE2 | Wiskott-Aldrich syndrome protein family member 2 |

| Symbol | Full name |
|---|---|
| WHAMM | WASP homolog associated with actin, Golgi membranes and microtubules |
| WHAMY | WHAMM and JMY related |
| XLF | Xeroderma pigmentosum, complementation group L |
| XPA | Xeroderma pigmentosum, complementation group A |
| XPB | Xeroderma pigmentosum, complementation group B |
| XPC | Xeroderma pigmentosum, complementation group C |
| XPF | Xeroderma pigmentosum, complementation group F |
| XPG | Xeroderma pigmentosum, complementation group G |
| XPO6 | Export 6 |
| XRCC1 | X-ray repair cross complementing 1 |
| XRCC4 | X-ray repair cross complementing 4 |
| XRCC5/Ku80 | X-ray repair cross complementing 5 |
| XRCC6/Ku70 | X-ray repair cross complementing 6 |

**SI Table 2.1. List of reagents and compounds used in this project.**

| Chemical/Reagent | Cat. number | Company |
|---|---|---|
| 1,6-Hexanediol | 240117 | SigmaAldrich, UK |
| 2-[4-(2-Hydroxyethyl)piperazin-1-yl]ethane-1-sulfonic acid | H8651 | SigmaAldrich, UK |
| 2-Fluoro-N-[2-(2-methyl-1H-indol-3-yl)ethyl]benzamide | 3950 | Tocris Bioscience, UK |
| 2-Propanol - Isopropanol | 149320000 | ThermoFisher, UK |
| 3-(4,5-dimethylthiazol-2-yl)-2,5-diphenyltetrazolium bromide | M6494 | ThermoFisher, UK |
| 3-aminophthalhydrazide | A8511 | SigmaAldrich, UK |
| 3-hydroxy-4-(2-sulfo-4-[4-sulfophenylazo]phenylazo) -2,7-naphthalenedisulfonic acid sodium salt | P3504 | SigmaAldrich, UK |
| 4′,6-diamidino-2-phenylindole | D1306 | ThermoFisher, UK |
| 4-Nitroquinoline N-oxide | N8141-1G | SigmaAldrich, UK |
| 50bp DNA step ladder | S7025 | SigmaAldrich, UK |
| Acrylamide ProtoGel 30% | EC-890 | National Diagnostics, UK |
| Agarose | BP160-500 | ThermoFisher, UK |
| Ammonium chloride | 11314609 | ThermoFisher, UK |

| Chemical/Reagent | Cat. number | Company |
|---|---|---|
| Ammonium persulfate (APS) | 215589 | SigmaAldrich, UK |
| Ampicillin sodium salt | A9518 | SigmaAldrich, UK |
| Annexin V conjugated with FITC | A13199 | ThermoFisher, UK |
| Aprotinin | 97062-752 | Avantor, UK |
| BD CS&T RUO Beads | 661414 | BD Biosciences, UK |
| BD Detergent solution concentrate | 660585 | BD Biosciences, UK |
| BD Extended Flow Cell Clean Solution | 660586 | BD Biosciences, UK |
| BD FACS clean | 340345 | BD Biosciences, UK |
| BD Sheath Additive | 660584 | BD Biosciences, UK |
| Betaine | B0300 | SigmaAldrich, UK |
| Biocleanse | TK200 | ThermoFisher, UK |
| BLUeye pre-stained protein ladder | S6-0024 | Geneflow, UK |
| BLUeye pre-stained protein ladder | S6-0024 | Geneflow, UK |
| b-mercaptoethanol | M6250 | SigmaAldrich, UK |
| Bovine Serum Albumin | BPE1600 | ThermoFisher, UK |
| Bradford Reagent | B6916 | SigmaAldrich, UK |
| Brilliant III Ultra-Fast SYBR QPCR MM | 600882 | Agilent Technologies, UK |

| Chemical/Reagent | Cat. number | Company |
|---|---|---|
| Bromophenol blue | A18469.09 | ThermoFisher, UK |
| Buffer EB | 19086 | Qiagen, UK |
| Buffer N3 | 19064 | Qiagen, UK |
| Buffer P1 | 19051 | Qiagen, UK |
| Buffer P2 | 19052 | Qiagen, UK |
| Buffer PB | 19066 | Qiagen, UK |
| Buffer PE | 19065 | Qiagen, UK |
| Ceralasertib (AZD6738, ATR inhibitor) | S7693-SEL | Stratech, UK |
| CometAssay LMAgarose | 4250-050-02 | R&D Systems, UK |
| CometAssay lysis solution | 4250-050-01 | R&D Systems, UK |
| Cyclohexamide | 14126 | Cayman Chemical, UK |
| D-(+)-Glucose | G8270 | SigmaAldrich, UK |
| Dimethyl sulfoxide | 022914.M1 | ThermoFisher, UK |
| Dithiothreitol | MB1015 | Melford, UK |
| DNase I | EN0521 | ThermoFisher, UK |
| Dried skimmed Milk (Marvel) | | ASDA/Tesco |
| Dulbecco's Modified Eagle Medium | BE12-604F | Lonza Bioscience, UK |
| Dulbecco's Modified Eagle Medium | D1145 | SigmaAldrich, UK |
| *Escherichia coli* DH5α | 18265017 | ThermoFisher, UK |
| Ethanol | 458600 | SigmaAldrich, UK |
| Ethylenediaminetetra-acetic acid | 798681 | SigmaAldrich, UK |

| Chemical/Reagent | Cat. number | Company |
|---|---|---|
| Etoposide | CAY12092 | Cambridge biosciences , UK |
| FastGene ICGreen 2x qPCR universal mix | P8-0058 | Geneflow, UK |
| Foetal Bovine Serum | FCS-SA/500 | BioSera/Labtech, UK |
| Formaldehyde 37% | BP531-500 | ThermoFisher, UK |
| Formamide (deionised) | AM9342 | ThermoFisher, UK |
| GeneRuler 1kb DNA ladder | SM0311 | ThermoFisher, UK |
| Geneticin | 329400050 | ThermoFisher, UK |
| Glycerol | 15514011 | ThermoFisher, UK |
| Glycine | G8898 | SigmaAldrich, UK |
| Hoescht 33342 | 62249 | ThermoFisher, UK |
| Hydrochloric acid | 124200000 | ThermoFisher, UK |
| Hydrogen Peroxide | H1009 | SigmaAldrich, UK |
| Immersion oil | 12847995 | Leica microsystems, UK |
| Industrial Methylated Spirit | 10552904 | ThermoFisher, UK |
| Isoginkgetin | 6483/10 | Tocris Bioscience, UK |
| Kanamycin sulphate | 15815168 | ThermoFisher, UK |
| KU-60019 (ATM inhibitor) | S1570-SEL | Stratech, UK |
| Leupeptin | J580-5MG | Avantor, UK |
| L-Glutamine 100x (200nM) | BE17-605E | Lonza Bioscience, UK |
| Lithium chloride anhydrous | CHE2360D2 | Scientific Laboratory Supplies, UK |

| Chemical/Reagent | Cat. number | Company |
|---|---|---|
| Lysogeny broth agar media | 22700025 | ThermoFisher, UK |
| Lysogeny broth media | 12780052 | ThermoFisher, UK |
| Methanol | 179957 | SigmaAldrich, UK |
| M-MLV RT buffer | 18057018 | ThermoFisher, UK |
| Moloney Murine Leukemia Virus Reverse Transcriptase | 28025013 | ThermoFisher, UK |
| Monopotassium phosphate | 12685087 | ThermoFisher, UK |
| Morpholinopropane sulfonic acid | A17214.22 | ThermoFisher, UK |
| N,N,N′,N′-Tetramethylethylenediamine | T9281 | SigmaAldrich, UK |
| Nedisertib (DNA-PK inhibitor) | CAY28405-10MG | Cayman Chemical, UK |
| Nobel agar | A5431 | SigmaAldrich, UK |
| Nonyl phenoxypolyethoxyl ethanol | 85124 | ThermoFisher, UK |
| Nuclease free water (not DEPC treated) | AM9938 | ThermoFisher, UK |
| Nucleoside triphosphate mix (10nM) | R0191 | ThermoFisher R0191 |
| Oligo(T) primers | 18418012 | ThermoFisher, UK |
| Opti-MEM reduced serum medium | 11058021 | ThermoFisher, UK |

| Chemical/Reagent | Cat. number | Company |
|---|---|---|
| Paq5000 DNA Polymerase | 600680 | Agilent Technologies, UK |
| Paq5000 DNA Polymerase master mix | 600872 | Agilent Technologies, UK |
| Penicillin-Streptomycin solution | LZ17-745E | Lonza Bioscience, UK |
| Pepstatin | 97064-248 | Avantor, UK |
| Phosphate Buffered Saline | 20-746120-7461-01 | Severn Biotech, UK |
| p-hydroxycinnamic acid | C9008 | SigmaAldrich, UK |
| Pladienolide B | 16538 | Cayman Chemical, UK |
| Potassium Chloride | 10735874 | ThermoFisher, UK |
| Primers (oligonucleotides generic) | - | SigmaAldrich, UK |
| Propidium iodide | 81845 | SigmaAldrich, UK |
| Proteinase K from *Tritirachium album* | P2308-10MG | SigmaAldrich, UK |
| Random hexamer primers | SO142 | ThermoFisher, UK |
| RNase A | EN0531 | ThermoFisher, UK |
| RNase Inhibitor | N8080119 | ThermoFisher, UK |
| RNasin® Plus RNase Inhibitor | N2611 | Promega, UK |
| Rucaparib camsylate | 6230 | Tocris Bioscience, UK |
| Sodium bicarbonate | 792519 | SigmaAldrich, UK |
| Sodium chloride | S/3160/63 | ThermoFisher, UK |

| Chemical/Reagent | Cat. number | Company |
|---|---|---|
| Sodium deoxycholate | 89904 | ThermoFisher, UK |
| Sodium dodecyl sulphate | 436143 | SigmaAldrich, UK |
| Sodium hydroxide | S/4920/53 | ThermoFisher, UK |
| Sodium orthovanadate | 205332500 | ThermoFisher, UK |
| Sodium phosphate dibasic | 10361474 | ThermoFisher, UK |
| Sodium phosphate monobasic | 10523864 | ThermoFisher, UK |
| Sodium fluoride | S1504 | SigmaAldrich, UK |
| Sonicated salmon sperm DNA | 15632011 | ThermoFisher, UK |
| Stellaris® FISH Probes, Human GAPDH with Quasar 670® Dye | SMF-2019-1 | Biosearch technologies, UK |
| Stellaris® FISH Probes, Human NEAT1 Middle Segment with Quasar® 570 Dye | SMF-2037-1 | Biosearch technologies, UK |
| Stellaris® RNA FISH Hybridization Buffer | SMF-HB1-10 | Biosearch technologies, UK |
| Stellaris® RNA FISH Wash Buffer A | SMF-WA1-60 | Biosearch technologies, UK |
| Stellaris® RNA FISH Wash Buffer B | SMF-WB1-20 | Biosearch technologies, UK |
| SYBR Safe DNA Gel Stain | S33102 | ThermoFisher, UK |

| Chemical/Reagent | Cat. number | Company |
|---|---|---|
| TopVision low melting point agarose | R0801 | ThermoFisher, UK |
| TransIT-X2® Transfection Reagent | MIR600 | Mirus Bio, US |
| Tris(hydroxymethyl) aminomethane | B2005 | Melford, UK |
| TopVision low melting point agarose | R0801 | ThermoFisher, UK |
| TransIT-X2® Transfection Reagent | MIR600 | Mirus Bio, US |
| Tris(hydroxymethyl) aminomethane | B2005 | Melford, UK |
| Triton X-100 | A16046.AP | ThermoFisher, UK |
| Trizma® base | T9424 | SigmaAldrich, UK |
| Trypsin, 0.5% (10x) with EDTA 4Na (liquid) | 15400054 | ThermoFisher, UK |
| Tween-20 | BPE337 | ThermoFisher, UK |
| Vectashield® antifade mounting medium with DAPI | H-1200-10 | Vector laboratories |
| Vectashield® antifade mounting medium without DAPI | H-1000 | Maravai LifeSciences, US |
| Xylene cyanol | 422690050 | ThermoFisher, UK |

**SI Table 2.2. siRNA sequences used for knockdown.**

| siRNA | Sequence 5'-3' | Reference |
|---|---|---|
| JMY #1 | GCAACUAGAAAGCAUCAAA | [127] |
| JMY #2 | CACUCGGAUUGAAGAUGAA | [127] |
| JMY #3 | CCAUCACACAGUACAACUA | [127] |
| NEAT1_2 | GGGUAAAUCUCAAUCUUAA | [232] |
| A* (NT) | UUCUCCGAACGUGUCACGU | [130] |

NT: non-targeting

**SI Table 2.3. Plasmids used during this project.**

| Plasmid | Backbound | Bacteria selection | Cell selection | Description | Reference |
|---|---|---|---|---|---|
| HA-hJMY | pCELF-HA | Ampicillin | G418 (geneticin) | HA-tag wild-type human JMY insertion. | [127] |
| FLAG-NLS-hJMY | FNpCDNA3 | Ampicillin | G418 (geneticin) | FLAG-NLS-tag wild-type human JMY insertion. | Created by subcloning by Dr Amanda Coutts |
| HA-NLS-mJMY | FNpCDNA3 | Ampicillin | G418 (geneticin) | HA-NLS-tag wild-type mouse JMY insertion. | [127] |
| HA-NLS-mJMY ΔWH2 | FNpCDNA3 | Ampicillin | G418 (geneticin) | HA-NLS-tag mouse JMY insertion lacking the WCA actin nucleation domain. | [127] |
| HA-NLS-mJMY W981A | FNpCDNA3 | Ampicillin | G418 (geneticin) | HA-NLS-tag mouse JMY insertion presenting a single mutation (W981A) compromising Arp2/3-dependent actin nucleation. | [127] |

pCELF-HA plasmid was a gift from Eric O'Neill (University of Oxford), and FNpCDNA3 plasmid was a gift from Robert Oshima (Addgene #45346)

**SI Table 2.4. List of primers used in this project.**

**RT-PCR**

| Gene | Forward 5´-3´ | Reverse 5´-3´ | Annealing temperature (ºC) | Predicted product size (bp) |
|---|---|---|---|---|
| DIABLO | AATCCCGACTGCTTCCTTGG | TGCAATAGGAACCGCACACA | 62 | 200 – 312 (CxE)* |
| MACF1 | GGGAACTCTGGTGGAAGAAA | TTGCCTCCTTGTGAACCTCC | 58 | 220 (CE)* - 290 |
| MDM4 | CTCTCGCACAGGATCACAGT | CCAGCTACATCCCACTCCTC | 52 | 160 – 230 (CxE)* |
| MED12L | TATCACACACACCCCATGCC | TTGCCTGAGAAGTCGCTGTT | 62 | 400 (CE)* - 560 |
| TNFSF12 | CGATCGCAGCCCATTATGAAG | ACAGGTAGTAGAGCCCAGCC | 65 | 150 (CE)* - 200 |

**RT-qPCR**

| Gene | Forward 5´-3´ | Reverse 5´-3´ | Annealing temperature (ºC) | Predicted product size (bp) |
|---|---|---|---|---|
| GAPDH | TTCATTGACCTCAACTACAT | GTGGCAGTGATGGCATGGAC | 62 | 87 |
| NEAT1_1 | GTGGCTGTTGGAGTCGGTAT | TAACAAACCACGGTCCATGA | 62 | 185 |
| NEAT1_2 | CATGGCAGTGGGAAGGGATT | GGAGTGACGGTGAGAATGCA | 62 | 127 |
| PHF5A | GTTGCCATCGGAAGACTGT | GCCCCTGGTAAGATCCATAGT | 58 | 121 |
| RRM2B | CCTTGCGATGGATAGCAGATAG | GCCAGAATATAGCAGCAAAAGATC | 62 | 108 |
| SF3A3 | GTCATGGCTAAAGAGATGCTCAC | TCCTCCTTTCGTAATCCATCCTT | 64 | 152 |
| SF3B2 | CCGATCCAGGGTAATCGCGA | AAAACCGGCCGATTCAGCAC | 62 | 86 |
| SF3B6 | GCCAAGAATGCATGTGATCACC | TCCTCCTTCTTCTTTGTGTCCA | 62 | 116 |
| TP53I3 (PIG3) | GTACGTCACTGTCCCCGAAG | AGCCTGAACATTTCCCACAAGA | 62 | 130 |
| XPC | TCTTCGGAGGGCGATGAAAC | AGGCAGCACTCTGGTAAAGC | 62 | 172 |
| XRCC5 | CCATGAGCTTGGCAAAGAAAG | GTGCAGCAGACACTGAAATAATC | 62 | 110 |

**ChIP-qPCR**

| Gene | Forward 5´-3´ | Reverse 5´-3´ | Annealing temperature (ºC) | Predicted product size (bp) |
|---|---|---|---|---|
| BAX | TAATCCCAGCGCTTTGGAAGG | TGCAGAGACCTGGATCTAGCAA | 62 | 102 |
| NEAT1 | AGGAAGAGACTGATGGGGCA | CTCCCTGTGCTTCTCGGAAA | 62 | 175 |
| TP53I3 (PIG3) | CCCAACGGCTCCTTTCTCTT | TGGTCCATTTTCCAGGCATG | 58 | 123 |
| XRCC5 | CTGGACAAAGGGCTCGTGAT | AAATGGGATGCACAAACGCC | 62 | 182 |

** Alternative splicing events: cassette exon (CE), exon retention (RE) and complex event (CxE)*

**SI Table 2.5. List of antibodies and probes.**

| Antibodies | Dilution | Supplier (Cat. Number) |
|---|---|---|
| Rabbit monoclonal anti-53BP1 | 1/500 | Cell Signaling Technology (#88439) |
| Mouse monoclonal anti-ACTB | 1/10,000 | SantaCruz (C4, #SC-47778) |
| Rabbit polyclonal anti-phosphoATM/ATR substrate | 1/200 | Cell Signaling Technology (#2851) |
| Mouse monoclonal anti-FLAG | 1/200 | Sigma-Aldrich (M2, #F1804) |
| Rabbit polyclonal anti-FUS/TLS | 1/2,000 | Proteintech (#11570-1-AP) |
| Rabbit monoclonal anti-GAPDH | 1/2,000 | Sigma-Aldrich (G9, #SC-365062) |
| Mouse monoclonal anti-HA.11 | 1/200 | BioLegend (16B12, #MMS-101P) |
| Rabbit polyclonal anti-JMY | 1/5,000 | Proteintech (#25098-1-AP) |
| Rabbit polyclonal anti-NONO | 1/2,000 | Proteintech (#11058-1-AP) |
| Rabbit polyclonal anti-NONO | 1/2,000 | Cell Signaling Technology (#90336) |
| Rabbit polyclonal anti-PHF5A | 1/1,000 | Proteintech (#15554-1-AP) |
| Rabbit polyclonal anti-PSPC1 | 1/2,000 | Proteintech (#16714-1-AP) |
| Rabbit polyclonal anti-SF3B6 (anti-SF3B14) | 1/2,000 | Proteintech (#12379-1-AP) |
| Rabbit polyclonal anti-SFPQ/PSF | 1/2,000 | Proteintech (#15585-1-AP) |
| Mouse monoclonal anti-SFPQ/PSF | 1/2,000 | Sigma-Aldrich (B92, #P2860) |
| Mouse monoclonal anti-TP53 | 1/5,000<br>2μL (ChIP) | SantaCruz (DO-1, #SC-126) |
| Rabbit polyclonal anti-phosphoSer$^{15}$ TP53 | 1/2,000 | Cell Signaling Technology (#9284) |
| Rabbit monoclonal anti-XPC | 1/1,000 | Cell Signaling Technology (#12701) |
| Rabbit polyclonal anti-XRCC5 | 1/5,000 | Proteintech (#16389-1-AP) |
| Rabbit monoclonal anti-γH2AX | 1/500 (IF)<br>1/1,000 (WB) | Cell Signaling Technology (#2577) |
| Donkey anti-mouse IgG conjugated with Alexa Fluor 488 or 594 | 1/500 (IF) | Invitrogene (#A-21207) |
| Donkey anti-rabbit IgG conjugated with Alexa Fluor 488 or 594 | 1/500 (IF) | Invitrogene (#A-21206) |
| Goat anti-rabbit conjugated with HRP | 1/10,000 | Merck (#AP187P) |
| Rabbit anti-mouse IgG conjugated with HRP | 1/10,000 | Merck (#AP160P) |

| Probes | Dilution | Supplier (Cat. Number) |
|---|---|---|
| Human NEAT1 middle segment probes conjugated with Quasar®570 (Stellaris®) | 1/200 | Biosearch Technologies (SMF-2037-1) |
| Human GAPDH probes conjugated with Quasar®670 (Stellaris®) | 1/200 | Biosearch Technologies (SMF-2019-1) |

**SI Table 2.6. List of plasticware used in this project.**

| Plasticware/materials | Cat. number | Company |
|---|---|---|
| 1.5mL Eppendorf tubes | 10451043 | ThermoFisher, UK |
| 0.2 mL PCR tubes | AB0620 | ThermoFisher, UK |
| 6, 12, 24 and 96-well plates | 657160, 665180, 662160, 650185 | Greiner Bio-one, UK |
| 6cm and 10cm dishes | 628160, 664160 | Greiner Bio-one, UK |
| Cryotube vials | 122263-TRI | Greiner Bio-one, UK |
| 5mL and 10mL serological pipettes | 606107, 607107 | Greiner Bio-one, UK |
| 75cm$^2$ flasks | 658175 | Greiner Bio-one, UK |
| 10, 200 and 1000μL pipette tips | AXT002, AXT035, AXT051 | Appleton Woods, UK |
| 15mL and 50mL falcon tubes | 188271, 227270 | Greiner Bio-one, UK |
| 13mm glass coverslips | 11588492 | ThermoFisher, UK |
| 96 and 384-well RT-qPCR plates | BC0800, BC1384 | ThermoFisher, UK |
| Cell Scraper | 08100241 | ThermoFisher, UK |
| 1.5 ml Bioruptor® Pico microtubes | C30010016 | Diagenode |

**SI Table 2.7. List of equipment used in this project.**

| Equipment | Cat. number | Company |
|---|---|---|
| Haemocytometer | 10490171 | SigmaAldrich, UK |
| 2.5, 10, 200 and 1000μL pipettes | 15994320 | Gilson, UK |
| Pipette gun | SLS7010 | Scientific Laboratory Supplies, UK |
| T100 thermal cycler | 1861096 | BioRad, UK |
| QuantStudio5 RT-qPCR machine | A28140 | ThermoFisher, UK |
| Rocker | S2035-E | Labnet International, UK |
| Bench incubator | MDH1001-M-E | Medline Scientific, UK |
| 800TS Absorbance Reader | 40-300 | Biotek, UK |
| BD Accuri™ C6 Plus flow cytometer | 560477 | BD biosciences, UK |
| PowerPac™ Basic Power Supply | 1645050 | BioRad, UK |
| Mini Trans-Blot® Cell | 1703930 | BioRad, UK |
| Mini-PROTEAN® Tetra Vertical Electrophoresis | 1658001FC | BioRad, UK |
| Pioneer Precision Balance | 30429814 | Ohaus, USA |
| ChemiDocTM XRS | 1708265 | BioRad, UK |
| CometAssay Electrophoresis System II | 4250-050-ES | R&D Systems, UK |
| CometSlide™ | 4250-004-03 | R&D Systems, UK |
| DMi8 inverted fluorescence microscope | - | Leica microsystems, UK |
| THUNDER Imager Live Cell & 3D Assay | - | Leica microsystems, UK |
| NanoDrop™ 8000 spectrophotometer | ND8000LAPTOP | ThermoFisher, UK |
| Prism™ Refrigerated Microcentrifuge | C2500-R | Labnet International, UK |
| Prism™ Microcentrifuge | C2500 | Labnet International, UK |
| AccuBlock™ Digital Dry Baths | C1302 | Labnet International, UK |
| Mini-sub® agarose gel tank | 1664000 | BioRad, UK |
| Humidified chamber | - | - |
| IncuCyte S3 live-cell analysis system | 4647 | Sartorius, UK |
| Bioruptor® Pico | B01060010 | Diagenode, UK |

**SI Table 2.8. List of software used in this project.**

| Software | Version |
|---|---|
| Adobe Illustrator | 27.2 |
| Adobe Photoshop | 24.1 |
| BD Accuri C6 Plus | 1.0.23.1 |
| cBioportal | 5.2.3 |
| CellProfiler | 4.2.1 |
| Cutadapt | GALAXY Version 1.16.6 |
| DESeq2 | GALAXY Version 1.1.0 |
| DEXSeq | GALAXY Version 1.1.0 |
| Enrichr | - |
| EventPointer | 3.0 |
| FastQC | GALAXY Version 0.72 |
| Filter | GALAXY Version 1.1.0 |
| FPKM count | GALAXY Version 2.6.4.1 |
| Gene ontology database | - |
| gProfiler | - |
| GraphPad Prism | 9.0.2 |
| HTseq-count | GALAXY Version 0.9.1 |
| IGV visualizer | 2.8.2 |
| Image LabTM | 6.0 |
| ImageJ/Fiji | 1.53t |
| IncuCyte | 2022C |
| Infer Experiment | GALAXY Version 2.6.4.1 |
| Inner Distance calculator | GALAXY Version 2.6.4.1 |
| Java | 1.8.0 |
| KEGG | - |
| Las X | 3.7.4.23463 |
| Mendeley | 1.19.8 |
| Microsoft Office 365 | 2212 |
| MultiQC | GALAXY Version 1.8 |
| NanoDrop™ 8000 | 2.3.3 |
| NCBI BLAST search | - |
| PCR primer stats | 1.0 |
| Phyton | 3.7.9 |
| Primer3Plus | 2.0 |
| QualiMap RNA-Seq QC | GALAXY Version 2.2.2d |
| QuantStudio 5 software | v1.5.2 |
| R and R studio | 2022.12.0+353 |
| Reactome | - |
| Sambamba | 0.8.2 |
| SortSam | GALAXY Version 2.18.2.1 |
| Spyder | 5.0 |
| STAR mapping software | GALAXY Version 2.7.8a |
| TopHat2 | GALAXY Version 2.1.1 |
| UCSC in-silico PC | - |